Contents

We learn geology the morning after the earthquake.

- Ralph Waldo Emerson (1803-1882)

1

The Taupo Volcanic Zone

1.1 Introduction

The Taupo Volcanic Zone (TVZ) is an extraordinary natural laboratory for observing a wide range of geophysical processes. For the last two million years, immense tectonic forces have ripped and torn the brittle crust, forming the Taupo Fault Belt (TFB) and uplifting a set of ranges nearly 500 m high along the Paeroa Fault. Shallow seismicity in the region is frequent and widespread, with the most recent significant event the 1987 $M = 6.3$ Edgecumbe earthquake, which was accompanied by a 7 km surface rupture and an estimated $300 million of damage. Many other faults within the TVZ are active and present varying degrees of seismic hazard. The role of tectonic processes in the evolution and present state of the TVZ are discussed in Section 1.3.

Volcanic processes and their underlying magmatic causes also play a major role in shaping the landscape, both directly, through the eruption of a thick sequence of Quaternary volcanic deposits, or indirectly, by supplying heat to drive hydrothermal circulation. The TVZ is one of the most productive rhyolitic centres on Earth, with an average eruptive rate of 0.3-0.4 $m^3 s^{-1}$ since 2 Ma (Wilson *et al.*, 1995). Eruptions are typically large and caldera forming, the most recent being the 1.8 ka eruption of a 35 km^3 magma chamber at Taupo (Wilson, 1993). However, smaller basaltic and andesitic eruptions also occur, most notably the 1886 AD Tarawera eruption (Nairn

and Cole, 1981) and on-going volcanism at the northern and southern terminations of the TVZ. These events are the surface expression of complex magmatic processes in operation from several kilometres depth, where magma pools prior to extrusion, to the mantle from which melt originates (Charlier *et al.*, 2005; Price *et al.*, 2005; Wilson *et al.*, 2009). Section 1.4 discusses volcanic and magmatic activity as they pertain to the tectonic and geothermal evolution of the TVZ.

Geothermal circulation of fluids through the fractured, porous TVZ crust is driven by the prodigious quantities of heat supplied by magmatic intrusion and alteration of the lower-crust. Geothermal fluids upflow at more than twenty distinct locations within the TVZ and, in addition to their scientific worth, are of both cultural and economic value. Geothermal circulation is intimately linked to magmatic and tectonic processes, and in some instances the locations of hot upwelling fluids coincide with inferred basement faults (Wood, 1996; Wood *et al.*, 2001) or magma bodies (e.g., Christenson *et al.*, 2002). Prior treatment of the tectonic and magmatic activity of the TVZ is therefore a useful precursor to the discussion of geothermal activity in Section 1.5.

1.2 Location and definition

The boundary of the Taupo Volcanic Zone encompasses volcanic centres extending along a northeast trend from Mt. Ruapehu in the Central North Island to White Island off the Bay of Plenty coast (see Figure 1.1(a)). Wilson *et al.* (1995) propose a dual demarcation of the TVZ boundary based on the age and location of volcanic activity: old (2-0.34 Ma) and young (340 ka to present) TVZ. In this work, as in Figure 1.1(a), all references to the TVZ assume the latter definition. This region includes the recently active Taupo, Kapenga, Okataina, Reporoa, Ohakuri, Rotorua and Whakamaru volcanic centres, the Taupo Fault Belt and its southern and northern extensions, and all active geothermal fields.

On a larger scale, the TVZ represents the termination of the Tonga-Kermadec arc as it intersects the continental crust of New Zealand's North Island. Oceanic back-

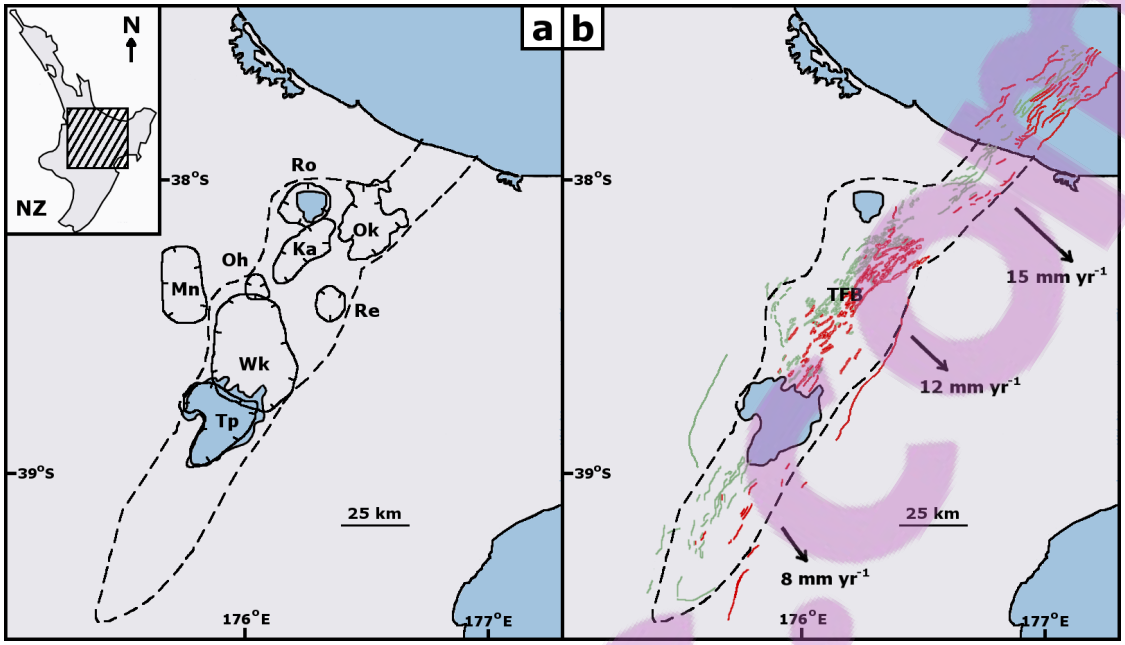

Figure 1.1: (a) Location of the Taupo Volcanic Zone (dashed line) in the context of New Zealand's North Island. The position of the Kapenga (Ka), Ohakuri (Oh), Mangakino (Mn), Okataina (Ok), Reporoa (Rp), Rotorua (Ro), Taupo (Tp) and Whakamaru (Wk) volcanic centres are shown (from Nairn *et al.* (1994), Wilson *et al.* (1995) and Gravely *et al.* (2007)). (b) Location of faulting within the TVZ (Rowland *et al.*, 2010) and offshore Bay of Plenty (Lamarche *et al.*, 2006). The traces of northwest and southeast dipping faults are marked in red and green respectively. The location of the Taupo Fault Belt (TFB) is also shown. Arrows indicate extension rates and directions from Wallace *et al.* (2004).

arc extension occurs along a NNE direction offshore from the TVZ in the Havre Trough, which itself is flanked by the Colville and Kermadec ridges. Both were formed by arc volcanism associated with subduction of the Pacific plate beneath the Australian plate; however, the two features have rifted apart from one another and the Kermadec ridge marks the position of the active arc. Several scenarios for the tectonic evolution of the North Island have been proposed (e.g., Nicol *et al.*, 2007; Schellart, 2007; Rowan and Roberts, 2008), but all involve the formation of a west dipping Hikurangi subduction margin extending from the east coast of the North Island through to Tonga since 17 Ma. Clockwise rotation of this margin at a rate of $\sim 3.5^\circ\,\mathrm{Myr}^{-1}$ is linked to extension in the TVZ (Nicol and Wallace, 2007).

Styles of volcanism and spatial relationships between magmatism and tectonism in the TVZ are segmented along strike. In the southern sections, from Mt. Ruapehu to Lake Taupo, volcanism is primarily andesitic (Price *et al.*, 2005; Charlier *et al.*, 2005) and faulting and magmatic activity coincide (Rowland *et al.*, 2010). It is argued that a similar relationship exists in the north of the TVZ, from the Okataina Volcanic Centre to the offshore Bay of Plenty, albeit at a greater rate of extension (Rowland *et al.*, 2010). In contrast, the central sections of the TVZ, which are the primary focus of investigations in this thesis, are characterised by voluminous rhyolitic volcanism (Wilson *et al.*, 1995), and offset corridors of magmatism (inferred from geothermal activity) and normal faulting (e.g., Bibby *et al.*, 1995; Rowland *et al.*, 2010).

1.3 Tectonism

High rates of tectonic extension are accommodated within the central TVZ by the reactivation of numerous faults. The intensity of faulting is particularly high within the Taupo Fault Belt (TFB), extending from the Taupo volcanic centre to the Okataina volcanic centre. This delineation diverges from the original description of the TFB (Grindley, 1960), which included faulting in the TVZ from Mt Ruapehu to the Whakatane Graben. As the attention of this thesis is focused on the central sections of the TVZ, all references to the TFB assume this restricted range.

Rowland and Sibson (2001) propose that the relative scarcity of faulting from these bounding volcanic centres reflects soft-linked segmentation between rifting segments. These accommodation zones transfer displacement between the discrete rifting segments and are expected to exhibit pronounced heterogeneity in distributions of both stress and fracturing. Within rift segments, faulting is primarily normal, producing dip-slip faults oriented sub-parallel to the strike of the rift. Faults strike orthogonal to the direction of extension, except in the Whakatane Graben where interaction with the North Island Dextral Fault Belt may introduce some obliquity (Rowland and Sibson, 2001; Acocella *et al.*, 2003; Mouslopoulou *et al.*, 2007).

Studies of the GPS velocity field for the North Island indicate a variable opening rate for the TVZ (Wallace *et al.*, 2004). Extension of 7-8 mm yr^{-1} south of Taupo increases to the northeast along strike and is ≈15 mm yr^{-1} at the Bay of Plenty coast (Figure 1.1(b)). This style of extension is consistent with the rotating arc model of Stern *et al.* (2006), in which the locus of rifting rotates in a clockwise direction at a rate of 7° Myr^{-1} about a pivot southeast of the southern termination of the TVZ. Alternatively, Villamor and Berryman (2006) propose a model in which oceanic rifting extends into the continental crust and progresses in a stepwise manner in a southwest direction. This produces a series of discrete rift segments, each opening at a constant rate along strike and at a magnitude proportional to the age of rifting for that segment.

1.3.1 The Taupo Fault Belt and Paeroa Fault

In the central TVZ, faulting is primarily localised within the Taupo Fault Belt, a 15 km wide, 60 km long corridor of high density normal faulting, close to the northwestern margin of the TVZ. Villamor and Berryman (2001) used topographical and fault trenching data to estimate a recent (< 64 ka) fault displacement rate through the TFB. These data indicated an opening rate of 1.9 mm yr^{-1} at the surface, increasing to 6.4 mm yr^{-1} at seismogenic depths for an inferred shallowing of fault dip. While this estimate is somewhat less than the 10-12 mm yr^{-1} indicated by GPS for the entire central TVZ (Wallace *et al.*, 2004), it is limited to that component of extension expressed as observable fault slip events within the TFB. Faults obscured by recent volcanic deposits, or extension accommodated on small scale structures, e.g., fractures, joints, etc., either within the TFB or the adjacent Taupo Reporoa Basin, are not included in this estimate. Such aseismic accommodation of extension plays an important role in the development of new faults and fault arrays and is the subject of further discussion in Chapter 3. Extension is also accommodated by dike injection, e.g., the 1886 Tarawera eruption (Nairn and Cole, 1981).

One of the largest faults within the TVZ is the Paeroa Fault, which is approx-

imately 30 km long at the surface and traverses the southeastern boundary of the TFB. Its southern termination corresponds with the location of geothermal upwelling at Orakeikorako. At the northern termination the fault splays into several smaller segments. The greatest offsets are located along the central sections where the Paeroa Range has been uplifted more than 500 m higher than the adjacent hanging-wall block. The fault is downthrown to the northwest (Figure 1.1(b)) and is oriented approximately parallel to the strike of the TVZ (see Figure 1.2). Villamor and Berryman (2001) estimate a long-term vertical displacement rate of $1.5\,\mathrm{mm\,yr^{-1}}$ for the fault, which makes it one of the fastest slipping in the TVZ. Dip of the fault plane is poorly constrained, but based on other TVZ faults is estimated as 70-80° at the surface, shallowing to 50-60° at seismogenic depths. A recent rupture history for the northern splays of the Paeroa Fault (Berryman *et al.*, 2008) indicates 3-4 ruptures per strand within the previous 16 kyr. Several strands ruptured concurrently and considerable variability in size and recurrence is observed. In four instances, surface rupture coincided with eruption at the nearby Okataina Volcanic Centre indicating a degree of interaction between tectonic and volcanic processes in the area.

The Paeroa Fault is also associated with several sites of geothermal circulation. Orakeikorako is a medium-sized (340 MW, from Bibby *et al.*, 1995) field located where the fault splays at its southern termination. Upflow of fluids here presumably takes advantage of the high fracture density associated with damage zones in fault tip regions (e.g. Curewitz and Karson, 1998; Kim *et al.*, 2004), or a possible relay structure linking the Paeroa Fault to the Whakaheke Fault further south (Rowland and Sibson, 2004). Circulation in these regions is further assisted through the renewal of permeability that accompanies fault rupture (e.g., Rojstaczer *et al.*, 1995; Sibson, 1990; Micklethwaite and Cox, 2004). Steady circulation of geothermal fluids can have a detrimental effect on permeability as fractures or pore space are sealed by mineralisation. Episodic fault rupture or migration of the fault tip may then generate the necessary stresses to reshear sealed fractures, or create new ones (Curewitz and Karson, 1998). Alternatively, fluid overpressuring accompanying a loss of permeability may lead to a cyclical regime, in which hydrofracturing is followed by

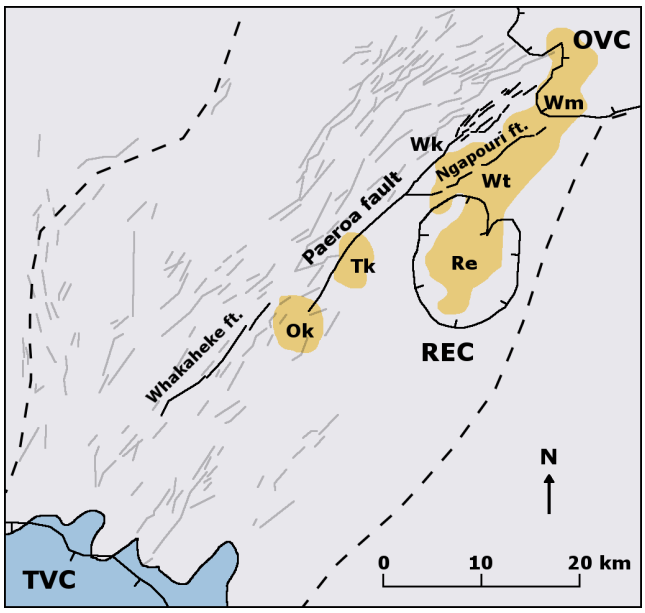

Figure 1.2: Location of the Paeroa fault and nearby features. The boundary of the TVZ is shown by a dashed line. The Orakeikorako (Ok), Te Kopia (Tk), Reporoa (Rp), Waikite (Wk), Waiotapu (Wt) and Waimangu (Wm) geothermal fields, delineated by the 50 Ω m resistivity contour, are shown in beige. Taupo (TVC) and Okataina Volcanic Centres (OVC), Reporoa caldera (REC) and the Ngapouri and Whakaheke Faults are also shown. Locations of other TVZ faults are shown in grey.

high mass flow rates and mineralisation, leading to fracture resealing (e.g Grindley and Browne, 1976; Henneberger and Browne, 1988; Sibson, 1990).

Te Kopia geothermal field is situated in the southern section of the Paeroa Fault. Outflow of hydrothermal fluids occurs principally in the footwall block with large areas of steaming, altered ground visible on the 220 m high fault scarp (Figure 1.3). Soengkono (1999) proposed that the location of this field corresponded to the intersection with fault perpendicular lineaments, perhaps representing older structures and sources of permeability. Alternatively, the footwall may exhibit enhanced permeability through fracturing caused by displacement gradients along the fault trace (Ferrill and Morris, 2001; Rowland and Sibson, 2004). Geothermal activity at Te Kopia has evolved over a period of 120 kyr (Bignall and Browne, 1994) in response to episodic fault rupture and uplift of the footwall block. A drop in the water table results in the draining of pore fluids from regions of the footwall and a cessation

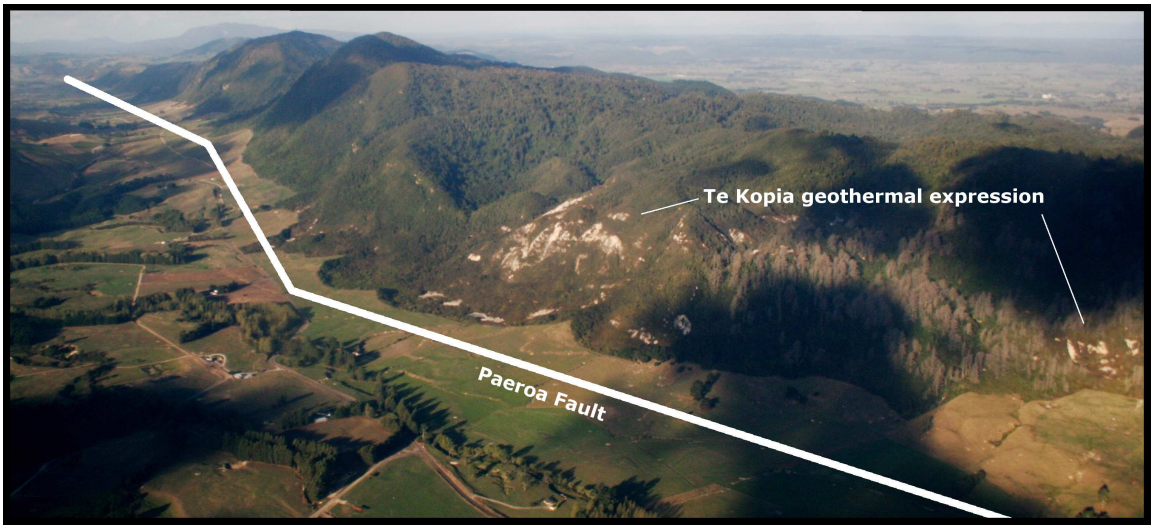

Figure 1.3: Aerial view of geothermal expression in the Paeroa Fault scarp at Te Kopia. The approximate position of the Paeroa Fault is indicated. Photo: J. V. Rowland, University of Auckland.

of surface geothermal expression. Evolution of the field is further complicated by widespread alteration of the stratigraphy and attendant permeability distribution by the precipitation of silica as quartz into open pore volumes and fractures. These concepts are discussed further in Section 1.5.3 and Chapter 7.

Geothermal expression also occurs further north on the Paeroa Fault at the Waikite hot springs. Rowland and Sibson (2004) suggest this outflow originates east of the fault and that its westward migration is limited by fault itself. This is consistent with resistivity studies (Risk *et al.*, 1994), which indicate that thermal waters flow from the east and may originate from a deeper source between Waikite and the adjacent Waiotapu geothermal field. Geothermal activity also occurs at the larger Waiotapu-Waimangu-Reporoa system located on the upthrown side of the Paeroa Fault. Circulation within this system probably takes advantage of structural permeability associated with the Ngapouri Fault (Wood, 1994a) and faulting associated with the Okataina Volcanic Centre and Reporoa Caldera (Nairn *et al.*, 1994). The degree of hydrological connection between the three fields is difficult to establish (Giggenbach *et al.*, 1994).

1.3.2 Seismicity

The TVZ is a seismically active region containing a large number faults that pose some degree of hazard to the region (Van Dissen *et al.*, 2003; Berryman *et al.*, 2008; Canora-Catalan *et al.*, 2008). The frequent nature of seismicity is a consequence of the high extension rate across the rift, which must be accommodated by discrete episodes of slip on existing faults, i.e., earthquakes. Deformation is largely extensional, which is reflected by the primarily normal earthquake focal mechanisms that prevail for shallow TVZ earthquakes (Hurst *et al.*, 2002). However, there is some evidence for an oblique component of rifting (Acocella *et al.*, 2003). Coseismic displacement of fault blocks is dip-slip, characterised by a loss of elevation in the hanging-wall and uplift of the footwall (e.g. Barrientos *et al.*, 1987; Beanland *et al.*, 1990). Fault rupture is also accompanied by a net withdrawal of the two fault blocks away from one another (see Figure 1.4(a)), thereby accommodating tectonic extension. Repeated episodes of this displacement pattern generates a fault scarp and a significant vertical displacement across the fault, e.g., the >500 m high Paeroa Ranges (Figure 1.4(b)).

The most recent large, surface-rupturing TVZ earthquake was the 1987 $M = 6.3$ Edgecumbe earthquake. Located in the Whakatane graben in the northern TVZ, the focal mechanisms of the main shock and aftershocks were predominantly normal with a small component of strike-slip (Anderson *et al.*, 1990). The fault plane is nearly planar and dips at 45±10° from a depth of 8 km to the near surface, where it steepens (Anderson *et al.*, 1990). The main shock opened up a 7 km long surface rupture of the Edgecumbe fault, which recorded a maximum vertical offset of 2.5 m (Beanland *et al.*, 1990) and doubled the height of the fault scarp. Previous activation of the fault is expected to have occurred close in time to the 1315 AD Kaharoa eruption and there is evidence of an earlier Holocene event. Thus the 1987 rupture relieved at least 700 years of stress build up on the fault.

The development and reactivation of existing faults is a frictional phenomenon and is therefore primarily restricted to the brittle upper-crust (Scholz, 1988). Fault

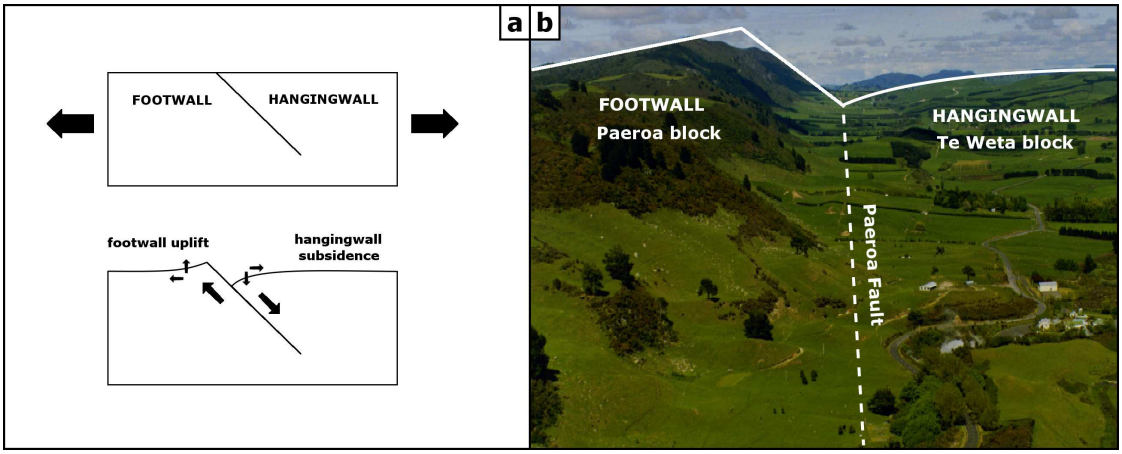

Figure 1.4: (a) Conceptualised displacements of the hanging-wall and footwall blocks during a normal dip-slip earthquake. Down-dip displacement of the hanging-wall block has both horizontal (withdrawal from fault scarp) and vertical (loss of elevation) components. Up-dip displacement of the footwall similarly results in withdrawal of the fault block and uplift at the surface. (b) Aerial view of the Paeroa Fault scarp, formed from multiple dip-slip displacement events illustrated in (a). The depression created at the base of the scarp has been infilled by alluvial sediments and thus the precise location of the fault trace is obscured. Its approximate position is shown by the dashed line. Photo: L. Homer, GNS Science.

reactivation occurs when shear stress on the fault plane exceeds a frictional threshold that depends on the normal stress on the fault. This is expressed by Amonton's law, i.e.,

$$\tau > \mu_s \sigma_n, \tag{1.1}$$

where τ is shear stress, μ_s is the static coefficient of friction of the fault plane, and σ_n is the normal stress. When this criterion is satisfied a rupture develops and propagates along the fault plane. During rupture propagation, fault friction follows a more complex constitutive law (Dieterich, 1979; Ruina, 1983); however, as the rupture encounters the ductile lower-crust the rupture front rapidly loses energy and is arrested (Scholz, 1998). Thus, earthquake nucleation and propagation is limited to the brittle upper-crust (Scholz, 1988), the lower limit of which is defined by the brittle-ductile transition (BDT). Based on locations of earthquake hypocentres, the

depth to this transition is approximately 6-8 km within the TVZ (Bryan *et al.*, 1999). This has important implications for geothermal circulation, which relies on basement permeability supplied by a pervasive network of faults and fractures (Rowland and Sibson, 2004). Limitation of fracture permeability to depths shallower than 8 km places an inferred lower bound on the extent of geothermal circulation (Bibby *et al.*, 1995). Providing the pattern of circulation within the TVZ represents convective flow through a porous medium heated from below, the aspect ratio of fields should be near unity. Under this assumption, the mean spacing of TVZ geothermal fields of 10-15 km is consistent with a convective system base at a depth of 5-8 km (Bibby *et al.*, 1995), which is in agreement with the seismogenic limit of 6-8 km (Bryan *et al.*, 1999).

1.4 Volcanism and magmatism

The Taupo Volcanic Zone is one of the most productive rhyolitic volcanic centres on Earth and comparable to the Yellowstone system in terms of erupted volume (Houghton *et al.*, 1995). Twenty-five caldera forming eruptions, localised within eight volcanic centres (see Figure 1.1(a)), have occurred since the onset of volcanism approximately 1.6 Ma (Houghton *et al.*, 1995; Wilson *et al.*, 1995; Gravely *et al.*, 2007; Wilson *et al.*, 2009). These events have produced 15-20 000 km^3 of erupted material, the largest component being high silica rhyolitic magma, but with lesser contributions by andesitic, dacitic and basaltic magmas in decreasing order (Wilson *et al.*, 1995). The cumulative effect of these eruptions has been the development of > 2 km thick series of layered ignimbrites of variable age, extent and material properties. These deposits are useful in dating the size and timing of fault rupture as they represent known time horizons (Villamor and Berryman, 2001; Nicol *et al.*, 2006; Berryman *et al.*, 2008; Canora-Catalan *et al.*, 2008; Wilson *et al.*, 2009).

1.4.1 Heat flux of the TVZ

Perhaps the most comprehensive account of heat transfer through the TVZ is given by Hochstein (1995). In this paper, total heat transferred through the crust is subdivided into four components: (i) episodic volcanic extrusion, (ii) quasi-continuous volcanic heat discharge, (iii) conductive heat transfer, and (iv) convective heat transfer by geothermal circulation. The final component, convective transfer, is estimated through the collation of chloride flux studies (Ellis and Wilson, 1955), surface heat loss surveys and natural-state reservoir modelling (see Hochstein, 1995, and references therein). Heat output from the majority of geothermal fields is on the order of 50-100 MW, consistent with a similar itinerary by Bibby *et al.* (1995) and one-dimensional analytical models of rainfall-recharge geothermal systems proposed by Weir (2009); the total convective transfer estimated to be between 3000 and 4000 MW for the 200 km length of the TVZ. Measured on a 'per 100 km segment' basis, this value is more than three times higher than other volcanic arcs, leading Hochstein (1995) to propose the convective component be further decomposed into a "heat sweep" and magmatic component. The heat sweep represents convective transfer by meteoric fluids only, while the remainder is supplied by magmatic fluids originating from dewatering of the accretionary prism and sediments underthrust by the subducting slab (Moore and Vrolijk, 1992). Based on geochemical observations, Giggenbach (1995) estimates the magmatic contribution to geothermal fluids to vary between 4 and 26% depending on the field.

Other estimates of heat transfer by geothermal circulation within the TVZ are on the order of 4000 MW (Stern, 1987; Bibby *et al.*, 1995), although Stern (1987) notes that omission of hidden geothermal systems, e.g., Mokai, would underestimate this value. For the 200 km long, 25 km wide TVZ corridor, this total convective heat transfer is equivalent to an average surface heat flux of approximately $0.8\,\mathrm{W\,m^{-2}}$, while Hochstein (1995) quotes a range of 0.6-0.8 $\mathrm{W\,m^{-2}}$. This heat flux is far in excess of the average conductive heat transfer through the continental crust of 0.05-0.07 $\mathrm{W\,m^{-2}}$ (Chapman, 1986).

1.4.2 Stratigraphy of the TVZ

The immense volcanic productivity of the TVZ, which has occurred at a mean rate of ≈0.3-0.4 $m^3 s^{-1}$ since 2 Ma (Wilson *et al.*, 1995), has had a considerable influence on the stratigraphy of the region. The shallow regions of the crust (< 2 km) are characterised by thick, variously welded ignimbrite sheets, buried andesite layers, rhyolite domes, and fluvial and lacustrine sediments (e.g. Wilson *et al.*, 1984; Browne *et al.*, 1992; Grindley *et al.*, 1994; Wood, 1994a; Wilson *et al.*, 1995, and references therein). The varied material properties of this stratigraphy influence both the geothermal circulation and faulting that abound within the TVZ (Rowland and Sibson, 2004; Rowland and Simmons, 2012).

Precise constraint on local TVZ stratigraphy is obtained through drilling associated with geothermal exploration, or from exposed fault scarps. For example, from exploratory drillholes at the Waiotapu geothermal field Grindley *et al.* (1994) reports the presence of several ignimbrite sheets with eruption ages between 1.18 and 1.45 Ma (Wilson *et al.*, 2010). These range in thickness from several 10's to several 100's of metres and, depending on the degree of welding, act as reservoir or confining units. In this region, ignimbrites are overlain at the surface by the Huka Falls formation, a series of lacustrine siltstones and sandstones deposited while most of the TVZ was covered by a large lake during a period of volcanic quiescence (Rosenberg *et al.*, 2009).

Elsewhere, drilling at the Rotokawa and Ngatamariki geothermal fields indicate a sequence of rhyolites and silicic tuffs, overlying the Wairakei Ignimbrite (Browne *et al.*, 1992). Beneath this layer is the extensive Rotokawa andesite, which is more than 1 km thick in places and the deepest volcanic unit in the area (the greywacke basement contact occurs directly below). The presence of such a large, thick andesite unit indicates a substantial role of andesitic volcanism in the history of the eastern TVZ.

Drilling at Wairakei and Tauhara geothermal fields indicates that the stratigraphy here is dominated by the relatively impermeable Huka Falls formation overlying the

Waiora formation, a series of sedimentary strata, breccias, and rhyolitic lavas and tuffs that serve as the geothermal reservoir (Wood, 1994b), before bottoming out in impermeable Wairakei ignimbrite (Grindley, 1982; Rosenberg *et al.*, 2009, and references therein). The Wairakei ignimbrite, laid down during a period of intense caldera eruptions between 320 and 340 ka (Houghton *et al.*, 1995; Wilson *et al.*, 1995, 2009), is up to 1 km thick in some drillholes but absent from others. Geothermal production mainly occurs in the Waiora formation, which is overlain by the Huka Falls formation, an impermeable caprock that separates the hot geothermal aquifer from cooler surface waters.

Nature of basement rock

Mesozoic metasedimentary rocks of the Torlesse terrane (Mortimer, 1994) outcrop to the east of the TVZ and are encountered in geothermal drilling at several locations within; however, consensus has not yet been reached on their extent beneath the TVZ. Stratford and Stern (2006) and Stern *et al.* (2006), on the basis of seismic velocity data, propose that extension of basement rock beneath the TVZ is accompanied by extensive magmatism, such that the intrusive, mantle derived rock is the abundant crustal component. Greywacke basement, which occurs outside the spreading region, is reduced to a minor component within.

Alternatively, others (Wilson *et al.*, 1995; Heise *et al.*, 2007; Rowland *et al.*, 2010) hold that greywacke basement rock is extensive and largely continuous throughout the TVZ, but interrupted in some locations by plutons and feeder dikes. Crustal extension, accommodated by faulting to the base of the brittle crust and subsidence of the downthrown fault blocks (i.e., the hanging-walls), has lowered the basement surface to its present position. Quaternary volcanic products therefore play an important role in filling the basin and obscuring the basement contact. The depth to greywacke contact is variable throughout the TVZ, but can be inferred from geophysical imaging and directly located by geothermal drilling. At the Broadlands-Ohaaki geothermal field, the basement contact is between 1000 and 2000 m depth and shallows toward the eastern margin of the TVZ (Hedenquist, 1990). At the nearby

Rotokawa geothermal system, drilling indicates greywacke at depths 2000 m and greater (Browne *et al.*, 1992). However, at the adjacent Wairakei field no basement has been intersected despite drilling to depths of 2700 m (Glynn-Morris *et al.*, 2009). Greywacke basement is encountered at Ngatamariki at a depth of >3000 m (Burnell and Kissling, 2009). Further north, at the Kawerau geothermal field, basement rock occurs at shallower depths of approximately 1000 m (Wood *et al.*, 2001). Additional constraint on the depth to basement is provided by geophysical investigations. For example, gravity maps can be used to infer the thickness of volcanic deposits overlying greywacke, providing the density contrast between the two is known. For mean TVZ volcanic infill and greywacke densities of 2180 $\mathrm{kg\,m^{-3}}$ and 2670 $\mathrm{kg\,m^{-3}}$, respectively, Rogan (1982) estimates depths to basement within the Taupo and Rotorua volcanic centres (see Figure 1.1(a)) of approximately 2-3 km. DC resistivity (Risk *et al.*, 1994) and magnetotelluric surveys (Heise *et al.*, 2007) also indicate a continuous basement layer, approximately 20 km thick beneath the Kaingaroa Plateau (immediately to the east of the TVZ) thinning to ∼10 km within the TVZ. In the Waiotapu region, Risk *et al.* (1994) inferred the basement contact at the Kaingaroa fault, effectively the eastern margin of the TVZ, to be only a few hundred metres beneath surface ignimbrites. West of this point the basement is progressively downthrown by a series of northwest dipping faults (Risk *et al.*, 1994).

1.4.3 Magmatic intrusion

Surface volcanism via dike injection, which occurred most recently during the 1886 AD Tarawera Basalt eruption forming the 17 km long Tarawera Linear Vent Zone (Nairn and Cole, 1981), is a second order contribution to the total volume of eruptive products. However, dike injection into the shallow crust plays an important role in the modulation of the tectonism, caldera volcanism and geothermal circulation of the TVZ (Rowland *et al.*, 2010). For example, Nairn *et al.* (2005) propose that dike injection primed an existing rhyolite magma body prior to its 1315 AD Kaharoa eruption from Tarawera vents, and also primed the nearby Waiotapu geothermal

system (through an influx of CO_2) for later hydrothermal eruptions. Dike injection has also been postulated to account for the shortfall in extension by fault displacement (6 mm yr^{-1}, from Villamor and Berryman, 2001) vs. total TVZ extension from GPS data (10-12 mm yr^{-1}, from Wallace *et al.*, 2004). For instance, emplacement of the 1-2 m wide 1886 AD Tarawera dike (Nairn and Cole, 1981) accommodated up to 200 years of accumulated extensional strain (Rowland *et al.*, 2010). While dike injection may not directly induce fault rupture (Seebeck and Nicol, 2009) in the TVZ, as it does in other rift settings (Rubin and Pollard, 1982; Rowland *et al.*, 2007), its relative contribution to extension accommodation indirectly controls the proportion that must be taken up by seismic mechanisms, e.g., frictional slip on faults, fractures and joints. Rowland *et al.* (2010) further suggest that when mafic dikes are intruding from the mantle, they either penetrate to the surface or initiate alternative styles of volcanism based on the current state of a postulated silicic mush zone - a region of elevated melt, dikes, sills and other intrusions at depths >4 km. Mafic dikes intersecting this layer prime the system for further rhyolitic diking or larger rhyolitic caldera forming eruptions (Nairn *et al.*, 2005).

Intrusion of mantle magma bodies into the TVZ mid-crust is thought to supply the necessary heat to sustain geothermal convection (Bibby *et al.*, 1995) and its associated anomalously high heat flux (Hochstein, 1995). The nature and frequency of these intrusions, and the attendant heat input they represent, then exerts an important control on the location, spacing and heat output characteristics of the TVZ geothermal fields. On the basis of the phase properties of an H_2O-NaCl system, McNabb (1992) proposed that the heat input at the base of the convective system could be described as a hotplate of temperature 350 to 400°C. Alternatively, Kissling (1998, 1999) found that models of hydrothermal circulation in the vicinity of a cooling pluton could produce geothermal fields with characteristics typical of the TVZ for periods of a few thousand years. Multiple intrusion events in similar locations were required to produce sustained and spatially stable convective cells.

Figure 1.5: Artist's Palette silica sinter terrace at Orakeikorako geothermal field. Photo: D E Dempsey, University of Auckland.

1.5 Geothermal activity

Outflow of high temperature geothermal fluids occurs at more than twenty locations throughout the Taupo Volcanic Zone. At many of these sites, interaction between the rising fluids and local hydrological flow have produced a stunning array of geyser activity, boiling mud pools, colourful sinter deposits (see Figure 1.5), hot springs and fumaroles (e.g., Hedenquist, 1990; Bignall and Browne, 1994; Hunt *et al.*, 1994; Scott and Cody, 2000; Bignall and Harvey, 2005; Glover and Mroczek, 2009). The high degree of protection provided to these regions through various resource management and environmental legal frameworks attest to their immense cultural and economic value to New Zealand. For instance, Orakeikorako, Waiotapu-Waimangu and Rotorua geothermal fields support important commercial tourist operations, while up to 700 MW of electricity generation occurs at the Wairakei-Tauhara, Broadlands-Ohaaki, Mokai, Kawerau, Ngatamariki and Rotokawa geothermal fields.

1.5.1 Convective cells

Hot upwelling of hydrothermal fluids throughout the TVZ is driven by magmatic heating within the crust. The density of water is strongly dependent on temperature, such that local heating of a volume of water causes expansion and buoyancy relative to its cooler surroundings. The volume of water begins to rise, while cooler water flows in from the side to replace it, renewing the cycle. At the surface, hot rising fluids encounter cooler meteoric groundwater, resulting in complex mixing processes and lateral flows. Cool surface waters, typically supplied by rainwater, percolate through fractures and cracks in the rock to the base of the brittle crust, completing the convective cycle. Geothermal systems are regarded as single-pass (Bibby *et al.*, 1995), i.e., water enters the system as rainfall recharge and exits into near-surface groundwater systems; this is a similar configuration to the black-smoker seafloor hydrothermal systems considered by Lowell and Burnell (1991).

Geothermal convection within the TVZ is notable for the multitude of convective cells in close horizontal proximity to one another. McNabb (1975) interpreted the ensemble as a single convective system produced by uniform heating of a porous medium from below. The problem of convection between two horizontal plates in a porous medium first received attention in papers by Horton and Rogers (1945) and Lapwood (1948). Adopting the approach taken by Rayleigh (1916), but modified to account for Darcy flow and permeability, they determined the onset of convection, parameterised by the Rayleigh number, as a function of vertical temperature gradient and material properties of the fluid. This work has since been extended by others to consider alternative boundary conditions (e.g., Nield and Bejan, 1998), temperature dependent material parameters (Strauss and Schubert, 1977), and non-isotropic permeability (Kissling, 2004). Wooding (1978) applied the theory to the TVZ to estimate an average field spacing of 10-15 km and a depth of circulation of 3 km. On the basis of more recent seismic data (Bryan *et al.*, 1999) this is now regarded as too shallow, and circulation probably traverses the seismogenic crust (∼8 km deep).

While natural convection is regarded as the principal mechanism for advection

of groundwater in the TVZ, topographical pressure gradients also play a role in subsurface heat and mass transfer (e.g., Smith and Chapman, 1983; Forster and Smith, 1989). The relative importance of these two forcings, topographical versus buoyancy, is estimated by considering the pressure perturbation of each, i.e.,

$$\Delta P_{topo} = \Delta h \rho_f g, \qquad \Delta P_{bycy} = \Delta \rho_f L g, \tag{1.2}$$

where Δh is the difference in elevation between recharge and upflow zones, ρ_f is fluid density at the surface, $\Delta\rho_f$ is the difference between ρ_f and the depth-averaged fluid density in an upflow zone, L is the vertical dimension of a geothermal plume, and g is the acceleration due to gravity. Due to a high density of faulting, topography in the central TVZ is varied and averages between 350 and 550 masl between Taupo and Rotorua; a conservative estimate for Δh would be 200 m, yielding $\Delta P_{topo} \sim 2$ MPa. For geothermal upflow temperatures between 250 and 300°C, corresponding to upflow densities of 800 to 850 kg m^{-3}, and supposing the base of the convective system lies between 6 and 8 km (Bibby *et al.*, 1995; Bryan *et al.*, 1999), ΔP_{bycy} probably ranges between 9 and 16 MPa. Thus, for the majority of geothermal systems in the TVZ, natural convection is likely to be the primary driver groundwater flow; however, in some locations, extreme topographical offsets could affect nearby geothermal systems, e.g., the Waimangu system near Mt Tarawera (1024 masl), the Waiotapu and Reporoa systems near the Paeroa Ranges (979 masl).

Bredehoeft and Papadopulos (1965), assuming steady vertical groundwater flow, developed a mathematical description of the temperature-depth profile in a confined layer. Depending on the rate and direction of flow, a linear conductive temperature gradient is deformed toward an exponential type-curve. The analysis can also be inverted to estimate groundwater velocity for a given temperature-depth profile. Figure 1.6(a) shows temperature-depth profiles taken from several TVZ geothermal fields, and the same profiles normalised against a vertical flow dimension of 7 km and approximate limiting temperatures for each of the profiles. Plotted together, these data appear to be well-bracketed by type-curves with β values between -10 and -50,

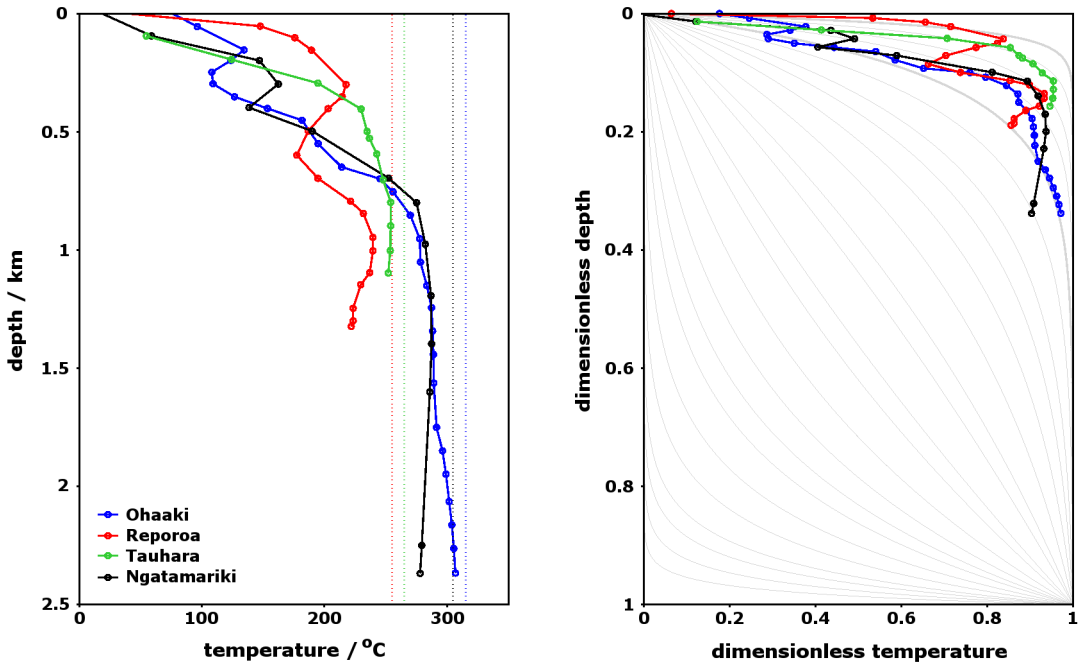

Figure 1.6: (a) Down-well temperature profiles of several TVZ geothermal systems (Wood, 1994a; Mannington *et al.*, 2004; Bignall, 2009; Clearwater *et al.*, 2012). (b) Dimensionless temperature-depth profiles, using vertical system depth of 7 km and limiting temperatures given by dashed lines in (a), superimposed on type-curves from Bredehoeft and Papadopulos (1965). Curves corresponding to β =-10 and -50 have been bolded.

where β is a combination of advective and conductive heat transfer parameters, given by

$$\beta = \frac{c_0 \rho_0 v_D L}{\kappa}, \tag{1.3}$$

where c_0, ρ_0 and v_D are the specific heat, density and vertical Darcy velocity of the fluid, L is the vertical dimension of the flow regime, and κ is the porosity-weighted effective thermal conductivity. Inverting (1.3), and for $c_0 = 4.2 \times 10^3\,\mathrm{J\,K^{-1}}$, ρ_0 = 800-900 $\mathrm{kg\,m^{-3}}$, $\kappa = 2.3\,\mathrm{W\,m^{-1}\,K^{-1}}$, $L = 7\,\mathrm{km}$, and β between -10 and -50, the temperature profiles in Figure 1.6 are consistent with upflow velocities between 8.7×10^{-10} and $4.8 \times 10^{-9}\,\mathrm{m\,s^{-1}}$.

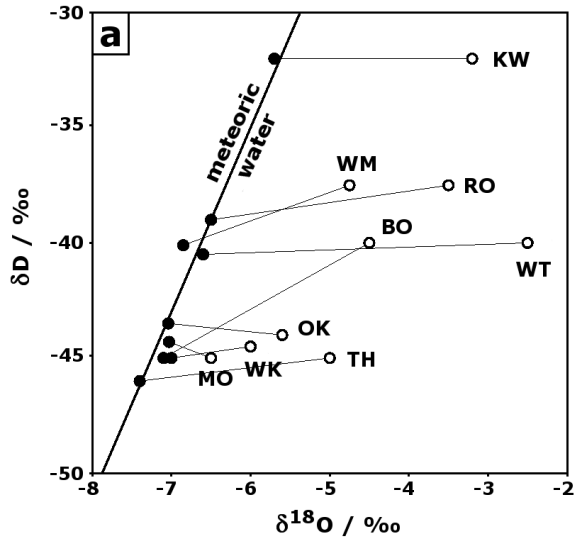

Figure 1.7: Isotopic composition of TVZ geothermal reservoir waters (open circles), corrected for steam loss and mixing, relative to local ground water (closed circles). Solid tie lines connect reservoir waters with their likely source of recharge. The meteoric water line is shown. After Dempsey *et al.* (2012d). BO = Broadlands-Ohaaki, KW = Kawerau, MO = Mokai, OK = Orakeikorako, RO = Rotorua, TH = Tauhara, WK = Wairakei, WM = Waimangu, WT = Waiotapu.

Source of recharge

Fluid flow through TVZ geothermal systems is regarded as 'once through', i.e., fluids enter the crust, percolate to depth where they are heated, and rise to be discharged at the surface (Bibby *et al.*, 1995). In this picture, fluids do not continually circulate, and the convective system is therefore recharged from an external source. McNabb (1992) cites geothermal fluid discharge of $3000\,\mathrm{kg\,s^{-1}}$ and proposes meteoric water (i.e., rainwater) entering the system at the surface as the principal contribution to recharge. Kissling (2004), using different estimates, comes to a similar conclusion, specifically that meteoric recharge comprises $\sim$2% of the total rainfall across the TVZ.

Magmatic dewatering also contributes to convective recharge, however these fluids typically enter at the base of the system. Magmatic contributions can be inferred

from anomalous isotopic ratios, e.g., ^{2}H, ^{3}He, ^{18}O, which deviate from those of surface waters that are typically in equilibrium with atmospheric values. For example, arc-type magmatic water is enriched with ^{18}O and deuterium (D); its mixture with meteoric water in TVZ geothermal systems results in elevated δD and δ^{18}O signals (see Giggenbach (1995) and Figure 1.7). As boiling can occur during upflow - temperature profiles often follow boiling point for depth curves - these data must be corrected for steam loss (Simmons *et al.*, 1994). Water-rock interaction also leads to ^{18}O enrichment (e.g., Craig, 1963).

Helium isotope studies are also used to identify the presence of magmatic fluids (e.g., Hulston and Lupton, 1996; Kennedy and van Soest, 2007). In the TVZ, the majority of geothermal fields exhibit elevated ^{3}He/^{4}He ratios, averaging six to seven times atmospheric values (Hulston and Lupton, 1996). Some fields on the margins of the rhyolitic central section of the TVZ have lower ratios, between one and four times atmospheric. Nevertheless, these data strongly suggest magmatic fluid contribution to TVZ geothermal fields. Giggenbach (1995) estimated magmatic fluid contributions for several TVZ geothermal fields, including Waiotapu (26%), Wairakei (8%), Mokai (4%), Kawerau (11%), Ohaaki (12%) and Rotokawa (7-19%).

Residence time

Stable isotope analysis of the deep waters at Wairakei geothermal field was conducted by Stewart (1978). These data showed a deuterium content similar to present day surface waters indicating fluids are meteoric in origin. Furthermore, meteoric waters older than 12 000 years have a distinct deuterium signal due to their 'glacial' origin, i.e., entering as recharge during the previous ice age. The absence of such a signal suggests the residence time at Wairakei is less than 12 kyr.

Giggenbach *et al.* (1994), on the basis of ^{13}C exchange between carbon dioxide and methane (Giggenbach, 1982), established residence times for geothermal fluids at Waiotapu geothermal system. Younger fluids predominate in the north with an age range of 0.3 to 3.3 kyr and a mean of 2 kyr. Progressing south, in the middle sections of the field, fluids are comparatively older, with ages of 6, 10 and 38 kyr

measured (mean 18 kyr). In the south of the field, ages of 11 to 280 kyr are given. The observed variety in fluid residence time is interpreted as north to south transport of fluids through the field at an approximate velocity of $40\,\mathrm{m\,kyr^{-1}}$. Alternatively, variable mixing of younger and older fluid sources in the north and south could account for the age distribution.

Kissling (2004), using Stewart's constraint on residence time and accounting for rainfall throughput, obtained an estimate for basement porosity of $\approx 1\%$. For an estimated rainfall catchment servicing TVZ fields of $4500\,\mathrm{km^2}$ and a depth of circulation of 8 km, $360\,\mathrm{km^3}$ of water are stored in the 1% porosity rock. If steady-state is assumed then a residence time of 3000 yr is obtained by dividing the total hosted fluid volume ($360\,\mathrm{km^3}$) by the geothermal outflow rate ($4000\,\mathrm{kg\,s^{-1}}$). Although this estimate is sensitive to the size of the rainfall catchment, the depth of circulation (6-8 km), and extended residence within high porosity near surface (< 2 km) volcanic deposits, it nevertheless provides an order of magnitude constraint on the porosity of the deeper crust. In simulations presented here, greywacke porosities of 1-3% are used.

Weir (2009) estimates geothermal residence time on the basis of a mathematical model for meteoric rainfall. This work uses the 2% rainfall infiltration rate from Kissling (2004), a porosity of 2%, and a circulation depth of 7 km, to estimate residence times on the order of 5 000 years. In addition, they describe suppression of the conductive geothermal temperature gradient in regions of infiltrating rainwater, the magnitude of this effect being proportional to the down-flow velocity. Heat output of geothermal fields is linked to the dimensions of the convective system, area of rainfall recharge, and maximum temperature within the plume. For TVZ parameters, the model produces an order-of-magnitude estimate of 200 MW for a single field.

1.5.2 Distribution of geothermal fields

The distribution of geothermal circulation in the TVZ, while manifest at the surface in many locations, is well-described by resistivity surveys of the near surface. The

flow of geothermally heated waters through the subsurface has a positive effect on the electrical conductivity of rock. Furthermore, while the salinity of these waters is typically no more than 0.2 to 0.3 wt % (Giggenbach, 1995), much less than the ∼3% of seawater, the presence of dissolved ions nevertheless improve local conductivity. Finally, hydrothermal alteration of near-surface volcanic deposits produces conductive clay-species, imprinting the past presence of geothermal activity on the rock itself, e.g., the extinct Ohakuri geothermal system (Henneberger and Browne, 1988). Within the TVZ, geothermal rocks are up to two orders of magnitude more conductive that non-geothermal rocks, which greatly assists in the identification of field boundaries (Risk *et al.*, 1994). Figure 1.8(a) presents electrical resistivity contours for the TVZ from a survey using a nominal array spacing of 500 m (Bibby *et al.*, 1995). These values represent the average resistivity of the upper 300 m of the crust. The eastern margin of the TVZ, often delineated by the Kaingaroa Fault, is well resolved by the high resistivity of greywacke in the Kaingaroa Plateau.

Resistivity values less than 50 Ω m are used to constrain regions of present geothermal activity and individual fields are plotted in Figure 1.8(b). The extensive Waiotapu-Waimangu-Reporoa-Waikite geothermal system, which occupies the Taupo Reporoa Basin, shares a continuous resistivity boundary. This may be due to shallow connections between the geothermal fields in the subsurface such that conductive fluids, and thus the resistivity anomaly, is smeared between fields. Alternatively, as discussed later in Chapters 6 and 7, this may represent a continuous zone of hydrothermally altered rock - a relic of past migration of the geothermal fields. Despite a continuous resistivity anomaly, Waiotapu, Waimangu and Reporoa are regarded as separate fields on the basis of non-contiguous zones of surface thermal manifestation and discrete inferred upflow zones. However, Bibby *et al.* (1994) showed that geothermal flow at Waikite and Waiotapu probably originates from the same deep upflow zone, thus these fields are continuous in Figure 1.8(b).

The Wairakei and Tauhara geothermal fields also share a continuous resistivity contour, despite their classification as separate fields. This continuity probably results from lateral flow between two separate deep upflows, due to the presence of the

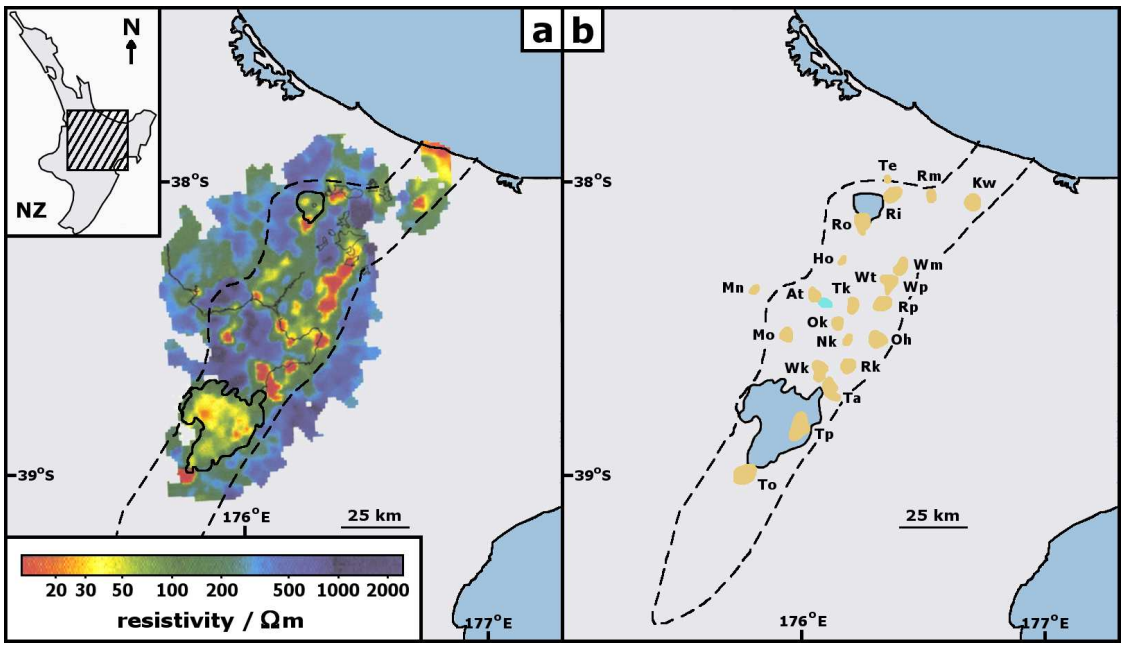

Figure 1.8: (a) Electrical resistivity map of the TVZ from Bibby *et al.* (1995). The Waikato river into which many geothermal fields drain, as well as several lakes in the OVC region are shown. (b) Positions and boundaries of TVZ geothermal fields shown in Table 1.1. To = Tokaanu, Tp = Taupo, Ta = Tauhara, Wk = Wairakei, Rk = Rotokawa, Oh = Ohaaki, Nk = Ngatamariki, Ok = Orakeikorako, Tk = Te Kopia, Rp = Reporoa, Wp = Waiotapu, Wt = Waikite, At = Atiamuri, Hr = Horohoro, Mo = Mokai, Mn = Mangakino, Ro = Rotorua, Ri = Rotoiti, Te = Taheke, Wm = Waimangu, Rm = Rotoma, Kw = Kawerau. The location of the extinct Ohakuri geothermal field is shown in blue.

impermeable Huka Falls formation at the surface (Mannington *et al.*, 2004).

The Taupo Reporoa Basin

The topographic low extending from the Taupo Volcanic Centre to the Okataina Volcanic Centre (see Figure 1.1(a)) and bounded to the east and west by the Kaingaroa and Paeroa Faults, respectively, is referred to here as the Taupo Reporoa Basin (TRB). This region was initially thought to be tectonic in origin (Rogan, 1982; Wilson *et al.*, 1984), produced by east tilting of the Paeroa block and down faulting at the Kaingaroa Fault, however, Nairn *et al.* (1994) demonstrated a volcanic origin for part of the depression, namely the Reporoa Caldera. The TRB is exceptional in the

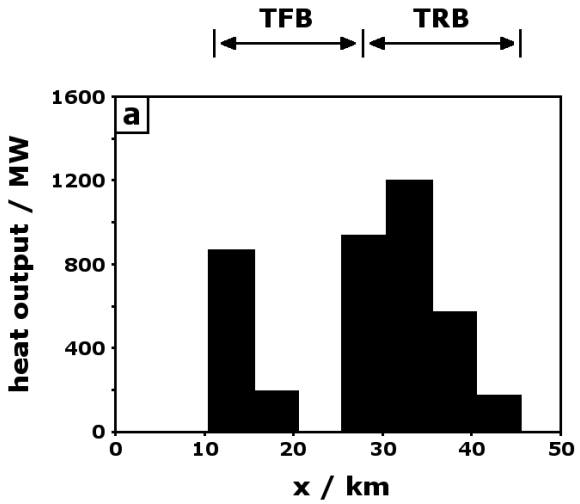

Figure 1.9: Across-strike geothermal heat output of the TVZ in 5 km bins from the Kaingaroa Fault, adapted from Bibby *et al.* (1995). Approximate extent of the Taupo Reporoa Basin (TRB) and Taupo Fault Belt (TFB) are shown.

context of the TVZ due to the extraordinary localisation of geothermal circulation within the region. The Waiotapu-Waimangu-Reporoa system, as well as Waikite, Te Kopia and Orakeikorako on the Paeroa Fault, and the Wairakei, Tauhara, Rotokawa, Ohaaki and Ngatamariki geothermal systems are within, or on, the boundaries of the TRB. Bibby *et al.* (1995) summarised this data by plotting the across-strike geothermal heat output (Figure 1.9) in 5 km wide bins from the eastern margin of the TVZ (using data reproduced in Table 1.1). These data show a peak in geothermal output within the TRB, a relative absence through the central sections including parts of the Taupo Fault Belt, and a reduced presence along the western margin of the TVZ (this includes the Mokai, Atiamuri, Mangakino, Horohoro and Rotorua fields).

The bimodal nature of Figure 1.9 has led many workers to speculate on the permeability structure of the upper-crust and the nature of the heat source beneath. Rift-scale numerical modelling of geothermal circulation by Kissling (2004) and Kissling and Weir (2005) assumed the TFB to represent a region of enhanced fracture permeability and a major conduit for down-flow of cool meteoric waters recharging the geothermal systems (Bibby *et al.*, 1995). This view is supported by observations of

high resistivity indicating cool temperatures to depths of 7 km (Bibby *et al.*, 2002), and by low geothermal temperature gradients relative to conductive gradients outside the TVZ (Thompson, 1980). Furthermore, MT imaging by Heise *et al.* (2007) identified a region of $> 4\%$ partial melt at a depth of 15-20 km, underlying a region of cooled intrusives at 6-8 km depth (Sherburn *et al.*, 2003). The TRB is thus proposed as the locus of modern magmatism (Rowland *et al.*, 2010), which drives geothermal heat transfer in the overlying brittle crust. This scenario is consistent with a geochemical analysis of TVZ geothermal fields undertaken by Giggenbach (1995). This indicated a 14% magmatic contribution to deep geothermal fluids for eastern TVZ fields, compared to 6% for western fields. The relatively higher production of magmatic fluids in the east implies correspondingly higher magmatic activity, or substantial differences in magmatic composition across the TVZ.

Western TVZ

Geothermal fields within and west of the TFB, including Mangakino, Mokai, Atiamuri and Horohoro, are typically of smaller area and lower heat output than those in the eastern TVZ (see Figure 1.8(b) and Table 1.1). The exception is Mokai geothermal field, whose estimated natural output of 400 MW supports 96 MW of geothermal power generation. The western TVZ is also unique in that it hosts an extinct geothermal system, Ohakuri, whose presence is inferred from widespread hydrothermal alteration (Henneberger and Browne, 1988). Cessation of geothermal activity occurred at least 160 kyr ago, although whether this was due to a change in the deep heat source, hydrothermal self-sealing or simple migration to the nearby Atiamuri system is unknown. The field, however, exhibits a suite mineralisation and alteration patterns, and serves to illustrate the evolution of a rock assemblage by the throughput of mineral-laden hydrothermal fluids.

Table 1.1: Itinerary of TVZ geothermal field areas and heat outputs. After Bibby *et al.* (1995) and Hochstein (1995). Waikite area from Wood (1994a).

Name	Heat output (MW)	Area (km^2)
Tokaanu	40-130	20 ± 5
Taupo	425 ± 175	30 ± 6
Tauhara	110	25 ± 8
Wairakei	420	25 ± 4
Rotokawa	220	18 ± 4
Ohaaki	85-190	12-16
Ngatamariki	55	7-11
Orakeikorako	660	9-14
Te Kopia	125-250	11-15
Reporoa	15	12-15
Waiotapu	540	18-24
Waikite	45-70	2-3
Atiamuri	10	8 ± 2
Horohoro	4	4 ± 3
Mokai	400 ± 160	14 ± 4
Mangakino	4	8 ± 4
Rotorua	470 ± 50	23 ± 3
Rotoiti	120-140	15 ± 5
Taheke	13	2-4
Waimangu	325 ± 80	20-26
Rotoma	$160 - 300$	20 ± 5
Kawerau	84-210	18-36

1.5.3 Hydrothermal alteration

Changes in the thermodynamic and chemical properties of water as it is transported from the base of the brittle crust to the surface has an attendant effect on the rock it flows through. Perhaps the simplest reaction is the precipitation or dissolution of minerals in response to the changing solubility of heating and cooling fluids. In geothermal systems, this commonly manifests in the near-surface as the precipitation into open pore spaces of dissolved silica as quartz (e.g., Facca and Tonani, 1965; Browne, 1978; Henneberger and Browne, 1988; Dobson *et al.*, 2003). Quartz also forms veins where hydrothermal flow occurs through fractures rather than con-

nected pore space, effectively sealing the fracture to further flow. Dissolved silica also participates in replacement reactions, altering near-surface volcanic deposits to produce weak, conductive clays. Silica precipitation in response to changes in pH, often brought about by mixing of heated, high pH waters with cooler, neutral groundwater, or by changes in dissolved CO_2, forms adularia. In systems where there is an abundant source of CO_2 (e.g., Ohaaki), depressurisation of rising fluids results in the precipitation of calcite.

At the extinct Ohakuri geothermal system, varying degrees of alteration are observed with increasing distance from the inferred upflow zone. The different styles of alteration imply different hydrothermal environments and thus provide some constraint on past activity at the system. For example, a high rank quartz/adularia zone trending northwest (Henneberger and Browne, 1988) may indicate a progressive migration of the primary hot upflow zone in this direction. It is notable that Atiamuri is the nearest geothermal system to Ohakuri and lies to its northwest, which suggests that either Ohakuri has migrated to Atiamuri, or that Ohakuri now represents the extinct component of an originally larger system. Considerable permeability reduction has occurred in the quartz/adularia zone by the precipitation of hydrothermal minerals into open pore volumes. This has the dual effect of increasing rock tensile strength and trapping rising fluids, resulting in transient fluid overpressures. Evidence of fluid channels at Ohakuri suggest these overpressures were relieved by hydraulic fracturing of the rock, and the sporadic presence of breccias indicate hydrothermal eruptions were not uncommon. Such behaviour is cyclical, as high mass flow rates following the creation of fracture permeability accelerate mineral deposition, and subsequent resealing of fractures (Grindley and Browne, 1976).

Age of geothermal fields

Hydrothermal alteration, being indicative of geothermal activity, provides a tool for estimating the ages of geothermal systems. For example, altered ignimbrite at Wairakei suggests this field has been active for at least 500 kyr (Grindley, 1965); this is particularly notable as it implies the geothermal system survived the Whakamaru

flare-up (∼330 ka Wilson *et al.*, 1986) and a series of large eruptions at Taupo caldera. At Kawerau, alteration of greywacke by geothermal fluids prior to its eruption 200 ka places a minimum age constraint on this field (Browne, 1979). Similarly, alteration and sinter deposits found at old, high lake levels suggest a minimum age of 22 to 50 ka for the Rotorua geothermal system (Wood, 1992). Based on a 300 m offset of altered Paeroa Ignimbrite along the Paeroa Fault, Bignall and Browne (1994) propose a minimum age of 120 kyr for the Te Kopia geothermal system. Ngatamariki may have been intermittently active since 500 ka, another survivor of the Whakamaru flare-up, although the most intense activity preceded this event, being associated with the emplacement of a dioritic pluton 550 ka (Arehart *et al.*, 2002).

For extinct geothermal fields, dating of hydrothermal deposits can help constrain the time since they were last active. For example, late-stage hot-spring activity at Ohakuri produced sinters that are overlain by the Kawakawa Tephra (20 ka) whereas acid-sulphate activity postdates the 42 ka Rotoehu Ash (Henneberger and Browne, 1988). Sinter deposits have also been dated for the extinct Mangatete hydrothermal system in the TFB, indicating this region was active only 8.5 kyr ago Drake *et al.* (2012).

1.6 Thesis outline

The diverse and complex geophysical processes operating within the Taupo Volcanic Zone serve as the inspiration for the computational modelling investigations undertaken in this thesis. The following chapters focus on two features of the region: (i) the abundant normal faulting that is a consequence of the high tectonic extension through the region, and (ii) the widespread geothermal circulation that efficiently mines heat from magmatic intrusions in the mid and lower-crust and transports it to the surface. Several interactions between these two processes undoubtedly operate on a variety of timescales, e.g., coseismic enhancement of fracture permeability, or longer term formation of fracture meshes in fault linkage and damage zones (e.g., Rojstaczer *et al.*, 1995; Sibson, 1996); immediate coseismic perturbation of the

pore-pressure field induced by changes in rock stress (Skempton, 1954); evolution of near-surface material properties as hydrothermal alteration produces dense, high strength, fracture susceptible, zones of silicification from weak, porous Quaternary volcanic deposits (e.g., Henneberger and Browne, 1988; Grindley and Browne, 1976); and direct fluid modulation of the frictional properties of faults and fractures, in some cases inducing failure where fluid overpressures develop (Sibson, 1990).

Chapters 2-4 address generic models for normal fault rupture and their implications for crustal evolution over multiple seismic cycles. Chapter 2 begins with a description of mechanisms for mechanical deformation of the crust, including pre-yield elastic behaviour, frictional plastic yield in the upper-crust, and a smooth transition to power-law viscous creep in the lower-crust. These rheologies are implemented in a two-dimensional, plane-strain slice of crust that hosts a single fault; the model approximates the across-strike kinematics of a generic normal fault zone. Seismic cycling of the fault is achieved through episodic modulation of frictional properties along the fault contact, with the model evolving self-similar patterns of elastic deformation after twelve seismic cycles. Patterns of coseismic displacement reveal uplift of the footwall and subsidence of the hanging wall, which is characteristic of large, surface-rupturing, normal fault earthquakes (Figure 1.4).

Chapter 3 provides a closer analysis of processes controlling the evolution of a fault zone. The concept of an extension budget is introduced, in which tectonic extension applied at the model boundaries is accounted for within the crust by various combinations of the available deformation mechanisms: elastic, frictional plastic and viscous strain accumulation, and fault slip. Shear bands of frictional plastic failure, interpreted as the onset of new faulting, form preferentially in the hanging wall of the active fault. This asymmetry is described in terms of a coseismic shear stress reduction that casts a failure shadow in the vicinity of the fault. Combined with observations of fault rotation, a model for fault zone evolution is proposed in which new faults form preferentially in the hanging walls of old ones. Faulting thus proceeds in a basinward direction, consistent with structural evolution in the western Gulf of Corinth, Greece (Goldsworthy and Jackson, 2001).

Chapter 4 describes an analysis of energy flows during the seismic cycle of an active normal fault. Several lines of evidence are presented indicating that these systems diverge from the typical elastic rebound model of earthquake deformation. For instance, a straightforward derivation shows that tectonic extension during the interseismic period decreases the total strain energy contained in the crust, which is contrary to the view that, during this period, such systems are loaded elastically. Resolving energy flows within each fault block shows that deformation of the footwall, which includes up-dip displacement and surface uplift, is consistent with the elastic rebound view; in this fault block interseismic elastic loading of the mid-crust supplies energy for deformation during fault rupture. However, a significant loss of elevation associated with down-dip displacement of the hanging wall liberates sizable quantities of gravitational potential energy. This is used to do work compressing the mid-crust, which creates elastic strain energy. Energy flows in this fault block are in the opposite direction to those predicted by elastic rebound.

Investigations are redirected in Chapters 5-8 to focus on three-dimensional models of geothermal circulation in the TVZ. In Chapters 2-4, a general model for normal fault rupture is developed (Chapter 2) and used as a tool to explore various aspects of the seismic cycle in extensional provinces, e.g., fault zone evolution (Chapters 3), and energy flow (Chapter 4). In contrast, the circulation-modelling component of this thesis comprises several distinct models, each of which investigates a specific aspect of the long-term, natural evolution of TVZ geothermal systems. For this reason, significantly more detail on model construction is furnished within the relevant chapters (6-8), while the more general aspects common to all models are presented in the introductory Chapter 5.

Geothermal circulation is modelled using the Finite Element Heat and Mass transfer code (FEHM) developed at Los Alamos National Laboratory, New Mexico (Zyvoloski, 2007). In Chapter 5, Darcy's Law for fluid flow in a permeable medium is introduced and the governing equations for heat and mass transfer are detailed. These equations, implemented in FEHM, describe the evolution of fluid flow in response to temperature and pressure driving forces. As the objective of this thesis is

to model the full depth of convection in the TVZ, a general procedure for the construction of such models is introduced. Consideration is given to a computational domain that capture convective recharge, thermal boundary conditions appropriate to the base of the convective system, and the porosity/permeability structure in which convection occurs. These features are common to the models presented in Chapters 6-8.

An investigation of TVZ circulation begins with modelling of large-scale convective systems in Chapter 6. In contrast to previous work by Kissling and Weir (2005) that investigated circulation in the entire TVZ, the focus here is restricted to the central sections where the bulk of the geothermal expression occurs (see Figure 1.8). A model is presented that approximates the average heat output and across-strike bimodal heat distribution of the TVZ (see Figure 1.9 and Bibby *et al.*, 1995). Individual convection cells resemble their TVZ counterparts in physical dimension and number, but, unlike Kissling and Weir's model, the precise positions of geothermal fields is not replicated. This rift-scale model of circulation provides a basis for a statistical investigation of convective recharge through the production of large ensembles of flow-paths. These are constructed using a particle backtracking technique that accounts for dispersion and diffusion through an iterative random walk. Flow-paths are used to constrain the positions and spatial relationships between catchment zones for the individual geothermal fields, as well as to investigate fluid residence times and their variability both within and outside a given field. The convective system evolves over a period of 300 kyr, with the positions of individual convection cells demonstrating non-stationary behaviour in time; based on this observation a distinction between geothermal regions as delineated by resistivity surveys versus those delineated by active upflow is proposed.

In Chapter 7, the evolution of a single geothermal field is considered in the context of crustal permeability modified by the passage of hydrothermal fluids. Specifically, the model quantifies the rate at which silica precipitates from cooling fluids as a function of mass flux and temperature gradient, and implements an iterative update of the permeability distribution in response to this process. Evolution of the

geothermal field is dominated by the formation of a low permeability cap-zone at the surface, where the steepest temperature gradients and highest mass flux rates are encountered. Establishment of a surface cap-zone has several effects on the reservoir beneath, including: (i) deflection of upflow to the field margins where surface permeability remains; (ii) an increase in heat content due to insulation from the cooler atmosphere; and (iii) masking of subsurface geothermal features as atmospheric cooling suppresses temperatures within the cap-zone.

The influence of active, dip-slip faults on geothermal convection, at both short and long timescales, is investigated in Chapter 8. A model for the development of a geothermal upflow zone localised along an inclined plane of low permeability is presented; this structure represents a dip-slip fault with a mature fault core operating as a fluid flow baffle. Separate convection cells develop in the adjacent fault blocks, with upflow adhering to the fault plane in both and minimal conductive heat transfer occurring between the two. Two short-term perturbations to natural-state circulation are modelled: coseismic pore-pressure disturbances induced by changes in rock stress, and a breakdown in the fluid baffling properties of the fault through an increase in permeability. Distributions of coseismic changes in pore-pressure are derived from corresponding changes in mean crustal stress taken from the mechanical fault model discussed in Chapters 2 to 4. A near-surface pressure increase associated with horizontal recoil of the fault blocks results in a short-term spike in heat and mass output through the geothermal system, which decays in the weeks following the modelled earthquake. In contrast, permanent changes in fault permeability have a reduced effect on mass flow in both the short- and long-term; however, the removal of the fault as a fluid-flow barrier permits a rapid migration of surface expression from the footwall scarp into the hanging wall.

Finally, in Chapter 9 the main conclusions drawn from the mechanical and circulation models are stated and discussed.

ceiiinosssttuv

- Robert Hooke (1635-1703)

2

Mechanical model of the crust

The Earth's outer crust deforms in response to immense forcings applied along the margins of tectonic plates. Mountain building, faulting and basin formation are all features of a continuously reworked landscape, through stretching, shearing, fracturing and compression of the crust. In this chapter, the physics of deformation of a brittle upper-crust and ductile lower-crust are discussed, with particular emphasis placed on extensional tectonic environments. The mechanical response of the crust to external forces is then modelled using the finite element method. The construction of a two-dimensional numerical model of a faulted crust under extension is described; this is used as a tool to investigate tectonic processes in generic normal fault zones (Chapters 3-4) and, in Chapter 8, perturbation of geothermal systems.

2.1 The deforming crust

The simplest description of material deformation originated with Robert Hooke in 1660 with his theory of linear elasticity. This asserted that, in response to an applied force, a spring deforms, i.e., changes length, and further, that the amount of deformation is linearly proportional to the size of the applied force. Mathematically, the force, F, exerted by a spring that has been deformed an amount, x, is described by

$$F = -kx, \tag{2.1}$$

where k is a constant describing the stiffness of the spring and the negative sign indicates that the force acts against the deformation, i.e., to restore its original length. This concept is extended to describe linear elasticity in a three-dimensional continuous medium in terms of a stress, $\boldsymbol{\sigma}$, and strain tensor, $\boldsymbol{\varepsilon}$

$$\sigma_{ij} = C_{ijkl}\varepsilon_{kl}, \tag{2.2}$$

where C is a fourth rank stiffness tensor. From symmetry considerations and assuming isotropy, the 81 components in C_{ijkl} can be reduced to two independent components (e.g., Segall, 2010), and (2.2) is rewritten

$$\sigma_{ij} = \frac{E}{1+\nu}\varepsilon_{ij} + \frac{E\nu}{(1+2\nu)(1-2\nu)}\varepsilon_{kk}\delta_{ij}, \tag{2.3}$$

or, making strain the subject,

$$\epsilon_{ij} = \frac{1+\nu}{E}\sigma_{ij} - \frac{\nu}{E}\sigma_{kk}\delta_{ij}, \tag{2.4}$$

where E is the Young's modulus of the material and ν is Poisson's ratio. This formulation permits the description of force and deformation as three-dimensional fields containing both shear and normal components. In this work, the sign convention common to physics and engineering literature is used, i.e., stress and strain are negative in compression.

Elastic strain is a temporary deformation and exists only while the stress state (responsible for the induced strain) is maintained. A reduction of stress causes a corresponding reduction of strain, enabling the material to recover its initial shape, i.e., elastic strain is recoverable.

2.1.1 Principal axes

Stress and strain components are commonly expressed relative to a Cartesian coordinate system, i.e., where the indices, i, j and k in (2.3) and (2.4) correspond to the x, y and z directions. The stress tensor is then populated by three normal components that occupy the diagonal, e.g., σ_{xx} which is a stress applied in the x direction on a plane normal to the x direction, and six off diagonal shear components, e.g., σ_{yz} which is a stress applied in the y direction on a plane normal to the z direction. However, for any stress state it is possible to choose an orthonormal coordinate system, distinct from the usual Cartesian axes, in which there are no off diagonal components of the stress tensor. The diagonal components that remain are termed the principal stresses and written σ_1, σ_2 and σ_3, where $|\sigma_1| > |\sigma_2| > |\sigma_3|$. They are obtained from an eigenvalue decomposition of the stress tensor, $\boldsymbol{\sigma}$.

In an extensional tectonic environment, the maximum principal stress is nearly vertical, i.e., $\sigma_1 \approx \sigma_z$, while the other two principal stresses lie in the horizontal plane, with the minimum principal stress, σ_3, lying along the axis of extension (Anderson, 1951). This approximation is probably reasonably accurate, except in the near vicinity of faults, the brittle-ductile transition, or sharp topographical gradients, which can rotate the principal stresses (e.g., Westaway, 1999).

2.1.2 Plane-strain

In some regions, deformation occurs predominantly along two axes (defining a plane) and is less significant or negligible along the third. For instance, extension in the TVZ at a rate of 7-15 $\mathrm{mm\,yr^{-1}}$ (Wallace *et al.*, 2004) can be resolved into a component of stretching along a NW-SE direction and a corresponding contraction in the vertical direction. Both of these motions occur along axes approximately perpendicular to the rift-axis, which is oriented approximately NE-SW and along which minimal deformation occurs.

The plane-strain approximation permits deformation along two axes, say x and z, while constraining deformation along the third to zero, i.e., $\varepsilon_{yy} = \varepsilon_{xy} = \varepsilon_{yz} = 0$.

For a linear elastic material, this places a further constraint on the corresponding stress components, specifically

$$\sigma_{yy} = \nu(\sigma_{xx} + \sigma_{zz}), \qquad \sigma_{xy} = \sigma_{yz} = 0. \tag{2.5}$$

2.1.3 Stress decomposition

The stress tensor, $\boldsymbol{\sigma}$, is often written in terms of its volumetric and deviatoric components, i.e.,

$$\boldsymbol{\sigma} = \mathbf{s} - p\mathbf{I} \tag{2.6}$$

where p is the pressure, defined as the negative of the mean stress, i.e., $p = -\frac{1}{3}tr(\boldsymbol{\sigma})$, $\mathbf{s}$ is the deviatoric stress tensor, and $\mathbf{I}$ is the identity matrix. The volumetric component, $-p\mathbf{I}$, describes volume changes associated with the evolving stress state, while the deviatoric component, $\mathbf{s}$, describes the distortion of the material.

2.2 Frictional plastic deformation

If the crust were purely elastic then a stress state induced by far-field tectonic forces could increase without limit, accompanied by an ever larger elastic deformation. In practice, deformation of the brittle crust is elastic only until its strength is exceeded, beyond which any subsequent deformation is anelastic, i.e., unrecoverable. Physically, this represents frictional sliding of one volume of rock against another and is therefore termed *frictional plasticity*. This sliding occurs along fracture planes that are presumed to exist abundantly throughout the crust at orientations that are optimal for reactivation within the prevailing stress field (Ranalli and Murphy, 1987). In practice, these structural discontinuities represent joints, dilational jogs and extensional shear fractures (Sibson, 1996, 2000) across which frictional shear displacements might be expected to occur.

Frictional plastic failure of a volume of rock is defined in terms of the Mises

equivalent stress, q,

$$q = \sqrt{\frac{3}{2} s_{ij} s_{ji}}, \tag{2.7}$$

which is derived from the second invariant of the deviatoric stress tensor, $\mathbf{s}$, defined in (2.6). Under plane-strain conditions, the Mises stress is also equal to twice the maximum shear stress, i.e., $q = \sigma_1 - \sigma_3$.

Frictional yield occurs when the Mises stress exceeds some threshold value, q_p, parameterising the brittle strength of the crust. A linear Drucker-Prager yield criterion is used to describe plastic hardening, i.e., the increasing strength, of the crust with pressure

$$q_p = (p - p_f) \tan(\beta) + d, \tag{2.8}$$

where p_f is the pore fluid pressure, which counteracts the trend of increasing rock strength with pressure, and β and d are material properties of the crust. Under plane-strain conditions β and d can be chosen such that (2.8) is functionally equivalent to a Mohr-Coulomb formulation, i.e.,

$$\tau = (p - p_f) \sin(\phi) + c \cos(\phi), \tag{2.9}$$

where τ is the maximum shear stress, ϕ is the internal angle of friction and c is the cohesion. Pore fluid pressure is generally assumed to be hydrostatic, i.e., $p_f = \rho_w g z$, where ρ_w is the density of water, g is the acceleration due to gravity and z is depth.

The implementation of the frictional plastic rheology is simplified by observing that if the fluid pressure increases linearly with depth, and if rock pressure is approximated by the overburden, then the relationship between τ and p in (2.9) can be replaced by a modified relationship that excludes p_f but preserves the linear relationship. The effects of hydrostatic fluid pressure are accounted for by choosing modified material parameters,

$$\tau = p\sin(\phi') + c'\cos(\phi'), \qquad \sin(\phi') = \frac{\rho_r - \rho_w}{\rho_r}\sin(\phi), \qquad c' = c\frac{\cos(\phi)}{\cos(\phi')}. \tag{2.10}$$

For the purposes of this work, nominal values of $\rho_r = 2800\,\mathrm{kg\,m^{-3}}$, $\rho_w = 1000\,\mathrm{kg\,m^{-3}}$, $\phi = 30°$ and $c = 1\,\mathrm{MPa}$, produce the modified parameters $\phi' = 18.7°$ and $c' = 0.91\,\mathrm{MPa}$. This modification reflects weakening of the crust by the hydrostatic pore-pressure term in Equation (2.9) (Townend and Zoback, 2000).

Frictional-plastic strain, ϵ_p, that accumulates at yield is predicted to localise along conjugate shear bands whose dip depends on the resolution of heterogeneities, the use of dynamic rock pressure in Equation (2.9) (Buiter, 2012) and the friction angle (Kaus, 2010). For a modified friction angle of 19°, Kaus (2010) predicts shear bands to localise along the Roscoe angles, which for a non-dilational crust are at 45° to σ_1. This dip angle is shallower than would be expected for a dilational crust at greater friction angles. The effects of strain softening are not considered in simulations presented in this thesis. Strain softening is not necessary to cause localisation of shear deformation into bands (Rudnicki and Rice, 1975), although it does introduce a finite length-scale independent of mesh dimension (Needleman, 1988). Other workers, e.g., Huismans *et al.* (2005), have incorporated strain softening for modelling the onset of faulting during lithospheric extension.

2.3 Viscous deformation

Anelastic deformation of the lower-crust by dislocation creep is modelled using a viscous power-law rheology. The viscous strain rate, $\dot{\epsilon}_v$, depends upon the local stress state via the Mises stress

$$\dot{\epsilon}_v = Aq^n \exp(-Q/RT), \tag{2.11}$$

where Q is the activation energy, A is a constant containing material and geometrical factors, n is the power-law exponent, R is the gas constant and T is the temperature

(in Kelvin). In models presented in this thesis, viscous parameters from Paterson and Luan (1990) are used (see Table 2.1). A linear crustal temperature gradient of $35°C\,km^{-1}$ is used, which is consistent with the elevated heat flux of the TVZ of $\sim 0.7\,W\,m^{-1}$ (Hochstein, 1995). At depths in the crust where viscous deformation is the dominant mechanism accommodating extension, (2.11) can be rearranged for the Mises stress, q_v, necessary to accommodate the imposed bulk strain rate

$$q_v = \left(\frac{\dot{\epsilon}_v}{A}\right)^{1/n} \exp(Q/nRT). \tag{2.12}$$

Thus at shallower depths, where the crust is cooler, a higher Mises stress is required to accommodate the applied extension rate by viscous deformation and, instead, brittle processes dominate. When q_v is equal to the Mises stress for frictional plastic yield, q_p, there is a transition in deformation mechanism. The depth at which this occurs is called the brittle-ductile transition (BDT); in the TVZ this occurs slightly deeper than the seismogenic depth of 6-8 km, defined as the depth above which 80% of upper-crustal seismicity occurs (Smith and Bruhn, 1984). Temperatures across this transition are in the range of 300-450°C and are associated with the onset of plasticity in quartzofeldspathic rocks (Scholz, 1988).

2.4 Computational model

The finite element method, implemented here using the software suite Abaqus/standard (Dassaut Systèmes Simulia Corp., 2008), is used to solve deformation and stress equations for an extending crust. Far-field boundary conditions and a cyclical fault friction regime drive the evolution of stress and deformation in time. This approach has previously been used by Ellis *et al.* (2006) and Nüchter and Ellis (2010) to develop 2-D models of fault systems in New Zealand tectonic settings.

It is assumed that deformation along strike of a dip-slip fault is negligible, which allows a 2-D slice of the crust to be modelled under plane-strain conditions. This slice is oriented perpendicular to the axis of the rift system and, based on the geometry

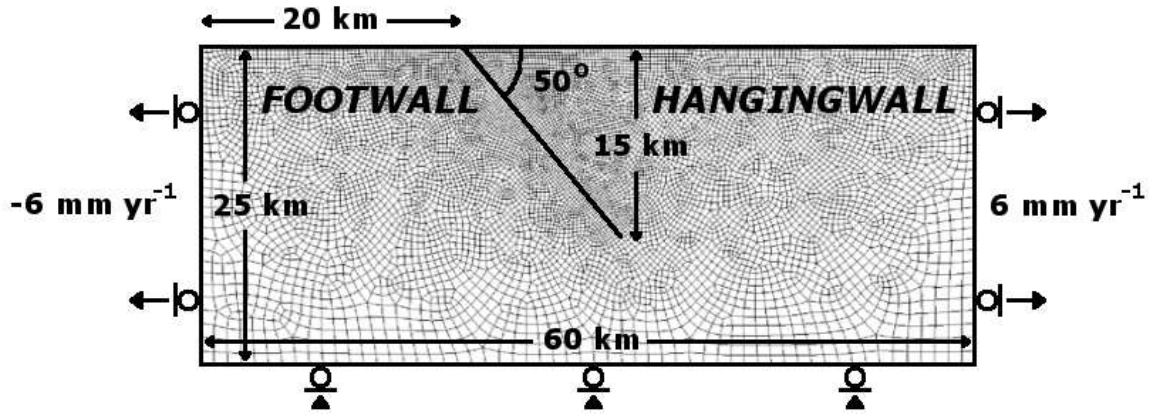

Figure 2.1: Model dimensions and boundary conditions.

of the TVZ, measures 60 km horizontally and 25 km vertically (Figure 2.1). This is presumed to be sufficient to contain the relatively shallow seismicity (≈ 8 km in thermally weakened rifts, e.g., Bibby *et al.*, 1995) and isolate fault behaviour from the influence of the side and lower boundaries.

Tectonic extension is applied as a velocity boundary condition imposed at the lateral boundaries of the model. Campaign GPS data (Wallace *et al.*, 2004) indicate that extension through the central regions of the TVZ is approximately 12 mm yr^{-1}. In these models, a horizontal velocity boundary condition of -6 and 6 mm yr^{-1} is applied to the left and right boundaries, respectively, to account for this forcing. The lower boundary is fixed at zero vertical displacement and the upper surface is unconstrained. Gravity is applied throughout the model as a body force.

2.4.1 Fault friction

A fault is modelled as a planar contact surface intersecting the crust at a dip angle of 50° to a depth of 15 km. Contact between the two surfaces of the fault is initially prescribed as 'locked', in which sliding of one surface against the other is prohibited by an infinite friction coefficient (Ellis *et al.*, 2006; Nüchter and Ellis, 2010). This prevents the fault from creeping over long periods of extension. To model fault slip

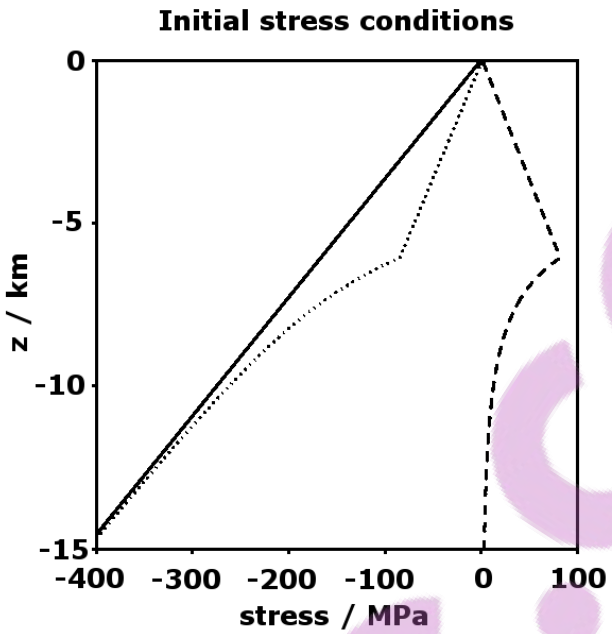

Figure 2.2: Stress components as a function of depth in the model following the stress 'spin-up' phase. Vertical (solid), horizontal (dotted) and Mises (dashed) stress components are shown.

frictional behaviour on the contact surface is switched to 'slipping', in which frictional sliding according to Amonton's law is permitted

$$\tau > \mu_d \sigma_n, \tag{2.13}$$

where τ is the shear stress, σ_n is the normal stress and μ_d is the dynamic coefficient of friction on the fault surface. Here, a slip weakened value for μ_d of 0.2 is used, which accounts for heating and fluid effects during fault slip (Scholz and Engelder, 1976). Switching between locked and slipping modes occurs after an arbitrary, specified time period, and is not in response to a shear stress failure condition. Thus the model is not suitable for investigating the shear stress increases that trigger earthquakes. Instead the focus is on stress and deformation of a faulted crust during the seismic cycle, i.e., the static response to multiple earthquakes.

Other constitutive models have been employed to describe evolving fault friction

properties as a function of displacement and time. Rate-state friction, first described by Dieterich (1979) and Ruina (1983), is one such formulation, and parameterises fault friction as a function of displacement and velocity. This description reproduces many of the subtleties of dynamic fault rupture, including slip stability regimes, rupture arrest, and post-seismic afterslip (e.g., Scholz, 1998) and is a valuable tool for understanding faults at shorter timescales. However, for the geological time periods considered here, a static description of fault friction is sufficient to characterise behaviour over multiple earthquake cycles.

An initial stress state for the model is evolved by applying the extension boundary conditions over geological time. This stress 'spin-up' (Hetland and Hager, 2006; Ellis *et al.*, 2006) phase produces a lithostatic vertical stress, σ_z, and a horizontal stress, σ_x, such that the Mises stress is equal to the lower of q_p or q_v, i.e., a crust at frictional plastic yield at shallow depths and viscous yield below the BDT. Deformation that occurs during the stress spin-up period is discarded at the beginning of a new simulation, while the stress state is retained as an initial condition. This initial Mises stress profile is shown as a function of depth in Figure 2.2.

A single seismic cycle refers to a long period of fault dormancy that is punctuated by a short, violent episode of fault slip and followed by a readjustment period of afterslip and aftershock activity; in these models, the seismic cycle is approximated by a two-step cycle. The interseismic period refers to the interval between earthquakes in which extension applied at the model boundaries alters displacements and stress within the model domain. This is followed by a seismic period, in which the friction coefficient on the fault surface is substantially lowered and displacements of the fault blocks are driven by an imbalance between gravitational and elastic forces. Due to the short length of the seismic period displacements at the model boundaries are negligible and any slip occurs due to stress imbalances accumulated during the interseismic period. Fault slip that occurs during the seismic period includes all possible afterslip.

The magnitude of coseismic displacements and stress changes depends on the length of the loading period that precedes an earthquake. In simulations presented

here, and unless otherwise stated, a seismic cycle with a constant interseismic period of 220 yr is considered. This is somewhat shorter than the typical recurrence interval on TVZ faults ($\sim 10^3$ yr: Van Dissen *et al.*, 2003; Berryman *et al.*, 2008; Canora-Catalan *et al.*, 2008), but produces more realistic slip magnitudes for the simplified fault zone geometry. For instance, a model for fault processes along an arbitrary transect through the central TVZ should include several structures of varying inclination, spacing and recurrence behaviour. Such multi-fault scenarios have been considered by others in the context of fault zone and basin evolution (e.g., Gupta *et al.*, 1998; Nicol *et al.*, 2006), however isolating fault specific effects (as opposed to those attributed to fault interactions) is difficult in such models. Nevertheless, the application of the full rate of TVZ extension to a single fault model leads to faster than normal interseismic loading, and produces larger slip events than might be expected for a multi-fault system in which displacement is distributed across many structures. A shortened interseismic period has therefore been chosen to offset this effect and prevent the production of unrealistic, high stress states.

2.5 Deformation during the seismic cycle

2.5.1 Surface displacement

Displacement of adjacent fault blocks determines the long-term evolution of basin topography. With regard to the seismic cycle, this displacement has two components; a slow vertical contraction, and rapid relative displacement of the fault blocks associated with coseismic stress redistribution. Figure 2.3 shows topographical changes at the surface of the model for the two components.

During the interseismic period, surface displacements are dominated by a relatively smooth, vertical contraction induced by tectonic extension. Coupling between the horizontal and vertical displacements arises from the second term on the RHS of Equation (2.4), which links diagonal components of the strain tensor to the pressure. Horizontal extension lowers the horizontal stress, and is accompanied by a

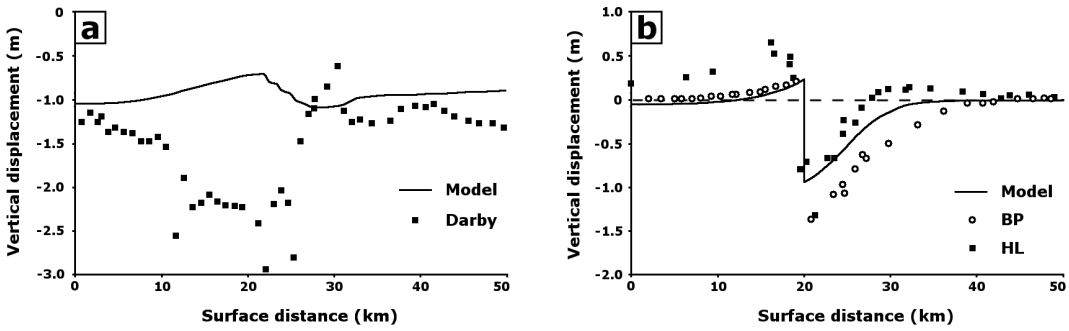

Figure 2.3: (a) Vertical displacement at the surface of the model during the interseismic period. TVZ subsidence rate data from Darby *et al.* (2000) has been integrated for a 220 yr period and superimposed (for an approximately west-east transect). (b) Coseismic vertical surface displacements produced by the model and for historical earthquakes at Borah Peak, Idaho (1983, $M = 6.9$) and Hegben Lake, Montana (1959, $M = 7.3$) (Barrientos *et al.*, 1987).

reduction in pressure and vertical sagging of the crust. In response to applied extensional boundary conditions of $12\,\mathrm{mm\,yr^{-1}}$, the model contracts vertically at a rate of $\approx 5\,\mathrm{mm\,yr^{-1}}$. Complementary geodetic measurements within the TVZ are difficult to obtain and likely vary with time, however, analysis of vertical levelling data by Darby *et al.* (2000) indicate vertical subsidence rates of 5-10 $\mathrm{mm\,yr^{-1}}$ north of Lake Taupo. This is consistent with model displacements in the hanging wall, although Figure 2.3(a) suggests that other subsidence processes are in operation in the western TVZ. This region coincides with the Taupo Fault Belt and a graben topography.

For earthquakes that rupture faults to the surface, the coseismic surface displacement profile is discontinuous across the fault scarp (see Figure 2.3(b)). The hanging wall block is displaced down dip by an amount that is related to the magnitude of the earthquake (e.g., Aki, 1972; Wells and Coopersmith, 1994; Canora-Catalan *et al.*, 2008). Up-dip displacement of the footwall block, termed 'footwall uplift', occurs concurrently, although is typically of smaller magnitude than that of the hanging wall. These displacements are driven by stress changes in the mid-crust that are discussed in Chapter 4. The total vertical offset at the fault scarp is 1.2 m, which is split 5:1 between the hanging wall and footwall, respectively (1.0 m hanging

wall subsidence and 0.2 m of footwall uplift).

The coseismic vertical displacement profile is consistent with that produced by two large normal fault earthquakes to have occurred in historical times. The 1959, $M = 7.3$ Hegben Lake earthquake in Montana, and the 1983, $M = 6.9$ Borah Peak earthquake in Idaho both produced well resolved surface ruptures with approximately 1.7 m maximum vertical offset. Surface levelling data for both earthquakes showed a minor component of footwall uplift and subsidence of the hanging wall that decreased with distance from the scarp. Figure 2.3(b) shows that hanging wall displacements for the model are qualitatively similar to the historical data. The reduced magnitude of displacements indicates the modelled earthquake is smaller than the historical comparisons. Discrepancies in the offsets might also be attributed to differences between the elastic properties of the model and those of the crust, e.g., Young's modulus (Gudmusson, 2004).

Earthquake magnitude can be estimated for a given fault plane displacement and material parameters of the crust. Hanks and Kanamori (1979) proposed the following relation between seismic moment, M_0, a measure of energy release, and moment magnitude, M, the common measure of earthquake size and severity.

$$M = \frac{2}{3}\log(M_0) - 10.7, \tag{2.14}$$

where M_0 is the seismic moment in dyne cm ($1\,\text{dyn cm} = 10^{-7}\,\text{N m}$) and is given by Aki (1972) as

$$M_0 = \mu \bar{u} A, \tag{2.15}$$

where μ is the shear modulus of the material, $\bar{u}$ is the fault displacement averaged across the fault plane, and A is the area of the fault plane that ruptured. For the two-dimensional models considered here, A must be inferred from realistic estimates of rupture lengths. A suite of these rupture lengths is provided in Canora-Catalan *et al.* (2008) and suggests that 10-25 km may be an appropriate length. This is slightly larger than the 1987 surface rupture of the Edgecumbe Fault (Section 1.3.2:

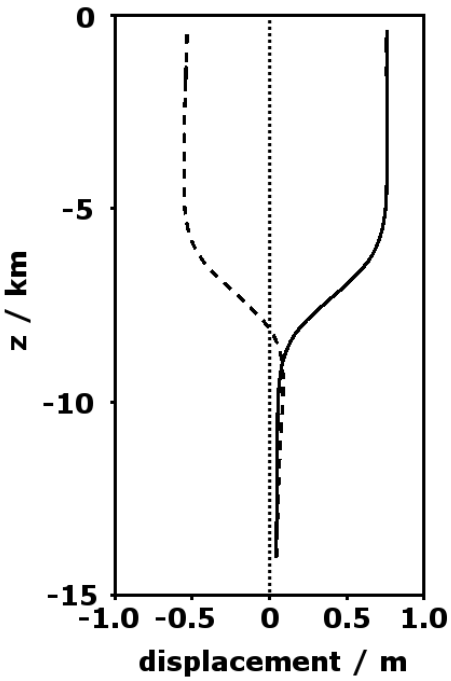

Figure 2.4: Coseismic fault parallel displacement (dip-slip) on the fault plane for the footwall (dashed) and hanging wall (solid). Note that up-dip displacement is negative.

Beanland *et al.*, 1990), but smaller than the largest TVZ fault (the 30 km Paeroa Fault: Section 1.3.1).

For the modelled earthquake, total dip-slip surface displacement of 1.5 m occurs to a depth of ≈6 km (see Figure 2.4). For a shear modulus of 4 GPa and rupture length of 20 km, Equations (2.14) and (2.15) give a moment magnitude for the modelled earthquake of $M = 5.8$. This is smaller than the historical earthquakes examined in Figure 2.3(b), consistent with a smaller vertical offset and perhaps less stiff crustal elastic properties. Recurrence interval also plays a role in earthquake magnitude, although the relationship is predicated on accurate determination of the long term fault displacement rate.

Coseismic dip-slip profiles for each fault block (Figure 2.4) suggest the crust can be described in terms of three deformational regimes. In the upper-crust, defined here

as 0-6 km depth, coseismic motion of the fault blocks along the scarp resemble those of rigid body displacement, i.e., the slip profiles are constant with depth. At these depths the fault scarp does not deform, but rather is displaced as a single coherent entity. From 6-10 km, both slip profiles decay from their maximum values to zero. This is the region where fault slip is arrested and characterises the transition from frictional (upper-crust) to ductile (lower-crust) deformation. This band is the brittle-ductile transition (BDT) and its position is consistent with seismogenic depths in the TVZ (Bryan *et al.*, 1999). At the top of the BDT, i.e., 6 km depth, displacements of the fault blocks are at their maximum values (-0.6 m in the footwall and 0.8 m in the hanging wall), however, at 10 km depth slip in both fault blocks is zero. Clearly, deformation is occurring in the mid-crustal region and is intimately linked to fault movements in the upper-crust. Below 10 km depth, slip is zero, despite the availability of a contact surface permitting frictional slip (the surface is prescribed to 15 km depth: see Figure 2.1). This is due to the low levels of shear stress that prevail in the high temperatures of the ductile lower-crust. Therefore the depth of faulting in the model is not prescribed, but rather is a natural feature of the rheology and determined by material parameters and the bulk strain rate (which constrains shear stress in the ductile crust).

2.5.2 Strain

Extension applied at the model boundaries is taken up within the crust by either rigid displacements of bodies relative to one another, i.e., displacement of the hanging wall relative to the footwall, or by distortion of the crustal shape. This distortion includes stretching, compression, and twisting, and is commonly termed strain (see Equation (2.4)).

After many seismic cycles the model evolves a state of dynamic equilibrium, characterised by self-similar changes in the distribution of elastic strain over a single cycle. The crust oscillates about a background state such that elastic strain changes incurred during the interseismic period are offset by changes of opposite magnitude

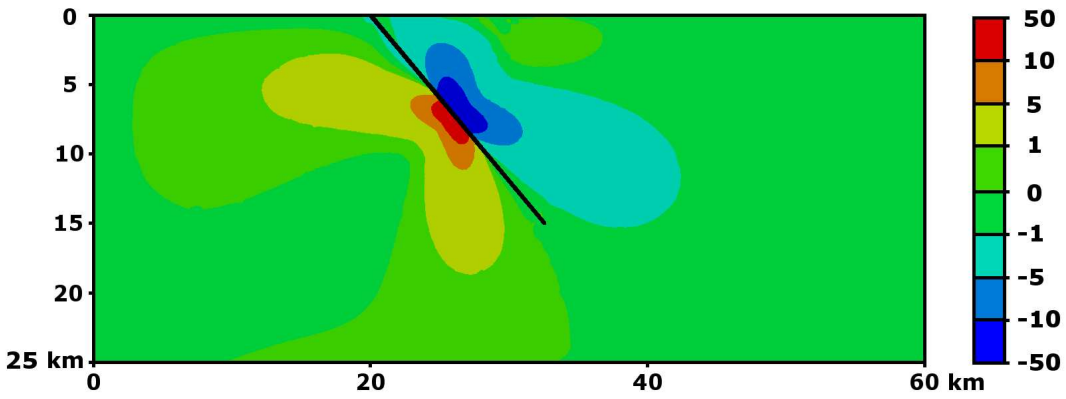

Figure 2.5: Change in fault parallel elastic strain during the 60 s seismic period. Note the non-uniform spacing of contour levels.

during the seismic period. Figure 2.5 shows changes in accumulated fault parallel elastic strain during a seismic period. For the sign convention used here, negative strain changes indicate compression; this occurs primarily in the hanging wall at depths of 6-10 km. Strain changes are approximately antisymmetric about the fault plane, although expansion in the footwall is of lower magnitude than the corresponding hanging wall compression. These strain changes are responsible for the dip-slip gradients observed on the fault plane in Figure 2.4. Their role in surface deformation is discussed further in Chapter 4.

2.6 Summary of models

This chapter details the construction of a mechanical model for static stress changes and displacements associated with dip-slip fault rupture over many seismic cycles. The chapters that follow detail the use of this model as a tool to investigate a variety of short- and long-term phenomena associated with normal faults.

Chapter 3 focuses on those components of deformation that operate in the brittle upper-crust, i.e., fault slip, temporary accumulation of elastic strain, and permanent accumulation of frictional-plastic strain. As the latter component represents the early

stages of fault formation, its occurrence in relation to existing faults provides insight into long-term evolution of fault systems. Coseismic displacements associated with modelled earthquakes, particularly horizontal recoil of the fault blocks away from one another, alter the near-surface stress-state and limits the accumulation of frictional plastic strain in the footwall. As a consequence, formation of new faults is favoured in the hanging wall of the active fault. The rate at which new faults form is limited by the number of active faults in the system, which is turn is modulated by the removal of old faults. An analysis of fault rotation to shallower dip angles is presented and separate coseismic and interseismic rotations are associated with distinct physical causes. These results inform a generic scenario of basinward fault migration that permits the development of new faults and the death of old ones (Dempsey *et al.*, 2012c).

In Chapter 4, flows of energy associated with the modelled fault rupture are considered; these provide the means of exploring cause and effect within the system. Both analytical and numerical evidence is presented for the rather counter-intuitive concept that total elastic energy decreases in the period preceding an earthquake. Elastic strain energy and gravitational potential energy (GPE), both of which are accumulated and released by reversible processes, operate as the main controls on deformation, with GPE being the principal cause of coseismic deformation in the hanging wall. Energy dissipated by friction between two sliding fault planes, viscous straining in the lower-crust, and brittle damage in the upper-crust is also considered.

The final use of the mechanical model is detailed in Chapter 8, where it is coupled to a model of geothermal fluid circulation. Specifically, changes in stress occurring during rupture of a 65° dipping fault are imported directly into a natural-state fluid model as a pore-pressure perturbation. Subsequent diffusion of these anomalous pressure distributions alters heat transfer in the near-surface for a period of several weeks after an earthquake. Stress changes occurring at the fault tip where there are large gradients in slip also perturb natural-state heat flow in this region; however, these are too deep to have an appreciable effect on geothermal activity at the surface.

Table 2.1: Symbols used in the text.

Symbol	Explanation
	Rheological parameters
ρ	density [$2800\,\mathrm{kg\,m^{-3}}$]
E, ν	Young's Modulus [10 GPa], Poisson's ratio [0.25]
C, ϕ	cohesion [1 MPa], material angle of friction [30°]
μ_d	dynamic fault friction coefficient [0.2]
μ_s	static fault friction coefficient [0.2]
$\dot{\varepsilon}_v$	viscous strain rate [$6.3\times10^{-15}\,\mathrm{s^{-1}}$]
A, Q, n, R	pre-exponential constant in Equation (2.11) [$5.0\times10^{-32}\,\mathrm{Pa^{-n}\,s^{-1}}$], activation energy [$135\,\mathrm{kJ\,mol^{-1}}$], power-law exponent [4], gas constant [$8.314\,\mathrm{J\,mol^{-1}\,K^{-1}}$]
T	temperature [K]
	Stress terms, components and conventions
$\boldsymbol{\sigma}$	stress tensor [Pa]
σ_1, σ_3	principal stresses [Pa]
p, p_f	mean stress, pore fluid pressure [Pa]
q, q_p, q_v	Mises stress, Mises stress at frictional plastic yield, Mises stress maintaining viscous strain rate [Pa]
τ, σ_n	shear and normal stress on fault surface [Pa]
CFS	Coulomb failure stress [Pa]
sign	negative values of stress indicate compression [Pa]
	Displacement and strain terms
x, z	cartesian coordinates, z is negative when directed downward [m]
u_x, u_z, u_{para}	horizontal, vertical and fault parallel displacements [m]

There are only two things you need to know about friction. It is always 0.6, and it will always make a monkey out of you.

- John Jaeger

3

Faulting and frictional plastic deformation

Brittle yield of the upper-crust occurs when stresses generated by tectonic forcings exceed rock strength. In this chapter, the behaviour of frictional plastic yield in the vicinity of a normal fault is investigated and those effects relevant to the structural evolution of extensional provinces are discussed. A scenario is presented that accounts for basinward migration of normal faulting, which is observed in Turkey (Dart *et al.*, 1995), the central Basin and Range province, USA (Horton and Schmitt, 1998), the Gulf of Corinth, Greece (Goldsworthy and Jackson, 2001), and the strike-slip Gar Basin in western Tibet (Sanchez *et al.*, 2010). The proposition is centred on the interplay between three concurrent processes: (i) localisation of frictional plastic strain in the hanging wall, (ii) the formation of a low shear stress shadow in the vicinity of the fault, which is maintained by continued fault activity, and (iii) the gradual shallowing of fault dip due to both interseismic and coseismic rotation of the fault plane.

Work presented in this chapter is drawn from a paper submitted to the Journal of Structural Geology in September 2011 and published March 2012 (Dempsey *et al.*, 2012c). Results and text included in this chapter are largely unchanged from the published version as permitted by the University of Auckland under the *2008 Statute and Guidelines for the Degree of Doctor of Philosophy (PhD)*. Co-authors of this work Dr Susan Ellis, Dr Julie Rowland, and Dr Rosalind Archer advised and commented

on the manuscript, however the bulk of the research and preparation for publication was undertaken by the thesis author (see accompanying declaration).

3.1 Introduction

Extension of the lithosphere in rifting basins is accommodated through displacement on normal dip-slip faults or by the emplacement of dikes, i.e., intrusive magmatism. Such structures are observed at rifting at both convergent (Taymaz *et al.*, 1991; Wilson *et al.*, 1995) and divergent plate margins (Ebinger, 1989), and intra-plate settings (Illies, 1972; Puskas *et al.*, 2007). Over time, the character of normal faulting evolves, with individual fault strands organising into sub-parallel en-echelon arrays and, with continued linkage, into large fault belts (Cowie *et al.*, 2005). However, fault planes may also become inactive (Jackson, 1999). Extension can cause fault planes to rotate about a horizontal axis, shallowing the dip angle to a point where continued reactivation of the fault becomes unlikely (Sibson, 1985). In addition, stresses generated by an existing fault have been hypothesised (Goldsworthy and Jackson, 2001) to induce a migration of faulting in a basinward direction (Dart *et al.*, 1995; Horton and Schmitt, 1998; Goldsworthy and Jackson, 2001; Sanchez *et al.*, 2010).

During discrete episodes of dip-slip on normal faults, extension is accommodated by translation of one fault block relative to the other. Displacement is primarily parallel to the fault plane, and therefore horizontal movements are accompanied by vertical displacements. This behaviour translates to uplift of the footwall block and a comparatively larger subsidence of the hanging wall (e.g., Barr, 1987). Conceptual models employ lithospheric flexure (Weissel and Karner, 1989; Kusznir *et al.*, 1991), domino rotation (Wernicke and Burchfiel, 1982), or isostatic rebound (Barr, 1987; Westaway, 1992) on either planar or listric fault surfaces to describe this deformation. However, field studies indicate that fault slip aggregated across a rift does not always account for the full geodetic extension rate (e.g., Villamor and Berryman, 2001; Wallace *et al.*, 2004). Additional deformation mechanisms or movements on

undiscovered faults must account for the shortfall.

Normal fault systems evolve and grow over many thousands of years in response to the continuous application of far-field tectonic extension (e.g., Villamor and Berryman, 2001; Bell *et al.*, 2009). Such evolution involves the initiation of new faults (Jackson and McKenzie, 1983), which is itself an indication that extension is not completely accommodated by existing structures. Potential causes of this shortfall include: a migration of the locus of extension away from the faulted region; a suspension of activity on pre-existing faults due to fault rotation (Jackson, 1999), restrengthening of the fault (Li *et al.*, 2003; Muhuri *et al.*, 2003) or stress shadowing by other faults (Cowie, 1998); distributed frictional deformation; or a suspension of alternative mechanisms of extension accommodation, e.g., dike emplacement (Rowland *et al.*, 2010).

The purpose of this work is to investigate specifically the role that frictional plasticity plays in the evolution of a normal fault system. From a theoretical perspective, frictional plasticity is the non-recoverable deformation of the crust through frictional sliding on hypothetical fracture planes. Such planes are presumed to exist abundantly throughout the crust (Ranalli and Murphy, 1987) at orientations that are optimal for reactivation within the prevailing stress field. Within the crust, these structural discontinuities may represent joints, dilational jogs, bedding planes or extensional shear fractures (Sibson, 1996, 2000) across which frictional shear displacements might be expected to occur. Coalescence of a multitude of these shear offset structures within a well constrained deformation band may be a central process leading to the formation of a new fault (e.g., Pollard and Fletcher, 2005). Thus, an investigation of frictional plasticity, treated as a precursor to fault formation, can address where subsequent faults should localise and provide insight into fault zone evolution.

This work builds on earlier models of Ellis *et al.* (2006) and Nüchter and Ellis (2010), which prescribe fault surfaces directly and model frictional sliding between fault blocks over many seismic cycles. The evolution of normal fault systems shortly after the onset of rifting is considered. Modelled deformation includes: discrete

episodes of slip between fault blocks that displace independently along the plane of contact; frictional plastic yield in the brittle upper-crust; and viscous flow in the lower-crust. The relative importance of each mechanism in accommodating the regional extension rate indicates the likelihood of development of additional fault structures and the positions of these relative to the primary fault. A gradual shallowing of the dip angle of the fault plane due to rotation is observed; this is a prerequisite for the development of cross-cutting faults (Profett, 1977; Nur *et al.*, 1986) as older structures rotate beyond the limit for reactivation (Sibson, 1985).

Results from the computational model are interpreted in the context of the western Gulf of Corinth, an asymmetric graben in mainland Greece, comprised of several major north-dipping faults accommodating extension of 12-14 $\mathrm{mm\,yr^{-1}}$ (e.g., Clarke *et al.*, 1997; Briole *et al.*, 2000; Floyd *et al.*, 2010). Geomorphological and stratigraphic evidence indicate a migration of faulting in a basinward direction (Goldsworthy and Jackson, 2001; Flotté *et al.*, 2005; Rohais *et al.*, 2007) as new faults developed in the hanging walls of older structures (Jackson, 1999). Flotté *et al.* (2005) propose a tectonic model utilising a low-angle detachment fault underlying steeper surface faults, although this model is not universally accepted and is not applied here (e.g., McNeill *et al.*, 2005). In this chapter, a model is proposed for basinward fault migration based on modelled distributions of stress and frictional plasticity in the vicinity of existing faults.

3.1.1 Previous numerical experiments

Computational modelling of fault systems on short timescales has been used to examine rupture propagation along a fault under rate-state friction constraints (Dieterich, 1979; Ruina, 1983), rupture propagation in an asymmetric geometry (Oglesby *et al.*, 2000), and near-fault coseismic deformation of an elastic crust (e.g., Freund and Barnett, 1976; Gupta and Scholz, 1998). Such studies constrain the dynamics of fault rupture and are useful in modelling ground acceleration and quasi-static coseismic displacements; however, they do not account for deformation in fault systems over

many seismic cycles.

Over longer timescales, numerical models of fault architecture and rift evolution, such as an extension to the propagator matrix method of Rundle (1980) by King *et al.* (1988) and Stein *et al.* (1988), have explored topographical development around normal faults in response to multiple earthquake cycles, and continual depositional and erosional processes. Their model indicates that the degree of lithospheric flexure and the width of the deformation region are controlled by the effective elastic thickness of the crust. Finite element models have expanded on these findings, investigating the effects of finite elastic strength in the upper-crust, and tracking patterns of failure in the vicinity of a fault (e.g., Melosh and Williams Jr., 1989; Bott, 1997). Plastic deformation reduces the effective elastic thickness of the crust, thereby controlling graben dimension by migrating the outer flexure hinge closer to the fault scarp (Bott, 1997).

Melosh and Williams Jr. (1989) detailed a finite element model that accommodates slip between 65° dipping conjugate elements and which tracks proximity to Mohr-Coulomb failure in the vicinity of a dip-slip fault. Their analysis indicates a maximum propensity to failure in the near-surface of the hanging wall, and also at the fault tip where the maximum gradient in dip-slip is encountered. On the basis of strain-energy minimisation, they argue that antithetic faults should form in the hanging wall in response to coseismic stress changes caused by rupture of the main fault. This result, which is specific to systems in which the main fault dips at 65°, does not account for coupling between gravitational potential and strain energy (Dempsey *et al.*, 2012b).

Henk (2006) uses a thermo-mechanical model with a viscoelastic-plastic rheology to investigate lithospheric extension and deformation about a reactivated thrust fault, for a variety of strength parameters and strain rates. These models also demonstrate strain localisation in the near-surface of the hanging wall, interpreted as a crestal collapse graben (McClay and Ellis, 1987). Others have used three-dimensional thermo-mechanical models (Braun *et al.*, 2008; Popov and Sobolev, 2008) to model rifting over large spatial and temporal scales (100's of km and millions of years), and

have reproduced rift bounding faults through bands of localised strain (Huismans *et al.*, 2005).

3.2 Distribution of frictional plasticity

The distribution of the differential stress (Figure 3.1(a)) reflects the brittle and viscous rheologies prevailing in the upper and lower-crust, respectively (see Figure 2.2 and Equations (2.9) and (2.12)). The maximum differential stress, marking the transition from brittle to ductile behaviour, occurs at a depth of 6 km. Perturbations to the profile in Figure 2.2 are observed close to the fault surface and are caused by coseismic movements of the fault blocks and gradients in slip at the fault tip. In the hanging wall, a broad maximum in q is centred on the BDT, while in the adjacent footwall there is a corresponding reduction compared to background levels for that depth.

Viscous deformation is the dominant contribution to deformation at the high temperatures and pressures found in the lower-crust (>9 km depth). Frictional plastic deformation or slip on the fault surface are absent from this region of the crust so that, during the interseismic period, 2.64 m ($12\,\mathrm{mm\,yr^{-1}} \times 220\,\mathrm{yr}$) of tectonic extension must be accommodated by viscous strain. As the strain rate, $\dot{\epsilon_v}$, is proportional to q^4 (see Equation (2.12) with $n = 4$), the additional accumulation of ϵ_v in Figure 3.1(c) along the fault root at depths >6 km points to an increase in the stress above the background level for this depth. This increase, evident in Figure 3.1(a), is attributed to the upper-crustal displacements of the fault blocks and the accommodation of these motions within the mid-crust. The extra viscous straining directly beneath the fault alters post-seismic deformation at the surface (Ellis *et al.*, 2006) and helps restore the stress state on the fault to its equilibrium state (Nüchter and Ellis, 2010).

Frictional-plastic strain accumulates exclusively in the upper-crust at depths shallower than 6 km and localises in shear bands that dip at approximately 45° from the horizontal, as discussed in Section 2.2. Qualitatively, frictional-plastic strain occurs

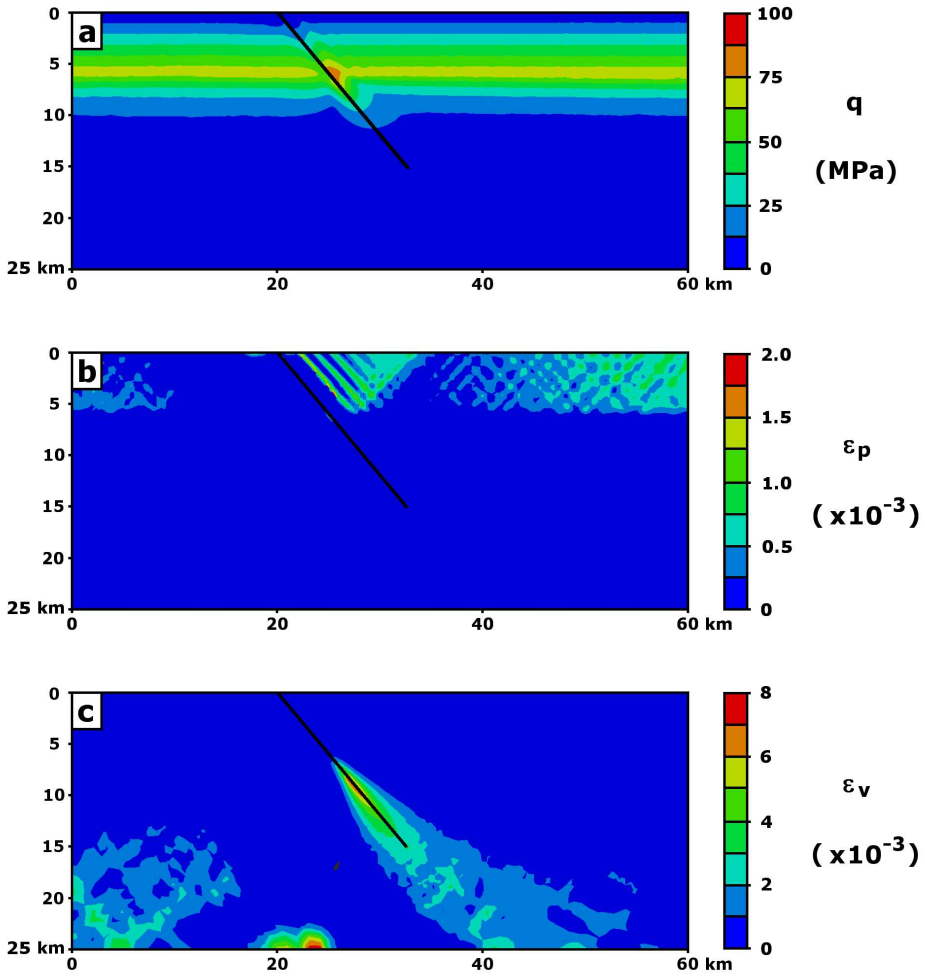

Figure 3.1: Distributions after 12 modelled seismic cycles of (a) Mises stress, q, (b) accumulated frictional plastic strain, and (c) accumulated viscous strain.

preferentially in a triangular wedge of the hanging wall block and is conspicuously absent from much of the footwall. Regions of increased plastic strain are also observed at the lateral boundaries of the model; however, these regions are outside the influence of the fault and represent background strain behaviour. The presence of multiple shear bands, as opposed to one or two bands of high strain, is consistent with the "distributed" mode of fracturing described by Schueller *et al.* (2010). They showed that if the applied extension rate cannot be accommodated by displacements on existing frictional plastic shear zones, which in turn are limited by the slip velocity

in both brittle and ductile media, then new shear zones form to accommodate the shortfall. However, with further deformation such that these shear bands experience strain softening due to accumulated plastic strain, it is expected that displacement would localise onto fewer structures.

3.2.1 Frictional plastic yield shadow

By definition, frictional-plastic strain accumulates in those regions where the differential (plane-strain Von-Mises) stress exceeds the threshold for failure, i.e., $q > q_p$. The accumulation of frictional-plastic strain then, to some extent, reflects the stress state of the crust. Figure 3.2(a-b) plots the proximity of the differential stress to the limit of frictional plastic yield, i.e., $q_p - q$, to a depth of 8 km, prior to and following fault rupture. The frictional plastic yield limit is pressure dependent and must therefore be recalculated following fault rupture to account for changes in mean stress. The sharp transition from brittle to ductile failure is evident at a depth of 6 km, below which viscous deformation maintains low stresses and ensures that $q < q_p$. In the brittle upper-crust and prior to fault rupture, the majority of the hanging wall is either at or within 0.1 MPa of failure. Coseismic stress changes generally decrease the proximity to failure by between 0.1 and 1 MPa.

Repeated fault slip and a small dynamic friction coefficient maintain the near-fault differential stress at up to 10 MPa below failure, creating a stress shadow. Under plane-strain conditions, the Von-Mises stress is twice the maximum shear stress, and thus its reduction is due to the repeated coseismic relief of shear stress on the fault plane. Shear stress drops during the modelled episodes of fault slip are approximately 0.5-1 MPa, which indicates that the magnitude of the stress-failure shadow varies by up to 10% over the seismic period. Greater stress drops associated with larger earthquakes and longer recurrence intervals are thus permitted for this fault, but the shear stress in the near-fault region cannot increase above q_p. If the differential stress is consistently restored (through a drop in stress) to its post-seismic value in Figure 3.2(b) for any recurrence interval, then it follows that stress drop, and

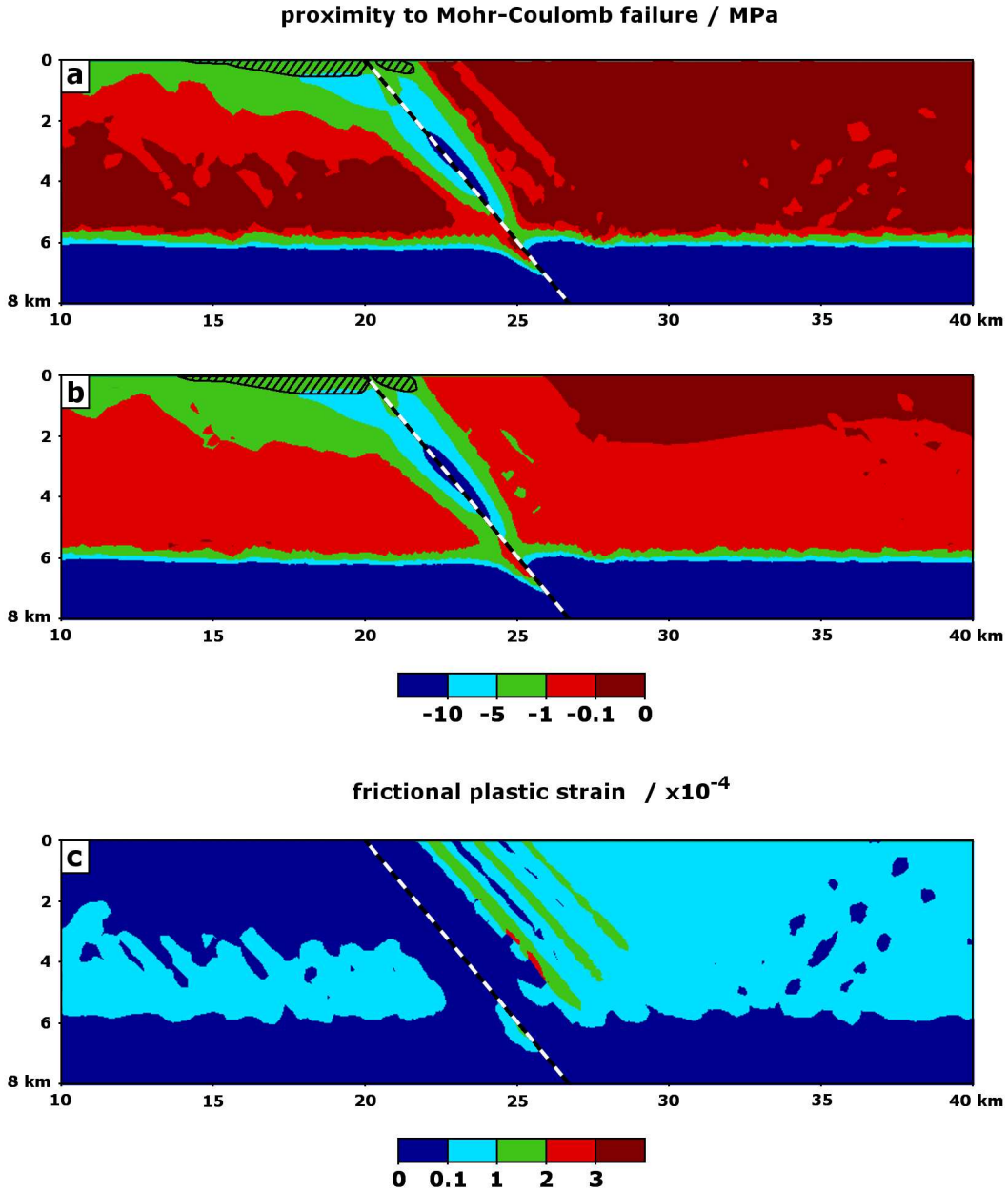

Figure 3.2: Proximity of the differential stress to Mohr-Coulomb failure, $q_p - q$, (a) prior to and (b) following an earthquake for a 50° dipping fault and a crust at dynamic equilibrium. The BDT is marked by a sharp decrease in proximity to failure and black hatching indicates regions where the crust is in tectonic compression, i.e., $|\sigma_x| > |\sigma_z|$. (c) Distribution of frictional-plastic strain accumulated during the 12th interseismic period. The position of the fault is marked by the black and white dashed line.

thus earthquake magnitude (Hanks and Kanamori, 1979), is limited by the frictional strength of the upper-crust.

Upward-directed fault slip along the footwall scarp during an earthquake causes an increase in elevation at the surface, but also a component of horizontal displacement away from the fault plane. During the brief seismic slip-events, displacements at the side boundaries of the model are approximately zero, and thus coseismic fault displacements result in a horizontal compression of the crust. This elastic deformation lowers the differential stress in the near-surface of the footwall and at depths less than 500 m, the compression is so great that the horizontal stress exceeds the vertical, i.e., $|\sigma_{xx}| > |\sigma_{zz}|$, and the stress regime is compressional (see hatched regions in Figure 3.2(a-b)). The shallow extent of these zones is principally a reflection of the low lithostatic vertical stress at shallow depths, which is exceeded by only a modest horizontal compression.

The presence of a slipping fault perturbs the differential stress in its vicinity, imposing a failure shadow on a crust that is otherwise at frictional yield. This failure shadow broadens near the surface, particularly within the footwall block, and tapers to a narrow width near the BDT. Figure 3.2(c) shows that frictional-plastic strain does not accumulate within the shadow, but rather the greatest accumulation is outside the shadow in the hanging wall block. Frictional plastic shear-bands are observed in this region, dipping at 45°, synthetic to the main fault, and intersecting the surface ($z = 0$) outside the edge of the failure shadow. Low levels of frictional plasticity are also observed in the footwall block at depths of 3-7 km where upward-directed fault slip and compression have not significantly altered the stress state. Except for a small region at the root of the fault, the majority of the fault plane is free from plastic deformation, although failure from dynamic loading during rupture propagation cannot be precluded as this has not been modelled.

Previous numerical experiments by Melosh and Williams Jr. (1989) indicated that formation of antithetic faults in the hanging wall of a main fault was energetically favourable over synthetic faults of a similar dip. This result was derived assuming immediate secondary fault formation in response to failure stresses induced by slip

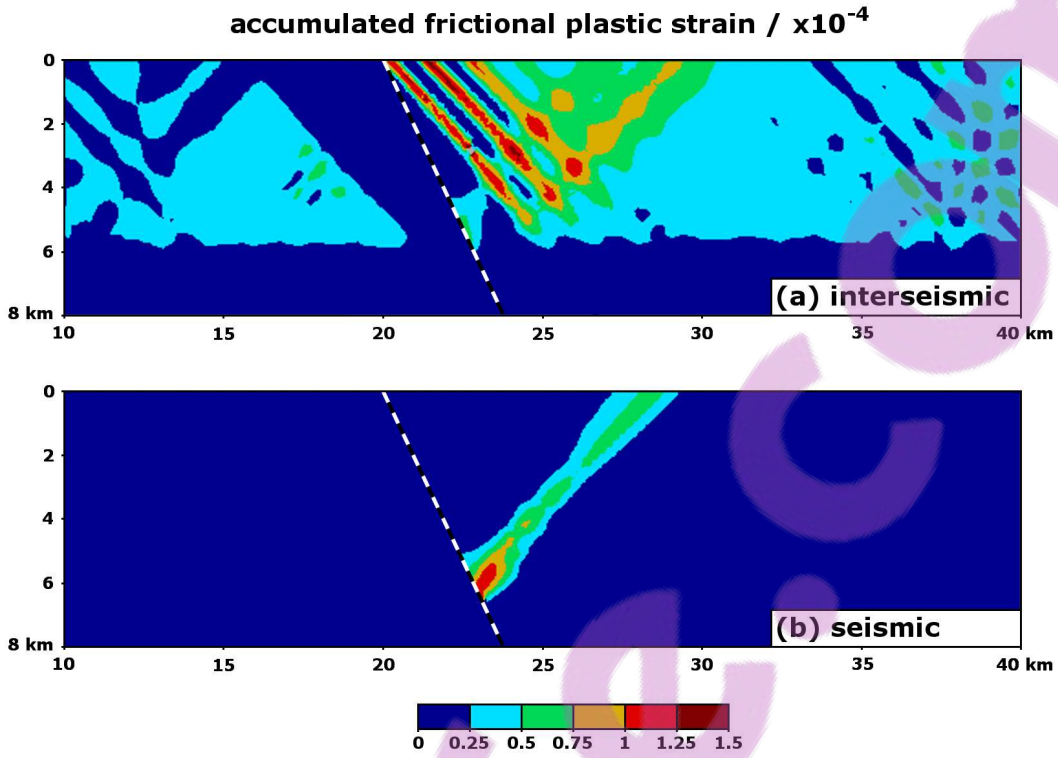

Figure 3.3: Frictional-plastic strain accumulated during (a) the 12th interseismic period, and (b) the 12th seismic period, for a model containing a 65° dipping fault. The position of the fault is indicated by the black and white dashed line.

on the main fault, i.e., coseismic antithetic faults. A similar result is replicated in the model presented here by considering frictional-plastic strain accumulated during the coseismic period in response to slip on a 65° dipping master fault (Figure 3.3(b)). For the model containing a 50° dipping fault, frictional-plastic strain during the seismic period is negligible as local bending at the surface of the hanging wall is less pronounced that for steeper faults. This result suggests a preference for coseismic antithetic faulting may be limited to master faults with steeper dip angles.

In contrast, in Figure 3.2(c) and Figure 3.3(a) a preference for synthetic fault formation is demonstrated; this is due to a steady accumulation of frictional-plastic strain in shear bands during the comparatively longer interseismic period. It should be emphasised this result is not inconsistent with Melosh and Williams Jr. (1989),

but rather indicates that the configuration of secondary faults is sensitive to the dip of the master fault and to the stage of the seismic cycle during which they form.

3.3 Extension budget

The extension rate of the modelled rift, which is applied as a velocity boundary condition at the lateral boundaries, must be accommodated within the crust by some combination of the available means of deformation, i.e., by fault slip, or the accumulation of elastic, frictional plastic, or viscous strain. The relative contribution of each to the total extension of the crust during a single seismic cycle comprises the extension budget. For instance, if during a single seismic cycle tectonic extension of 2.64 m is comprised of 0.66 m of horizontal elastic strain, 0.66 m of horizontal frictional-plastic strain, and 1.32 m horizontal component of fault slip, then the relative contribution of each component is 0.25, 0.25 and 0.5, respectively. Depending on the means of deformation available, the extension budget will vary with both depth (e.g., viscous strain does not accumulate in the upper-crust) and time (e.g., fault slip occurs only during the seismic period). Figure 3.4 shows a representative extension budget with depth for the (a) interseismic and (b) seismic periods, and (c) a full seismic cycle, where each component is normalised against the total extension (2.64 m) during the full cycle.

Figure 3.4(a) indicates that viscous strain is the sole contributor to deformation at depths greater than 9 km and, due to its slow accumulation rate, occurs principally during the interseismic period. Small changes in elastic strain are also observed at these depths, although, summed over the interseismic and seismic periods, their net effect is nearly zero, which is characteristic of the dynamic equilibrium of the system.

Figure 3.4(c-d) indicates that the presence of a rupturing fault permits extension of the upper-crust to be distributed between the two brittle failure mechanisms of fault slip and frictional plastic deformation. However, the accumulation of each component is mutually exclusive, i.e., fault slip occurs rapidly during the seismic period (Figure 3.4(b)) whereas frictional-plastic strain accumulates slowly during the

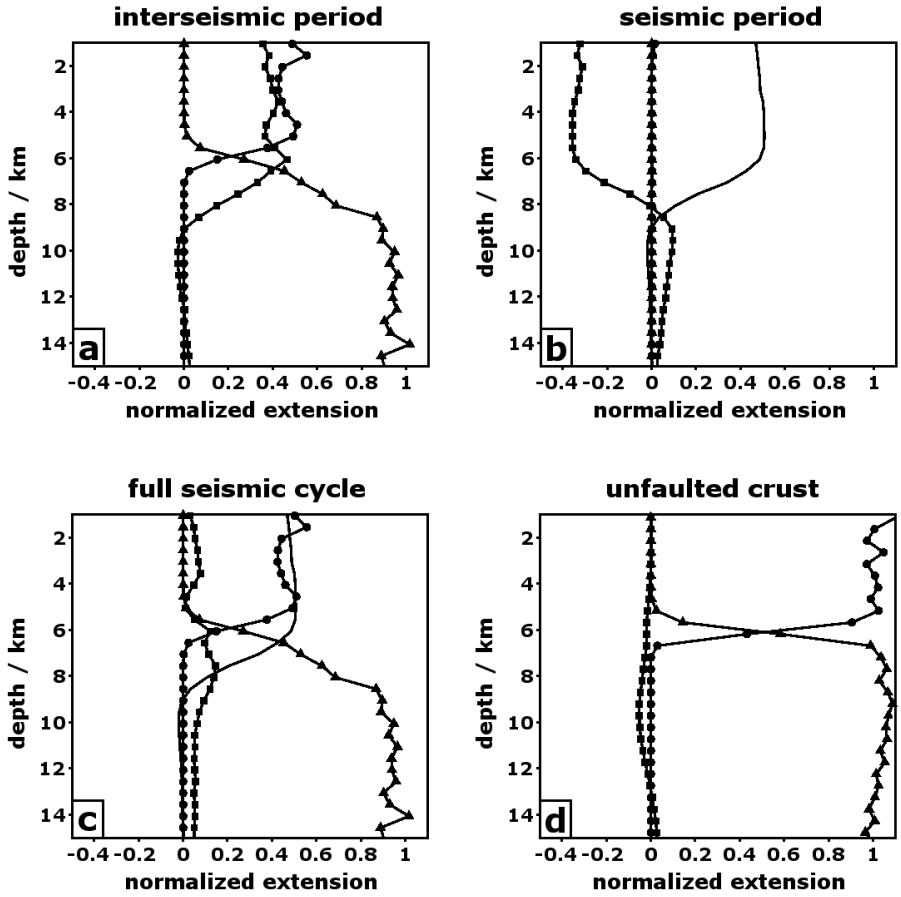

Figure 3.4: (a) Interseismic and (b) seismic components of the (c) full seismic cycle extension budget. The contribution of fault slip (no marker), elastic (square), frictional-plastic (circle) and viscous (triangle) deformation mechanisms at each depth add to give the unit normalised extension profile. This extension budget has been constructed for deformation in the interval defined by $10 < x < 40$ km. (d) Extension budget for a crust at a critical stress state in the absence of faulting.

interseismic period (Figure 3.4(a)). Coseismic frictional-plastic strain accumulation is significant for steeper dipping faults (see Section 3.2.1). A significant component of transient elastic strain accommodates extension during the interseismic period, but is replaced by fault slip in the following seismic period. It also causes a reduction of the maximum shear stress, $(\sigma_1 - \sigma_3)/2$, throughout the crust wherever the least principal compressive stress is horizontal, i.e., $\sigma_3 = \sigma_{xx}$. Accumulation of frictional-plastic strain ceases for a brief post-seismic period until extension restores the pre-seismic

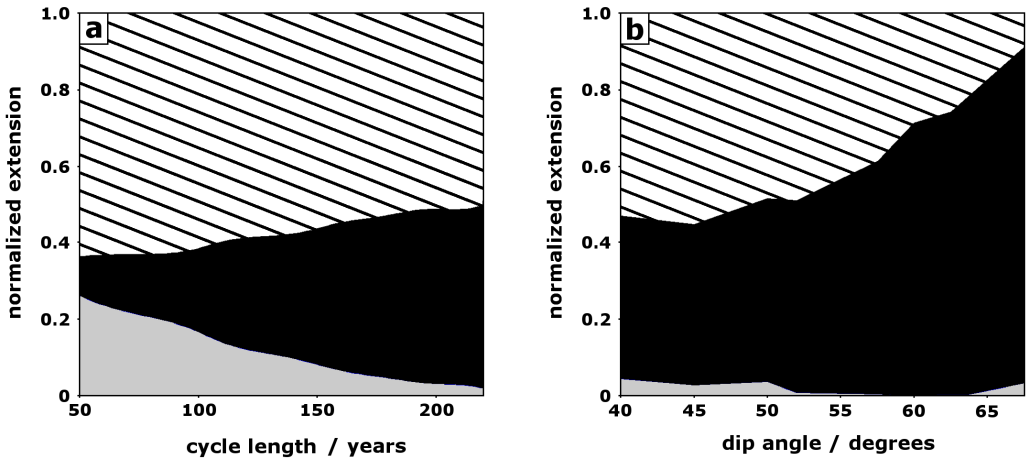

Figure 3.5: Elastic (grey), frictional-plastic (black) and fault slip (black hatched) normalised components of the extension budget averaged over the upper-crust ($0 < z < 5\,\text{km}$). (a) Extension budget components against the length of the seismic cycle. (b) Extension budget components against the dip angle of the fault, for a seismic cycle of length 220 yr.

stress state to frictional yield (Dempsey *et al.*, 2012b).

Figure 3.4(a) and (c) show that the transition from purely brittle deformation, including fault slip and frictional-plastic straining, to purely viscous deformation occurs over a 5-9 km depth interval. Frictional plastic deformation terminates over a shallower 5-6.5 km depth interval, with a small overlap between the brittle and viscous rheologies indicative of the exponential decrease in viscous strain rate with decreasing temperatures (Equation (2.12)). Fault slip penetrates further into the brittle-ductile transition zone, terminating over depths of 6.5-9 km. This bimodal truncation of the two frictional behaviours is due to the relative frictional weakness of the fault (μ=0.2 compared with the intact crust $\mu = \tan(\phi') \approx 0.3$) and indicates a mixed brittle-viscous region between a purely brittle upper-crust and purely viscous lower-crust. In this region, weakened, embrittled faults are able to penetrate the mostly viscous lower-crust (Scholz, 1988, 1998), while frictional plasticity is limited to shallower depths.

Figure 3.5(a) considers the composition of the full cycle extension budget within

the upper-crust (< 5.0 km depth) as a function of the loading period that precedes an earthquake. For this analysis, each simulation was "spun-up" to the same dynamic stress equilibrium, using a nominal interseismic period of 220 years, and followed by a single seismic cycle at the modified length. Thus, Figure 3.5(a) considers the effect of seismic cycle length independent of the previous rupture history. It also illustrates extension accommodation in the upper-crust at different times during the interseismic period. As in Figure 3.4, components were normalised against the total extension applied over the full cycle. For longer seismic cycles, distributed frictional-plastic strain accounts for a proportionally larger share, e.g., approaching 50% of the total extension for an interseismic period 220 years in length. During the early stages of the interseismic quiescence following fault rupture, tectonic extension is mostly taken up by the accumulation of elastic strain throughout the upper-crust, which is later exchanged for fault slip. Extension reduces horizontal stress, σ_{xx}, which causes the differential stress to approach the limit of frictional plastic failure, q_p, and switches large areas of the crust from elastic to frictional plastic behaviour. Elastic strain is temporarily saturated in these regions, and subsequent accumulated strain is frictional plastic. Each successive increment of extension during the interseismic period then has two compounding effects: (i) to effect stress changes that switch ever larger regions of the crust from elastic to frictional plastic deformation and (ii) to accumulate frictional-plastic strain within an increasing volume of yielding crust and elastic strain within a decreasing volume of elastic crust. Horizontal stress is increased in the subsequent earthquake step due to coseismic displacements of the fault blocks.

Fault dip also exerts control on the composition of the upper-crust extension budget (see Figure 3.5(b)). For a system in dynamic equilibrium with a seismic cycle 220 years in length, a shallow fault, $\theta = 40 - 50°$, accommodates more than half of the applied extension through fault slip, with the shortfall accommodated by frictional plasticity. However, steeper faults accommodate a decreasing proportion of the total extension through displacement of the fault blocks. This decrease is because the production of a given amount of horizontal extension requires an increasing

component of vertical movement, and thus a correspondingly larger earthquake, at steeper angles of fault dip. A reduction in the fault-slip component of the extension budget must be compensated by an increase in other components, which for an upper-crust at dynamic equilibrium must be frictional-plastic strain. This result is largely independent of the elastic properties of the crust, and the partitioning of upper-crustal extension between the accumulation of frictional-plastic strain and episodic fault slip appears to be controlled principally by the geometry of the system.

3.3.1 Fault listricity

A fault geometry in which the dip angle shallows with depth has been proposed to account for observations of reverse drag in the hanging wall stratigraphy (e.g., Janecke *et al.*, 1998). Such listric normal faults typically dip at steep angles ($70-80°$) near the surface but are inferred to shallow in regions where overpressured pore fluids are encountered (Bruce, 1984), or where viscosity contrasts rotate the principal stresses (Bradshaw and Zoback, 1988). In the TVZ, faults dip steeply at the surface, however, seismological observations (Beanland *et al.*, 1990) and kinematic arguments (Villamor and Berryman, 2001) suggest that fault dip shallows to $45-60°$ at seismogenic depths. In this section, the effect of fault listricity on distributions of frictional-plastic strain is considered.

An arc geometry is used to approximate the listric fault geometry with depth. The fault dips at 80° at the surface, shallows to 55° at a seismogenic depth of 8 km, and has a final dip of $\approx 22°$ at 15 km depth. The same seismic cycle regime as for the planar fault is imposed and results are presented for the eleventh seismic cycle

Figure 3.6 *(following page)*: Deformation and frictional plastic behaviour associated with a listric fault geometry. (a) Coseismic vertical displacement profile at the surface (c.f. Figure 2.3(b)). (b) Coseismic fault parallel displacement at the fault scarp for the footwall (dashed) and hanging wall (solid) blocks (c.f. Figure 2.4). (c) Distribution of frictional plastic strain after eleven seismic cycles (c.f. Figure 3.1(b)). (d) Mises stress failure shadow prior to fault slip (c.f. Figure 3.2(a)). (e-g) Extension budget (c.f. Figure 3.4).

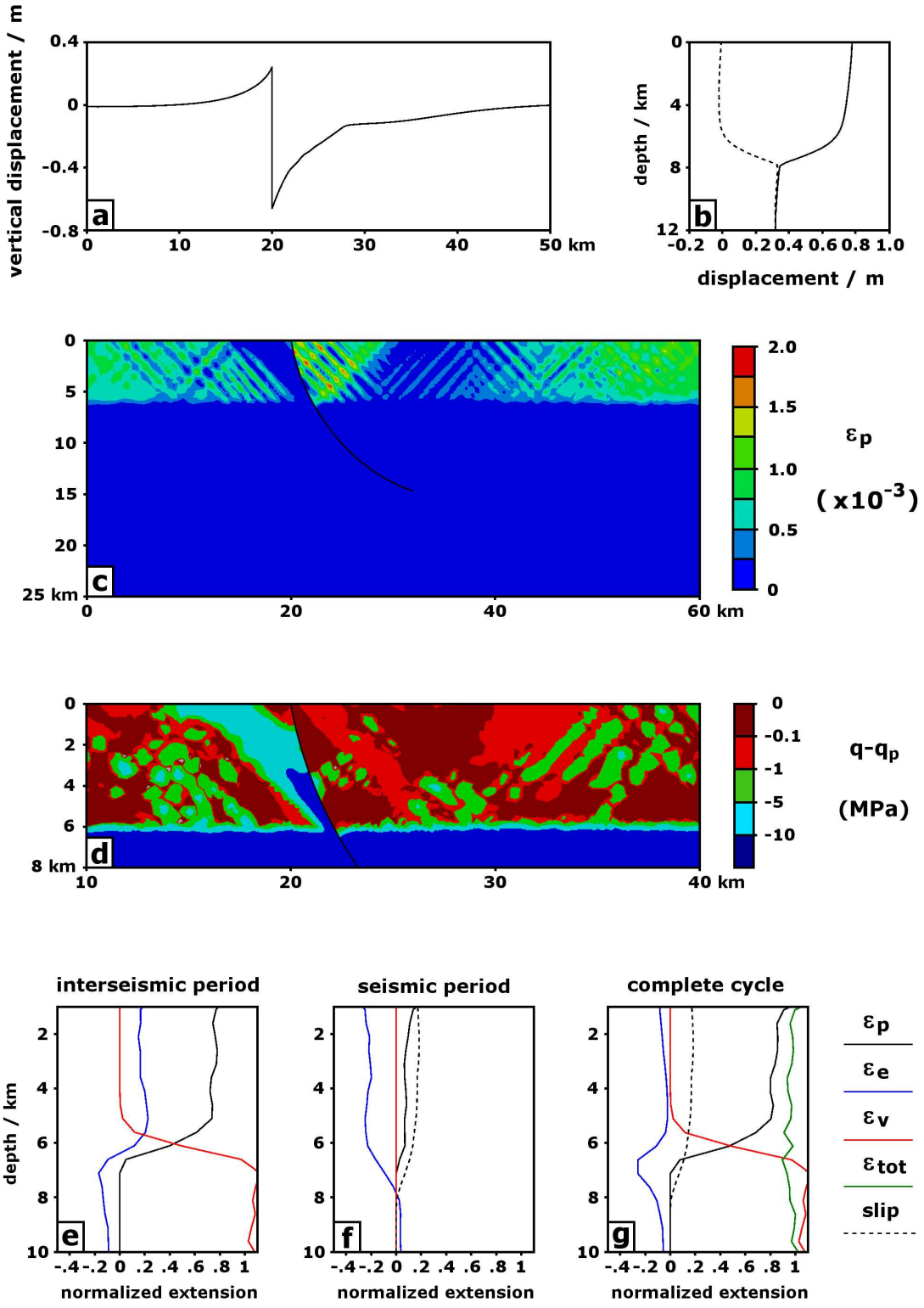
vertical displacement / m
0.4
0
-0.4
-0.8
a
0
10
20
30
40
50 km
depth / km
0
4
8
12
b
-0.2 0 0.2 0.4 0.6 0.8 1.0
displacement / m
0
5
10
15
20
25 km
c
0
20
40
60 km
2.0
1.5
1.0
0.5
0
εp
(x10-3)
0
2
4
6
8 km
d
10
20
30
40 km
0
-0.1
-1
-5
-10
q-qp
(MPa)
interseismic period
seismic period
complete cycle
depth / km
2
4
6
8
10
e
f
g
-.4 -.2 0 .2 .4 .6 .8 1
normalized extension
εp
εe
εv
εtot
slip

(Figure 3.6).

Coseismic displacements at the surface of the model are qualitatively similar to the planar fault geometry (Figure 2.3), exhibiting uplift of the footwall and subsidence of the hanging wall. As the interseismic period is 220 years in length for both geometries, comparisons can be made between the two profiles. Surface displacements for the listric geometry are significantly less than for the shallow planar fault, which indicates that extension applied for a given period is producing a smaller slip event. This is consistent with Figure 3.5(b) showing fault slip as a diminishing proportion of the extension budget with increased dip angle. Fault parallel dip-slip profiles are also qualitatively similar to their planar counterparts (Figure 2.4), but again at a reduced magnitude reflecting the smaller slip event.

Frictional plastic strain accumulates in the upper-crust at a greater rate for the listric fault than for the planar geometry. Its distribution has features in common with Figure 3.1(b), including pronounced intensity in the immediate hanging wall, a conspicuous absence from the immediate footwall, and distributed straining outside the influence of the fault near the lateral boundaries. Suppression of frictional plastic strain accumulation in the footwall is once more due to a failure shadow extending from the fault surface into this block. The failure shadow has a smaller horizontal dimension than the shallow planar fault (Figure 3.2), which indicates horizontal coseismic recoil associated with this geometry is less effective at reducing stress in the footwall.

An extension budget for the listric geometry (Figure 3.6(e-g)) reveals the extent to which frictional plastic strain accommodates the shortfall in upper-crust extension that is not accounted for by the fault. Over a full cycle, fault slip takes up $15-20\%$ of the applied extension with frictional plastic strain accounting for the balance. In terms of an equivalent planar geometry, Figure 3.5(b) indicates this proportion is equivalent to a fault dipping at 65-70°. In contrast to the planar geometry, an appreciable quantity of frictional plastic strain accumulates rapidly during the coseismic period. This represents $\approx 10\%$ of the total frictional yield for the seismic cycle and Figure 3.7(a) indicates that it occurs exclusively in the hanging wall block, and prin-

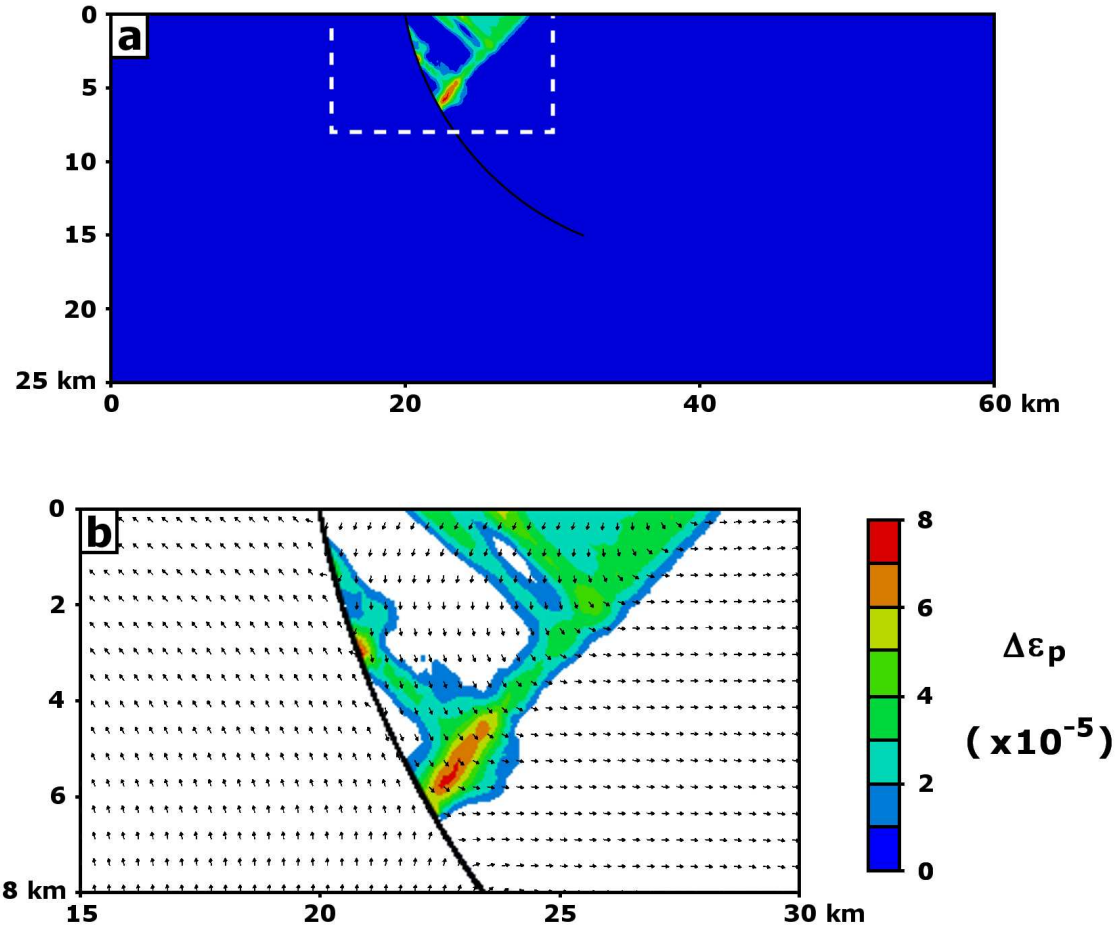

Figure 3.7: (a) Frictional plastic strain accumulated during a single seismic period, $\Delta\varepsilon_p$. (b) Vectors of displacement direction overlaid on the distribution of hanging wall frictional plastic strain. Note that the limits of (b) are delineated in (a) by a white dashed line, and that the lowest contour level has been replaced by white to contrast with the displacement vectors. A rigid body displacement of $+0.1\,\mathrm{m}$ has been applied to the vertical component of the vectors in (b) to better resolve horizontal displacements. This corresponds to a displacement observation in a moving frame of reference and does not alter the interpretation of strain (a displacement gradient).

cipally within an antithetic shear band that splays near the surface. Localisation of frictional plastic strain in this region occurs due to coseismic displacements that are consistent with further extensional failure. Vectors of displacement direction superimposed on the strain distribution (Figure 3.7(b)) show divergence in the horizontal displacement at the surface of the model where the shear band splays. This is caused by reverse drag of the hanging wall block, which induces distributed extension at the surface and encourages shear on an antithetic fault to depth.

3.4 Fault plane rotation

Coseismic displacement of the fault blocks parallel to the fault plane, which accommodates extension and reduces near-fault shear stresses, is perhaps the most conspicuous aspect of deformation associated with faulting (Barr, 1987; Segall, 2010). However, observations of normal faults dipping at shallow angles ($< 30°$) that preclude reactivation within an Andersonian stress regime (Wernicke, 1995), or a regime of cross-cutting faults (Profett, 1977; Nur *et al.*, 1986), suggest a secondary process of rotation via a bookshelf or domino-style mechanism. Such motion, resolved at the fault plane, is equivalent to a displacement of the fault block perpendicular to the fault plane. Furthermore, for a rotation, as opposed to a rigid body translation, displacement must increase linearly with distance from some pivot, i.e., a point of no displacement.

Figure 3.8 plots fault perpendicular displacement along the fault and against depth during (a) the interseismic and (b) seismic periods, with a regression line fit to the data in the brittle layer ($< 8\,\text{km}$ depth). During both periods, displacement profiles in the upper-crust are approximately linear and have gradients of 59 and $66\,\text{mm}\,\text{km}^{-1}$ (i.e., millimetres of fault perpendicular displacement per kilometre of depth) for the interseismic and seismic periods, respectively.

The magnitude of fault plane rotation can be calculated from the gradients of the regression lines in Figure 3.8. A linear fault-normal displacement profile, u, is expressed as a function of depth, $u = m(z - z_0)$, where m is the gradient of regression

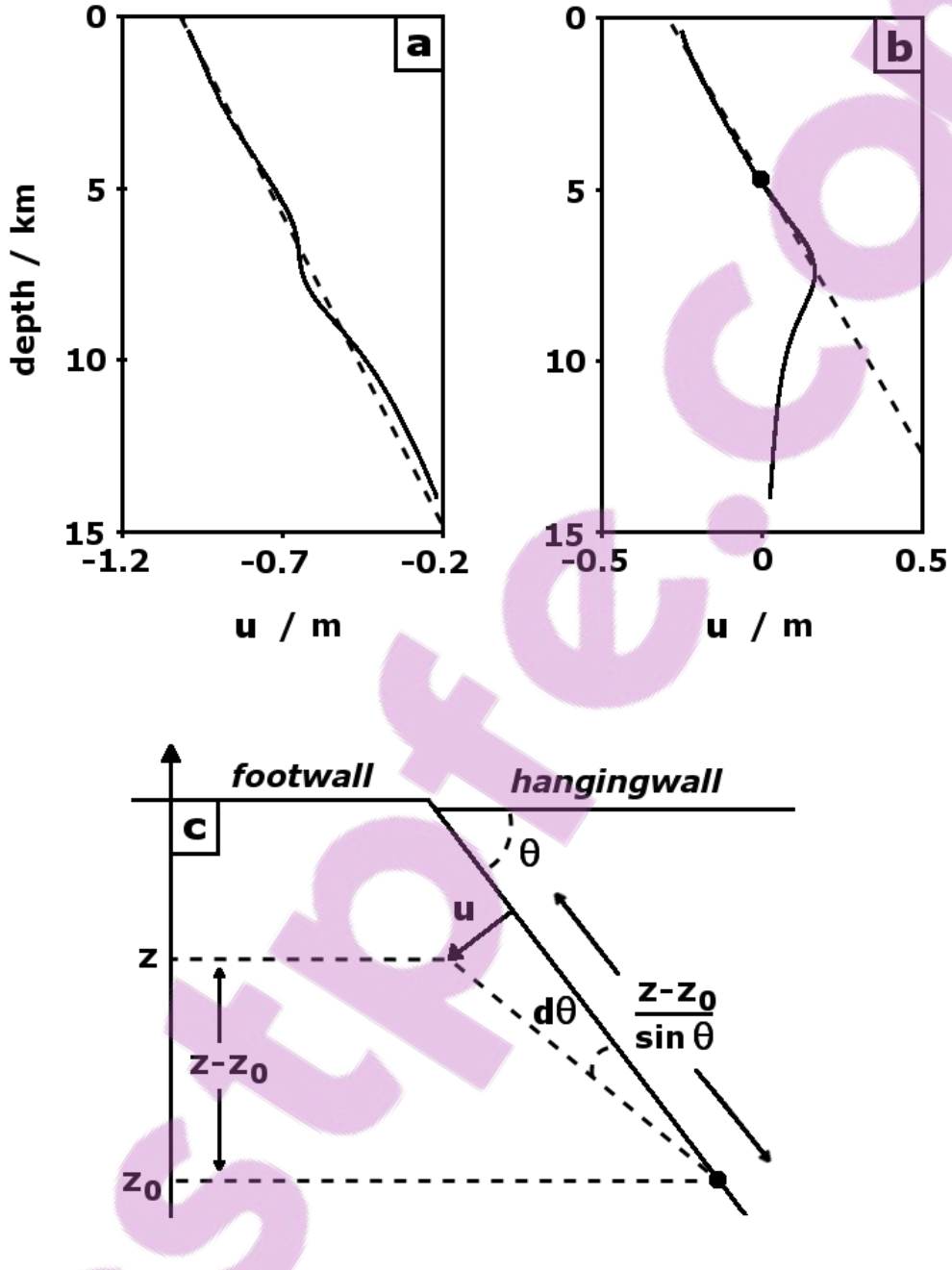

Figure 3.8: Fault perpendicular displacement along the fault surface during (a) the interseismic and (b) seismic period. A linear regression profile has been fit to the data above a depth of 8 km. (c) Geometric arguments used to derive fault rotation from fault perpendicular displacement profiles. Note that negative displacements in (a) and (b) correspond to the direction of the vector **u** in (c). The position of the axis of rotation is indicated in (b) and (c) by a black circle.

line through the displacement data, and z_0 is the depth of the fixed horizontal axis, or pivot, about which rotation occurs. The depth of the pivot corresponds to the intersection of the regression line in Figure 3.8(a-b) with the vertical $u = 0$ axis. During the interseismic period, the pivot ranges in depth from 18 to 18.7 km, with a mean of 18.4 km. For the seismic period, rotation of the fault plane occurs about a pivot at a depth of 4.7 km. A displacement, u, some vertical distance $z - z_0$ above the pivot induces a rotation, $d\theta$, of the fault plane (Figure 3.8(c)), given by

$$d\theta = \tan^{-1}(u.\sin\theta/(z - z_0)) = \tan^{-1}(m.\sin\theta) \qquad (3.1)$$

Using $m = 59$ and $66\,\mathrm{mm\,km^{-1}}$, rotations of the fault plane are calculated; they are 2.4 and 2.7 millidegrees during the interseismic and seismic periods, respectively. This corresponds to a long term rotation rate of 23.5° every million years (for a seismic cycle that repeats every 220 years), although a reduction in this rate would presumably be observed as the fault rotates out of the range for reactivation.

The total rotation during a seismic cycle is distributed approximately equally between the interseismic and seismic periods. The amount of coseismic rotation is proportional to the length of the interseismic period that precedes it, and is thus also proportional to earthquake magnitude. Furthermore, coseismic rotation about an axis at a depth of 4.7 km, 14 km shallower than that for the interseismic period, suggests that a different forcing causes each rotation. For instance, during the interseismic period, far-field tectonic extension deforms the entire crust, causing vertical contraction in addition to horizontal spreading, effectively flattening the crust and the fault that is hosted within. The effect of this deformation on fault dip is evident in Figure 3.9(a), which presents the exaggerated change in position of the fault surface and topography during the interseismic period.

In contrast, displacements at the lateral boundaries during the short seismic period are too small to account for the observed rotation. However, large and rapid stress changes in the mid-crust, which cause uplift of the footwall and accommodate collapse of the hanging wall, may be responsible. Footwall uplift is caused by a

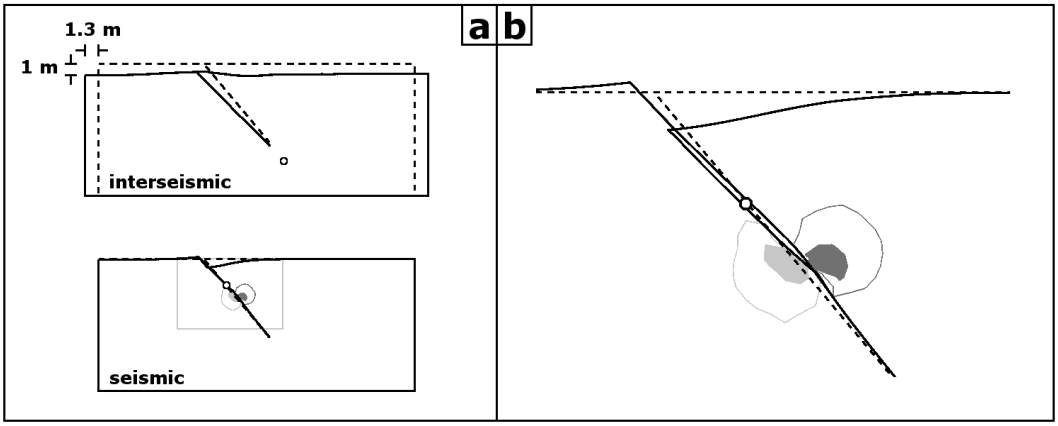

Figure 3.9: Deformation of the entire model domain and fault plane, exaggerated 2000 times, during (a) the interseismic and seismic periods. Boundary extension of 1.3 m at both lateral boundaries, along with a vertical contraction of 1 m, is marked. (b) Coseismic deformation in finer detail for the grey box in (a). Pivots about which rotation occurs are shown by open circles. Contours indicate coseismic mean stress change: light grey, unfilled = -0.25 MPa, light grey, filled = -0.5 MPa, dark grey, unfilled = +0.25 MPa, dark grey, filled = +0.5 MPa.

decrease in stress and rapid decompression of the crust between 6 and 9 km depth in the footwall block. Figure 3.9(b) shows the decrease in pressure associated with this uplift, superimposed on the deformed topography and fault plane. A drop in pressure corresponds to an increase in volume in that region, which, while primarily directed up-dip along the fault plane, also includes a fault normal component. This expansion applies a force to the hanging wall and a torque about the pivot at 4.7 km depth. This expansion also accounts for a component of the pressure increase in the adjacent hanging wall. The expanding footwall does work on the hanging wall, which, in addition to the compression caused by dip-slip of the fault block above, yields a reduction in volume and an increase in stress. As this rotation occurs due to stress changes at the fault tip, the depth of the pivot about which rotation occurs is primarily controlled by the depth of faulting.

3.5 Evolution of a normal fault system

Where pre-existing faults do not adequately accommodate the geodetic extension rate, parts of the crust are subjected to a horizontal, positive strain. In regions of the crust where the shear stress is below the Mohr-Coulomb failure limit, extension is accommodated by elastic strain. However, continued elastic stretching generates shear stresses that eventually induce failure on any pre-existing fracture planes and material discontinuities. Shear stresses are maintained at near critical values (Townend and Zoback, 2000) by incremental frictional failure on these minor structures in response to each subsequent increment of extension. These processes constrain the maximum stress state attainable by the crust and therefore impose an upper limit on the amount of extension that is temporarily accommodated as elastic strain.

However, no such constraint exists for accommodation of extension through frictional-plastic strain, which accumulates following the saturation of elastic strain. In the model presented here, frictional plastic deformation localises in shear bands that form at 45° to the maximum principal compressional stress, which is vertical in an extensional tectonic regime. That these shear bands represent the development of new faults is speculative, although they do satisfy two criteria associated with fault structures: (i) the shear bands accommodate dip-slip displacement and (ii) these structures are localised, rather than distributed (Schueller *et al.*, 2010), zones of deformation, in this case the width of several elements (approximately 1 km). In these models, shear zone width is sensitive to mesh dimension, as a description of strain softening behaviour (Needleman, 1988) has not been incorporated. Physically, a localisation of frictional plasticity represents a continuous reactivation within a particular region of those small discontinuities, e.g., joints, dilational jogs, fractures, etc., accommodating shear displacements. Providing each subsequent reactivation increases the length of the activated structure, a region of frictional plastic shear may be regarded as a sort of proto-fault. Although this model does not describe the evolution of a proto-fault-style shear zone into a true fault that perturbs stresses in its vicinity, it does provide insight into the early onset of proto-fault development.

Basinward migration of normal fault structures has been inferred from stratigraphic studies in Turkey (Dart *et al.*, 1995), the central Basin and Range province, USA (Horton and Schmitt, 1998), the Gulf of Corinth, Greece (Goldsworthy and Jackson, 2001), and the strike-slip Gar Basin in western Tibet (Sanchez *et al.*, 2010). Structurally, new faults develop in the hanging wall block of older faults producing a series of sub-parallel faults spaced every 2-5 km. Goldsworthy and Jackson (2001) proposed several mechanisms for the cessation of rupture on one fault and concurrent development of an adjacent structure including: topographic stresses in a domino-style topography modulated by the strength of the active fault; density contrast between sedimentation of the hanging wall basin and erosion of the uplifted footwall; and rolling-hinge evolution along a migrating lower-crustal flow front (Buck, 1988; McKenzie *et al.*, 2000). However, they note that, with the exception of the rolling hinge, which itself requires a migrating magma source, these mechanisms do not account for the preferred basinward direction of migration. Alternatively, inward migration within a rift may result from brittle necking of strong crustal layers, where thinner brittle layers are easier to fault relative to thicker brittle layers outside the rift (Buiter *et al.*, 2006).

The migration of fault activity first requires that new faults form, which occurs when existing faults do not accommodate the total geodetic extension rate. For instance, Figure 3.4 shows that, for a 220 year interseismic period, a single fault dipping at 50° accounts for approximately half the extension applied to the upper-crust, with the balance accommodated by off-fault frictional-plastic strain. As fault slip and frictional-plastic strain accumulate during the seismic and interseismic periods respectively, the competing accumulation of elastic versus frictional-plastic strain during the interseismic period is considered, with the caveat that the elastic component is replaced by fault slip during an earthquake. Elastic strain accumulates only in those regions of the upper-crust maintained below the limit of frictional plastic failure, which is largely within the near-fault stress-failure shadow (Figure 3.2(a)). Elsewhere, tectonic extension applied for long time periods ensures the crust is close to failure and thus strain is accommodated by frictional plasticity.

For a system containing a single fault, frictional-plastic strain accommodates a significant component of the extension budget (Figure 3.5(b)). In terms of rift basin evolution, the model describes an area soon after the onset of extension in which only a single mature fault developed (see Figure 3.10(a)). The full extension rate cannot be accommodated by this structure, and thus frictional-plastic strain accommodates the shortfall. Frictional-plastic strain localises into shear zones in the hanging wall. In the model presented here, these shear zones are synthetic to the main fault, and are therefore consistent with a scenario of migration of fault activity into the hanging walls of existing faults. However, the formation of secondary faults antithetic to the main fault, i.e., a graben geometry, is observed in many locations (e.g., Jackson and McKenzie, 1983) and also in numerical experiments (Melosh and Williams Jr., 1989). Preference of one over the other has been considered from an energy minimisation perspective (Melosh and Williams Jr., 1989); however, Figures 3.2 and 3.3 indicate that the geometry of the primary fault, and the precise phase of the seismic cycle during which secondary fault formation occurs, may also play a role. Other factors that may control the geometry of secondary structures include the initial localisation of shear bands onto pre-existing planes of weakness or crustal heterogeneities, and the effects of gravitational spreading and basal detachment shear during rifting (e.g., Brun *et al.*, 1994).

Localisation of frictional plastic deformation into proto-faults occurs outside the stress-failure shadow of the main fault in the hanging wall block (Figure 3.10(b)). The extent of the failure shadow therefore exercise a degree of control on the location of these proto-faults and perhaps also the spacing of a sub-parallel array of

Figure 3.10 *(following page)*: Conceptual evolution of a normal fault system over time. (a) Shortly after the onset of rifting the crust hosts a single fault that imposes a stress-failure shadow as in Figure 3.2 (grey shading). (b) Frictional-plastic proto-faults, and (c) eventually new faults, develop in the hanging wall. (d) Continual rotation of faults out of the angle for reactivation reduces the component of extension accommodated by fault slip and promotes the development of new proto-faults. (e) Recovery of the failure shadow around inactive faults allows cross-cutting proto-faults to develop.

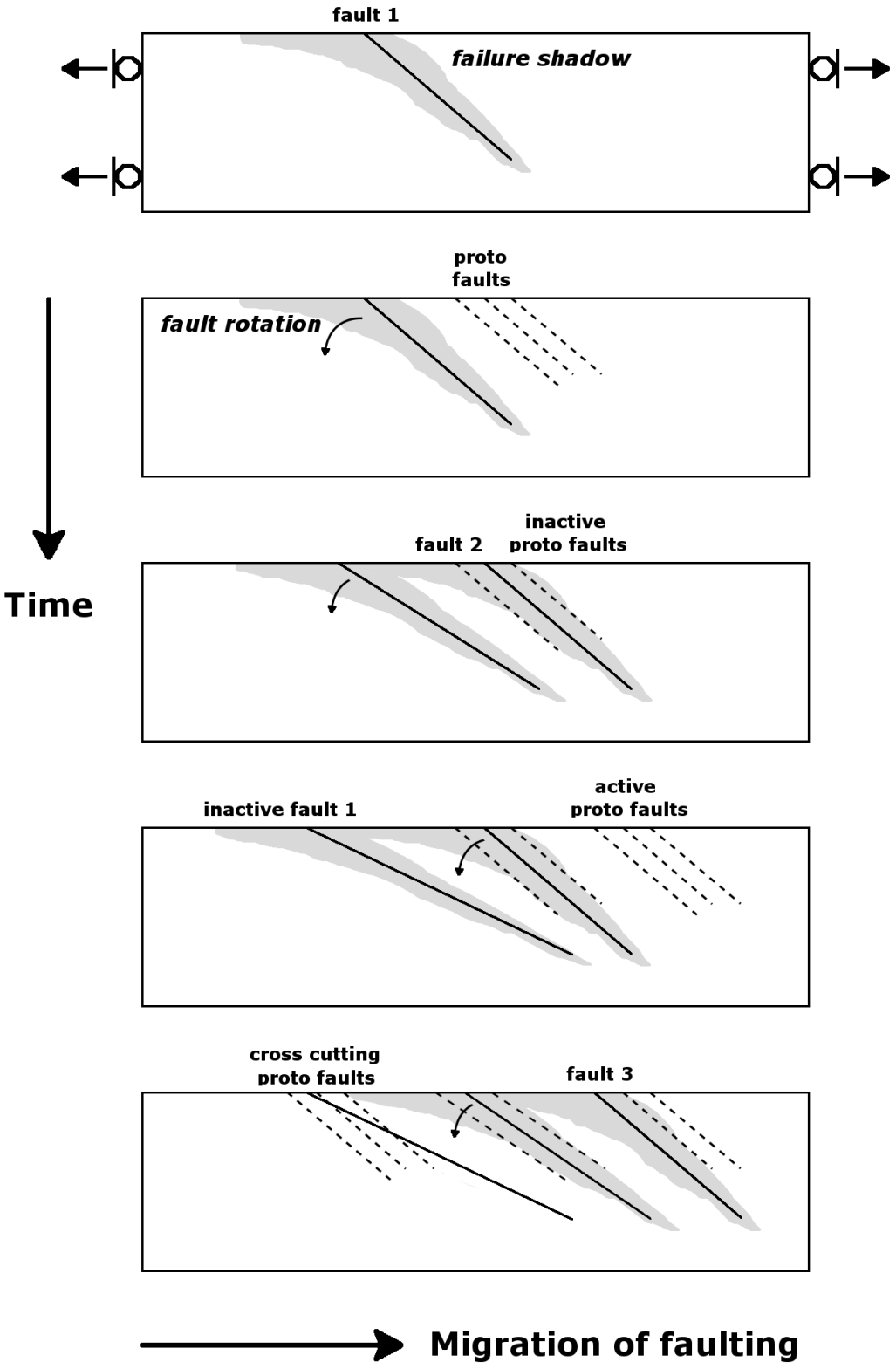
fault 1
failure shadow
proto
faults
fault rotation
inactive
fault 2
proto faults
Time
inactive fault 1
active
proto faults
cross cutting
proto faults
fault 3
Migration of faulting

faults. If the -1 MPa contour is used to estimate the dimension of the failure shadow, Figure 3.2(a) would suggest a minimum spacing of 10 km for footwall faults and 2 km for hanging wall faults. The latter is slightly smaller than the average fault spacing in the western Gulf of Corinth of 5-8 km (Rohais *et al.*, 2007); however, as the dimensions of the stress-failure shadow depend on the thickness of the brittle upper-crust and fault dip, direct comparison between model and field studies is not possible. For example, crustal thickness in the Gulf of Corinth of 10-12 km (Briole *et al.*, 2000) is somewhat thicker than the 6-8 km for the models described in this thesis. For this crust, failure shadows should be larger than those modelled here and, consequently, minimum fault spacings for both fault blocks should increase. Fault dips in the western Gulf of Corinth are not well constrained, although the dip of the fault plane modelled here is consistent with those used by Briole *et al.* (2000) in modelling normal fault earthquakes in the Corinth Rift.

Coalescence of frictional plastic deformation into a single shear zone, culminating in the formation of new discrete fault structure has important implications for the extension budget. The introduction of a second stress-failure shadow (Figure 3.10(c)) increases the area available for interseismic elastic-strain accumulation and reduces that available for frictional-plastic straining. Proto-faults previously developing adjacent to the new fault would become inactive as deformation within its stress-failure shadow is switched to elastic/fault slip (Figure 3.10). Fault slip will then account for a greater component of the extension budget. Frictional-plastic straining will initiate in the hanging wall of the new fault, although at a reduced rate reflecting the extension accommodated by the second fault.

Rotation of faults to shallower dip angles, either through interseismic stretching or coseismic stress changes in the mid-crust (see Section 3.4), has the opposite effect on the upper-crustal extension budget. The eventual removal of a fault that was accommodating extension (Figure 3.10(d)), and the subsequent recovery of stresses within its failure shadow to Mohr Coulomb yield (Figure 3.10(e)), increases the extension shortfall, which is then accommodated by frictional plasticity. The formation of proto-faults in the hanging wall of the second fault then accelerates and the cycle

continues. In addition, the recovery of the stress-failure shadow of the inactive fault would permit the development of new, cross-cutting faults in this region (Nur *et al.*, 1986).

The net effect of the processes discussed above is a preference for the migration of faulting into the hanging walls of existing faults. However, an appropriate timescale to attach to this evolutionary scenario is unclear, largely due to ambiguity in the rate of formation of new faults. In the model presented here, the frictional plastic shear strain rate in the hanging wall where proto-faults form is approximately $7 \times 10^{-16}\,\mathrm{s}^{-1}$, which for faulting to seismogenic depths (6-8 km) represents a slip rate on the order of $0.15\,\mathrm{mm\,yr}^{-1}$. At this rate, a proto-fault should exhibit several 10's of meters of offset after several hundred kyr. Goldsworthy and Jackson (2001) described uplift of coastal faults in the western Gulf of Corinth and suggested that the morphology might be generated in less than a million years. One might further expect acceleration of the slip rate with increasing rift maturity due to along-strike linkage of fault segments (Cowie and Roberts, 2001; Bell *et al.*, 2009).

3.6 Chapter summary

The onset of extension and subsequent evolution of normal faulting within the brittle crust was investigated via a computational model for an extending elastic-viscous-plastic crust. Extension applied at the boundaries of the model is accommodated in the upper-crust through dip-slip on a fault contact surface or the accumulation of frictional-plastic strain, and in the lower-crust through viscous deformation. Between these two layers, a mixed brittle-viscous region develops, which exhibits a rapid decrease in frictional-plastic straining, a slower decay in fault slip, and the onset of viscous deformation.

Frictional-plastic strain localises preferentially within the hanging wall due to the distribution of shear stress near the fault. Coseismic displacements of the fault blocks create a stress-failure shadow that extends disproportionally into the footwall thereby favouring the formation of new faults in the adjacent hanging wall block.

The dimension of the failure shadow at the surface is broadly consistent with the observed fault spacing in normal fault arrays of several kilometres.

Rotation of the fault plane about a horizontal axis at depth is observed to occur during both phases of the seismic cycle. A long term rotation rate of $23.5^\circ\,\mathrm{Myr}^{-1}$ is divided into almost equal components of far-field tectonic rotation during the interseismic period and rapid rotation induced by mid-crustal stress changes during the seismic period. The subsequent shallowing of the fault plane over many seismic cycles provides one avenue by which faults may be become inactive, accelerating the frictional-plastic straining and proto-fault formation that accommodates the extension shortfall.

The juxtaposition of these competing processes within an extending crust is consistent with the evolution of new faulting into existing hanging walls. However, a basinward migration of faulting cannot occur indefinitely without a corresponding migration of the locus of extension. Where the position of extension is static in time, recovery of the stress-failure shadow around inactive faults may permit the eventual return of faulting to the older footwalls. Cross-cutting of old, shallow structures by younger, steeper faults is permitted, providing that they form outside the stress-failure shadow that extends disproportionally into the footwall block.

As a final note, this simplified model for normal fault evolution requires careful interpretation in the context of a richly complex crust. Material properties, stratigraphy and tectonic forcings that vary along-strike and with depth also exert important controls on the evolution of deformation and stress around faults, and, by extension, the development of new structures. The mechanisms and scenarios described here do not constitute a complete or prescriptive theory, but rather serve as an illustration of the evolutionary processes that may prevail in specific locales, e.g., the western Gulf of Corinth.

My position is perfectly definite. Gravitation, motion, heat, light, electricity and chemical action are one and the same object in various forms of manifestation.

- Julius Robert von Mayer (1814-1878)

4

Energetics of extension and fault rupture

In this chapter, those processes leading to coseismic displacement of the fault blocks are considered. Mid-crustal stress changes, alluded to in Chapter 2, associated with slip arrest are considered from the perspective of energy flow and work. In addition to identifying fault behaviour, work flows permit the assignment of roles of cause and effect with respect to fault block displacements. For instance, modest elevation changes ($\sim$1 m) associated with coseismic uplift of the footwall require the production of vast quantities of gravitational potential energy. Work done to effect this uplift is derived from a drop in stress, and thus elastic strain energy, in the mid-crust. Similarly, subsidence of the hanging wall and an associated drop in gravitational potential energy must be offset by a gain in energy elsewhere. The interplay between these energy sources, and other dissipative mechanisms are considered.

Work presented in this chapter is drawn from a paper submitted to Geology in July 2011 and published in March 2012 (Dempsey *et al.*, 2012b). Results and text included in this chapter are largely unchanged from the published version as permitted by the University of Auckland under the *2008 Statute and Guidelines for the Degree of Doctor of Philosophy (PhD)*. Co-authors of this work Dr Susan Ellis, Dr Rosalind Archer, and Dr Julie Rowland advised and commented on the manuscript, however the bulk of the research and preparation for publication was undertaken by the thesis author (see accompanying declaration).

4.1 Elastic rebound

The conventional view of earthquakes asserts that elastic strain energy (Reid, 1911; Isacks *et al.*, 1968; Sibson, 1974, 1977) accumulates slowly within the crust by the action of plate tectonic forces and is concentrated and released through rupture on localised faults. This description of the seismic cycle implies that work done by tectonic forces stores elastic energy (EE), which in turn is expended to do work accelerating and deforming the crust during an earthquake via elastic rebound. This model was developed for strike-slip systems (Reid, 1911) where gravitational forces do not contribute to the work budget. However, geodetic observations of normal earthquakes on dip-slip faults record a significant drop in elevation of the hanging wall (e.g., Barrientos *et al.*, 1987; Koukouvelas and Doutsos, 1996)., which implicates gravitational potential energy (GPE) as a contributor to coseismic deformation in extensional tectonic environments (e.g., McKenzie, 1978; Stewart, 1980; Rowland and Sibson, 2001).

Elastic rebound has received support from the study of convergent and strike-slip fault systems using simplified assumptions in which a fault is represented by a dislocation within an elastic medium (Chinnery, 1961; Mansinha and Smylie, 1971; Okada, 1985). Considerable success has been achieved by matching predictions from these simple models to surface displacements measured by geodesy, supporting the idea that accumulated elastic strain energy is released during an earthquake. Elastic models have also been extended to consider dynamic rupture propagation owing to non-steady (rate-state) friction (Dieterich, 1979; Ruina, 1983) or fault normal stress (Oglesby *et al.*, 1998). Such analyses commonly neglect effects from gravity, background stresses, and anelastic strain accumulated over the seismic cycle, although they may consider post-seismic visco-elastic effects (Thatcher and Rundle, 1984). The focus of these studies has been the immediate effects of fault motion, and the transfer of elastic strain energy to seismic wave radiation.

Recent examinations of the energy budget for thrust fault systems (Cooke and Murphy, 2004; Del Castello and Cooke, 2007) indicate a response consistent with elas-

tic rebound, i.e., elastic strain energy is expended to do work against friction on the fault and against gravity deforming the surface. They also show a smaller component of radiated seismic energy, although for low seismic efficiencies this component can be regarded as negligible (McGarr, 1994; Kanamori, 2001; Scholz, 2002). More sophisticated rheological models consider the accumulated effects of many earthquakes over thousands to millions of years, and account for the release of elastic energy by anelastic viscous and frictional plastic strain on and around a fault or shear zone (Huismans *et al.*, 2005; Braun *et al.*, 2008). However, these do not explicitly model a frictional fault contact surface, but rather interpret localisation of shear strain in bands as fault formation (as detailed in Chapter 3).

The following sections address the energy/work budget of a normal dip-slip fault within an extending elastic-viscous-plastic crust using the 2-D finite-element model described in Chapter 2. The analysis presented contrasts the ability of stored EE and GPE to do work against friction, gravity, or elastic forces, and cause brittle or ductile deformation during the seismic cycle. For extensional tectonic settings, it is shown that a modification to elastic rebound theory is required to account for observed energy and stress changes. The concept of elastic rebound is not sufficient to describe global elastic strain accumulation and its potential to do work in an extensional regime (Tarantola *et al.*, 1979; Koseluk and Bischke, 1981).

4.2 Extension, energy and crustal stress

As a first step toward discussing strain energy changes induced by tectonic forces, simplified spring analogues for horizontal displacement of the crust are discussed. When considering issues of extensional strain and elastic strain energy it is useful to first consider the zero-energy state of the system. Approximating the crust as a spring, the zero-energy state corresponds to the length of the spring in the absence of forces. Applying a force to compress, i.e., shorten, the spring stores elastic strain energy, which represents a potential to do work at some later time (see Figure 4.1(a)). If the compressive force applied to the spring is abruptly removed the spring will rapidly extend to its original length, expending EE to do work accelerating and

displacing the spring. This is analogous to elastic rebound of the crust in a convergent tectonic environment.

For an extensional tectonic regime in which earthquakes occur in the context of a stretching crust, one might consider a modified spring analogue with tension replacing compression. Additional extension of the already tensile spring increases its EE (see Figure 4.1(d)), which, when released, does work accelerating and displacing the spring: an elastic rebound. However, this scenario is not consistent with the state of stress within the crust. A consequence of lithostatic loading is that, with the exception of the near-surface in extensional regimes, normal stresses within the crust are always compressive. Thus, a volume of rock brought to the surface from depth expands in response to the removal of lithostatic forces. Such physics underpins the violent and rapid expansion of rock associated with well-bore breakout (Zoback *et al.*, 1985) and rock-burst phenomena (e.g., Cook *et al.*, 1966). It also attests to the vast reservoirs of EE that exist within the crust and are accessible via changes in the stress state. In terms of the spring analogue, an increment of extension is equivalent to a reduction of compression and, associated with this, a reduction in EE (Figure 4.1(b)).

In terms of horizontal stress and strain, and recalling that these quantities are negative in compression, a crustal volume is considered in which a small increment of tectonic extension occurs. This extension is associated with a small, positive change in horizontal stress. As the existing horizontal stress state is compressive, and thus negative, the addition of a positive stress change moves the crust incrementally closer to the zero stress state (Figure 4.1(b)). The corresponding changes in elastic strain and elastic strain energy are negative. The reduction of internal energy indicates that work has been done by, not on, the crustal volume, and implies that extension might be caused by the crust itself, rather than imposed by some external force. The continuous reduction of EE in the period preceding an earthquake undermines a central tenet of elastic rebound theory and suggests that other forms of energy may be responsible for displacing and accelerating the crust during an earthquake.

This line of argument is extended in the next section by considering a formal

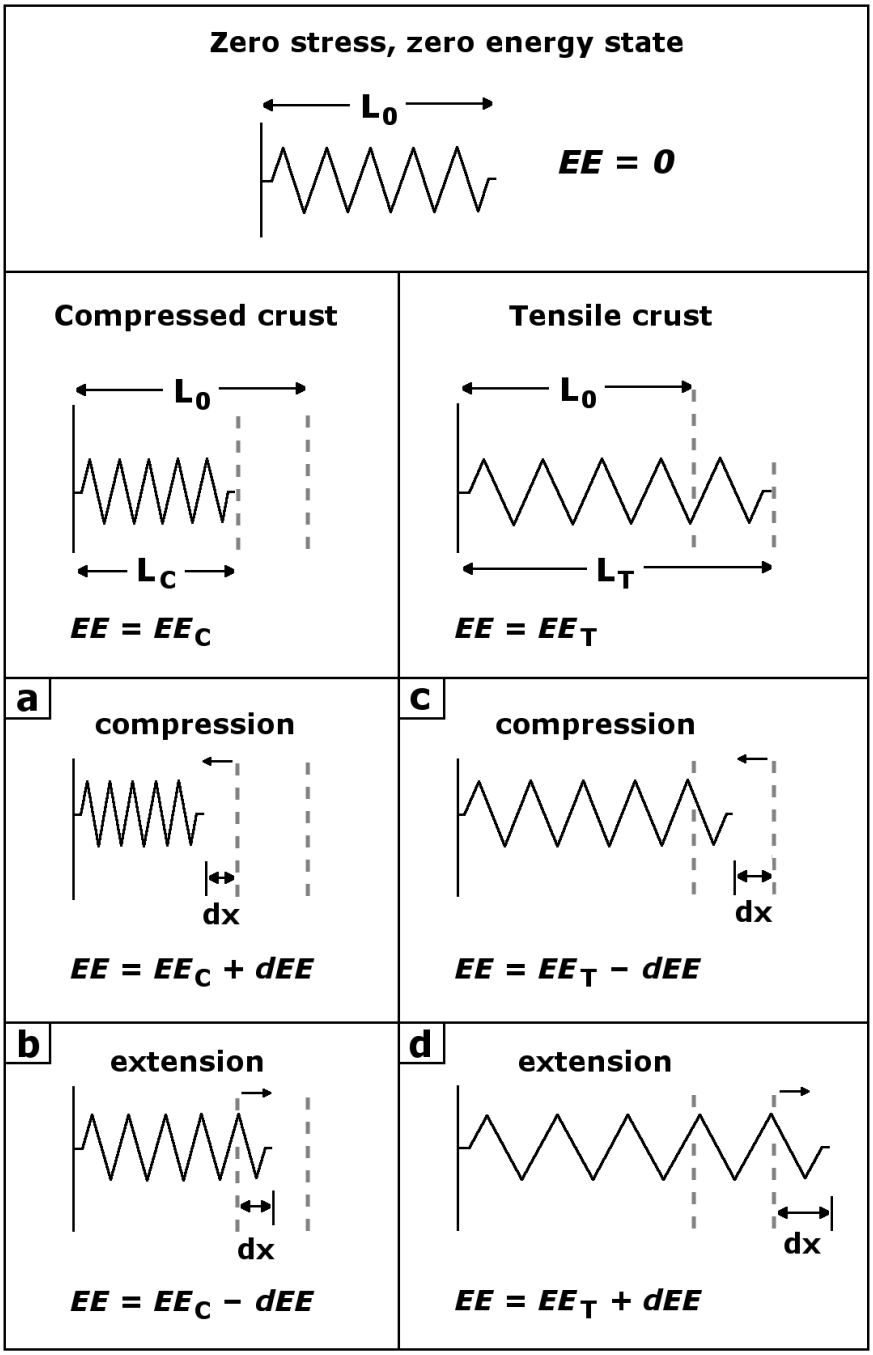

Figure 4.1: Spring analogues for crustal energy arguments. A spring at equilibrium length, L_0, has no elastic strain energy, i.e., EE = 0. Compressing the spring stores an amount of strain energy, EE_C, which is either (a) increased, +dEE, or (b) decreased, -dEE, by additional compression and extension respectively. Putting the spring in tension stores an amount of strain energy, EE_T, which is (c) decreased, -dEE, or (d) increased, +dEE, by additional compression and extension, respectively.

description of strain energy, and the stress and energy changes associated with extension of a compressed crust.

4.2.1 Strain energy calculations

Setting the problem

As a starting point, consider the axial strains as given by Hooke's law in (2.4), i.e.,

$$\varepsilon_i = \frac{1}{E}\left[(1+\nu)\sigma_i - \nu(\sigma_x + \sigma_y + \sigma_z)\right], \tag{4.1}$$

where it is assumed the principal stresses and strains are oriented along the Cartesian axes. Under these conditions, shear components can be neglected.

As an initial condition, it is assumed that the crust is subject to a vertical lithostatic loading and that both horizontal principal stresses are some proportion of the vertical, i.e.,

$$\sigma_z = (1-\lambda)\rho g z, \qquad \sigma_x = k\sigma_z, \qquad \sigma_y = \kappa\sigma_z, \tag{4.2}$$

where λ is the pore fluid factor, ρ is rock density, g is acceleration due to gravity and z is depth (negative downward). Constants k and κ describe the proportion that each horizontal stress is of the vertical, and in practise range between 3 for compressive regimes and $\frac{1}{3}$ for extensional ones.

Consider the change in strain energy induced by some infinitesimal increment of extension. Associated with this extension are incremental changes in the axial stresses and strains, the former of which are constrained by the plane-strain assumption in (2.5),

$$\Delta\sigma_y = \nu(\Delta\sigma_x + \Delta\sigma_z). \tag{4.3}$$

The initial stress state given in (4.2) is not constrained by the plane-strain assumption. Recalling that $\Delta\varepsilon_y = 0$ for plane-strain, the remaining two incremental axial

strains are given by (4.1)

$$\begin{aligned}\Delta\varepsilon_x &= \frac{1+\nu}{E}\left[(1-\nu)\Delta\sigma_x - \nu\Delta\sigma_z\right], \\ \Delta\varepsilon_z &= \frac{1+\nu}{E}\left[(1-\nu)\Delta\sigma_z - \nu\Delta\sigma_x\right].\end{aligned} \tag{4.4}$$

Strain energy

Elastic strain energy, EE, within some volume, V, is given by

$$\mathrm{EE} = \int_V \sigma_{ij}\varepsilon_{ij}dv. \tag{4.5}$$

Considering then the change in strain energy within an infinitesimal volume subject to an infinitesimal stress perturbation

$$\Delta\mathrm{EE} = \Delta\sigma_x\varepsilon_x + \Delta\sigma_z\varepsilon_z + \Delta\sigma_y\varepsilon_y + \sigma_x\Delta\varepsilon_x + \sigma_z\Delta\varepsilon_z, \tag{4.6}$$

where $\Delta\varepsilon_y = 0$ and shear stresses have been neglected. Inserting (4.1), (4.3) and (4.4) into (4.6), the energy perturbation can be written using only stress terms

$$\begin{aligned}\Delta\mathrm{EE} &= \Delta\sigma_x\frac{1}{E}\left[\sigma_x - \nu(\sigma_y+\sigma_z)\right] \\ &+ \Delta\sigma_z\frac{1}{E}\left[\sigma_z - \nu(\sigma_x+\sigma_z)\right] \\ &+ \nu(\Delta\sigma_x+\Delta\sigma_z)\frac{1}{E}\left[\sigma_y - \nu(\sigma_x+\sigma_z)\right] \\ &+ \sigma_x\frac{1+\nu}{E}\left[(1+\nu)\Delta\sigma_x - \nu\Delta\sigma_z\right] \\ &+ \sigma_z\frac{1+\nu}{E}\left[(1+\nu)\Delta\sigma_z - \nu\Delta\sigma_x\right].\end{aligned} \tag{4.7}$$

This expression is simplified by substituting expressions for the principal stresses in (4.2). Equation (4.7) then becomes

$$\Delta\mathrm{EE} = \frac{1}{E}(1-\lambda)\rho g z\left[f_x(\nu,k,\kappa)\Delta\sigma_x + f_z(\nu,k,\kappa)\Delta\sigma_z\right], \tag{4.8}$$

where

$$\begin{aligned} f_x(\nu,k,\kappa) &= k-\nu(\kappa+1)+\nu(\kappa-\nu(k+1)) \\ &+ \quad k(1+\nu)(1-\nu)-\nu(1+\nu), \end{aligned} \tag{4.9}$$

$$\begin{aligned} f_z(\nu,k,\kappa) &= 1-\nu(k+\kappa)+\nu(\kappa-\nu(k+1)) \\ &\quad -\nu k(1+\nu)+(1+\nu)(1-\nu). \end{aligned} \tag{4.10}$$

Sign and size of stress perturbations

Horizontal extension is driven by a change in the horizontal stress, i.e., a non-zero $\Delta\sigma_x$. As no stress is applied to the upper surface, σ_z is lithostatic and the only change is due to a decrease in elevation through vertical contraction, i.e.,

$$\Delta\sigma_z = (1-\lambda)\rho g z \Delta\varepsilon_z. \tag{4.11}$$

Substituting (4.11) into (4.4) gives

$$\Delta\sigma_z\left[\frac{E}{(1+\nu)(1-\lambda)\rho g z}-(1-\nu)\right] = -\nu\Delta\sigma_x. \tag{4.12}$$

For representative material parameters, $E = 1\times10^{10}\,\mathrm{Pa}$ (10 GPa), $\nu = 0.25$, $\rho = 2.8\times10^{3}\,\mathrm{kg\,m^{-3}}$, $\lambda = 0.4$, and at depths greater than 1 km ($z < -1\times10^{3}\,\mathrm{m}$), then the second term in brackets is negligible and (4.12) is written

$$\Delta\sigma_z \approx -\frac{\nu(1+\nu)(1-\lambda)\rho g z}{E}\Delta\sigma_x. \tag{4.13}$$

In extension, $\Delta\sigma_x$ is positive and thus from (4.13) the vertical stress change is also positive. However, as $E >> \rho g z$, $\Delta\sigma_z$ is very small in comparison to $\Delta\sigma_x$ and the second term in (4.8) can be neglected, i.e.,

$$\Delta\mathrm{EE} = \frac{1}{E}(1-\lambda)\rho g z f_x(\nu,k,\kappa)\Delta\sigma_x. \tag{4.14}$$

Once more considering the signs of terms in (4.14), $\Delta\sigma_x$ is positive (in extension), z is negative and $\lambda < 1$, which means the sign of ΔEE is determined by f_x.

In the models considered here, the out-of-plane stress state, parameterised by κ, is the average of the two in plane stresses, and therefore

$$\kappa = \frac{k+1}{2}. \tag{4.15}$$

Substituting (4.15) into (4.9) gives

$$f_x(\nu, k) = 2(k - \nu - \nu^2 - \nu^2 k). \tag{4.16}$$

From (4.14), when $f_x > 0$ then $\Delta\text{EE} < 0$ and the extending increment of crust loses elastic strain energy. This condition holds for horizontal stress states satisfying

$$k > k_e = \frac{\nu}{1-\nu}, \tag{4.17}$$

which for a representative value of ν of 0.25 simplifies to $k_e = 1/3$. Continued extension beyond this threshold stress state ($k < k_e$) effects a regime change, from one in which work is *done by* the extending crust, to one in which work is *done on* the extending crust.

Connection to frictional plasticity

Recall that in Section 2.2 a frictional plastic description of brittle failure of the upper-crust was introduced. Frictional plastic strain accumulates in regions of the crust where the shear stress exceeds the Mohr-Coulomb failure stress, given in (2.9). For the extensional stress state considered in this section, expressions for shear stress ($\tau = \sigma_x - \sigma_z$), mean stress ($p = -(\sigma_x + \sigma_y + \sigma_z)/3$) and pore fluid pressure ($p_f = -\lambda\rho g z$) can be substituted, to obtain a relationship between the principal stresses for a crust at yield

$$\frac{\sigma_x - \sigma_z}{2} = \left[-\frac{(\sigma_x + \sigma_y + \sigma_z)}{3} + \lambda\rho g z \right] \sin(\theta) + c.\cos(\theta). \tag{4.18}$$

Making additional substitutions for the stress states parameterised in (4.2) and (4.15), and recognising that, except for near-surface depths, the first term on the RHS of (4.18) is much larger than the second, (4.18) is rewritten

$$\frac{k_f - 1}{2} \approx \left[-\frac{k_f + 1}{2} + \lambda \right] \sin(\theta), \tag{4.19}$$

where k_f parameterises the stress state at the onset of frictional plastic failure.

For a representative value of θ of 30° and under hydrostatic conditions, $\lambda = 5/14$ and the yield stress state is given by $k_f = 4/7$. Alternatively, for a dry crust, $\lambda = 0$ and the yield stress state is $k_f = 1/3$. The latter scenario corresponds to the threshold stress state above which work is done by the extending crust (i.e., $\Delta\mathrm{EE} < 0$). Note that k_f is the lower limit of the stress state, and continued extension accumulates anelastic strain but does not further lower k. For both saturated and dry rock $k_f \geq k_e$, which indicates the crust is limited to stress states in which it loses strain energy in extension. The correspondence between k_e, an elastic parameter derived from linear elasticity theory, and k_f, a frictional parameter derived empirically from rock friction experiments (Byerlee, 1978) is intriguing.

Volumetric and distortional strain energy

Decomposing the stress tensor (Equation (2.6)) allows consideration of the relative contributions of volumetric, $\mathrm{EE_{VOL}}$, and distortional strain energy, $\mathrm{EE_{DIS}}$, to extensional processes. From (4.8)

$$\Delta\mathrm{EE} = \frac{1}{E}(1 - \lambda)\rho g z \left[f_x(\Delta s_x - \Delta p) + f_z(\Delta s_z - \Delta p) \right]. \tag{4.20}$$

Expanding the pressure change, Δp, in terms of the axial stress perturbations, i.e.,

$$\Delta p = -\frac{1}{3}(\Delta\sigma_x + \Delta\sigma_y + \Delta\sigma_z), \tag{4.21}$$

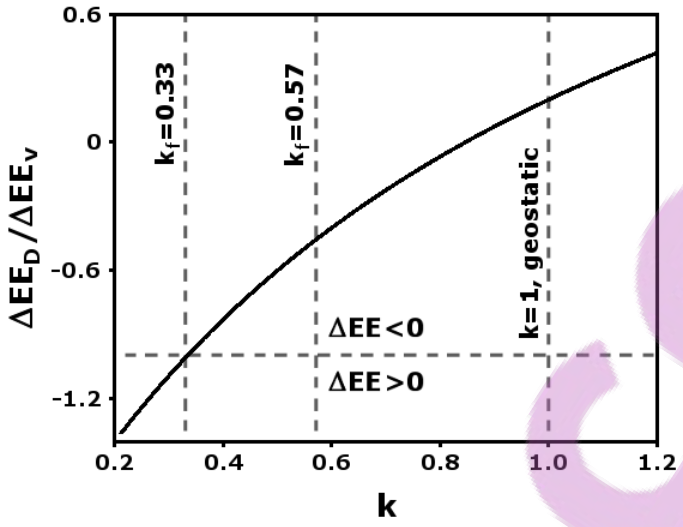

Figure 4.2: Ratio of distortional to volumetric strain energy change as a function of a stress state parameterised by k. Frictionally limited stress states for dry ($k_f = 0.33$) and saturated ($k_f = 0.57$) crust, along with a geostatic stress state ($k = 1$) are shown as vertical dashed lines. The transition from work done by, to work done on the extending crust ($\Delta\mathrm{EE} = 0 \rightarrow \Delta\mathrm{EE}_{\mathrm{DIS}} = -\Delta\mathrm{EE}_{\mathrm{VOL}}$) is shown by the horizontal line.

---

and using (4.3) and (4.13), expressions for the perturbations are obtained

$$\Delta p = -\frac{1+\nu}{3}\Delta\sigma_x, \qquad \Delta s_x = \frac{2-\nu}{3}\Delta\sigma_x, \qquad \Delta s_z = \Delta p. \tag{4.22}$$

Collecting terms in Δp from (4.20), and substituting expressions for f_x and f_z from (4.9), (4.10) and (4.15), the change in volumetric strain energy during extension is written

$$\Delta\mathrm{EE}_{\mathrm{VOL}} = \frac{2}{E}(1-\lambda)\rho g z \left[(k+1)(1-2\nu)\right]^{\dagger} \frac{(1+\nu)^2}{3}\Delta\sigma_x. \tag{4.23}$$

The remaining terms describe the change in distortional strain energy

$$\Delta\mathrm{EE}_{\mathrm{DIS}} = \frac{2}{E}(1-\lambda)\rho g z \left[\left(\frac{1-2\nu}{1+\nu}\right)(k-\nu-\nu k) + k - 1\right]^{\ddagger} \frac{(1+\nu)^2}{3}\Delta\sigma_x. \tag{4.24}$$

Note that (4.23) and (4.24) differ only with respect to the central bracketed terms, indicated by a dagger and double dagger, respectively. Notable features of these

expressions include

(a) For $\nu = 0.5$, the crust is incompressible and volume changes are impossible. Consistent with this observation, the $(1 - 2\nu)$ term in (4.23) is zero and so $\Delta\text{EE}_{\text{VOL}} = 0$, i.e., no energy is associated with a volume change. Further, if the crust is in a geostatic stress state, i.e., $k = 1$, $\Delta\text{EE}_{\text{DIS}}$ is also zero.

(b) The sign of $\Delta\text{EE}_{\text{DIS}}$ depends on the sign of the double daggered term in (4.24). For a representative value of ν of 0.25, extension causes an increase in distortional strain energy for stress states satisfying $k < 0.85$. As the brittle limited stress state under extension is parameterised by k_f between 0.33 and 0.57, $\Delta\text{EE}_{\text{DIS}} > 0$ probably holds for most extensional provinces, except where the onset of extension is recent.

(c) The ratio of distortional to volumetric strain energy changes for $\nu = 0.25$ is given by

$$\frac{\Delta\text{EE}_{\text{DIS}}}{\Delta\text{EE}_{\text{VOL}}} = \frac{13k - 11}{5k + 5}. \tag{4.25}$$

Figure 4.2 plots this expression for potential extensional stress states, parameterised by k. Note that when $k = k_e = 0.33$ distortional strain energy gained is equal to volumetric strain energy lost.

4.3 Energy conservation and work balance

Energy arguments presented thus far make a case for strain energy reduction throughout the crust during periods of extension. While this applies to the long quiescence between earthquakes, it does not contribute to an understanding of energy flow and sources of work during fault rupture. To investigate these effects, and also to validate the arguments put forward in previous sections, the numerical model is used to construct a full energy balance over the seismic cycle. This includes changes in stored EE and GPE, as well as energy dissipation by frictional plastic (PE), viscous (VE) and fault frictional (FE) processes. External work (W) done by surface tractions at the model boundaries, and by the gravitational body force, is also considered. External

work done by gravity causes changes in GPE. Strain energy is further decomposed into volumetric, $\mathrm{EE_{VOL}}$, and distortional, $\mathrm{EE_{DIS}}$, components (see Section 4.2.1). Conservation of energy for the system is expressed as W=EE+VE+PE+FE. Individual components are calculated according to

$$EE = \int_V \boldsymbol{\sigma} : \boldsymbol{\varepsilon}_e \, dV, \tag{4.26}$$

$$PE = \int_V \boldsymbol{\sigma} : \boldsymbol{\varepsilon}_p \, dV, \tag{4.27}$$

$$VE = \int_V \boldsymbol{\sigma} : \boldsymbol{\varepsilon}_v \, dV, \tag{4.28}$$

$$FE = \int_S \boldsymbol{t}_f \cdot \mathbf{s} \, dS, \tag{4.29}$$

$$W = \int_V \mathbf{f}_g \cdot \mathbf{u} \, dV + \int_S \mathbf{t} \cdot \mathbf{u} \, dS, \tag{4.30}$$

where the strain tensor, $\boldsymbol{\varepsilon}$, has been decomposed into elastic, $\boldsymbol{\varepsilon}_e$, frictional plastic, $\boldsymbol{\varepsilon}_p$, and viscous, $\boldsymbol{\varepsilon}_v$, components. Work done against fault friction is dissipated as heat and derived from the fault traction, $\mathbf{t}_f$, generating slip, $\mathbf{s}$. Finally, work done by external forces includes a body force component (gravity), $\mathbf{f}_g$, and tractions at the boundaries, $\mathbf{t}$, which induce a displacement field, $\mathbf{u}$.

The application of far-field tectonic forces over many seismic cycles produces an extensional stress regime, i.e., $|\sigma_x| < |\sigma_z|$ and $\sigma_x, \sigma_z < 0$, in which the continuous accumulation of horizontal elastic strain is limited by the Mohr-Coulomb yield criterion (Equation 2.9). Frictional plastic deformation occurring post-yield corresponds to accumulating slip on pre-existing fracture planes accompanied by the dissipation of EE as heat. This energy dissipation is constant in time, except for a brief post-seismic period (see PE profile in Figure 4.3) in which the upper-crustal stress state is below yield (see Chapter 3, Figure 3.2). The reduction in the rate of accumulation of PE is due to a coseismic increase in horizontal compression, which lowers shear stresses and suppresses frictional plastic failure. This effect is reversed by continued tectonic extension following an earthquake.

Viscous deformation in the lower crust dissipates deviatoric stress, and thus EE_{DIS}, produced by extension. This occurs at an almost constant rate and is largely

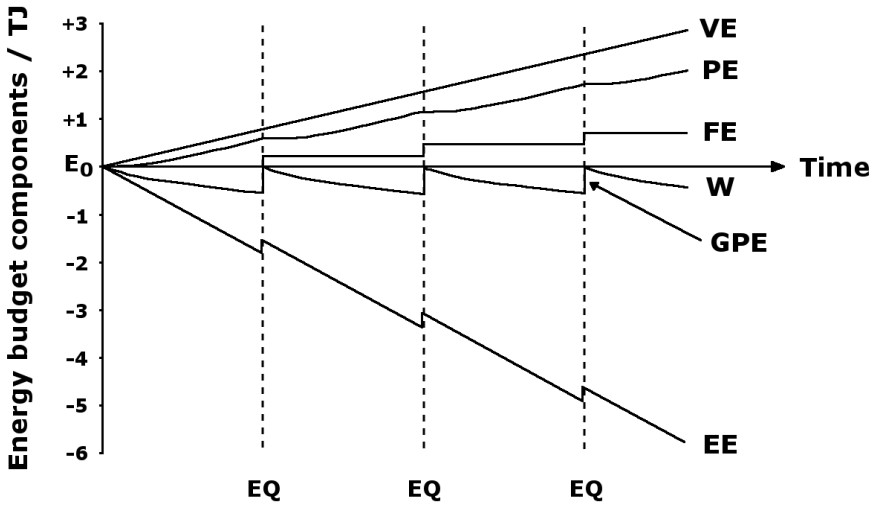

Figure 4.3: Evolution over several seismic cycles of the energy budget components, i.e., W=EE+PE+VE+FE, summed over the model domain and relative to their initial values E_0. VE = energy dissipated by viscous strain; PE = energy dissipated by frictional plastic strain; FE = energy dissipated by frictional slip along the fault; W = work done by external forces, including gravity and tractions at the boundaries; EE = changes in elastic energy. Note that W includes changes in GPE as indicated for the final coseismic period. The timing of earthquakes (EQ) are marked by dashed lines.

insensitive to the earthquake cycle. Combined with the frictional plastic deformation operating in the upper-crust, anelastic deformation ensures a steady dissipation of EE as heat, and thus the EE profile trends downward during the interseismic period. Energy is only dissipated by fault friction during the seismic period and thus the interseismic work profile, W, is obtained by summing PE, VE and EE components. The downward trend of W during this period indicates that work is being done by, not on, the crust between earthquakes. This is consistent with arguments put forward in Section 4.2. In contrast, models of thrust faulting (Del Castello and Cooke, 2007; Cruz *et al.*, 2010) demonstrate that external work is done on the crust during the interseismic period in compressional regimes.

Relative to the interseismic period, an earthquake is a brief event during which displacements at the lateral boundaries are negligible, i.e., in Equation (4.30) $\mathbf{u}|_S \approx 0$. While displacements at the surface are non-zero (see Figure 2.3(b)), this surface is

free of tractions and thus does not contribute to (4.30). Any change in W during the seismic period must therefore represent work done by gravity alone, i.e., a negative change in GPE. During an earthquake, energy flow is limited to a decrease in GPE, and increases in EE and FE, as frictional plastic and viscous deformation are only appreciable on longer, interseismic timescales. These energy flows are an aggregate of three concurrent processes: (i) a localised reduction in stress in the mid-crust that does work against friction and gravity to uplift the footwall, (ii) gravitational collapse of the hanging wall, which compresses the mid-crust and creates EE, and (iii) widespread horizontal compression of the upper-crust, which creates EE and temporarily suppresses frictional plastic deformation. While the final two processes differ in scale only, their consequent effects on surficial processes warrant distinction.

4.3.1 Fault block energy budgets

Coseismic components of the energy budget are resolved within each fault block by extending the fault plane to the base of the model and summing components either side. Energy values are quoted in terajoules (1 TJ=10^{12} J) and represent energy flow within a one metre wide slice of crust. Representative values associated with rupture of an entire fault might be extrapolated by multiplying by the along-strike distance (in metres) and accounting for tapering in the magnitude of these quantities toward the fault tip. However, such approximations do not account for slip arrest and shear stresses generated at the lateral fault tips, and are thus not necessarily accurate. Per metre strike quantities are quoted here for comparison purposes only.

Changes in energy budget components (Figure 4.4) indicate that mechanisms of deformation differ across the fault plane. In the footwall, for instance, energy changes are characteristic of an elastic rebound. Approximately 0.85 TJ of EE are expended to produce 0.43 TJ of GPE, manifesting as surface uplift (Figure 2.3(b)), and 0.14 TJ frictional heating along the fault. The EE expended is mostly volumetric with a small distortional component, and represents a reduction in stress that drives an expansion of the mid-crust and vertical movement of the footwall. The remaining EE_{VOL}, approximately 0.28 TJ, is used to do work on the hanging wall block. Expansion of

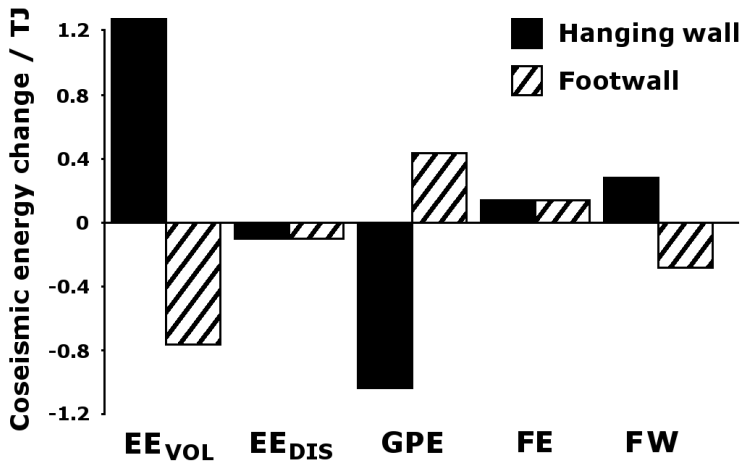

Figure 4.4: Coseismic energy changes within the hanging wall (solid) and footwall (hatched) blocks. Note that EE has been divided into volumetric, EE_{VOL}, and distortional, EE_{DIS}, components. In addition, a component of internal work, FW, is done by the footwall on the hanging wall.

the footwall exerts a force on the hanging wall that results in a normal displacement of the fault plane of up to 0.2 m at mid-crustal depths (see Chapter 3, Figure 3.8(b)). This work, termed FW, is internal and not included in the external work term, W, in Figure 4.3.

Energy changes within the hanging wall attest to a contrasting mechanism of deformation. In this block, 1.0 TJ of GPE, 0.1 TJ of EE_{DIS} and 0.28 TJ of internal work done by the footwall, FW, is converted to 1.3 TJ of EE_{VOL} and 0.14 TJ of frictional heating along the fault. In physical terms, the GPE reduction that occurs due to a loss of elevation is used to do work compressing the crust, thereby creating EE. Work done to cause this compression is derived primarily from a loss of GPE rather than an elastic 'bounce-back' of the fault block. In this sense, the elastic response of the hanging wall differs fundamentally to that of the footwall.

4.4 Spatial distribution of energy flow

In this section, energy flows are contoured in space. This allows identification of energy flows to, or from, specific regions of the crust or fault blocks. In the previous

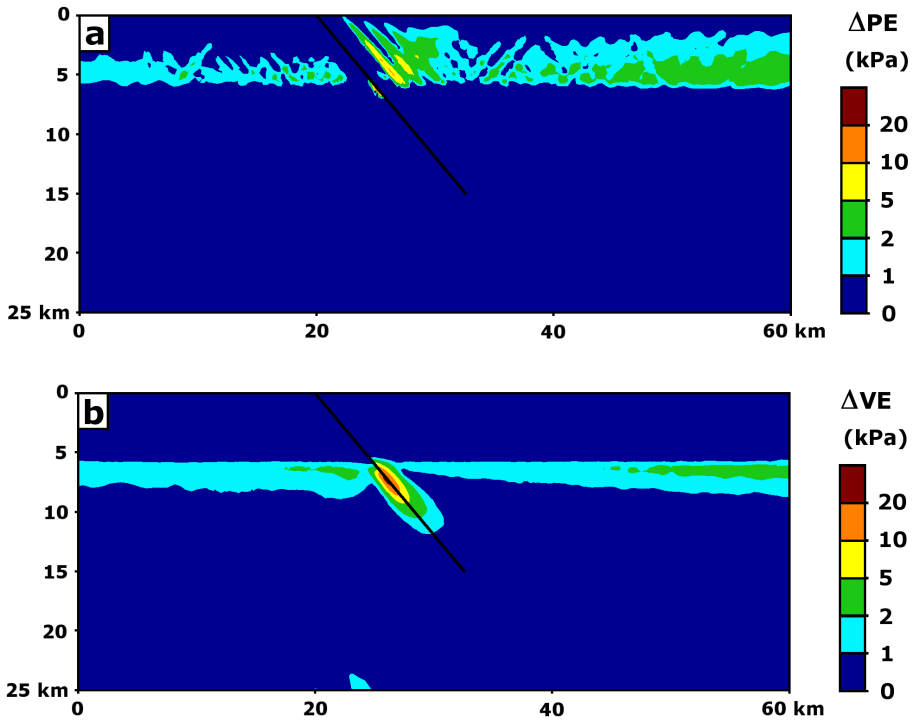

Figure 4.5: Contours of energy (per unit volume) dissipated by (a) frictional plastic strain, and (b) viscous strain. Note that contour levels are not evenly spaced.

section, aggregate energy changes, both within the crust and the individual fault blocks, are described; these were obtained by integrating energy densities across volumes of interest. Changes in these energy densities, which are dimensionally equivalent to stress, are presented below.

4.4.1 Anelastic interseismic dissipation of energy

During the interseismic period, two mechanisms of anelastic failure, operating in the upper and lower crust respectively, limit the production of unrealistic stress states by continuous tectonic extension. As described in Section 4.3, frictional plastic failure and viscous creep dissipate elastic energy as heat at a reasonably sedate pace, but in appreciable quantities over interseismic timescales (Figure 4.3).

For obvious reasons, the distribution of energy dissipated by frictional plastic

straining is similar to the distribution of frictional plastic accumulation itself (Figure 3.1(b)). Energy dissipation occurs nearly exclusively above depths of $\approx 6\,\mathrm{km}$, and preferentially within the hanging wall block, the reasons for which are discussed in Chapter 3. However, the magnitude of frictional plastic energy dissipation increases with depth in the crust, which is due to increased confining stresses with depth. Recall that frictional plastic deformation is an approximate description of frictional slip occurring on pervasive, optimally oriented failure surfaces. Shear stresses do work against friction to displace one side of the failure surface relative to the other. However, the necessary shear stress required to overcome friction increases with depth (Equation (2.9)), and thus for a given displacement (roughly parameterised by the extension rate, which is constant with depth) a greater quantity of energy is dissipated.

Similarly, energy dissipated by viscous flow shows characteristics in common with the distribution of viscous strain (Figure 3.1(c)). This includes its exclusive limitation to depths greater than 6 km, and an anomalous dissipation along the fault root. Energy dissipation is a maximum near the brittle-ductile transition where shear stresses are highest (Figure 2.2) and decreases with depth as viscous deformation operates with increasing efficiency (sustaining a constant bulk strain rate at lower shear stresses). Viscous dissipation of energy is anomalously high along the fault root where viscous strain localisation is observed in Figure 3.1(c). High strain rates, and thus energy dissipation, are promoted by an anomalous Mises stress generated by coseismic mid-crustal stress changes.

Rudnick and Fountain (1995) estimate an average radiogenic heat production of the crust in continental arc settings as $0.8\,\mu\mathrm{W\,m^{-3}}$. For a 220 yr interseismic period, this approximately corresponds to the 5 kPa contour level in Figure 4.5. Thus shear frictional heating exceeds radiogenic heat production in some small, near fault regions, but is on the same order of magnitude across wider regions of the mid-crust.

Hochstein (1995) suggested that the high heat flux through the TVZ is in part caused by plastic deformation of the ductile lithosphere. This model assumes that

mechanical work done deforming the crust is eventually converted to heat, with the work rate being proportional to the average yield stress. Summing contributions from the ductile lower crust and upper mantle suggests this mechanism accounts for no more than half the observed heat output, although Hochstein (1995) proposes several scenarios in which the surface heat flux may exceed heat input at the base. The effects of plastic shear heating are also considered by Regenauer-Lieb and Yuen (1998) during lithospheric necking; they highlight the importance of thermomechanical feedback on localisation of deformation into shear zones. This feedback is not incorporated in the current model as frictional plastic strain rate is independent of temperature in this rheology.

4.4.2 EE and GPE exchange

Further insight into footwall elastic rebound and hanging wall collapse is gained by identifying those regions from which energy is given up and to which energy flows. Dissipation of heat by fault friction and internal work (FE and FW in Figure 4.4) are both restricted to the fault plane, however, changes in EE_{VOL}, EE_{DIS} and GPE occur throughout the crust.

Distortional changes in strain energy are consistent with the elastic rebound interpretation, i.e., EE_{DIS} accumulates in the upper-crust (shallower than 8 km) during the interseismic period, and is subsequently released during fault rupture (Figure 4.6(a)). A particularly large release of EE_{DIS} occurs within the footwall close to the fault plane and is associated with up-dip displacement of the fault block. Concurrently the near fault region at mid-crustal depths (8-12 km) experiences an increase in EE_{DIS}, principally within the hanging wall. This is associated with an increase in stress at the maximum gradient in fault slip (Figure 2.4). This anomaly is largely dissipated by viscous deformation in the interseismic quiescence following an earthquake (Ellis *et al.*, 2006).

Changes in EE_{VOL} and GPE are approximately an order of magnitude greater than EE_{DIS} and are thus primary drivers of coseismic deformation. In the footwall, at a depth of 8-10 km, there is a large decrease in EE_{VOL} representing a rapid decrease

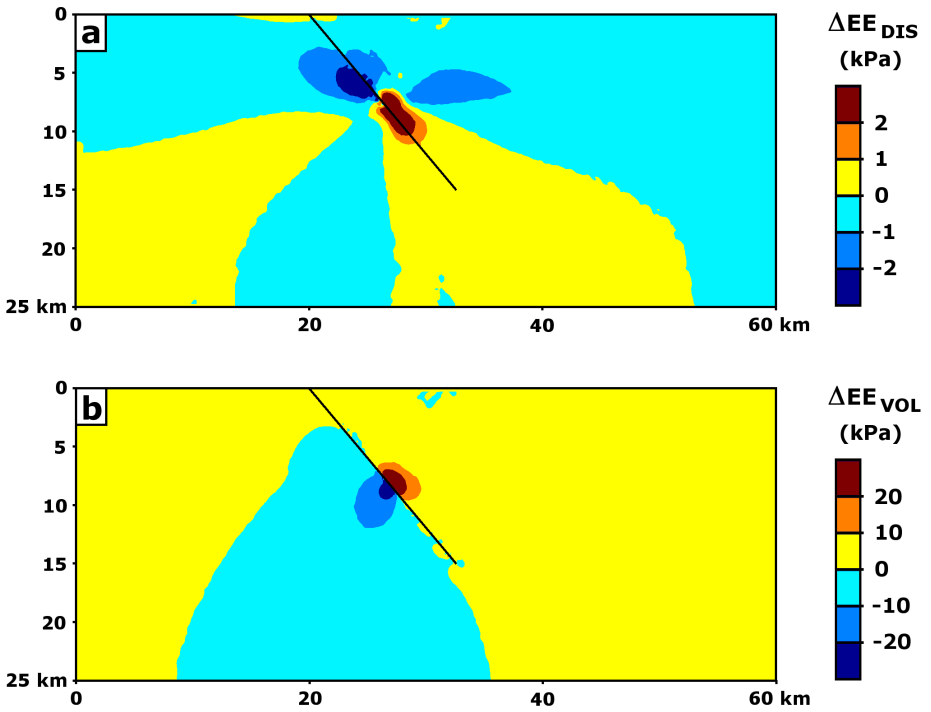

Figure 4.6: Contours of coseismic change in energy density throughout the crust for (a) EE_{DIS}, and (b) EE_{VOL}. Note that contour levels for (a) are an order of magnitude smaller than (b), and units for energy density are dimensionally equivalent to stress. As the model is in dynamic equilibrium, interseismic changes in EE_{DIS} and EE_{VOL} are equal in magnitude but opposite in sign to those occurring in the seismic period.

in mid-crustal stress and associated expansion of the crust. This energy, which had accumulated in the preceding interseismic period, does work against gravity resulting in uplift of the footwall and the creation of GPE (Figure 4.7). Vectors of displacement direction show that footwall uplift occurs in the wider context of fault block rotation (Nur *et al.*, 1986).

In the hanging wall, coseismic displacement is down-dip or directed horizontally away from the fault. The crust immediately adjacent to the fault subsides by up to 1 m at the surface and a reduction in GPE from this region is observed (Figure 4.7). A concurrent increase in EE_{VOL} occurs at depths of 6-10 km corresponding to mid-crustal compression and the cessation of slip on the fault plane.

In addition to these localised elastic changes, there is also a widespread, low

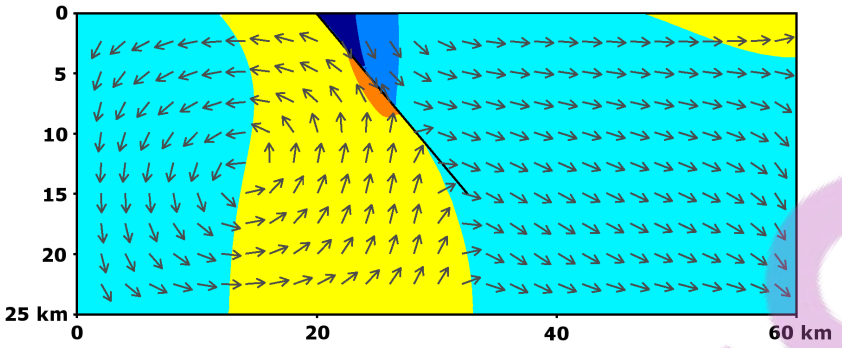

Figure 4.7: Contours of coseismic change in gravitational potential energy density. Vectors indicate displacement direction during the seismic period.

level increase in EE_{VOL} throughout the majority of the upper-crust. This increase is approximately 50% larger than the simultaneous reduction in EE_{DIS} (Figure 4.6(a)), and thus the net change in EE is positive during an earthquake. The increase in EE_{VOL} is due to horizontal compression of the crust as fault blocks withdraw from each other and may be linked to the expulsion of fluids at the surface due to fracture closure at depth (Muir-Wood and King, 1993; Muir-Wood, 1994).

4.5 Interpretation of hanging wall displacement

Energy flow during frictional plastic failure can be regarded as analogous to that described for faults, but at a smaller scale. A small increment of dip-slip on an optimally oriented fracture plane results in a small loss of GPE, dissipation of FE, and an increase in EE_{VOL}. Similarly a local increase in horizontal stress ensures the region remains below the Mohr-Coulomb failure limit until the next episode of failure on that fracture plane.

Coseismic energy flows in the hanging wall occur in the opposite direction to those attributed to elastic rebound of the footwall. Figure 4.8 presents a spring-block schematic accounting for coseismic displacement, stress and energy changes within the hanging wall for an extending crust. Dip-slip of the fault block occurs when the sum of the shear components of the vertical lithostatic stress, F_G, a gravitational force

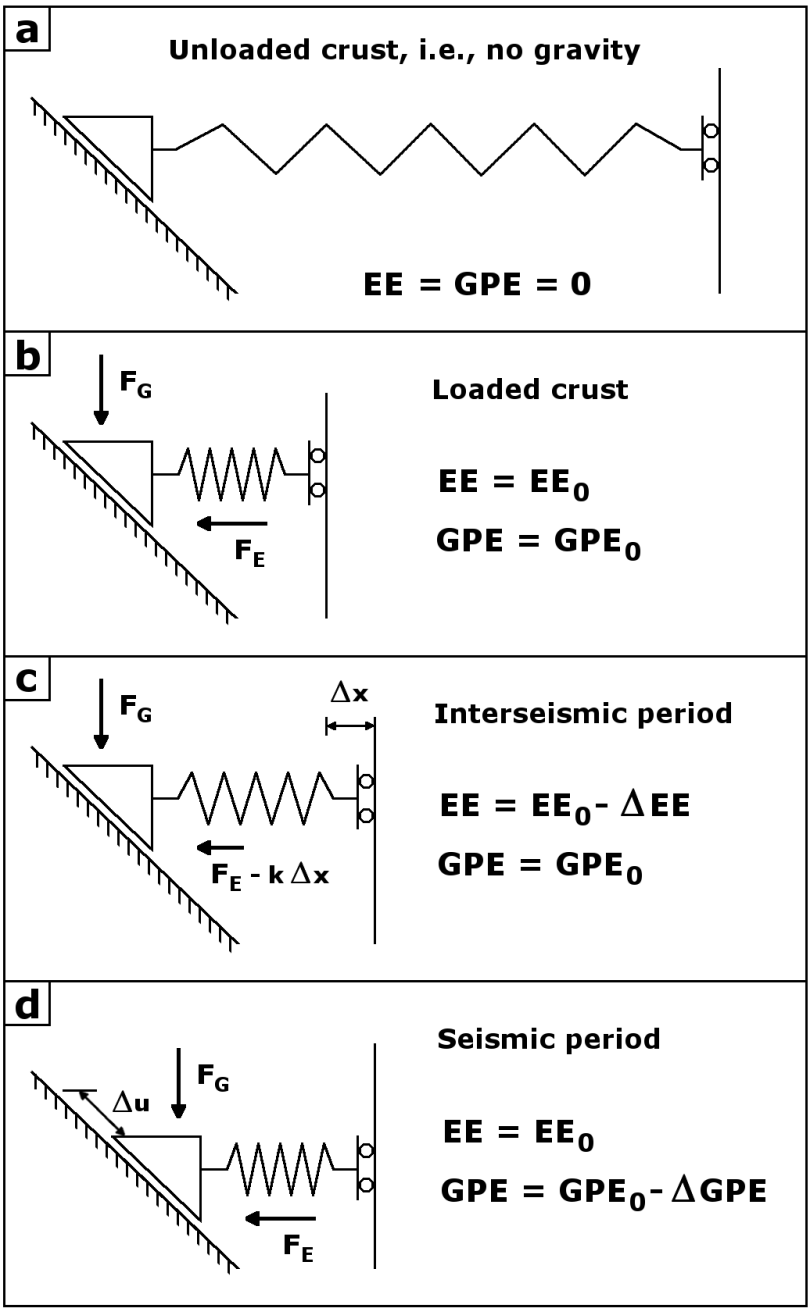

Figure 4.8: A spring (of stiffness k) and block model accounting for observed displacements, stress, and EE and GPE changes in the hanging wall. (a) The unloaded spring, equivalent to the absence of gravity. (b) Gravitational loading, F_G, compresses the crust vertically and induces a horizontal spring force, F_E. The sum of opposing shear components of F_G and F_E is below the threshold for frictional slip. (c) An increment of tectonic extension, Δx, decreases EE and reduces the spring force until the threshold for friction slip is exceeded. (d) Dip-slip of the hanging wall recompresses the spring, creating EE at the cost of GPE, and restores the balance of forces on the fault.

directed down-dip, and the horizontal stress, F_E, an elastic force directed up-dip, exceeds the static frictional threshold. Tectonic extension, in addition to decreasing EE through a reduction in the horizontal stress, also causes a reduction in the up-dip shear stress, while leaving the gravitational shear component unchanged. After sufficient extension and reduction of the up-dip shear stress a fault rupture occurs, at which time gravitational forces cause the hanging wall to accelerate down-dip, expending GPE. The horizontal component of down-dip displacement of the fault block recompresses the wider crust, creating EE, and increasing F_E along the fault. This continues until the net shear stress is less than the dynamic frictional threshold, which is typically less than its static counterpart, and fault slip is arrested.

In contrast to the steady accumulation of EE required for an elastic rebound, GPE released during a collapse of the hanging wall does not accumulate during the interseismic period. Rather, GPE is always present but is only made available to do work through the removal of elastic and frictional constraints, i.e., by imposing a material discontinuity (a fault) and then permitting slip to occur on its surface. Far-field tectonic extension is not directly responsible for loading the crust in the classical sense, i.e., by increasing its potential to do work. The presence of a nearly constant gravitational field serves this role. Instead, extension alters the balance of stresses on the fault plane until failure of an already loaded crust occurs.

4.6 Chapter summary

Tectonic extension operates in a non-intuitive manner when applied to the compressional stresses of a lithostatically loaded crust. Total elastic strain energy decreases as the horizontal compressive stress is reduced by continued extension. Although distortional strain energy increases in response to an increasing difference between horizontal and vertical stress, this is offset by a much larger decrease in volumetric strain energy. The net effect, that strain energy is lost by the crust, implies that work is not being done on the crust, as its internal energy does not increase. This has clear implications for the loading period that is typically assumed to precede rupture of a normal fault.

An energy budget provides a powerful tool for analysis of complex systems in which multiple processes operate concurrently. For a single fault, the following processes are considered: anelastic deformation occurring in the pre-seismic period, which limits the build-up of stress in the crust; simplified frictional processes occurring on the fault contact surface; and work done, against or by, elastic and gravitational forces - two sources of energy potential. The analysis confirms that during the interseismic period elastic strain energy is depleted by three processes: (i) frictional plastic deformation in the upper-crust, particularly in the hanging wall, (ii) viscous deformation in the lower crust, particularly at the fault root, and (iii) work done by the crust in displacing its lateral boundaries, i.e., extension. During the seismic period, a net gain in elastic energy, at the expense of gravitational potential energy, is observed highlighting the key role gravity plays in normal fault rupture.

Contrasting styles of deformation are observed across the fault plane. In the footwall, a drop in stress at mid-crustal depths drives expansion and up-dip displacement of the fault block. At the surface this is expressed as increasing uplift with proximity to the fault scarp, while at depth, expansion does work on the adjacent hanging wall, effecting a small rotation of the fault plane (see Chapter 3). Energy flows in this fault block are consistent with the elastic rebound interpretation, where elastic energy is slowly accumulated in the period preceding fault rupture, before being rapidly expended to cause coseismic displacement of the crust.

In the hanging wall, energy flows are in the opposite direction, and the cause of deformation is less intuitive. Down-dip displacement of the fault block is achieved by an imbalance between the downward directed gravitational force opposed by an upward resistance to elastic compression. In energy terms, gravitational potential energy is expended to cause mid-crustal compression and an increase in volumetric strain energy. Superimposed on this local effect is a wider horizontal compression associated with the two fault blocks retreating from one another. This results in a widespread, but temporary, reduction in shear stress and a brief cessation of frictional plastic deformation in the upper-crust.

For an identical sand, it can be assumed that the volume discharged is proportional to the head and inversely proportional to the thickness of the sand layer that the water passes through.

- Henry Darcy (1803-1858)

5

Circulation model of the crust

5.1 Introduction

Water is transported within the brittle upper-crust of the Taupo Volcanic Zone through a pervasive network of fractures, formation contacts and connected pore space (e.g., Grindley and Browne, 1976; Sibson, 1994; Rowland and Sibson, 2004). The journey begins at the surface with the infiltration of meteoric water, i.e., rainfall, into the subsurface. Surface water percolates slowly downward to the base of the brittle crust, where heating from magmatic intrusion induces thermal expansion and a buoyant instability. Fluids from a wide area are drawn together into narrow, vertical conduits of hot upflow, sweeping heat from broad regions of the lower crust and carrying it to the surface.

This chapter presents a general discussion of the construction of three-dimensional numerical models of circulation of heated fluids throughout the TVZ. In the chapters that follow (6-8), a suite of models is presented considering different spatial scales, permeability formulations and incorporating a variety of perturbing processes. Details that are specifically relevant to these models are presented in the corresponding chapter, while more general features common to all models are described here.

Fluid flow is described by Darcy's law, in which mass flow is driven by fluid pres-

sure gradients, assisted by the innate permeability of the host rocks, and resisted by fluid viscosity. Modelling of both single- and multi-cell systems allows an investigation of geothermal circulation on both individual-field and rift scales. Analysis of these models is described in the chapters that follow: field recharge, catchment delineation and residence times at the rift scale in Chapter 6; silica deposition and permeability modification in Chapter 7; and short- and long-term dip-slip fault effects in Chapter 8.

5.2 Heat and mass transport

Numerical models of hydrothermal circulation, which range in scope from a high resolution study of the upper reservoir (e.g., Kiryukhin, 1996; Mannington *et al.*, 2004; O'Sullivan *et al.*, 2009), to broader studies of single (e.g., Rabinowicz *et al.*, 1998; Jupp and Schultz, 2000) and multi-cell systems (Kissling and Weir, 2005; Coumou *et al.*, 2008; McLellan *et al.*, 2010), all share a common mathematical description. Darcy's law, formulated empirically in 1856 by the engineer Henry Darcy (Darcy, 1856; Freeze, 1994), describes the flow of fluid along pressure gradients, ∇P, with the velocity proportional to the magnitude of ∇P, permeability, and the reciprocal of viscosity. Darcy's law is written

$$\mathbf{v}_D = \frac{k}{\mu}\left[\nabla P - \rho g \hat{\mathbf{z}}\right], \tag{5.1}$$

where $\mathbf{v}_D$ is the Darcy velocity, k is permeability, μ is dynamic viscosity, P is pressure, ρ is fluid density, g is the acceleration due to gravity, and $\hat{\mathbf{z}}$ is a unit vector in the z-direction. The second term in brackets in (5.1) accounts for the hydrostatic pressure gradient caused by the weight of the overlying water column.

Darcy's law is analogous to Ohm's law for transport of electrical charge, Fick's law for transport of chemical species, and Fourier's law for transport of heat:

$$\mathbf{J} = -\sigma_J \nabla V, \qquad \mathbf{j} = -D\nabla\phi, \qquad \mathbf{q}_{cond} = -\kappa\nabla T. \tag{5.2}$$

In each of these equations, as in Darcy's law, transport of the quantity in question (electric charge, $\mathbf{J}$; chemical species, $\mathbf{j}$; thermal energy, $\mathbf{q}_{cond}$; and fluid mass, $\mathbf{v}_D$) occurs down gradients of some controlling parameter (electric potential, V; species concentration, ϕ; temperature, T; and fluid pressure, P) and is modulated by a conductive term that depends on the medium of transport (electrical conductivity, σ_J; chemical diffusivity, D; thermal conductivity, κ; and permeability divided by dynamic viscosity, k/μ).

Expressions for mass and heat transport are derived by incorporating Darcy's Law into corresponding expressions for mass and energy conservation

$$\frac{dA_m}{dt} + \nabla \cdot \mathbf{f}_m + q_m = 0, \tag{5.3}$$

and

$$\frac{dA_e}{dt} + \nabla \cdot \mathbf{f}_e + q_e = 0, \tag{5.4}$$

which simply expresses that changes in the fluid mass, A_m, and energy per unit volume, A_e, are due to corresponding mass, $\mathbf{f}_m$, and energy fluxes, $\mathbf{f}_e$, on the surfaces bounding that volume, as well as sources or sinks, q_m and q_e, within the volume. The accumulation and flux terms are given by

$$A_m = \phi\rho, \tag{5.5}$$

$$A_e = (1-\phi)\rho_r c_p T + \phi\rho u, \tag{5.6}$$

$$\mathbf{f}_m = \rho\mathbf{v}_D, \tag{5.7}$$

$$\mathbf{f}_e = \rho h\mathbf{v}_D - K\nabla T, \tag{5.8}$$

where ϕ is porosity, ρ_r is rock density, c_p is the specific heat of the rock, u is the internal energy of the fluid, h is the enthalpy of the fluid, and K is the effective

thermal conductivity. Equations (5.1) and (5.5)-(5.8) are incorporated into (5.3) and (5.4) for a full description of heat and mass transport. These equations can be generalised to consider two-phase (e.g., water and steam) and multi-component (e.g., water and CO_2, water and NaCl) fluid flow. However, models presented in this thesis do not address such conditions; the reader is directed to Grant and Bixley (2011) for a full treatment.

5.3 Finite Element Heat and Mass transfer (FEHM)

Computational models of geothermal circulation presented in this thesis are constructed using the Finite Element Heat and Mass transfer (FEHM) code developed at the Los Alamos National Laboratory, New Mexico (Zyvoloski, 2007). This code solves the heat and mass transport equations described in the previous section, for multi-phase, multi-component flow in single or double porosity/permeability media. FEHM also has the ability to perform coupled stress/displacement calculations as well as reactive transport and tracer modelling; however, this functionality is not employed in the models detailed here.

Time derivatives in the heat and mass transport equations are discretised using a standard first-order fully-implicit method, while spatial derivatives are discretised using a control volume finite element (CVFE) technique. This method forms mass conservative control volume equations on an underlying finite element grid. This method is similar to the method described by Zyvoloski (1983), where the non-linear fluid parameter's (e.g., density, viscosity) coefficients are separated from the purely geometric coefficients of the grid block (e.g., areas, distances, volumes). The resulting equations are solved using a Newton-Raphson iterative method. Spatial differencing is second-order accurate although this is typically reduced to first-order by upwinding of the transmissibility term. Time stepping is also first-order accurate. Material properties of the fluid, i.e., density, viscosity and enthalpy, are defined as

rational polynomials (ratios of cubic functions) of temperature and pressure fitted to the National Bureau of Standards steam tables (Haar *et al.*, 1984). Analytical derivatives of the material properties are thus straightforward to obtain.

5.4 General procedure for model construction

The three-dimensional fluid circulation models presented here share several features in common with the mechanical fault models described in Chapter 2. As a general method, construction of a computational model requires specification of: (i) a restricted domain that sufficiently bounds processes of interest, as well as a mesh that discretises the domain; (ii) boundary conditions that drive the processes within the model; and (iii) an initial state from which the model evolves in time. Each of these features are addressed as they pertain to the construction of geothermal circulation models in the following chapters; specific information relevant to each of the model is given in its corresponding chapter.

5.4.1 Computational domain and meshing

The extent to which a given physical process can be represented by a numerical model is restricted by the available computational resources. For instance, limited memory results in a corresponding limit on the number of elements that can be used to discretise the domain; a trade-off therefore exists between the spatial dimensions of the model (domain size) and the resolution (element size) at which the problem is modelled. For example, the computational domain used to model rift-scale circulation in Chapter 6 is nearly twenty times larger, in volume terms, than the domains used to model single-cell systems in Chapters 7 and 8. Consequently, element dimensions in the smaller domains are up to an order of magnitude less than those used to mesh the larger one, and convection is therefore imaged at a higher resolution.

In the models detailed in this thesis, mass is not injected at the lower or side

boundaries to simulate the effects of plume recharge. Mass injection is the traditional approach in reservoir modelling (e.g., Kiryukhin, 1996; Mannington *et al.*, 2004; O'Sullivan *et al.*, 2009) where maximum resolution of the upper plume is desirable and achieved at the expense of a restricted domain. Here, plume recharge is derived from the downward percolation of fluid in the region surrounding the central upflow zone. The computational domain must therefore be sufficiently broad and deep to capture this feature of the circulation.

While there exists considerable latitude in selecting the horizontal dimensions of the model domain, there is less flexibility in choosing the vertical dimension. In the models detailed here, convection occurs to the base of the computational domain, which should therefore be chosen to correspond with the expected depth of convection in the TVZ. On the basis of geometric arguments for large-scale convection (McNabb, 1975; Bibby *et al.*, 1995), as well as the limit of brittle deformation and fracture permeability as inferred from seismic observations (Bryan *et al.*, 1999), a vertical model dimension of 8 km has been chosen. This is the same depth to which Kissling (2004) and Kissling and Weir (2005) modelled large-scale convection in the TVZ. Others have used slightly shallower domains (7 km) in modelling coupled circulation and deformation in the TVZ (McLellan *et al.*, 2010).

In contrast to the irregular meshes used in Abaqus fault models (Chapters 2-4), FEHM models are discretised using a variety of regular meshes. For example, in Chapter 7 a rectilinear mesh is used for high resolution modelling of silica deposition in the near-surface, and in Chapter 8 a curvilinear mesh is used to model geothermal upflow along an inclined fault plane. Specific details on the construction of these meshes can be found in the relevant chapters.

Careful mesh design at the top of the model can be used to simulate the effects of topography on fluid circulation. This is particularly important in reservoir modelling, where lateral topographic flows interact with geothermal upflow in the near-surface. However, as the models here are not specific to any geographical loca-

tion a topographical mesh has not been implemented.

5.4.2 Boundary conditions

For the mass conserving models of geothermal circulation considered here, i.e., models that account for plume recharge through fluid recirculation, no-flow boundary conditions are specified at each boundary of the computational domain. At the upper surface, a constant pressure boundary condition of 0.1 MPa is applied, which represents atmospheric pressure.

Convection of fluid within the computational domain is achieved through the input of heat at the base of the model. This can be implemented in two ways: by prescribing an enthalpy source to be distributed across some area, or by prescribing a fixed temperature. The first approach is often adopted in reservoir models (e.g., Kiryukhin, 1996; Mannington *et al.*, 2004), where enthalpy sources are specified at the base of the model corresponding to the expected heat output of the geothermal field at the top of the model. In the models presented here, the second approach is adopted; a temperature distribution is specified at the base of the model and the convection cells that develop are compared with their TVZ counterparts. At steady-state the two approaches are identical, i.e., a given steady basal heat-flow distribution corresponds to a steady basal temperature distribution.

Temperature boundary conditions applied at the base of the model reflect the temperatures associated with the onset of quartz plasticity (300-350°C) and the transition from brittle to ductile deformation. In the TVZ, the BDT, as delineated by the lower limit of upper-crust seismicity (Bryan *et al.*, 1999), occurs between 6 and 8 km depth, which is consistent with geometric arguments for the configuration of an ensemble of convection cells (McNabb, 1975; Bibby *et al.*, 1995). The choice of temperature boundary conditions is justified on the basis of the correspondence between quartz plasticity temperatures and the position of the depth of the BDT. The assumption here is that since fracturing, and thus permeability, are limited to

a specific depth interval, the majority of fluid flow is also restricted to this domain. This approach neglects a flux of fluid from the mantle. Furthermore, the maximum rock temperature to which those fluids are subject is that which occurs at the onset of quartz plasticity, $\approx 300-350$°C. Kissling and Ellis (2011) used a more sophisticated approach to apply an evolving temperature distribution at the BDT informed by a separate mechanical model for lithospheric deformation (SULEC). Brittle-ductile transition temperatures in this model are approximately 350°C.

Other fluid flow codes, e.g., a modified version of TOUGH2 (Kissling, 2004; Croucher and O'Sullivan, 2008), can describe fluid flow at supercritical temperatures and pressures up to 800°C and 100 MPa. In restricting model temperatures to less than 350°C, we do not consider the supercritical conditions that might be encountered in the vicinity of shallow intrusions or due to the influx of magmatic fluids. Furthermore, at the model permeabilities used in this thesis, two-phase conditions do not occur. This simplification is suitable for the purposes of these modelling studies, i.e., analysis of large-scale convective behaviour, but will not capture the finer-scale behaviour associated with boiling and shallow steam-zones.

Atmospheric boundary conditions are maintained at the top of the model by imposing an effectively infinite heat sink. Nodes in the uppermost layer of the mesh are denoted atmospheric, and assigned a specific heat capacity $1\times10^{15}\,\mathrm{J\,kg^{-1}K^{-1}}$, which is twelve orders of magnitude greater than that specified for crustal rocks. Heat flow into atmospheric nodes therefore has a negligible effect on their temperature, and the layer operates as a constant temperature heat sink. In these models, an atmospheric temperature of 20°C is used. As these models do not consider air/water mixtures, atmospheric nodes are fully saturated and thus represent a surface layer of cold groundwater (rather than cold atmosphere).

Others (e.g., López and Smith, 1995; Zhang *et al.*, 2005) use a modified surface boundary condition that, instead of fixing atmospheric temperature, enforces $dT/dz = 0$ in regions of upflow - this permits a description of surface discharge of el-

evated enthalpy, e.g., hot-springs. As FEHM does not support this type of boundary condition, the models detailed here do not accurately portray heat transfer through hot-springs.

5.4.3 Initial conditions

In the mechanical fault model, a visco-plastic yield stress-state is obtained by applying the extensional boundary conditions for a period of 90 kyr to a crust with an initial stress-state that is geostatic (i.e., $\sigma_{xx} = \sigma_{yy} = \sigma_{zz}$). Numerical experiments are then conducted using the evolved at-yield stress-state as an initial condition, while displacements accumulated during the stress spin-up phase are discarded. A similar approach is followed in evolving natural-state circulation.

An initial temperature of 20°C is specified throughout the computational domain at the beginning of the simulation. Application of the temperature boundary conditions at a depth of 8 km causes heating of fluids at the base of the model. These heated fluids rise buoyantly, beginning the process of convection, and transporting energy and high temperature fluids to other parts of the model. A quasi-steady-state temperature distribution is obtained by applying the boundary conditions over long time-periods (100-300 kyr); this is similar to the stress spin-up period imposed for the fault model. Numerical experiments are then conducted using the natural-state convective temperature distribution as an initial condition.

5.5 Distribution of permeability

Crustal permeability is probably the least well known, and yet most important, parameter controlling fluid flow in numerical simulations (Ingebritsen *et al.*, 2010). Permeability varies by many orders of magnitude depending on rock type and the degree of fracturing and alteration (e.g., Browne, 1978; Brace, 1980), although both modelling studies (Cathles *et al.*, 1997) and seismic investigations (Talwani and Acree,

Table 5.1: Bounding values of porosity, ϕ, and permeability, k, used in simulations.

	Chapters 6 and 8		Chapter 7	
z (km)	k ($\log(\mathrm{m}^2)$)	ϕ (%)	k ($\log(\mathrm{m}^2)$)	ϕ (%)
0	-13.8	10	-12.9	20
-2	-14.5	6	-14.5	6
-8	-14.7	2	-14.7	2

1985) would indicate that values greater than $10^{-16}\,\mathrm{m}^2$ are required for sustained advective heat flow. For a given rock type, permeability can also vary with depth, often in response to the increased overburden pressure, which promotes fracture closure and compaction of pore spaces (Saar and Manga, 2004). Previous workers have proposed power-law (Manning and Ingebritsen, 1999) and exponential (Saar and Manga, 2004) permeability-depth relations to represent mean permeability in brittle, continental crust.

Models in this thesis implement an exponential permeability-depth relationship, although the specific parameters fitted by Saar and Manga (2004) are eschewed in favour of a parameter set calibrated by the thermal and dimensional properties of TVZ convection cells. In permeability terms, the models are divided into two sub-domains, with the upper 2 km representing layered, high-porosity, Quaternary volcanic deposits, and the lower 6 km, low-porosity, fractured greywacke basement rock. An exponential permeability-depth relationship for each sub-domain is derived from a fit to bounding values of permeability given in Table 5.1. These bounding values are selected heuristically with the objective of reproducing single-cell heat flows and dimensions consistent with those in the TVZ (see Table 1.1). The range of permeabilities in Table 5.1 are consistent with those used in previous workers undertaking TVZ modelling studies, e.g., 5-100 $\times\, 10^{-15}\,\mathrm{m}^{-2}$ from Kissling and Weir (2005), 1-200 $\times\, 10^{-15}\,\mathrm{m}^{-2}$ from Mannington *et al.* (2004).

5.5.1 Heterogeneity and anisotropy

Spatial variation in the distribution of permeability, i.e., heterogeneity, produces complex patterns of fluid flow. The effects of spatially correlated permeability heterogeneity on convection within a fault zone were considered by López and Smith (1996); in their models flow reflected connections between high permeability regions, while the position of upflow and recharge zones were related to regions of of high and low permeability. Gerdes *et al.* (1998) used a variogram model to construct synthetic heterogeneity that replicates both the statistical properties and spatial correlation of permeability in sedimentary rocks. Implementing this heterogeneous permeability in a 2-D hydrothermal circulation model, they demonstrate channelisation of fluids through circuitous, highly-conductive pathways, as well as the inherent unpredictability of a flow regime that depends on this heterogeneity. Matthäi *et al.* (2004) approximated heterogeneity in their model of 2-D convection and silica transport (see Chapter 7) by partitioning the domain into seventeen permeability sub-domains reflecting a central fault zone and several layered rock units. This is similar to the approach of Kissling and Weir (2005), who sub-divided the TVZ into sixteen regions of distinct permeability and basal heat flow to model the rift-scale convective system.

In this thesis, where permeability heterogeneity is considered (Chapters 6-8), two- or three-dimensional, spatially correlated permeability fluctuations are implemented; these are similar to the two-dimensional permeability distribution used by López and Smith (1996). The fluctuation field is superimposed upon the mean, depth-dependent permeability distribution specified in Table 5.1. Based on power spectral densities derived from seismic bore-hole data in fractured, pyroclastic sequences (Dolan *et al.*, 1998) and hydrocarbon reservoirs (Leary and Al-Kindy, 2002), fluctuation fields with spatial correlation satisfying $f^{-\beta}$ are constructed, where f are spatial frequencies and β is a power law parameter. Values of β from 1, representing 'pink', or 'flicker', noise, to 1.5 are used. Physically, such correlations may derive from the fractal

distributions of fractures (e.g., Leary and Al-Kindy, 2002) that develop in crusts approaching a critical stress state (Crampin, 1994; Heffer, 2007), although Bean (1996) demonstrated that rock lithology also contributes to $1/f$ scaling behaviour.

In numerical modelling studies, differences in rock permeability with direction, i.e., anisotropy, are simplified to consider horizontal and vertical permeability. For example, in modelling large-scale TVZ convection, Kissling and Weir (2005) accounted for enhanced permeability along predominantly horizontal formation contacts by a ten times increase of horizontal permeability with respect to vertical. Similarly, Mannington *et al.* (2004) detailed a reservoir model of the Wairakei geothermal system in which horizontal permeability is up to forty times greater than vertical in the production zone; however, anisotropy was minimal in the basement region. An investigation of the effects of permeability anisotropy is outside the scope of this thesis, and anisotropy here is limited to a three-times-greater increase in horizontal permeability relative to vertical.

5.5.2 Coupled porosity and permeability

The distributions of porosity throughout the crust is particularly important in calculating fluid residence times in Chapter 6 and silica deposition in Chapter 7. In these models, the porosity distribution is calculated as some function of the specified permeability distribution (Table 5.1). Fluid flow through high porosity volcanic deposits in the upper 2 km of the TVZ is probably dominated by connected pore pathways. Under these circumstances, Zhang *et al.* (1994) suggests that permeability, k, varies with the cube of porosity, i.e., $k \propto \phi^3$, provided the porosity is above some critical value, ϕ_c. Below this value, a loss of connectivity causes rapid reductions in permeability. The cubic-law porosity-permeability relationship has previously been used in modelling limestone dissolution in karst systems (Chaudhuri *et al.*, 2008, 2009).

An alternative relationship, derived from studies of well core from the Brae oilfield (Leary and Al-Kindy, 2002), an Upper Jurassic reservoir adjacent to a zone of normal

faulting in the South Viking Graben (Stow *et al.*, 1982), and considerations of a crust at the limit of mechanical 'criticality' (Leary, 2002; Heffer, 2007), suggests that porosity is correlated to the logarithm of permeability. This model is more appropriate for low porosity basement rock where permeability is dominated by fracturing rather than connected pore space.

The two porosity-permeability relationships used are

$$\begin{aligned} k &= A_1\phi^3, \\ \phi &= B_1\log(k) + B_2. \end{aligned} \tag{5.9}$$

Coefficients A_1, B_1 and B_2 are calculated from bounding values of porosity and permeability assigned at the upper and lower boundaries of each geological unit. These values have in turn been inferred from past numerical modelling studies of the TVZ (Kissling and Weir, 2005; Mannington *et al.*, 2004) and by matching thermal properties of modelled plumes to their TVZ counterparts. Bounding values for porosity and permeability are given in Table 5.1. The critical porosity for the cube-law relationship is 4% (from Zhang *et al.*, 1994) below which permeability drops rapidly.

5.6 Summary of models

The models detailed in the following chapters investigate geothermal convection in the TVZ, in general terms, at a variety of spatial scales, and perturbed by a variety of short- and long-terms processes. The first model, summarised in Chapter 6, considers rift-scale circulation models of the TVZ that are similar in scope to work by Kissling and Weir (2005) and McLellan *et al.* (2010). The investigation presented here is limited to an 80 km along-strike section of the central TVZ where the majority of the geothermal fields are located and bimodality in across-strike heat output is observed (see Figure 1.9). The objectives of this model are to: (i) address the effects of permeability heterogeneity and temperature boundary conditions on the

dimensional and thermal characteristics of a system of convection cells; (ii) undertake a statistical investigation of plume recharge by considering an ensemble of several thousand particle flow-paths; and (iii) investigate the long-term spatial stability of the geothermal plumes.

In Chapter 7, the focus is shifted to a smaller, single-field scale and geothermal circulation is considered in the context of a time-dependent permeability distribution. This approach contrasts with reservoir models, which generally consider short, exploitation-relevant time-frames (<100 years) in which permeability is approximately static. However, over long time-periods permeability evolves in response to tectonic and chemical processes (Grindley and Browne, 1976). Specifically, this set of simulations considers the effects of silica deposition on porosity and permeability under a gradient reaction regime (essentially an equilibrium assumption). Modelled hydrothermal cells demonstrate self-sealing, in which low porosity/permeability cap regions form above the upflow zone, resulting in significant deflection upflow and the development of lateral flows.

Finally, in Chapter 8, the short- and long-term effects that active dip-slip faults might exert on geothermal systems are considered. Geothermal upflow is evolved over long time-periods in the presence of a low permeability fault that operates as a fluid baffle. The deflected plume is subjected to several perturbations that are associated with rupture of the fault. For instance, large changes in rock pressure associated with an earthquake, and which were the focus of modelling studies in Chapters 2 to 4, are imported into the circulation model as a change in pore fluid pressure. Diffusion of these pressure anomalies alters heat transfer through the system for a period of several weeks following the earthquake. The effects of an abrupt increase in cross-fault fluid communication via a coseismic increase in fault-core permeability are also modelled. This perturbation results in a substantial increase in cross-fault circulation coupling and has important consequences for the stability of surface geothermal expression.

Quite a number of such mud-volcanoes extend on the steaming slopes of the Pairoa peak, playing in the gayest colours of red, white and yellow.

- Ferdinand von Hochstetter (1829-1884)

6

Rift-scale models

The geothermal fields of the TVZ are the surface manifestation of an extensive, large-scale, multi-cell convective system hosted within the faulted upper crust. This chapter details a model of a hypothetical circulation system that approximates both the dimensions and permeability of the TVZ's rifting upper crust, as well as statistical properties of its geothermal systems. The model, coupled to a particle tracking investigation, yields new insight into mass recharge in geothermal systems, including the size and distribution of catchment zones for a given field, the age of fluids exiting a field, and the variability of this property in space. A method is developed for approximating geothermal field catchment zones based on their position and heat output; the method is applied to the TVZ and high-temperature geothermal fields in Iceland. Finally, the spatial stability of geothermal fields is investigated on time-scales similar to their known lifetimes.

Work presented in this chapter is drawn from a paper submitted to Journal of Geophysical Research in May 2012 and published October 2012 (Dempsey *et al.*, 2012d). Results and text included in this chapter are largely unchanged from the prepared manuscript as permitted by the University of Auckland under the *2008 Statute and Guidelines for the Degree of Doctor of Philosophy (PhD)*. Co-authors of this work Dr Stuart Simmons, Dr Julie Rowland and Dr Rosalind Archer advised and commented on the manuscript, however the bulk of the research and preparation

for publication was undertaken by the thesis author (see accompanying declaration). The prepared manuscript is based on an earlier work presented at the 32nd NZ Geothermal Workshop in 2011 (Dempsey *et al.*, 2011).

6.1 Introduction

In the Taupo Volcanic Zone (TVZ) of New Zealand's Central North Island, fluids are circulated through the brittle crust by a large-scale convective system. Geothermal fluids upwell at more than twenty distinct locations, many of which host direct-use industries, electricity generation or tourism operations. Convection is thought to be driven by a high rate of rift-related magmatic intrusion occurring at mid- to lower-crustal depths (Bibby *et al.*, 1995). Cold fluids percolate through the upper-crust to mine heat at the brittle-ductile transition (BDT) and transport it efficiently to the surface (McNabb, 1975; Bibby *et al.*, 1995). This process bears similarities with the capture and lateral transport of thermal energy by topographically driven flows in mountainous regions (Forster and Smith, 1989). Fluid flow in the TVZ is assisted by fault and fracture permeability maintained by a high rate of tectonic extension ($12\,\mathrm{mm\,yr^{-1}}$; Wallace *et al.*, 2004) and moderate formation permeability in the uppermost 2 km. The stratigraphy at these depths is characterised by layered, variously welded, ignimbrites, pyroclastic tuffs and air-falls, deposited during voluminous Quaternary rhyolitic volcanism (Wilson *et al.*, 1995).

On the basis of their uniformity, McNabb (1975) proposed that the distribution of geothermal fields in the TVZ was analogous to that of convection in a porous medium heated from below. Heat is transported from the lower to the upper surface in discrete plumes, a feature that is consistent with recent magnetotelluric imaging of the brittle crust, which suggests the presence of conductive pipe structures at depths of 2 to 10 km (Bertrand *et al.*, 2012). This conceptual model suggests that the locations of geothermal fields do not necessarily correspond to specific deep heat sources (Bibby *et al.*, 1995); however, the role of the time-varying magmatic system as a driver of convection remains an open question (Rowland *et al.*, 2010). In recent

years, numerical modelling studies of TVZ circulation have yielded new insight into the deep structure of convective plumes, their recharge, and stability on geological timescales. For example, using a variable heat input through 16 separate, basal domains (calibrated by the corresponding surface output at that location), Kissling and Weir (2005) constructed a large-scale circulation model in good agreement with the locations and outputs of TVZ geothermal fields. In their model, recharge of the geothermal plumes occurs through a high permeability region in the centre of the domain, which corresponds to the enhanced structural permeability inferred to exist in the Taupo Fault Belt (Bibby *et al.*, 1995).

McLellan *et al.* (2010) presented a suite of generic multi-cell convection models that incorporated several TVZ-like features, including inclined fault structures, contrasts in basement permeability, and rift-related deformation. Their models demonstrated preferential formation of convective plumes above basement fault structures that focus upwelling. Furthermore, the stability of geothermal fields in space and time was explored; greater stability was demonstrated for a surface convective (as opposed to conductive) boundary condition while decreased stability was associated with increasing ignimbrite permeability.

In this chapter, a similar approach to McLellan *et al.* (2010) is adopted; insight into TVZ circulation and other large-scale convective systems is gained through an investigation of generic circulation models. Convection occurs in a computational domain that is dimensionally consistent with the TVZ, and average properties of the modelled geothermal fields are calibrated against their TVZ counterparts, e.g., field heat outputs, across-strike heat distribution. However, specification of arbitrary heterogeneity in both the crustal permeability field and basal temperature distribution precludes precise replication of TVZ circulation. Nevertheless, the model allows an investigation of individual plumes in the context of large-scale convection and yields specific insights into the mass recharge of geothermal fields. Particular emphasis is placed on the size and distribution of catchment zones from which mass recharge is drawn and the residence time of fluids within the crust.

Delineation of catchment zones by numerical methods is a common practice in

the ground water community (e.g., Vassolo *et al.*, 1998; Kunstmann and Kinzelbach, 2000; Frind *et al.*, 2002; Rock. and Kupfersberger, 2002; Frind *et al.*, 2006) with particular consideration given to the establishment of wellhead protection areas and contaminant transport. The catchment area for a given well is defined as the source region from which water can travel and be captured by the well, within some nominal time period. A variety of time-of-travel zones (TOTs) are constructed for the purpose of excluding or containing specific contaminants, e.g., 100-250 days for bacterial contaminants, and 25 years for chlorinated solvents in New Brunswick, Canada (Frind *et al.*, 2006). The geothermal field catchment is defined in a similar way, with the upflow zone that gathers and concentrates fluids substituting for the well, and TOTs representing regions from which similarly aged fluids are drawn.

Catchment zones can only be delineated where there is sufficient knowledge of the subsurface flow distribution. In ground water applications, a two- or three-dimensional flow field can be obtained numerically from a variety of software packages (e.g., MODFLOW (Feyen *et al.*, 2004); FEFLOW (Rock. and Kupfersberger, 2002); STGF (Vassolo *et al.*, 1998)) providing aquifer properties and boundary conditions are sufficiently constrained. Once the flow field is known, several methods exist for tracking the position of particles captured by the well back in time, i.e., backward particle tracking. For example, an adjoint-state based approach can be used to assign probability distributions to the upstream area; these represent both the likelihood that a contaminant particle originated at a particular location as well as a probabilistic description of the time since the contamination event occurred (e.g., Neupauer and Wilson, 2003b; Frind *et al.*, 2002). This method was applied by Neupauer and Wilson (2003a) to delineate catchment zones and to describe exposure to a contaminant that decays in time. Frind *et al.* (2006) used the approach to analyse more general well vulnerability issues, including, for a given catchment contamination event, the degree, onset and persistence of contaminant exposure.

An alternative method of catchment delineation involves the reconstruction of particle flow-paths that terminate at a given point, i.e., the wellhead, and subsequent contouring of particle locations after a given time. Particle tracks are con-

structed by reversing the sign of the fluid velocity distribution and propagating their positions backward in time by advective and dispersive processes. Using a random walk to account for particle dispersion, Uffink (1989) described the catchment zone around a pumping well in a probabilistic sense. Kunstmann and Kinzelbach (2000) used this approach to delineate a catchment zone for the Gambach aquifer in Germany by the 0.5 probability isoline, i.e., the area within which particles are more likely than not to reach the well. Uncertainty in ground water systems has received increasing attention in recent years. For example, Vassolo *et al.* (1998) applied a Monte-Carlo scheme to account for uncertainty in both recharge rates and aquifer permeability; the approach yields a distribution of catchment zones with varying degrees of confidence. Kunstmann and Kinzelbach (2000) present an alternative method in which input uncertainty propagation occurs concurrently with particle tracking; they compare their method with Monte-Carlo techniques and demonstrate significant computational savings.

This chapter describes the construction of a generic large-scale circulation model constrained by TVZ dimensions and material parameters, and calibrated against mean properties of the ensemble of geothermal fields. Fluid flow is modelled in three-dimensions using the heat and mass transfer code FEHM (Zyvoloski, 2007). This code has previously been used to model natural convection in air (Stauffer *et al.*, 1997) and single-cell geothermal systems (Dempsey *et al.*, 2012e,a). In Section 6.4, the implementation of a particle tracking algorithm accounting for advective and dispersive transport is discussed. The delineation of catchment zones for each of the modelled geothermal fields is detailed and the consistency of these catchments with one-dimensional geothermal heat and mass transport arguments (Weir, 2009) is evaluated. An alternative, first-order method of catchment construction based on Voronoi tessellation is proposed and compared with those delineated by particle tracking. This second method, while less accurate, does not require knowledge of the fluid velocity field; its application to convective systems in the TVZ and Iceland is discussed.

In Section 6.8, the spatial stability of the modelled geothermal fields is investi-

gated over a period of 300 kyr. During this time, fields demonstrate lateral migrations of up to 5 km, and in several instances are observed to merge together into larger fields. The degree of volatility these fields display is an inherent property of the convective regime and is not caused by a dynamic permeability distribution or changing thermal boundary conditions. This result has implications for both the modelling of rift systems to steady-state, as well as patterns of relic hydrothermal alteration at the surface, which reveal the past existence of geothermal activity.

6.2 Model setup

Circulation is modelled in a computational domain large enough to encompass the majority of the geothermal fields in the central TVZ. The domain measures 50 km across strike, 80 km along strike and is 8 km deep; the across-strike dimension is large enough that lateral boundaries do not influence upflow zones, while an 8 km vertical dimension corresponds to the approximate depth extent of the BDT (Bryan *et al.*, 1999). The base of the convective system is expected to correlate with the BDT as this represents the onset of quartz plasticity and thus the limit of fracture permeability deemed necessary to sustain convection. Circulation is modelled on a regular grid with horizontal and vertical nodal spacing of 500 and 400 m, respectively. This represents an improvement in resolution compared to the $1 \times 1 \times 0.5$ km blocks used by Kissling and Weir (2005) in their model of the TVZ, although it is noted that the model domain used here is smaller. Mass recharge of TVZ geothermal systems is primarily meteoric, although Giggenbach (1995) suggested a magmatic component of up to 6 and 14% might contribute to western and eastern systems, respectively. In the model presented here, a no-flow boundary condition is enforced at the lower boundary, i.e., a magmatic fluid flux is not considered. Initially, the model is everywhere 20°C and mass fluxes are zero.

Permeability structure influences the heat output and dimensional characteristics of both the ensemble and individual convection cells. As discussed in Section 5.5, in constructing a permeability distribution, several geophysical factors, both general

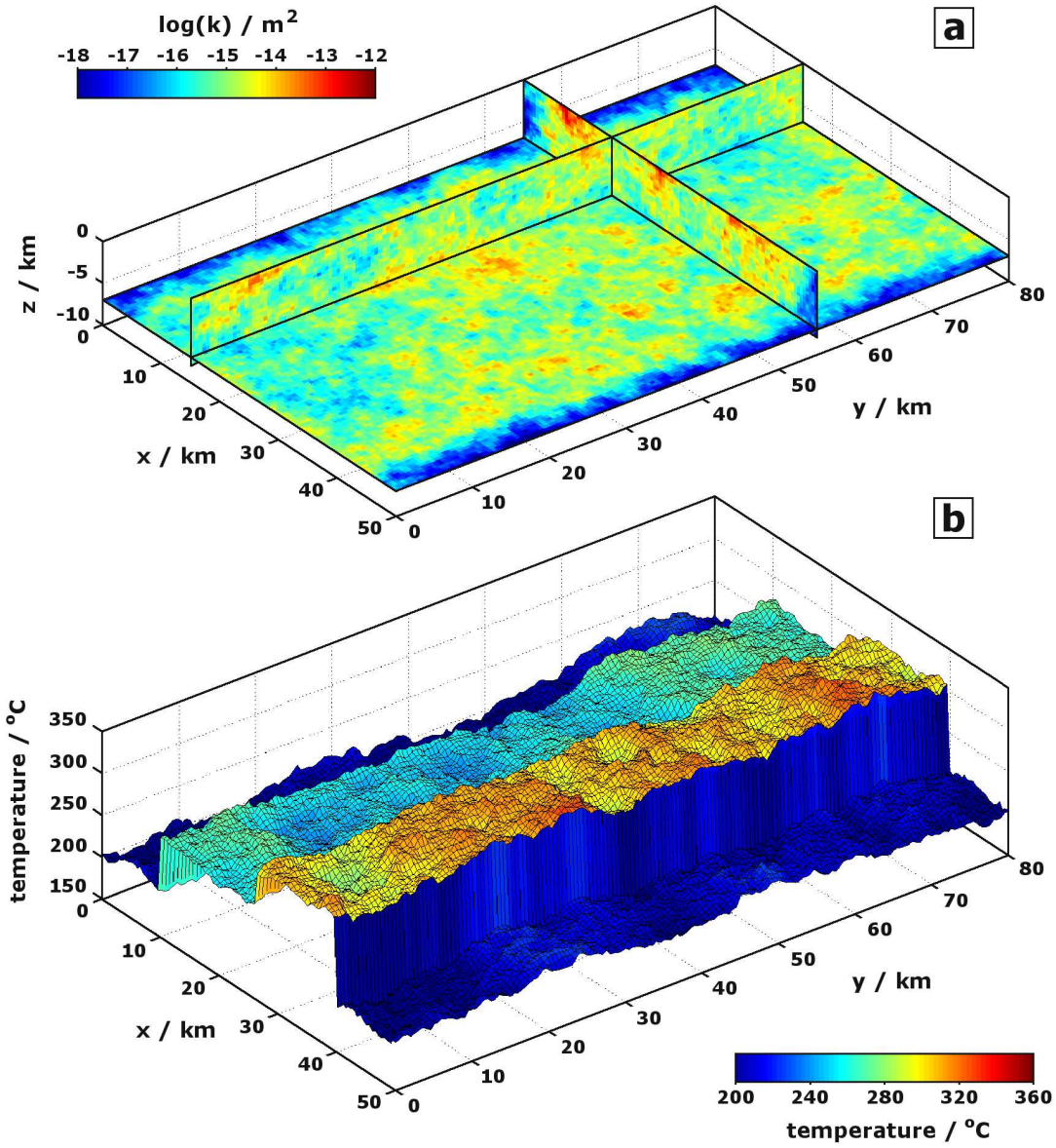

Figure 6.1: (a) Slices through the heterogeneous 3-D permeability distribution. Observation planes are positioned at $x = 35\,\text{km}$, $y = 55\,\text{km}$, and $z = -7\,\text{km}$. (b) Temperature boundary condition applied at the base of the crust.

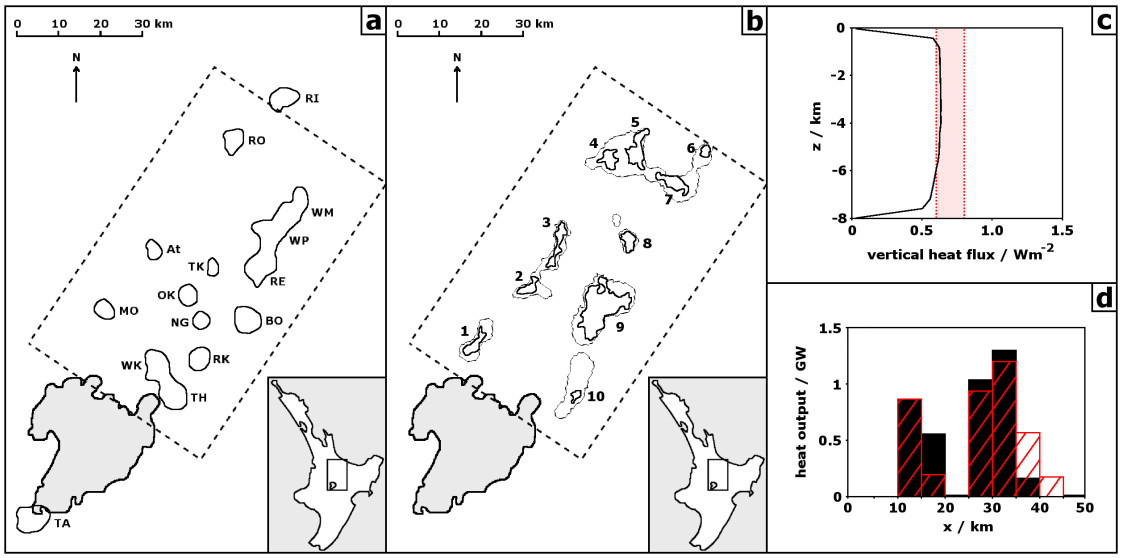

Figure 6.2: (a) Locations of geothermal fields within the TVZ and (b) the model domain (dashed outline). At = Atiamuri (10), BO = Broadlands-Ohaaki (190), MO = Mokai (400), NG = Ngatamariki (55), OK = Orakeikorako (660), RE = Reporoa (15), RI = Rotoiti (190), RK = Rotokawa (220), RO = Rotorua (470), TA = Tokaanu (60), TH = Tauhara (110), TK = Te Kopia (250), WK = Wairakei (420), WM = Waimangu (325), WP = Waiotapu (540). Field heat outputs from Bibby *et al.* (1995) are given in brackets. (b) Modelled geothermal fields after 500 kyr simulation time, demarcated by the $2\,\mathrm{W\,m^{-2}}$ (heavy black) contour of vertical heat flux. The $0.1\,\mathrm{W\,m^{-2}}$ contour is also shown (thin black). Areas and heat outputs corresponding to the numbered fields are given in Table 6.1. (c) Mean vertical heat flux over the model domain with depth. The target interval from Hochstein (1995) is shaded red. (d) Model across-strike heat distribution binned every 5 km (black) compared to TVZ distribution (red, from Bibby *et al.*, 1995). For the purposes of comparison, model heat output has been scaled to match TVZ heat output of Bibby *et al.* (1995).

and TVZ-specific, are considered including: (i) a 2 km thick, surface layer of relatively permeable volcanic strata overlying 6 km of greywacke basement; (ii) exponential decay in permeability with depth from $0.53 \times 10^{-14}\,\mathrm{m^2}$ (5.3 mD) at the surface to $0.15 \times 10^{-14}\,\mathrm{m^2}$ at the basement contact ($z = -2\,\mathrm{km}$) representing increasing pore compaction with depth, and from $0.15 \times 10^{-14}\,\mathrm{m^2}$ to $0.66 \times 10^{-15}\,\mathrm{m^2}$ at the base of the model representing closure of basement fractures with increasing confining stress; and (iii) a spatially correlated fluctuation field that captures the stochastic nature of fracture distribution contributing to crustal permeability. Permeability outside

Table 6.1: Modelled field properties: Q = heat output, A = area, n = approximate number of particle tracks, $\bar{t}_r$ = mean residence time, $\bar{x}_r$ = mean return distance, C = catchment area. Field numbers refer to Figure 6.2(b). The calculation of residence time, return distance and catchment area are discussed in Section 6.5.

field	Q (MW)	A (km^2)	n (10^3)	$\bar{t}_r$ (kyr)	$\bar{x}_r$ (km)	C (km^2)
1	105	17	65	22.3	4.1	176
2	100	13	56	12.0	4.5	70
3	133	21	143	17.6	5.6	157
4	143	18	85	15.3	5.5	97
5	240	32	267	15.3	6.3	259
6	70	7	64	22.7	5.8	104
7	157	24	194	20.5	6.9	187
8	112	15	120	13.0	4.9	91
9	833	93	638	16.1	8.2	499
10	44	6	37	32.6	5.0	83

the rift ($x < 5\,\text{km}$ and $x > 45\,\text{km}$) is two orders of magnitude less than its in-rift counterpart. Horizontal permeability is three times higher than the quoted vertical permeabilities.

Faulting in the TVZ is particularly dense in some parts of the TFB (Figure 1.2), somewhat sparser in accommodation zones between rifted segments (Rowland and Sibson, 2004), and much less common east of the Paeroa Fault and within the Taupo Reporoa Basin. In such a varied environment, the relationship between geothermal fields and structural permeability is not clear-cut; some geothermal systems coincide with fault tips (e.g., Orakeikorako), others mid-way along faults (e.g., Te Kopia), some in calderas (e.g., Reporoa, Waimangu), and still others where there is no obvious faulting and basement permeability must be inferred (e.g., Rotorua, see Wood (1992); Kawerau, see Wood *et al.* (2001)). Furthermore, geothermal expression is conspicuously absent from the densely faulted TFB (although recent investigations of sinter deposits near Mangatete suggest this may not always have been the case (Drake *et al.*, 2012)), a region that, at first glance, might regarded as a prime candidate for geothermal upflow. To explore the importance of structural heterogeneity on

large-scale geothermal circulation A spatially correlated, heterogeneous fluctuation field is superimposed upon the homogeneous, depth-dependent permeability profile described in Section 5.5.1 (see also Table 5.1). The purpose of this heterogeneity is to capture, in a statistical sense, the spatial variability of structural permeability associated with a non-uniformly faulted crust.

Spatial fluctuations have a power-law-scaling exponent, β, of 1.5; this was selected as a combination of pure 'pink' noise associated with a critical crust (e.g., Leary and Al-Kindy, 2002) overprinted on geological features that impart structure, e.g., formation contacts, faults, etc. Fractal, scale-invariant distributions of cracks and fractures have been observed in both sedimentary (e.g., Heffer and Bevan, 1990) and igneous rocks (Leary, 1991); they form as a consequence of slow tectonic loading (or unloading, see Chapter 4) of the crust to the limit of mechanical failure (Heffer, 2007), such as occurs in the TVZ. The degree of spatial correlation used here was found to give the best results in terms of localizing discrete upflow-zones; at lower values of β ($\lesssim 1.3$) convective cells form long chains, behaviour that is not observed in the TVZ (with the possible exception of the combined Waimangu-Waiotapu-Reporoa fields). For higher values of β ($\gtrsim 1.7$), very high ($10^{-13}\,\mathrm{m}^2$) and very low ($10^{-16}\,\mathrm{m}^2$) permeability domains, 10's of kilometres in width, are formed; this distribution does not capture the distributed nature of faulting and structural permeability throughout the TVZ. For β on the edges of these domains, i.e., ~ 1.3 or ~ 1.7, the properties of the convective circulation that develop can depend upon the specific permeability realisation, e.g., for $\beta = 1.3$ convection cells will sometimes, but not always, link up into chains. Figure 6.1 shows the modelled permeability distribution for several arbitrary 2-D slices. Low permeability in the rift boundaries ($x < 5\,\mathrm{km}$ and $x > 45\,\mathrm{km}$) is evident.

Convection is generated by the application of an across-strike, piece-wise temperature boundary condition applied at the base of the model. Figure 6.1(b) shows this is comprised of a low temperature background (200-210 °C) at the margins of the rift, a warmer hotplate between 10 and 26 km (265°C), and a high temperature hotplate between 26 and 40 km (310°C). Such a partitioning of the hotplate bound-

ary condition was required to replicate the bimodal across-strike heat output of the TVZ (Figure 1.9). Physically, it is an approximation of the eastward migration in the locus of magmatism - as evidenced by a similar migration in the locus of volcanism, Rowland *et al.* (e.g., 2010) - and thus magmatic heat sources. Regions from which magmatism has moved on, or in which magmatic intrusion is less frequent, are represented by lower temperatures. Superimposed on the large-scale temperature structure is a smaller-scale, spatially correlated temperature fluctuation; while this has some influence on the location, size and heat output of convection cells, it was found to be a less significant control than the permeability structure. The temperature fluctuation field shares the same spatial correlation as the permeability distribution, i.e., an exponent, β, of 1.5, and represents heterogeneity in the magmatism that drives convection in the TVZ. In these models, boundary temperature heterogeneity is constant in time. It does not account for the enhanced convective scavenging at hot-spots that would tend to smooth a heterogeneous distribution. In future, a more complex model could account for time-varying heterogeneity representing a more-dynamic environment of episodic magmatic intrusion buffered by convective cooling.

6.3 Description of circulation

The computational domain corresponds to a region of the TVZ containing approximately thirteen geothermal fields (Figure 6.2(a)). After 500 kyr of simulation time, the model attains a circulation state in which large-scale convection occurs through ten discrete fields, as demarcated by the $2\,\mathrm{W\,m^{-2}}$ vertical heat flux contour (Figure 6.2(b)). At 250°C, maximum surface temperatures are slightly cooler than some fields in the TVZ (e.g., Ohaaki, see Figure 6.3(a)), although Kissling and Weir (2005) note that surface temperatures increase with improved model resolution; this may go some way toward accounting for the discrepancy. In other, lower-temperature fields (e.g., Wairakei-Tauhara, Te Kopia), a reasonable match is obtained between measured temperature profiles and the modelled geothermal fields. However, the match

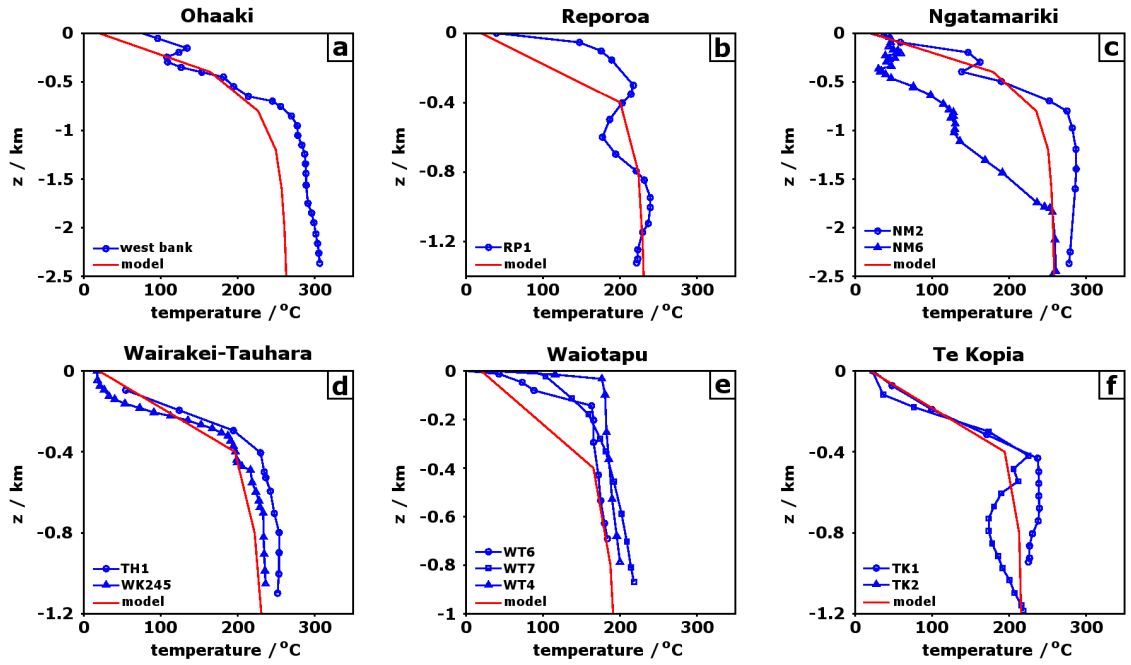

Figure 6.3: Comparison between temperature profiles from six TVZ geothermal systems and the best match produced by the model. Temperature data for the fields are from the following sources: (a) Ohaaki, Clearwater *et al.* (2012); (b) Reporoa, (Wood, 1994a); (c) Ngatamariki, Bignall (2009); (d) Wairakei-Tauhara, Mannington *et al.* (2004); O'Sullivan *et al.* (2009); (e) Waiotapu, Bibby *et al.* (1994); (f) Te Kopia, Bignall (1994).

is generally worse at the near-surface, either where the mesh is too coarse capture sharp, boundary-layer temperature gradients (e.g., Reporoa, Waiotapu), or where cooler, possibly topographically-driven, inflows interfere with the upflow (e.g., Ngatamariki). Nevertheless, below 500 m, the model adequately represents hydrothermal temperature gradients in the TVZ. Thus it is suitable for the investigations in this chapter, which focus on circulation to depths of 8 km, i.e., the full convective system.

The modelled fields range in area from 6 to 93 km^2 and in heat output from 44 to 833 MW (see Table 6.1). Most fields have outputs between 100 and 250 MW; this is consistent with a one-dimensional, rainfall-recharge model for geothermal systems proposed by Weir (2009) who found that, for TVZ parameters, fields of 200 MW should be favoured. The average field output is smaller than those collated

by Bibby *et al.* (1995) based on chloride flux calculations (Ellis and Wilson, 1955). An increase in model heat output can be achieved (via an increased mass flux) by raising the permeability; however, this has the effect of lowering surface temperatures. Permeability ranges used in these models represent a calibration trade-off between the heat output of the modelled hydrothermal plumes, and their temperatures at near-surface (<1 km) depths.

Qualitatively, modelled fields are smaller in area than their TVZ counterparts, although a precise judgment is difficult when making a comparison between resistivity contours, used to delineate TVZ fields, and the heat flow contours used in the model. In addition, interactions between hot upwelling fluids and surface hydrological processes, which may lead to more prevalent lateral outflows, have not been considered here. The model includes a particularly large field that, at 830 MW and 93 km^2, is slightly larger than the combined Waiotapu, Waimangu and Reporoa systems (see Table 1.1).

The mean vertical heat flux through the rift is 0.61 $W\,m^{-2}$ (Figure 6.2(c)), which is consistent with estimates for the 200-km-long TVZ arc of 0.6-0.8 $W\,m^{-2}$ (Hochstein, 1995); however, in the central section where the majority of the geothermal fields are found, the average heat flux is probably higher. The piece-wise hotplate temperature boundary condition applied to the base of the model (Figure 6.1(b)) produces an across-strike heat output that exhibits a similar bimodality to that observed by Bibby *et al.* (1995) for the entire TVZ (Figure 6.2(d)). In making this comparison, total model heat flow was scaled by a factor of ≈ 2 to match data used by Bibby *et al.* (1995).

Mass recharge of geothermal cells occurs by downward percolation of cold fluids throughout 84% of the rift ($5 < x < 45$ km). These down-flows suppress temperatures below the conductive gradient that exists outside the rift (see Figure 6.4(a)), with temperatures as low as 50°C recorded at a depth of 6 km. In Section 1.5.1, type-curve analysis of temperature-depth profiles in TVZ geothermal systems indicated upflow velocities on the order of 8.7×10^{-10} to $4.8 \times 10^{-9}\,m\,s^{-1}$. The same analysis can be applied to derive groundwater velocity for the temperature-depth

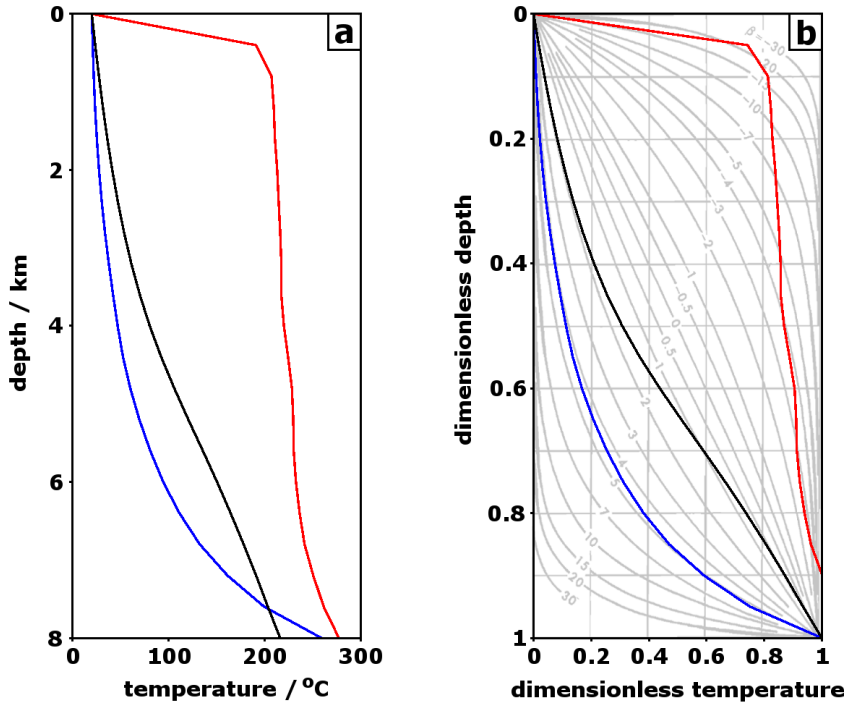

Figure 6.4: (a) Temperature-depth profiles at three sites within the modelled convective system: within an upflow zone (red), inside the rift but outside the upflow zones (blue), and outside the rift (black). (b) The same profiles, dimensionalised against the height of the convective system (8 km) and upper and lower boundary temperatures, and superimposed upon groundwater velocity type-curves from Bredehoeft and Papadopulos (1965).

profiles in Figure 6.4. For example, the normalised down-flow temperature profile has a β value of ~ 4.5. Again inverting Equation (1.3), and for $c_0 = 4.2 \times 10^3\,\mathrm{J\,K^{-1}}$, $\rho_0 = 1000\,\mathrm{kg\,m^{-3}}$, $\kappa = 2.3\,\mathrm{W\,m^{-1}\,K^{-1}}$, and $L = 8\,\mathrm{km}$, the type-curve analysis in Figure 6.4(b) gives a down-flow velocity of $3.1 \times 10^{-10}\,\mathrm{m\,s^{-1}}$. In the model, the average down-flow velocity along the profile is $3.2 \times 10^{-10}\,\mathrm{m\,s^{-1}}$, which is in good agreement with type-curve analysis.

Temperature-depth profiles outside the rift and in the upflow zone do not conform to the type-curve shape as well as the down-flow profile. Nevertheless, taking $\beta = 1$ for the out-of-rift profile (in fact it ranges from 2 at the surface to 0.5 at the base of the convective system) type-curve analysis suggests downward percolation at a

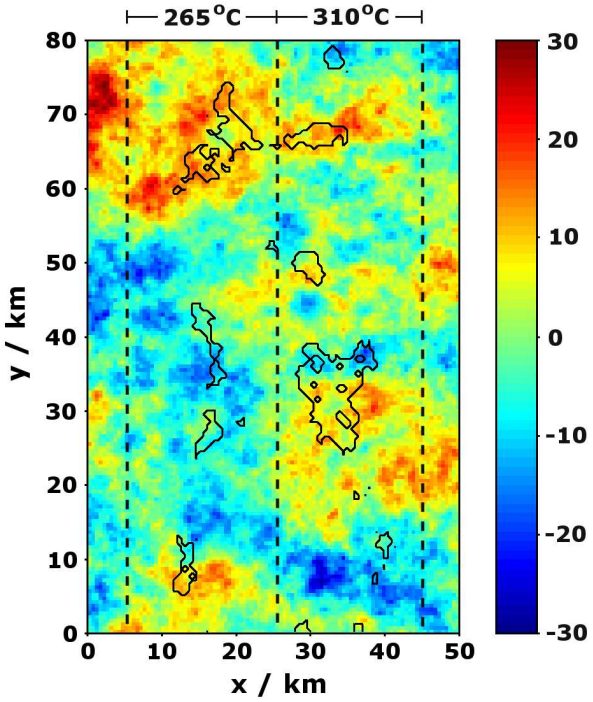

Figure 6.5: Correlation between surface geothermal field position (black contours) and the spatially correlated temperature anomaly imposed upon the basal temperature boundary condition. The positions of the rift and the transition between the 265°C and 310°C hotplates are indicated by dotted lines.

rate of $6.8 \times 10^{-11}\,\mathrm{m\,s^{-1}}$, which is close to the actual depth-averaged value of $4.8 \times 10^{-11}\,\mathrm{m\,s^{-1}}$. Upflow velocities are more difficult, in part due to the poor resolution of high temperature gradients at the model surface. The mean upflow velocity for the profile in Figure 6.4 is $1.1 \times 10^{-8}\,\mathrm{m\,s^{-1}}$, higher than the range calculated for TVZ geothermal systems in Section 1.5.1, and corresponding to a type-curve of β =-140 (for a mean upflow fluid density of $870\,\mathrm{kg\,m^{-3}}$). Type-curve fitting to the modelled profile suggests a lower β value of perhaps -30, although this process may not be accurate for the non-standard curve shape.

The positions of the geothermal fields at the surface of the model are related to heterogeneity in both the basal temperature boundary conditions and the crustal permeability distribution. Figure 6.5 indicates that field positions tend to, but do not always, correlate to hotter regions of the crust; however, it is acknowledged that a

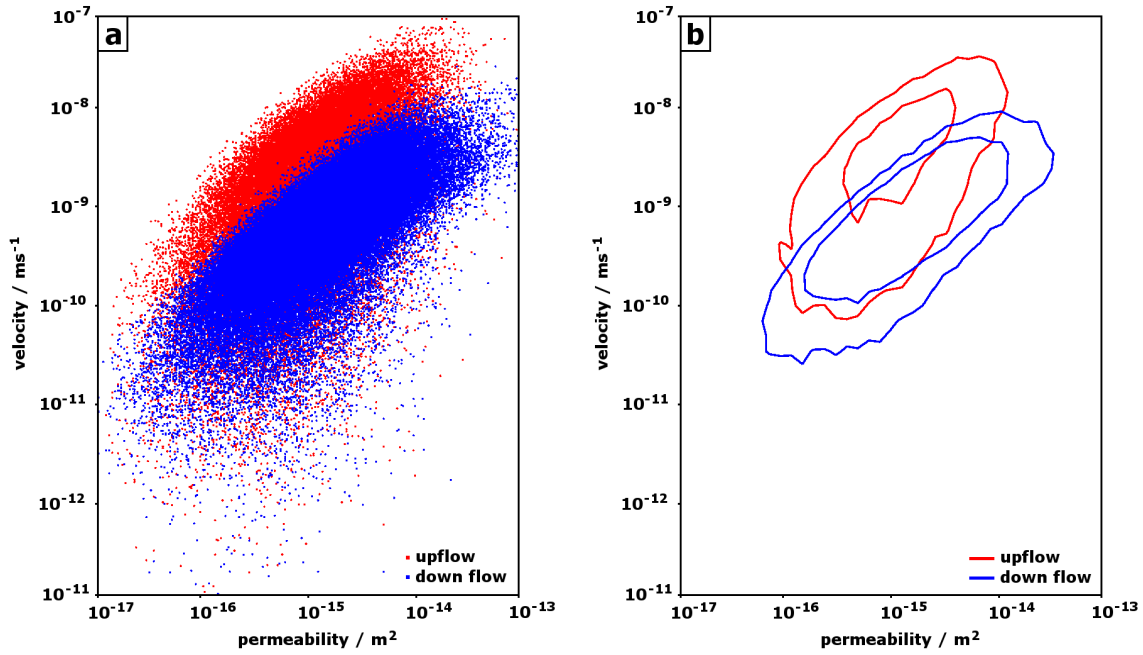

Figure 6.6: (a) Magnitude of the vertical velocity plotted against permeability for every in-rift ($10 < x < 40$ km) node in the model. Upward- and downward-directed fluid velocities are plotted in red and blue, respectively. (b) The same data converted to a probability density function and contoured at two arbitrary levels of .03 and 0.12.

fluctuation magnitude of 60°C probably underestimates the true size of temperature fluctuations in the heterogeneously intruded mid-crust. Increasing the magnitude of this fluctuation may promote a stronger relationship between mid-crustal thermal anomalies and the positions of upflow zones.

Figure 6.6 demonstrates that the relationship between permeability and the position of geothermal fields is not straightforward. Intuitive relationships are evident, such as, for example, a positive correlation between velocity and permeability, and a tendency for higher velocities in upflow zones (due to both a lower viscosity and the effects of buoyancy). Less intuitive, is the absence of compartmentalisation of upflow and down flow into high and low permeability domains, respectively.

The positions of geothermal fields in the TVZ, as well as regions of mass recharge, are features of a single convective system that is unstable and (quasi-) stationary for

the global permeability structure and basal temperatures. An unstable system is one in which alternative circulation systems exist for sufficiently large changes of the permeability structure or thermal boundary conditions (Chandrasekhar, 1961). Upflow zones, while having positions determined by global considerations, are nevertheless free to take advantage of any high-permeability conduits in their near-vicinity, e.g., fault-tip damage zones, fault intersections, just as mass recharge will be more vigorous in similar, high-permeability structures located in regions of down flow. So, while portions of the modelled geothermal systems correlate with high permeability zones, the opposite is not true, i.e., high permeability does not necessarily correlate with the location of geothermal systems. With regard to the TVZ, this is simply a statement that although many geothermal fields are associated with fault tips and accommodation structures (Rowland and Sibson, 2004), there are other, more densely-faulted regions (e.g., the TFB) that are apparently devoid of hydrothermal activity.

6.4 Particle tracking method

Fluid flow-paths are constructed by considering the movement of particles at positions $\mathbf{x}_t$ and at times t subject to advective, diffusive and dispersive forces. The position of a particle at some later time $t + \Delta t$ is given by Kitanidis (1994) as

$$\mathbf{x}_{t+\Delta t} = \mathbf{x}_t + (\mathbf{v} + \nabla \cdot \mathbf{D})\Delta t + (2\Delta t)^{\frac{1}{2}}\mathbf{V}\xi, \tag{6.1}$$

where $\mathbf{v}$ is the particle velocity (equal to the Darcy velocity divided by porosity), ξ is a vector of normally distributed random numbers with mean zero and unit variance, and $\mathbf{D}$ is the 3×3 dispersion tensor (e.g., Wood *et al.*, 2003) given by

$$D_{ij} = (D_m + \alpha_T|\mathbf{v}|)\delta_{ij} + (\alpha_L - \alpha_T)v_i v_j/|\mathbf{v}|, \tag{6.2}$$

where D_m is the molecular diffusivity, and α_L and α_T are the longitudinal and transverse dispersivities. $\mathbf{V}$ is a 3×3 tensor satisfying $\mathbf{V}\mathbf{V}^T = \mathbf{D}$ (Kitanidis, 1994) and is obtained from Cholesky decomposition of $\mathbf{D}$.

The second term on the right hand side of Equation (6.1) is solved using an explicit, 4^{th}-order Runge-Kutta algorithm with a time step size of ∼30 years. This term represents advective advancement of the flow-path adjusted for drift introduced by spatial variation in the dispersion tensor; neglecting the $\nabla \cdot \mathbf{D}$ term in (6.1) leads to a non-physical accumulation of mass in low dispersion regions. The third term on the RHS of (6.1) represents the random walk; it is calculated at particle mid-points, i.e., $\mathbf{x}_{t+\Delta t/2}$, and applied at the end of each iteration.

Spatial variation in the dispersion tensor is due to a heterogeneous velocity field associated with the similarly heterogeneous permeability field. In practice, molecular diffusivity, D_m, increases with both temperature and the temperature-dependent viscosity, and therefore this term should also contribute to $\nabla \cdot \mathbf{D}$; however, as the temperature and pressure dependence is unconstrained over the necessary intervals, a constant, but artificially high, value of D_m of $1 \times 10^{-8}\,\mathrm{m^2\,s^{-1}}$ is chosen. Following Goode (1996), the intent is to demonstrate the maximum likely effect of diffusion.

Dispersivity coefficients vary with both the scale of fluid flow and the geological media to which they are ascribed (Schulze-Makuch, 2005). As with molecular diffusivity, constant values for α_L and α_T are selected. An estimate of longitudinal diffusivity is obtained from scaling relationships constructed by Schulze-Makuch (2005); for a well-consolidated geological media and at a flow scale of 500 m (corresponding to the mesh dimension) a value of 17.9 m is chosen. Based on data in Gelhar *et al.* (1992) and, again, for a flow scale of 500 m, a transverse dispersivity of 1 m is used.

Within the crust, $\mathbf{v}$ varies continuously in both space and time; however, model output is restricted to discrete positions (the nodes) and time steps. Linear interpolation is used to calculate the velocity field at time, τ, between two time steps, τ_i and τ_{i+1}, and at position, $\mathbf{x}$, within a cuboid volume defined by eight corner nodes at positions, $\mathbf{x}_{1,2,\ldots 8}$. Linear interpolation of velocity within an element satisfies conservation of mass and is thus a desirable interpolation scheme.

Each particle flow-path provides a small amount of information on the nature of geothermal recharge; a complete picture is established by considering several tens

of thousands of flow-paths. Here, the instantaneous recharge properties for a given geothermal field are considered, i.e., a set of flow-paths that all terminate within the boundary of the field at a precise time. A set of flow-paths satisfying this condition is obtained by releasing particles at random locations within the geothermal field boundary and back-tracking their positions in time. The number of particles released from a given location is proportional to the mass flux at that location; this prevents bias introduced by the over- and under-sampling of low and high mass-flux regions, respectively. Particle back-tracking is implemented numerically by making the replacement $\mathbf{v} \rightarrow -\mathbf{v}$ in Equations (6.1) and (6.2). The procedure is equivalent to solving a Kolmogorov backward equation for a general stochastic process. In total, 1.7 million particle tracks were constructed for the ten modelled geothermal fields (Table 6.1), with larger flow-path ensembles constructed for larger fields with greater mass throughputs.

6.4.1 Effects of thermal dispersion on convection

As each fluid particle carries an amount of heat energy, mass dispersion can influence the transport of heat within a hydrothermal plume. While accounted for in the particle tracking algorithm implemented in post-processing, mass dispersion and its associated effects on heat transport are not included explicitly in the governing equations in FEHM. An approximate description of thermal dispersion can be included by prescribing an effective thermal conductivity, which is increased to account for enhanced heat transport; transverse and longitudinal thermal dispersion can be differentiated by a tensor description of the thermal conductivity (Nield and Bejan, 1998). However, for the conditions under which convection occurs here, the effects of thermal dispersion on plume structure can be shown to be negligible.

Tyvand (1977) derived expressions for the perturbation by thermal dispersion of natural convection in a porous medium heated from below. At large Péclet numbers, the onset of convection is delayed and the size of convection cells either increased or decreased depending on the ratios of vertical to horizontal dispersion and permeability. However, for small Péclet numbers, such as those encountered at Darcian flow

velocities, the effects of dispersion are negligible. In our simulations, the Péclet number, defined $Pe = v_D L_p/\alpha_f$ where v_D is the Darcy velocity (up to $10^{-7}\,\mathrm{m\,s^{-1}}$ in the upflow zone), L_p the particle diameter and α_f the thermal diffusivity ($\sim 10^{-7}\,\mathrm{m^2\,s^{-1}}$), has values of 10^{-3}-10^{-6} for millimetre- to micrometre- sized particle distributions. These values are well below the threshold for which thermal dispersion is significant. In contrast, where convection is driven by a solute gradient and the molecular diffusivity is much smaller than the thermal diffusivity, larger Péclet numbers occur. Under these conditions, dispersion must be accounted for in the transport equations (e.g., Hassanzadeh *et al.*, 2009).

6.5 Single field recharge

This section discusses particle tracking for a single modelled field and develops techniques to be applied later to the ensemble of fields. For modelled field 1 (see Figure 6.2(b) and Table 6.1), approximately 65 000 flow-paths terminating at $t = 500\,\mathrm{kyr}$ were constructed. For each flow-path, the following statistics are calculated: (i) the time taken from a particle's infiltration outside the field (source) until its return within the field (return), i.e., the residence time; (ii) the horizontal distance travelled during this time (return distance); and (iii) the proportion of the residence time spent in the greywacke subdomain ($z < -2\,\mathrm{km}$), termed basement affinity. These data are represented by relative frequency histograms in Figure 6.7(a-c). Field recharge properties are also illustrated spatially by constructing a probability density function that describes the likelihood of a particle originating from a specific location (Figure 6.7(d)); this is one representation of the catchment of the geothermal field. Average residence times and basement affinity can then be represented spatially by contouring their values within the catchment (Figure 6.7(e-f)).

Fluid recharge for modelled field 1 occurs up to 10 km distant from the main upflow zone, although the majority of particles ($> 80\%$) are sourced between a distance of 1 and 6 km. The relative frequency histogram shows a peak at 2.5 km, which corresponds to a large fluid contribution from a region centred at $\{x, y\} = [10, 9]\,\mathrm{km}$

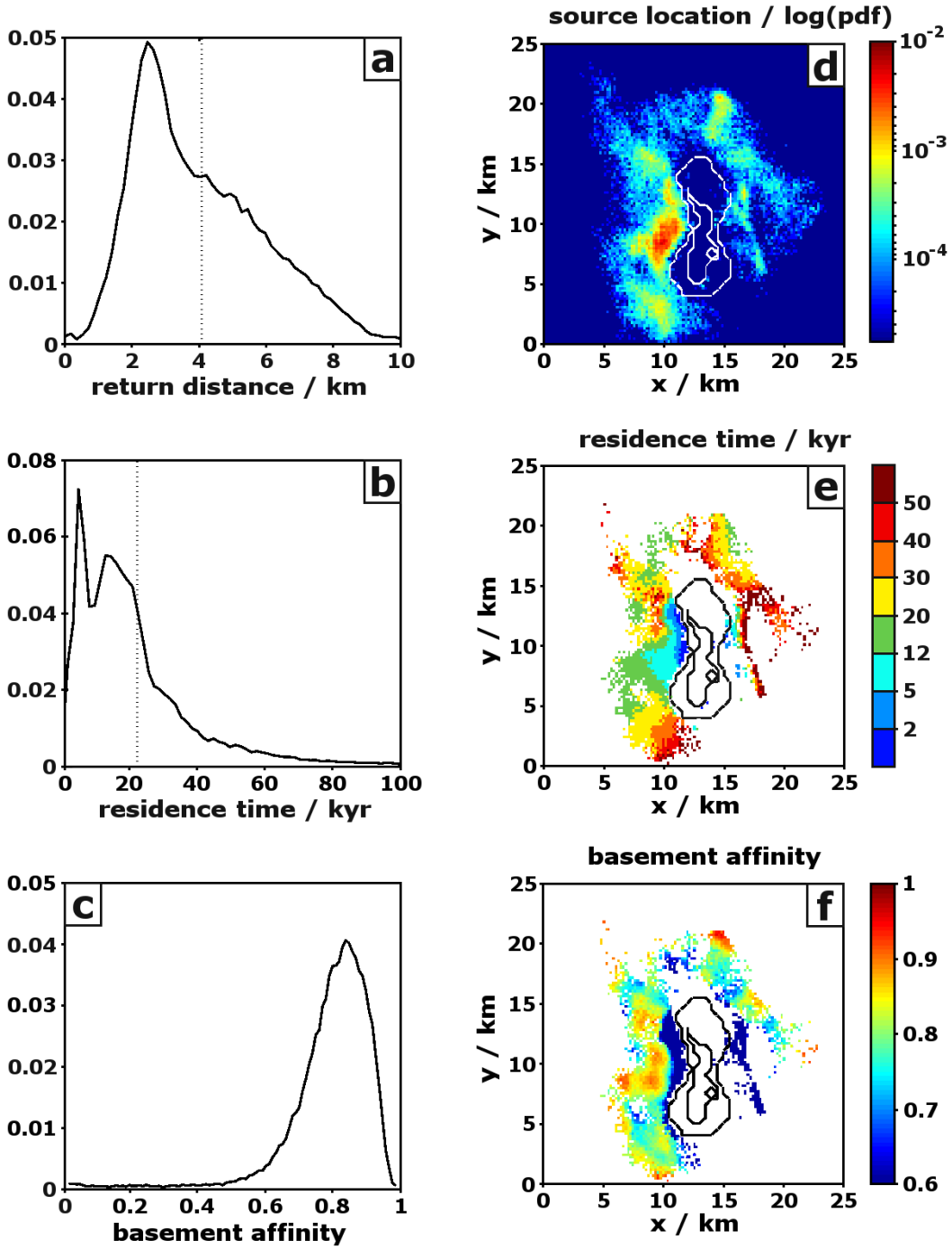

Figure 6.7: Statistics for $\sim 65\,000$ particle tracks for field 1 (see Figure 6.2(b)). (a) Relative frequency histogram of return distances. Mean of 4.1 km is marked by the dashed line. (b) Relative frequency histogram of residence times. Mean of 22.3 kyr is marked by the dashed line. (c) Relative frequency histogram of basement affinity. (d) Probability density function of particle source location. (e) Mean residence time at particle source. (f) Mean basement affinity at particle source.

(see Figure 6.7(d)). This anomaly is characteristic of the non-uniform distribution of recharge in the region surrounding the geothermal field. For instance, several high recharge zones occur to the left of the field with another located at the top right; in contrast very little recharge is sourced from a large region to the bottom right. This variation in recharge contribution is sensitive to both the proximity and size of neighbouring geothermal fields, as well as the imposed permeability heterogeneity, e.g., high and low recharge coincides with regions of high and low permeability. A similar result was obtained by Kissling and Weir (2005) in their rift-scale model of the TVZ; they found regions of strong down-flow coinciding with a central high permeability zone corresponding to the Taupo Fault Belt.

The distribution of particle residence times is also highly variable, with the majority of particles spending between 5 and 50 kyr in transit through the crust. The shape of Figure 6.7(b) is similar to that of a tracer breakthrough curve, demonstrating both a fast rise and a long tail; this is due to the majority of particles taking the shorter flow-paths, and a decreasing minority taking tortuous, meandering paths (Moreno *et al.*, 1988; Tsang and Neretnieks, 1998). The average residence time for the entire field is 22.3 kyr. This number is higher than the 12 kyr upper limit obtained by Stewart (1978) based on the absence of a glacial isotopic signal in deep fluids from Wairakei geothermal field (see Section 1.5.1). Giggenbach *et al.* (1994), studying isotopic compositions of CO_2 and CH_4 at Waiotapu geothermal field, obtained residence times of 2 kyr in the north of the field, with increasing age as fluids further south were sampled. In the central sections of the field, the mean residence time was 18 kyr, while in the southern section ages of 11 to 280 kyr were obtained; these ages are more consistent with those in modelled field 1.

Spatially, residence times vary depending on the proximity of a recharge source to the field; Figure 6.7(e) reveals that, on average, younger fluids are sourced closer to the field than those recharging at a greater distance. Recharging fluids spend the vast majority of their time within the basement, which is consistent with both the lower permeability (and thus lower fluid velocity) ascribed to this subdomain, as well as its being three times thicker than the surface cover sequence of volcanic rocks and

their reworked equivalents. Basement affinity also demonstrates considerable spatial variability (Figure 6.7(f)), which is attributed to heterogeneities in the permeability structure.

6.5.1 Catchment delineation

The size of the catchment area of the geothermal field, defined as the area outside the field from which recharge is drawn, can be approximated by considering the areal coverage of the set of points representing flow-path source locations. As each flow-path has an infinitesimally small cross-section, a discretisation-based approach is employed; the surface area around a given field is discretised and grid cells are regarded as part of the catchment if they contain a flow-path source. This inevitably leads to some dependence of the estimated catchment area on the grid cell dimension, e.g., larger grid cells deemed part of the catchment have a greater chance of covering part of the non-catchment area. Furthermore, catchments that account for given percentages of the total recharge (i.e., the total particle number) can be constructed; catchment area also depends on this recharge threshold. Figure 6.8(a) shows the catchment area for field 1 calculated for discretisations ranging between 50 and 1000 m, at several different recharge thresholds, e.g., the 90% threshold represents the smallest catchment area that accounts for 90% of the total recharge. As expected, greater proportions of recharge are accounted for by larger catchments. The data in Figure 6.8(a) indicate that catchment size has an approximately linear dependence on discretisation for values greater than 400 m; this represents the increasing error with which the edge of the true catchment is pixelated. Extrapolating the linear trend back to an infinitely discretised domain (discretisation dimension of zero) then provides an estimate of the catchment size for a given threshold.

For domain discretisations less than 400 m, the estimated catchment area begins to fall sharply to zero; this occurs because the pixel dimension is approaching the mean spacing between particle source locations. As pixels are reduced in size, the number of empty pixels occupying the space between points in the particle location cloud increases, and regions that were previously considered part of the catchment

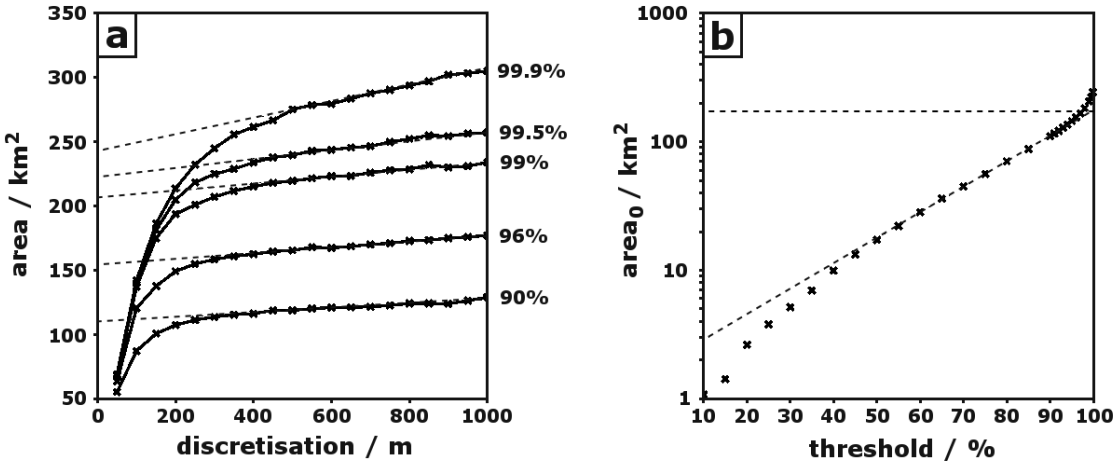

Figure 6.8: (a) Catchment area of field 1 for domain discretisations between 50 and 1000 m. Catchment threshold levels of 90, 96, 99, 99.5, and 99.9% are shown. Least squares linear trends are fit to the data for discretisations greater than 400 m, and intercept the vertical axis at the zero-discretisation catchment area ($area_0$). (b) Zero-discretisation catchment area versus catchment threshold. A least squares linear trend is fit to the data for catchment thresholds between 50 and 95% (inclined dashed line). For a 100% catchment threshold, the fitted line predicts a catchment area of 176 km^2 (indicated by the horizontal dashed line).

are no longer counted. This effect is avoided by extrapolation of the data while it behaves linearly.

Zero-discretisation catchment areas ($area_0$) are plotted against recharge threshold in Figure 6.8(b). The relationship between catchment area and recharge threshold is approximated by an exponential; extrapolation of this trend to a 100% recharge threshold furnishes an estimate of the field's catchment. For field 1, the estimated catchment area is 176 km^2. In practice, the 100% catchment area should be infinitely large (or equal to the domain area) as there exists a finite possibility that, given favourable dispersive transport steps, fluid anywhere could be transported to the upflow zone. The data in Figure 6.8(b) begin to demonstrate this quality for recharge thresholds greater than 97%. Extrapolating the approximately exponential trend that exists between recharge thresholds of 50 and 95% up to a value of 100%, represents an acceptable truncation of this behaviour.

6.5.2 Effects of dispersion and time step size

Figure 6.9 shows the effects of neglecting dispersion in the particle tracking algorithm (Equation 6.1). The iterative application of a random walk to the particle trajectory results in a smoother distribution of recharge source that is intuitively more physical than that obtained by advection-only particle tracking. Relative frequency histograms of return distance and residence time are smoother with increasing dispersion, although distribution averages are largely unaffected. The smoothing effect is attributed to a sort of 'mixing', whereupon a particle that is being propagated along a given 'pure-advection' streamline (associated with deterministic return characteristics) is displaced onto a different streamline by the random walk. This happens multiple times during a single particle trajectory.

This smoothing effect also extends to the probability density functions (PDF) constructed to illustrate regions from which recharge is drawn. For particle tracking with no dispersion (Figure 6.9(f)), the PDF is spikey and exhibits regions from which large volumes of recharge are drawn immediately adjacent to regions of zero recharge. The introduction of "maximum-likely" dispersion coefficients (see Section 6.4) smoothes the PDF and any local features it contains, with some being eliminated entirely (for example, a small feature labelled α in Figure 6.9(e) is absent in (d)). It also increases the total area from which fluids are drawn, i.e., the field's catchment. For example, at full dispersion the catchment for field 1 is 176 km^2, compared with 101 km^2 if dispersion is reduced by a factor of 10 and 35 km^2 if dispersion is not accounted for.

The size of the time step, Δt, used in solving Equation (6.1) also has an effect on the set of flow-paths generated. For the 4^{th}-order Runge-Kutta algorithm used to solve the advective component of (6.1), error scales with $(\Delta t)^5$ and cumulative error with $(\Delta t)^4$ and thus numerical accuracy is relatively high. Reducing the time step improves the accuracy of the method at the expense of computational resources, while selection of an unnecessarily large time step exacerbates the amount of 'overshooting' of the particle flow-path, i.e., the extent to which a particle is propagated

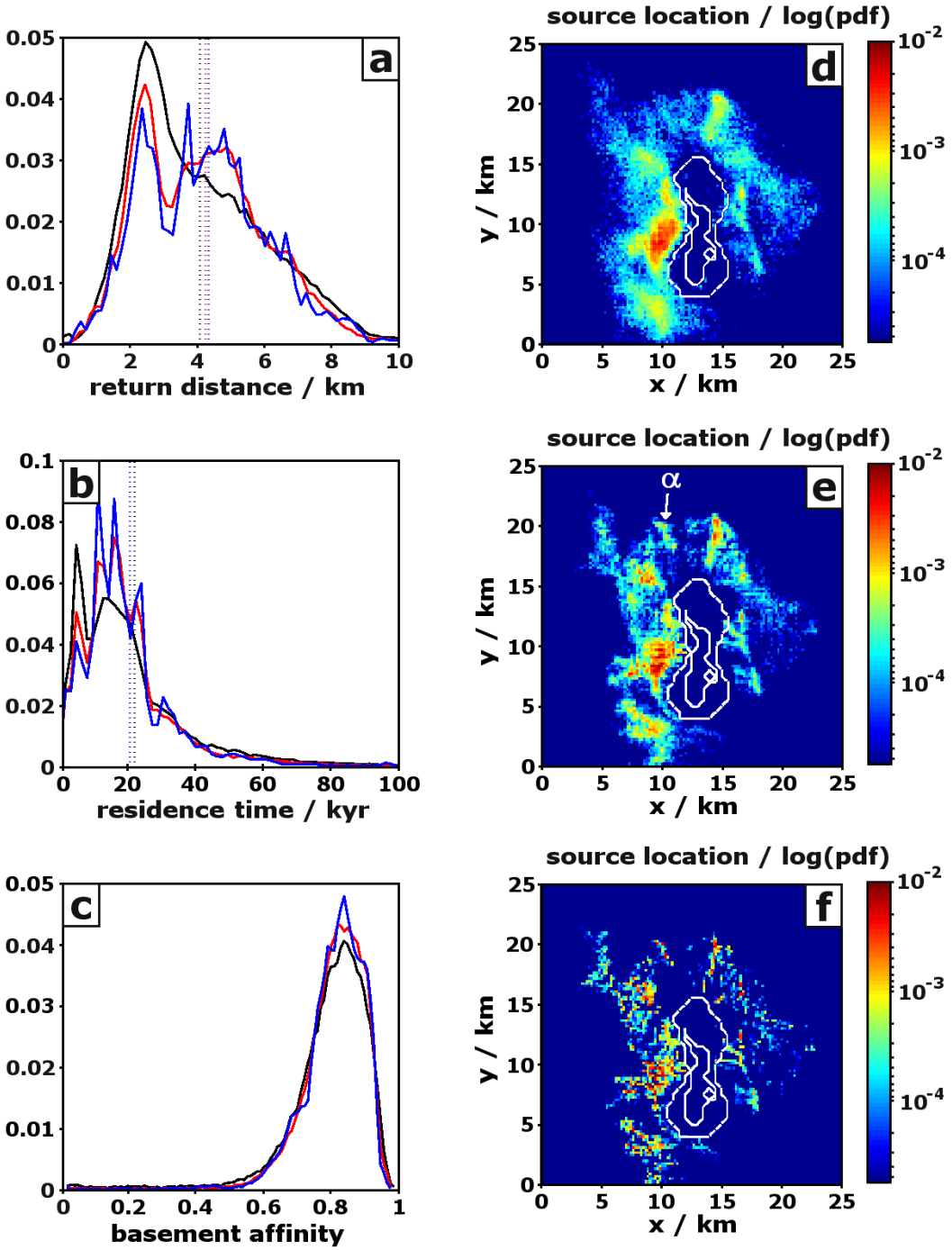

Figure 6.9: Effect of dispersion on particle tracking. (a) Return distance relative frequency histograms for particle tracking with full dispersion (black), dispersion reduced to 10% (red), and no dispersion (blue). (b) Residence time relative frequency histograms. (c) Basement affinity relative frequency histograms. (d) Probability density function of particle source location for full, (e) reduced, and (f) no dispersion. The feature labelled α in (e) is referred to in the text.

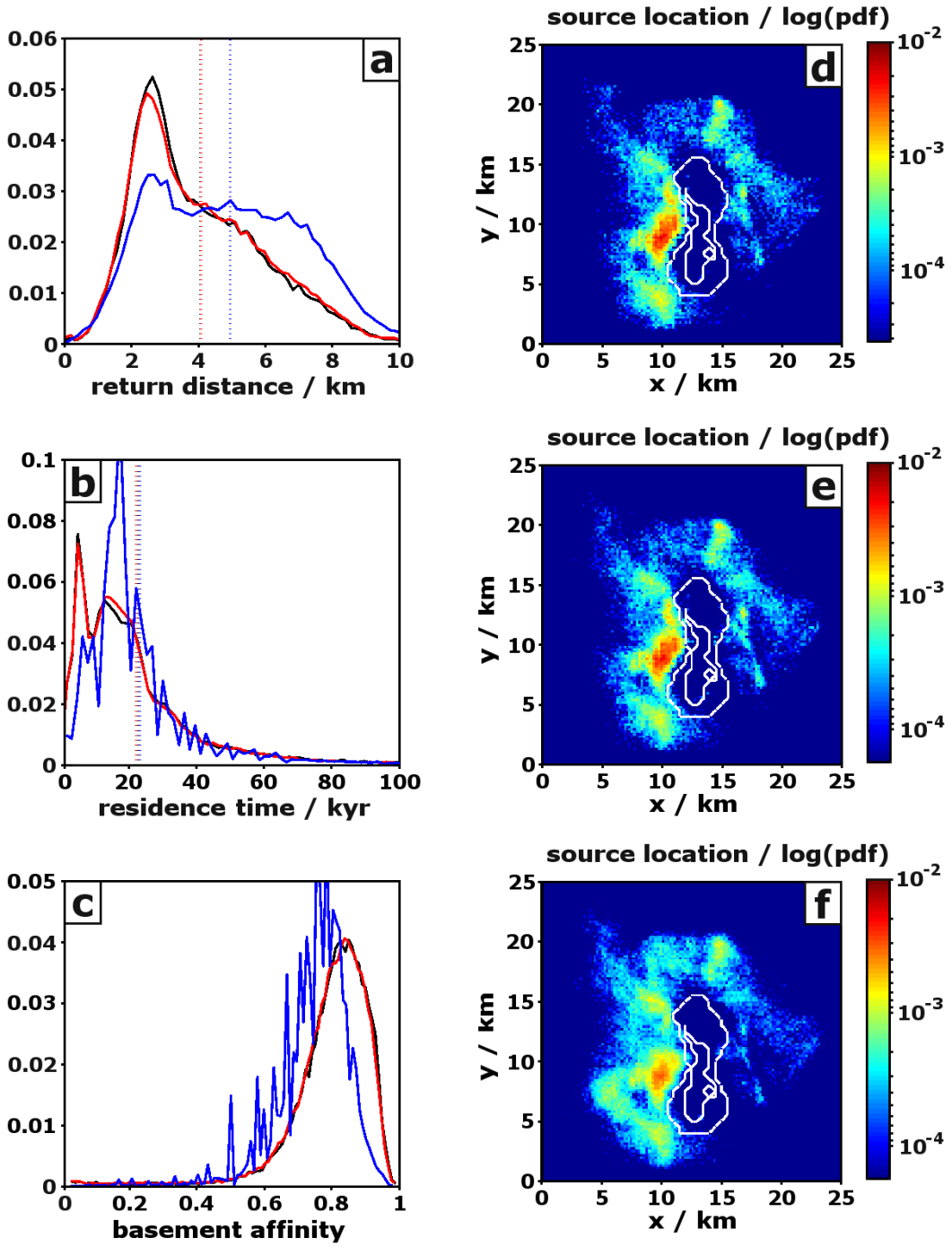

Figure 6.10: Effect of time step size on particle tracking. (a) Return distance relative frequency histograms for particle tracking with time step size of 6.3 (black), 31.7 (red), 793 years (blue). (b) Residence time relative frequency histograms. (c) Basement affinity relative frequency histograms. (d) Probability density function of particle source location for time step size of (d) 6.3, (e) 31.7, and (f) 793 years.

into a region it would have otherwise avoided if a shorter time step were used.

Figure 6.10 shows relative frequency histograms and source location PDFs associated with particle tracking at time steps five times shorter (6.3 years) and twenty-five times longer (793 years) than those used in Figures 6.7 and 6.9. Increasing the time step across the range considered here has only a minor effect on the shape and average properties of the relative frequency histograms, although a degree of spikiness is introduced into the residence time histogram due to the reduced temporal resolution. Paradoxically, increasing the time step results in smoothing of the source location PDF; this occurs because the spatial resolution of the flow-path, given approximately by $|\mathbf{v}|\Delta t$, begins to approach and exceed the spatial resolution of permeability structures imaged by the PDF, whose size is parameterised by the model mesh dimension, i.e., $\sim$500 m.

Smoothing of the source location PDF artificially increases the catchment area of the geothermal field by biasing the return distance histogram to higher values (Figure 6.10(a)). For example, for the three time step sizes shown in Figure 6.10, 6.3, 30.7 and 793 years, the corresponding catchments sizes are 171, 176 and 187 km^2. Catchment sizes for the ten modelled geothermal fields shown in Table 6.1 were calculated for particle tracking using a time step of 30.7 years and thus are likely to overestimate the true catchment size.

These results demonstrate a classic trade-off in numerical methods: that greater accuracy is obtained for smaller time steps at the cost of increased computational run-time. In such cases, there is no correct parameter value. However, it has been demonstrated that further improvements to ensemble properties (Figure 6.10) and catchment delineation are small; a nominal time step of 30.7 years is used for the rest of this chapter.

6.6 Rift-scale particle tracking

Recharge characteristics for the set of ten modelled geothermal fields are shown in Figure 6.11 and are colour-coded for each specific field. Relative frequency histograms

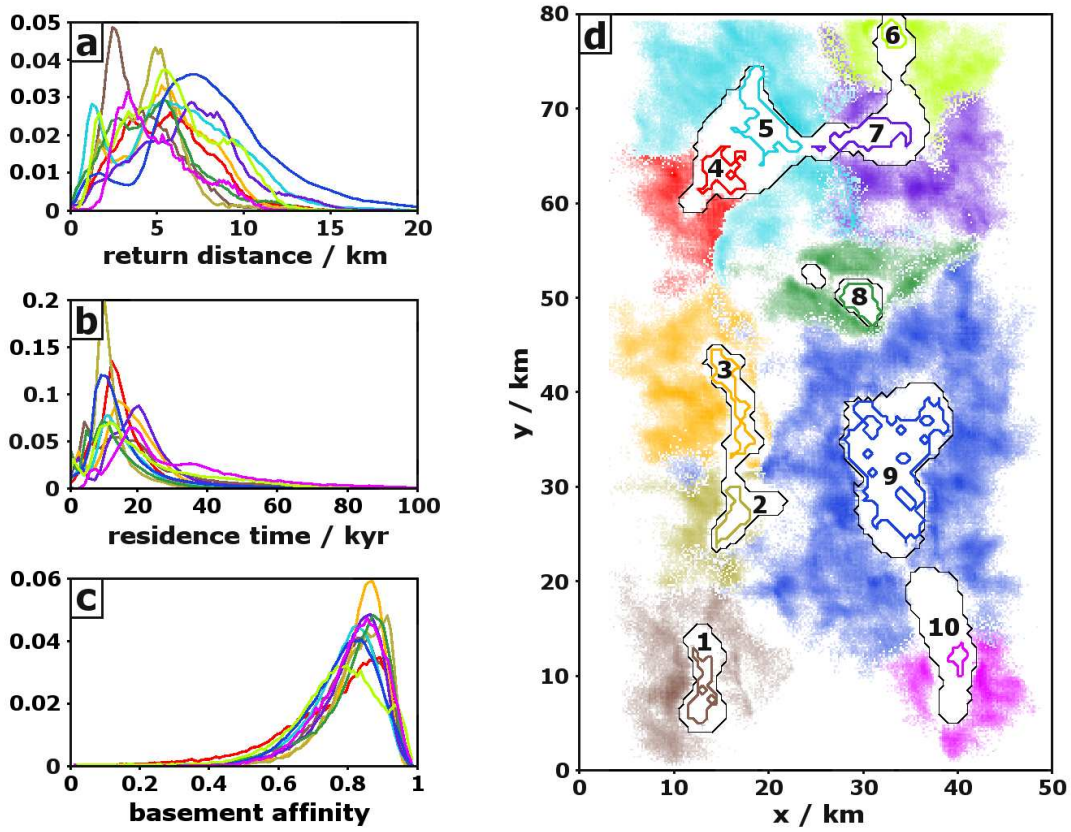

Figure 6.11: Recharge statistics for the ten modelled geothermal fields. (a) Return distance, (b) residence time, and (c) basement affinity relative frequency histograms. (d) Particle source locations and geothermal field boundaries delineated by $2\,\mathrm{W\,m^{-2}}$ vertical heat flux contour. Each field outline, its corresponding particle source cloud and profiles in (a-c) are associated with a distinct colour. Colour intensity in (d) is proportional to the probability density for particle source at that location. The black line delineates the $0.1\,\mathrm{W\,m^{-2}}$ vertical heat flux contour.

for the ten fields have similar shapes but peak at different average residence times and distances. For instance, return distances for the largest field, 9, are higher than the others, indicating that this field draws recharge over a greater area. Similarly, the peak in residence time for field 2 is lower than any of the other fields, which is consistent with this field having the lowest residence time (12.1 kyr).

Spatially, each geothermal field draws recharge from a region 10-15 km distant from its field boundary and, like field 1 (Figure 6.7(d)), these regions are not evenly

distributed around the field. For example, field 5 draws recharge from two separate zones, a larger one above and a smaller one below the field boundary; catchments for fields 2 and 3 occur almost exclusively to the left of the field; recharge of field 4 is limited to a 90° wedge to the bottom left of the field; and catchments for fields 8 and 10 appear to have been 'pushed' away (upward and downward, respectively) by the large catchment for field 9. Indeed, the catchment for field 9 is so extensive, fluids are drawn from the other side of the rift, between the catchments for fields 2 and 3. Recharge zones are also largely mutually exclusive, with only a small degree of overlap observed between the catchments for fields 5 and 7, and 6 and 7. The conspicuous gap near the centre of the lower boundary in Figure 6.11(d) is partially filled by the catchment of a small upflow zone that, due to its low output, was not included in the study.

6.6.1 Residence times

Particle source location and residence time data for the ten modelled fields are collated and presented in Figure 6.12. These fields show similar heterogeneity in terms of recharge location to that noted for field 1 (Figure 6.7(d)); again, this is attributed to both the abutment of catchments for neighbouring fields and the heterogeneity prescribed to the crustal permeability structure. Higher values of the PDF in Figure 6.12(a) represent the more significant regions supplying mass recharge to the geothermal fields; these are the first regions included in the construction of threshold recharge catchments (see Section 6.5.1 and Figure 6.8).

The distribution of residence time, contoured at fluid source and exit location, also suggests considerable heterogeneity in the age of recharging fluids. The majority of fluids are between 5 and 30 kyr old; however, localised infiltration zones are observed where fluids take much longer (> 50 kyr) to reach the field. As a general rule, younger fluids are sourced close to the field, with those less than 5 kyr old derived almost exclusively from within 1-2 km of the field boundary.

Fluids exiting within a field are generally less than 20 kyr in age; this is consistent with residence time estimates derived by Giggenbach *et al.* (1994) from isotopic

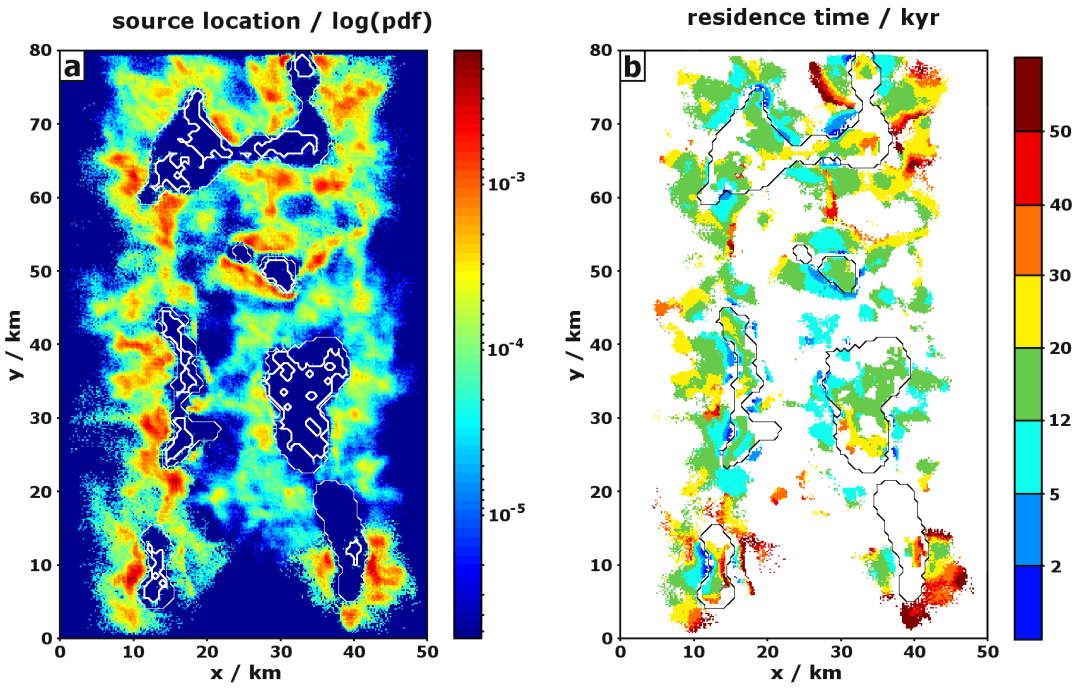

Figure 6.12: (a) Superimposed probability density functions for particle source location for each of the ten fields in the modelled rift. The 0.1 and 2 W m^{-2} vertical heat flux contours are marked by thin and thick white lines, respectively. (b) Mean residence time at particle source and exit (see Figure 6.7(e)) for the modelled geothermal fields. The 0.1 W m^{-2} vertical heat flux contours is marked by a black line.

analysis of fluids at Waiotapu geothermal field. It is, however, higher than the upper limit placed by Stewart (1978) of 12 kyr for deep fluids at Wairakei. Fluid age is not constant with position within a given field; for example, field 1 shows that fluids increase in age with proximity to the right hand boundary, while fluids within field 9 get older near the bottom of the field. Indeed, the spatial variation in fluid age at field 9 bears some resemblance to that determined by Giggenbach *et al.* (1994) at Waiotapu, specifically, 2 kyr in the north of the field, 18 kyr in the middle sections, and 11-280 kyr in the south. This in-field variety in age suggests a similar variety in the out-of-field source location and may also have implications for the variability in geochemical composition within a field. It is evidently misleading to treat geothermal fluids from a given field as a single, mixed product.

Tuning residence times

The average age of fluids exiting within a geothermal field is sensitive to the average porosity and permeability distributions of the crust through which those fluids flow. Thus, where residence time data is available for a specific geothermal field, distributions of these material parameters can be calibrated to an extent by the age data. For example, mean residence times for the modelled geothermal fields range between 10 and 30 kyr, which is consistent with geochemical age data at Waiotapu (Giggenbach *et al.*, 1994) but not at Wairakei (Stewart, 1978). This section briefly considers steps that might be taken to calibrate the model against the younger, Wairakei age data.

The time taken for a particle to complete a single flow-path depends on the particle velocity, v. Particle velocity is related to the Darcy velocity, v_D, via the porosity, ϕ, and v_D is itself dependent on the permeability, k. Thus residence time is sensitive to both permeability, which modulates the speed of the fluid flow, and the porosity, which determines the time spent 'in residence' within a given pore space before moving on. In the models presented here, k and ϕ are related (see Section 5.5.2) and therefore cannot be tuned independently of one another to produce the desired residence time (i.e., < 12 kyr). Adjusting one variable also changes the other with the effect on residence time dependent on the nature of the relationship between k and ϕ.

Residence time, t_r, is inversely proportional to particle velocity, v, and is therefore directly proportional to ϕ and inversely proportional to k (see Equation (5.1)), i.e., $t_r \propto \phi/k$. In the upper 2 km of the model domain, permeability is presumed to be dominated by connected pore space (Zhang *et al.*, 1994) such that $k \propto \phi^3$, while beneath this permeability is fracture dominated (Leary and Al-Kindy, 2002) and $\phi \propto \log(k)$. Eliminating ϕ, these relationships can be written

$$t_r(k) \propto \begin{cases} k^{-\frac{2}{3}} & z > -2\,\text{km}, \\ \frac{1}{k}e^k & z < -2\,\text{km}. \end{cases} \tag{6.3}$$

Differentiating t_r with respect to k yields a set of relationships that can be used to ascertain the effect of tuning permeability on residence time

$$\frac{dt_r}{dk} \propto \begin{cases} -\frac{2}{3}k^{-\frac{5}{3}} & z > -2\,\text{km}, \\ \frac{1}{k}e^k\left(1-\frac{1}{k}\right) & z < -2\,\text{km}. \end{cases} \tag{6.4}$$

As permeability is always positive but also very much less than one for the systems considered here (i.e., $0 < k << 1$), Equation (6.4) indicates that dt_r/dk is negative in the upper 2 km of the model and positive below. If the objective is to lower field residence times, this would be achieved by either reducing permeability in the greywacke subdomain ($z < -2\,\text{km}$) or increasing it in the near-surface volcanic layer ($z > -2\,\text{km}$). Figure 6.11(c) shows that particles spend the greater proportion of their time in the former subdomain and therefore a reduction in the greywacke permeability would likely render the greatest improvement.

6.6.2 Catchment area

For the ten fields modelled here, a positive correlation is observed between catchment size, and the geothermal field area and heat output (Figure 6.13). Assuming that the heat content of a geothermal field is dominated by the "heat-sweep" component (as opposed to magmatic fluid sources), larger catchments enable greater volumes of water to mine heat from wider areas of the mid-crust. The dimensions of the upflow zone, a proxy for field area, must also increase if a greater throughput of fluid is to be accommodated for fixed permeability conditions.

Ferguson and Grasby (2011), comparing hot-spring temperature data against local basin geometry for ten locations in North America, suggest that, instead, the magnitude of hydrothermal anomalies may be controlled by the aspect ratio of the flow system, i.e., its depth divided by its length. For high aspect systems, flow is primarily horizontal and little convective scavenging occurs. However, their data consider a range of aspect ratios - 1:100-1:2 - much greater than those presented here (1:1.7-1:0.65); as such, a broad trend of lower thermal output for increased aspect ratio is not expected to manifest in the results of this chapter.

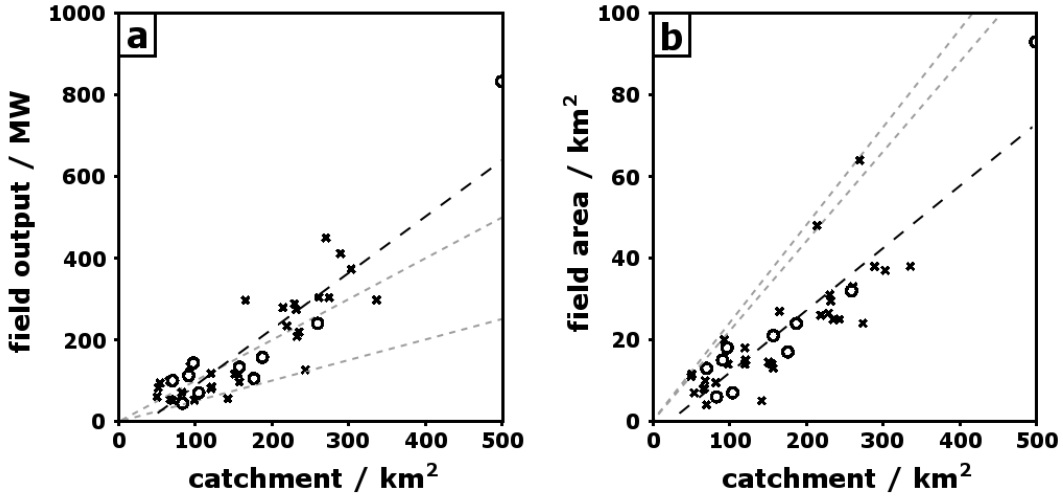

Figure 6.13: (a) Field heat output and (b) field area versus catchment size. Circles indicate data in the specific rift simulation presented here; crosses are for geothermal fields from four other large-scale models with different permeability and basal temperature realisations. Dashed lines indicate lines of best fit and have gradients of (a) 1.38 MW km^{-2} and (b) 0.15, respectively. Grey dotted lines show linear relationships derived by Weir (2009) using model parameters (see Equation (6.5))

Weir (2009), in consideration of simplified one-dimensional geothermal fields, derived linear relationships between their size, output and catchment area, i.e.,

$$Q = \rho_d h_u v_d C, \qquad A = \frac{\rho_d v_d}{\rho_u |v_u|} C, \tag{6.5}$$

where Q is field output, ρ_d and ρ_u are fluid density in the down-flow and upflow zones, respectively, h_u is fluid enthalpy in the upflow zone, v_d and v_u are fluid velocities in the down-flow and upflow zones, respectively, A is field area, and C is catchment size. Choosing representative values from the model of $\rho_d = 1000\,\mathrm{kg\,m^{-3}}$, $\rho_u = 850$-$900\,\mathrm{kg\,m^{-3}}$, $h_u = 0.5$-$1 \times 10^6\,\mathrm{J\,kg^{-1}}$, $v_d = 1 \times 10^{-9}\,\mathrm{m\,s^{-1}}$, and $v_u = 5 \times 10^{-9}\,\mathrm{m\,s^{-1}}$, the relationships in (6.5) can be written as $Q = c_1 C$ and $A = c_2 C$, where $c_1 = 0.5$-$1\,\mathrm{MW\,km^{-2}}$ and $c_2 = 0.22$-0.24. These linear relationships are juxtaposed on the catchment data in Figure 6.13 and show that the 1-D analytical representation is in order-of-magnitude agreement with the 3-D numerical model.

6.7 Voronoi delineation of catchments

Visual inspection of the catchment zones in Figure 6.11(d) suggests that, to first order: (i) the catchment for a given field occupies the area immediately adjacent to that field; and (ii) larger catchments tend to displace smaller catchments. Such a distribution of distinct regions is indicative of Voronoi tessellation; a geometric construction that divides an area into discrete compartments based on proximity to a number of nodes. Here, the area to be divided is the surface of the computational domain and the nodes are the geothermal fields. Voronoi diagrams find application in a wide variety of mathematical (e.g., Delaunay triangulation, file searching (Aurenhammer, 1991)), physical (e.g., crystal growth (Kobayashi and Sugihara, 2002; Dempsey *et al.*, 2010); soap bubbles (Williams, 1968)) and biological systems (e.g., spider's webs (Aurenhammer, 1991); cellular structure (Marcelpoil and Usson, 1992)). Voronoi diagrams are constructed by a crystal growth method, in which each of the nodes represents a small crystal and the set of nodal crystals simultaneously grow outward until either the domain is filled or they are surrounded on all sides by other crystals. The partitioning of the domain that results is the Voronoi diagram.

As an alternative method for delineating catchment zones, a Voronoi diagram is constructed using the outlines of the modelled fields as the nodes; the distribution of catchments thus generated is compared to those produced by the particle tracking method (Figure 6.11(d)). As noted previously, larger catchments appear to displace smaller ones; this suggests a specific subset of Voronoi diagrams, termed the Apollonious model (Aurenhammer, 1991), may be of use. These diagrams are generated by considering non-equal growth rates for each of the seed crystals; here, larger geothermal fields are weighted with faster growth rates. The Voronoi diagram is generated iteratively by attaching new pixels to an existing region that represents the partially-grown field catchment. The number of pixels added at each iteration depends on the heat output of the geothermal field (the growth rate modifier), thus ensuring that the catchments of larger fields grow faster than smaller ones. A pixel is available for incorporation into a catchment providing it is: (i) not already included

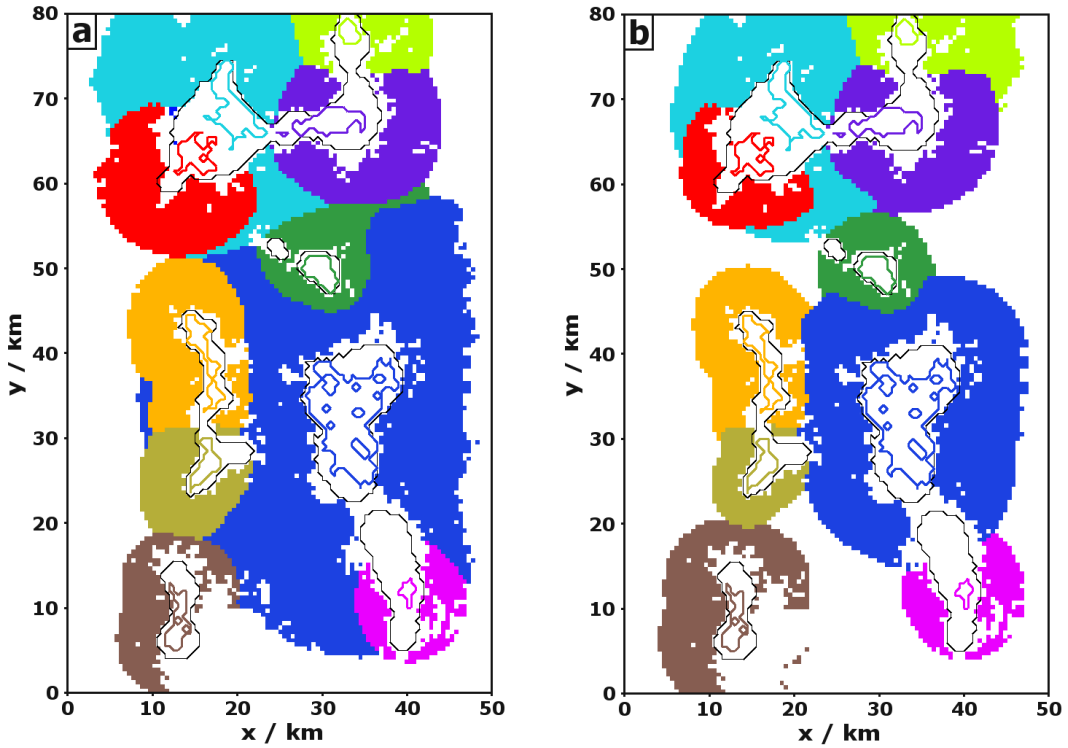

Figure 6.14: Field catchments constructed from Voronoi tessellation halted after (a) an arbitrary growth period, and (b) after each catchment has grown to an area related to the size of its heat output (see Section 6.6.2 and Figure 6.13(a)).

in some other field's catchment; and (ii) outside the $0.1\,\mathrm{W\,m^{-2}}$ vertical heat flux contour, which appears to be a constraint on the catchments in Figure 6.11(d). This method is a two-dimensional implementation of the Voronoi dynamics method used by Kawano and Ohashi (2006) and Dempsey *et al.* (2010) to describe the growth of an ensemble of sea ice crystals in two and three dimensions.

Figure 6.14 shows two catchment distributions delineated by the Voronoi method: in the first (Fig. 6.14(a)), iterative growth is stopped when the catchments qualitatively resemble those given in Fig. 6.11(d); in the second (Fig. 6.14(b)), growth of each catchment stops when its area is equal to that given in Table 6.1. Comparison between the unconstrained catchments (Fig. 6.14(a)) and those delineated by particle tracking indicate that the Voronoi method is only first-order accurate; it does not account for specific permeability structure and dispersive effects that produce

the heterogeneity in Figure 6.14(d). Nevertheless, several features of the Voronoi catchments bear a striking resemblance to their particle tracking counterparts, including: an asymmetric bias for recharge from the left hand sides of fields 1, 2 and 3; dominant catchments for fields 5 and 9 that appear to displace their neighbours; an isolated sub-catchment of field 9 on the other side of fields 2 and 3; and a narrow catchment corridor for field 8 appearing between the catchments for fields 7 and 9.

Area-constrained Voronoi catchments, while slightly smaller than their unconstrained counterparts, also represent a reasonable, first-order approximation to those in Figure 6.11(d). In particular, the field 9 catchment is improved in that it no longer abuts those of fields 1 and 10 below it; however, the small sub-catchment to the left of fields 2 and 3 is lost, and its shared boundary with the field 8 catchment is much less extensive. The size and shape of the other catchments are mostly preserved. The addition of area constraints on catchment size removes the heuristic element of catchment delineation used to construct those in Figure 6.14(a).

6.7.1 TVZ catchments

Unlike the flow-path ensemble method, generation of Voronoi catchments does not require specific knowledge of the 3-D crustal velocity field; catchments are instead constructed from geothermal field positions and heat outputs. The method can therefore be applied to the TVZ and other large-scale convective systems providing both these quantities are sufficiently constrained. Heat outputs for TVZ geothermal systems have been collated by Bibby *et al.* (1995), although a large standard error of $\pm 50\%$ is associated with most of the calculated values. Nevertheless, these heat outputs serve as a starting point for constructing Voronoi catchments following the outlined method. The heat outputs are also used, in conjunction with the catchment area - heat output relationship established in Figure 6.13(a), to calculate constrained catchment areas (see Figure 6.14(b)). For this purpose, TVZ heat outputs have been scaled such that the total TVZ heat transfer is equal to the total model heat transfer; this preserves the relative size of the geothermal fields to one another, while preventing the construction of unrealistically large catchments. The outputs

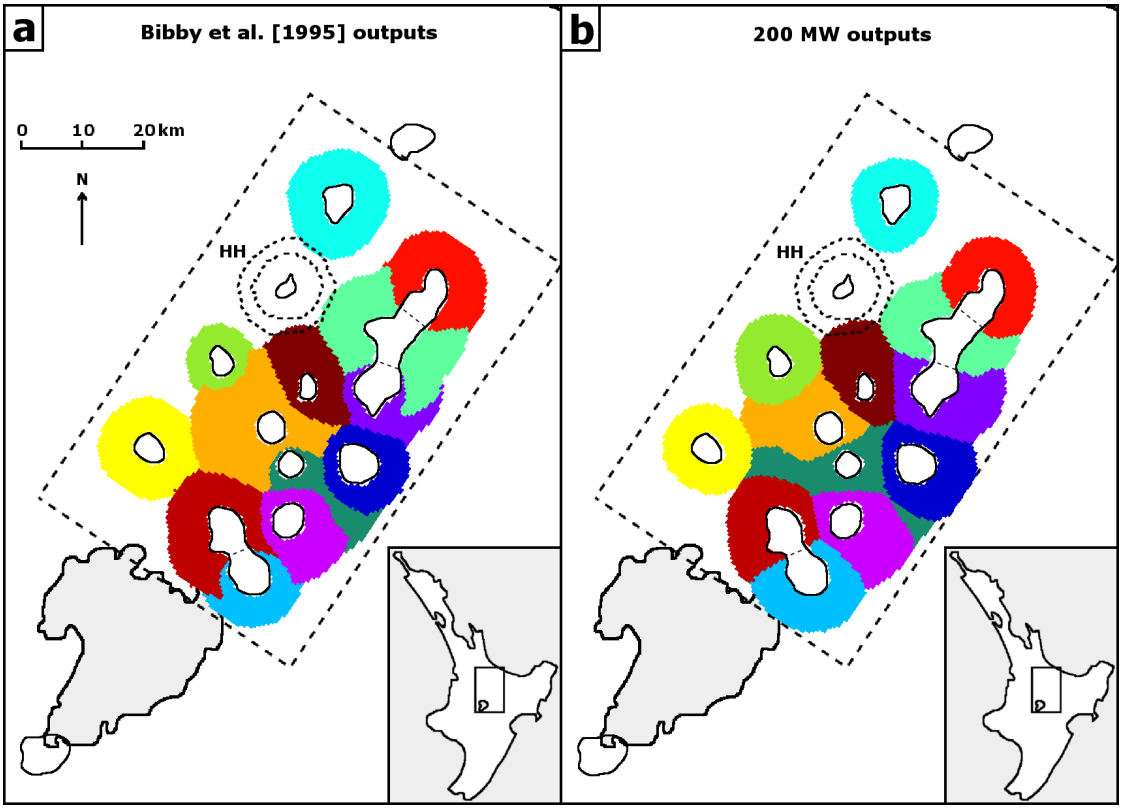

Figure 6.15: (a) Proposed catchment zones for TVZ geothermal fields based on Voronoi tessellation and using scaled field heat outputs from Bibby *et al.* (1995) and catchment areas based on Figure 6.13(a). The Horohoro geothermal prospect is labelled HH and catchment boundaries associated with 100 and 400 MW resources are delineated. (b) Field catchments using a homogeneous field output of 200 MW.

of Atiamuri and Reporoa have been artificially increased to a minimum of 50 MW to avoid the production of negligibly small catchments for these fields. As a final caveat, it is noted that this analysis does not account for the effects of topography on subsurface flow and rainfall distribution, which may play an important role in mass recharge of geothermal systems.

Figure 6.15(a) shows Voronoi catchments generated for the scaled geothermal field outputs given by Bibby *et al.* (1995) (see Figure 6.2). The majority of fields have catchments that abut those of neighbouring fields, with only the northern Rotorua field isolated from the rest (although it may abut the Rotoiti catchment to the northeast, which has not been included). Many of the fields have asymmetric catch-

ments, e.g., Orakeikorako draws the majority of its fluids from the west, Te Kopia from the north, Tauhara and Rotokawa from the south, etc. Recharge zones for Rotorua, Mokai and Ohaaki have approximately circular shapes and are largely unaffected by neighbouring fields. In contrast, there is considerable distortion of catchments for the Waiotapu-Waimangu-Reporoa, Orakeikorako-Te Kopia-Ngatamariki and Wairakei-Tauhara neighbouring sets.

Figure 6.15(b) shows similar Voronoi catchments constructed under the assumption that all fields have equal heat output. Both the modelling results reported here (Table 6.1), as well as analytic heat and mass transfer arguments (Weir, 2009) suggest geothermal fields should manifest less variability than that reported in Bibby *et al.* (1995). Under these circumstances, Figure 6.15(b) represents an end-member catchment distribution, with the true distribution probably lying somewhere between Figs. 6.15(a) and (b).

The absence of a geothermal field and associated catchment from an empty region bounded by the Rotorua, Waiotapu, Te Kopia and Atiamuri catchments, is an intriguing feature of Figure 6.15. In practice, this region is approximately centred on the Horohoro geothermal prospect: a small thermal area and region of anomalously high conductivity into which a single cold well was drilled in 1986 (Bibby *et al.*, 2005). Heat output from the thermal area is an estimated 4 MW (Allis, 1987) and thus too small to account for the catchment absence in the region. No gap of equivalent dimension is observed in Figure 6.11(d); the entire rifting section of the modelled crust plays host to either the recharge or upflow component of the large-scale convective system. However, an opening of a similar size could be created if the catchment of, for example, field 3 were omitted. Extending this reasoning to the gap noted in Figure 6.15 suggests that this section of the crust does not participate in the large-scale convective system, perhaps due to relative impermeability of the rocks here. Alternatively, the potential geothermal resource at Horohoro may have been underestimated; the opening is large enough to accommodate a recharge zone for a field up to 400 MW in size without significant disturbance of neighbouring catchments. However, this interpretation is not without difficulties, as it is progressively

harder to mask the presence of larger resources.

6.7.2 Iceland catchments

At least twenty high temperature geothermal systems are found in Iceland, distributed throughout its central active volcanic belt (Arnórsson, 1995). Like the TVZ, geothermal convection is ultimately driven by rifting and the intrusion of magma into the crust (e.g., Flóvenz and Sæmundsson, 1993), although the depths of the convective systems are perhaps slightly shallower, with a seismically-delineated BDT in the Reykjanes Peninsula of 6-7 km (Fridleifsson and Elders, 2005). Heat outputs of individual fields range from several tens of megawatts up to 710 and 1265 for the Hengill and Torfajökull systems, respectively (Ketilsson *et al.*, 2009).

The procedure for constructing Voronoi catchments for Iceland geothermal fields is the same as that followed in constructing TVZ catchments. Ketilsson *et al.* (2009) list heat outputs for many of the fields; where unknown, a nominal value of 100 MW is assigned. A catchment area for each field is constructed using the heat output - catchment area relation in Figure 6.13(a); discrepancy between this relationship and one derived for a slightly shallower convective system is expected to be minor. As specific field areas constrained by resistivity contours were unavailable, each field was assigned a circular area of 25 km^2 serving as the seed of its catchment. Catchments are then grown iteratively following the method outlined in the previous section (Figure 6.16).

In contrast to TVZ catchments (Figure 6.15), the majority of geothermal fields in Iceland are spaced sufficiently far away from one another that no abutment of their catchments is observed. For these fields, catchments are circular. Geothermal fields in the Reykjanes Peninsula are spaced closer together. Here, catchment shapes are influenced by the presence of neighbouring fields, particularly the Reykjanes-Eldvörp-Svartsengi and Sandfell-Krýsuvík-Trölladyngja triplets. For example, Trölladyngja is predicted to draw the majority of its recharge from the north, Sandfell from the west, and Krýsuvík from the south and east.

Catchments of several Icelandic systems on the Reykjanes Peninsula extend into

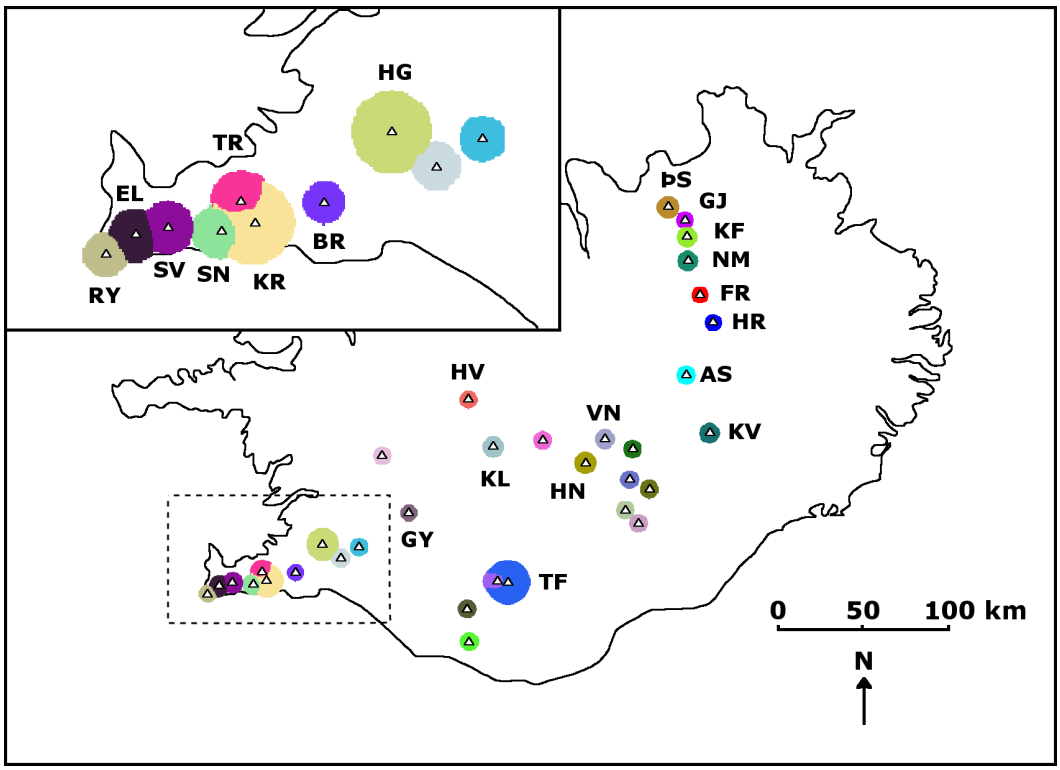

Figure 6.16: Proposed catchment zones for high temperature geothermal systems in Iceland constructed from Voronoi tessellation. Inset shows close up of catchments in the Reykjanes Peninsula. RY = Reykjanes (45), EL = Eldvörp, SV = Svartsengi (150), SN = Sandfell, KR = Krýsuvík (445), TR = Trölladyngja, HG = Hengill (710), BR = Brennisteinsfjöll (25), GY = Geysir (25), KL = Kerlingarfjöll (195), HV = Hveravellir (70), TF = Torfajökull (1265), HN = Hágöngur (215), VN = Vonarskarð (145), KV = Kverkfjöll (155), AS = Askja (135), HR = Hrúthálsar (20), FR = Fremrinámar (50), NM = Námafjall (155), KF = Krafla (155), GJ = Gjástykki (55), ÞS = Þeistareykir (240). Field heat outputs in MW (from Ketilsson *et al.*, 2009) are given in brackets. For unknown, unlabelled systems, a nominal output of 100 MW has been used.

the ocean, which is consistent with the contribution of seawater to geothermal fluids at Reykjanes, Svartsengi and Krýsuvík (Arnórsson, 1995). For these systems, the chloride concentration of geothermal reservoir waters assumes the same role as deuterium concentration in TVZ systems, i.e., an indicator of the source from which mass recharge is drawn. In contrast to deuterium, which gives an indication of source latitude - higher values are found for systems further to the north - chloride in the Reykjanes Peninsula is predominantly derived from seawater intrusion.

Increased chloride concentration in the geothermal waters then indicates that mass recharge is drawn from regions nearer the ocean. Chloride concentration data compiled by Arnórsson and Gunnlaugsson (1985) and Arnórsson (1995) are consistent with catchment locations shown in Figure 6.16. For example, the highest concentrations are attained for Svarksengi (13,507 ppm) and Reykjanes (19,648 ppm), whose catchments overlap the ocean. Mid-level chloride concentrations occur at the Tröll-adyngja system (1000 ppm), which is also situated on the Reykjanes Peninsula but whose modelled catchment does not extend into the ocean. Further inland, chloride concentrations are very much lower (50-100 ppm), reflecting the absence of a marine contribution to mass recharge.

6.8 Evolution over geological time

An assessment on the stability of TVZ geothermal fields can be made based on their age and ability to endure volcanic activity. Minimum age estimates range from 500 kyr for Wairakei, 400 kyr for Ngatamariki (Arehart *et al.*, 1997), 200 kyr for Kawerau (Browne, 1979), and 120 kyr for Te Kopia (Bignall and Browne, 1994), indicating these features are stable on timescales of several 100 kyr. Both Wairakei and Waimangu geothermal fields appear to have maintained activity during recent volcanism, albeit with significant changes to surficial features for the latter (e.g., Simmons *et al.*, 1993). Furthermore, geothermal activity at Te Kopia has apparently occurred concurrently with frequent seismic episodes on the Paeroa Fault (Bignall and Browne, 1994).

In the previous section, geothermal circulation was described for a given point in time, i.e., after 500 kyr of simulation time. The modelled across-strike heat flow distribution (Figure 6.2(d)) and individual field characteristics (Figure 6.2) at this time are consistent with their TVZ counterparts, suggesting the model is, to some approximation, a representation of a hypothetical TVZ. However, during the 300 kyr of simulation time preceding the circulation state presented in Figure 6.2, significant movement in the positions of the geothermal fields occurs. This is in spite of

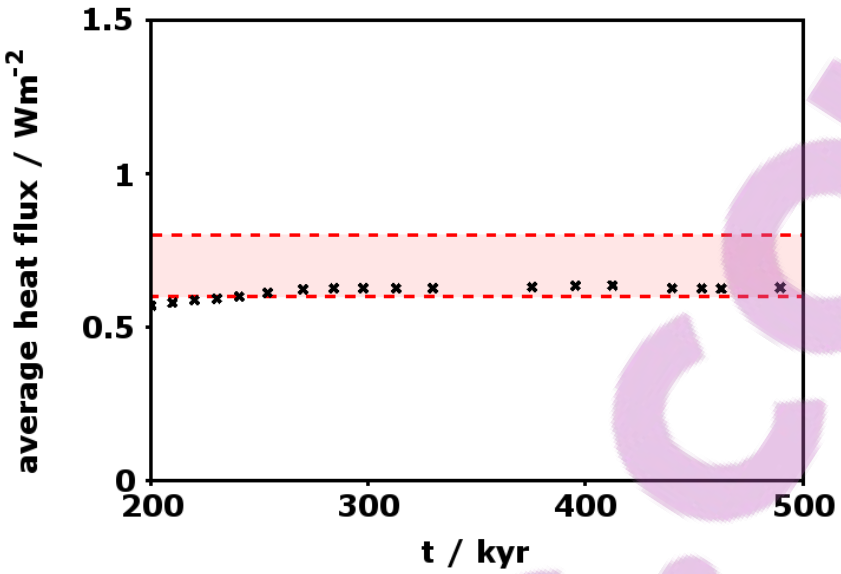

Figure 6.17: Heat flux through the rift ($5 < x < 45$ km) averaged over a depth interval of 1 to 6 km. The target interval from Hochstein (1995) is shaded red.

an approximately steady average heat output of the rift (Figure 6.17), and static permeability properties and temperature boundary conditions (Figure 6.1).

Figure 6.18 plots the evolving positions of geothermal fields at the surface of the model using the vertical axis to represent simulation time. Field boundaries are delineated in the horizontal plane by the $2\,\mathrm{W\,m^{-2}}$ vertical heat flux contour for that time step. For a field that does not change position in time, subsequent contours plot immediately above one another and an isosurface plotted through these yields a vertical column. Several of these column-like structures are identified in Figure 6.18 (marked 1a-1b) and represent field stability over periods of 100-300 kyr.

In contrast to the relative stability of fields 9 and 10, other fields exhibit a degree of transience, manifesting as a horizontal component of the isosurface. For example, several instances (Figure 6.18, 2a-2b) are observed in which two fields migrate towards one another at rates of 1-3 km per 100 kyr and combine to form a single larger field. Similar migratory behaviour in the positions of convection cells was observed by McLellan *et al.* (2010) in their model of large-scale TVZ convective sys-

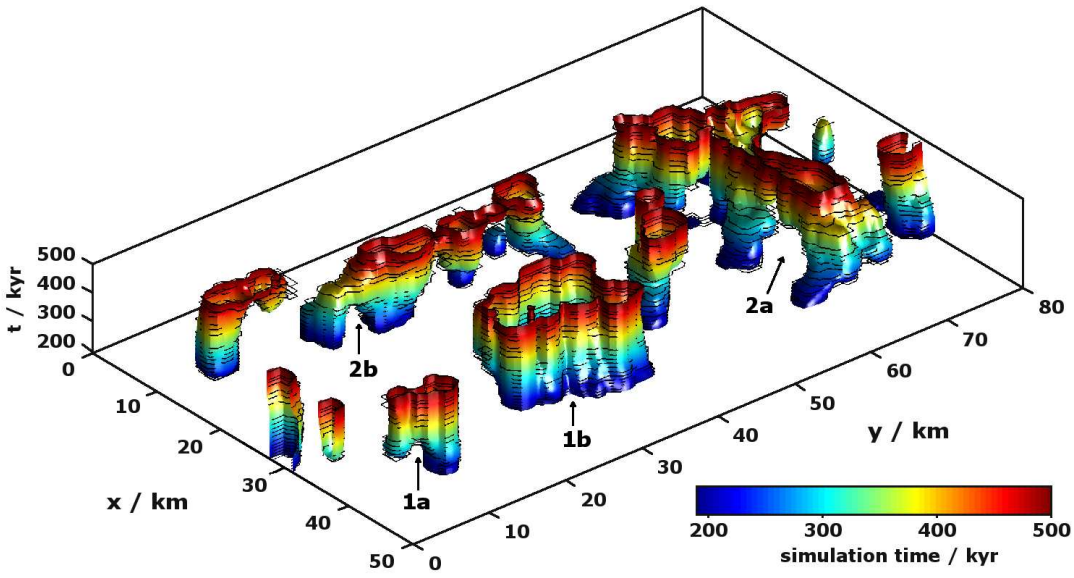

Figure 6.18: Evolution of field positions and dimensions over 300 kyr of simulation time. Isosurfaces contour 2 W m^{-2} vertical heat flux over 19 simulation time steps (vertical axis). Black contours indicate raw data from which surfaces are interpolated. Field positions in Figure 6.2(b) correspond to the top level of the figure. Labels 1a-1b, and 2a-2b are referred to in the text.

tems. Unstable convection is a consequence of high permeability and heat flow, and, although the eventual establishment of a stable circulation pattern cannot be ruled out, this prospect is largely irrelevant. The results indicate that, even in the absence of dynamic permeability and basal thermal regimes (i.e., time-varying magmatism), a degree of instability (on geological time-scales) is an inherent property of the convective system. The existence of a steady circulation state is largely meaningless if it cannot be achieved on a reasonable time-frame, i.e., before tectonic or magmatic processes perturb the system and alter the steady-state to be obtained.

Migration in the position of geothermal fields has implications for patterns of hydrothermal alteration at the surface. Figure 6.19 plots the time since hydrothermal circulation has been hosted at the surface of the model, and therefore shows the final distribution of geothermal fields (red) in the context of previous circulation. This plot shows that for many fields upflow has previously occurred outside their present

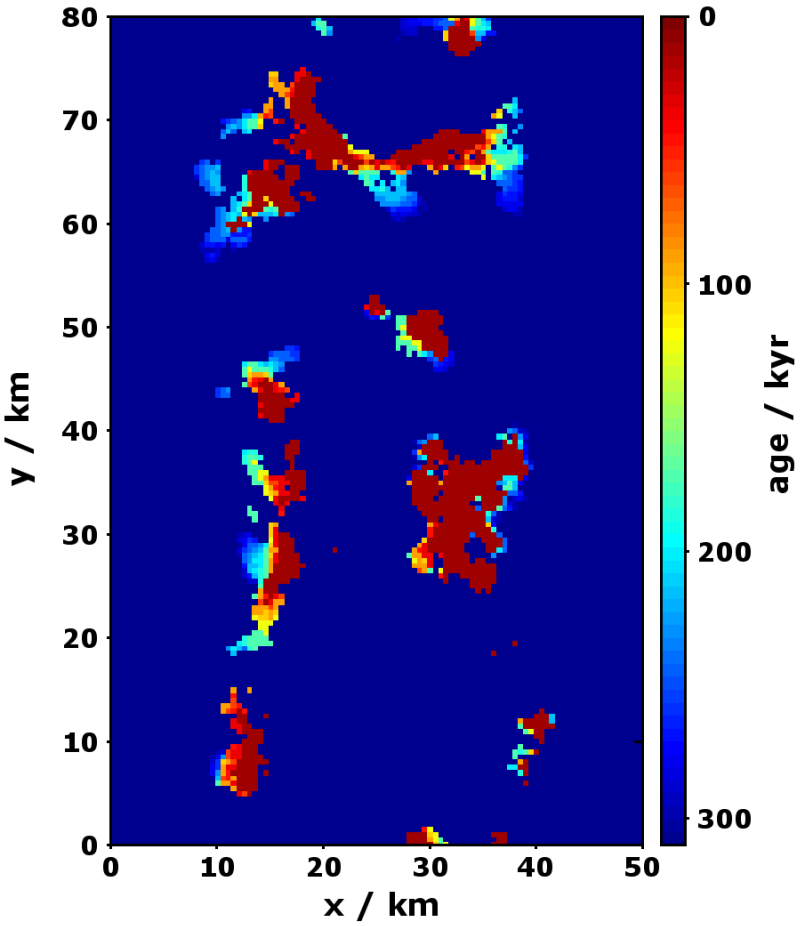

Figure 6.19: Age of geothermal circulation at the surface.

boundary. However, over geological time scales the region influenced by a given field, i.e., the region of past and present activity, is limited in extent. Within the TVZ, regions of previous hydrothermal circulation are frequently inferred from alteration of the rock and its subsequent effect on resistivity (Risk *et al.*, 1994). Figure 6.19 is then partially analogous to a resistivity map, albeit one that documents the age, rather than extent, of alteration. It further suggests that field boundaries demarcated by resistivity contours (past and present circulation), do not necessarily correspond to field boundaries constrained by heat flux.

Figure 6.19 also shows large areas of the rift ($5 < x < 45\,\mathrm{km}$) have remained free from geothermal activity for the entire length of the simulation. In particular,

a narrow corridor along the line $x = 20\,\text{km}$ (for $y < 60\,\text{km}$), corresponding to the central minimum in Figure 6.2(d), operates to limited degree as a recharge zone for geothermal upflow in field 9 (Figure 6.11(d)). This region corresponds to the Taupo Fault Belt (see Section 1.3.1), both in position and partially in function. Previous circulation models (Kissling and Weir, 2005) have invoked the TFB as a region of elevated structural permeability and demonstrated a preference for down-flow in this region. However, in the model presented here, no special permeability conditions are required to keep this region free of hydrothermal activity. Rather, down-flow occurs preferentially along the central axis as a consequence of the wider circulation system that is evolved in response to a specific realisation of the heterogeneous permeability distribution and thermal boundary conditions.

6.9 Chapter summary

A 3-dimensional numerical model of a rift-scale convective system approximating circulation in a "TVZ-like" setting has been presented. Circulation is modelled to a depth of 8 km, with convection driven by a two-temperature hot plate boundary condition imposed at the lower boundary. Permeability distributions are assigned to two subdomains, surface volcanic and basement greywacke, and spatially correlated heterogeneity is superimposed upon their average properties. A large-scale convective system comprising ten separate geothermal systems is evolved after a period of 500 kyr; this circulation state represents a statistical analogue of the TVZ.

Advective particle back-tracking with a random walk component that accounts for the effects of dispersion and diffusion has been used to investigate sources of mass recharge for the modelled geothermal fields. For each field, several 10's of thousands of flow-paths were constructed, enabling a statistical representation of residence time, return distance and their spatial variation both within and outside a given field. Flow-path ensembles for the ten modelled fields indicate that recharge is drawn from a region up to 10 km distant from the field boundary, with average residence times ranging from 12-30 kyr. The age of fluids exiting within a field also

varies significantly with position, which probably reflects different source locations and may be associated with intra-field variety in geochemical composition.

Mass recharge for each field is drawn from minimally overlapping catchment zones that range in size from 70 to 500 km^2 and are asymmetrically distributed about a given field's boundary. The size of the catchment zone is linearly related to both the area and heat output of a geothermal field, consistent with 1-D analytical results given in Weir (2009). It has been shown that Voronoi polygons seeded at the locations of the modelled geothermal fields, with growth rates and areas proportional to heat output, provide a reasonable approximation to the distribution of catchment zones derived from particle tracking. As a description of the subsurface flow field is not required, Voronoi catchments are simpler to construct than their flow-path counterparts; the technique has been used to establish approximate catchments for TVZ and Iceland geothermal systems.

For the TVZ, catchments are closely spaced and distributed asymmetrically about their parent fields. An empty region, apparently devoid of geothermal activity or mass recharge, is observed between Rotorua and Te Kopia geothermal fields; crustal permeability in this region may be low enough to exclude its participation in the large-scale convective system. Alternatively, an underestimated Horohoro prospect may account for the discrepancy. Catchments for the Iceland geothermal systems are spaced much further apart than in the TVZ, and show little interaction except for those on the Reyjkanes Peninsula. Catchment extension into the ocean for several of these fields is consistent with the appearance of seawater in these geothermal systems (Arnórsson, 1995).

The stationarity of geothermal fields in time has been investigated for a period of 300 kyr. Over this time moderate migrations of up to 5 km in the position of some upflow zones are observed. The model also exhibits convergence of two fields into one larger field. This non-stationarity on geological time-scales has implications for steady-state modelling of such systems, as well as relic alteration patterns such behaviour should imprint on the crust. For instance, cessation of activity at Ohakuri geothermal system in the TVZ may have been caused by magmatic or plumbing

changes at depth, but may also simply represent northwest migration of activity to the nearby Atiamuri field (Henneberger and Browne, 1988).

Having considered natural variability in geothermal systems in static permeability and basal temperature regimes, the focus is now shifted to investigate several processes that perturb natural geothermal circulation on geological time-scales ($> 100\,\mathrm{kyr}$). In the next chapter, a model is discussed in which mass fluxes and temperature gradients directly alter the permeability distribution through the deposition of silica into open pore space. In this formulation, geothermal fields display self-sealing behaviour, forming a low-permeability cap-zone at the surface, which results in a continuously changing flow regime. The formation of a surface cap-zone has important implications for the distribution of geothermal expression at the surface, as well as the thermal structure of the reservoir beneath.

In Chapter 8, long- and short-term effects of geothermal circulation due to the presence of an active dip-slip fault are considered. Over long time-periods, the fluid baffling properties of the fault cause hot upflow to localise along the fault plane, with the locus of surface expression occurring in the footwall scarp of the fault. This circulation state is then perturbed by a pore-pressure anomaly caused by coseismic crustal stress changes (which are derived from the mechanical model; see Chapter 2) and an increase in cross-fault permeability and hydraulic communication. The result is increased heat and mass transfer rates at the surface that decay over a period of several weeks, and a steady migration in surface geothermal expression from the footwall scarp into the hanging wall.

Top five elements in the Earth's crust by abundance: **O (46%)**, **Si (27%)**, *Al (8%), Fe (6%), Ca (4%).*

7

Silica deposition in geothermal systems

As geothermal fluids pass through fractures and open pore spaces, they interact chemically with the rock. These interactions alter both the chemical composition of the fluid, as well as the strength and permeability of the rock through which it flows. This chapter considers the operation of one such process, equilibrium silica deposition, over geological timescales, with particular focus on the negative feedback it exerts on permeability and fluid flow. A gradient reaction regime is assumed (Phillips, 1979) such that silica deposition in volume terms can be formulated as a function of mass flux and temperature gradient. A relationship between porosity and permeability (Section 5.5.2) links modification of these two properties, and a series of simulations are performed in which the permeability distribution is updated at the conclusion of each sub-simulation.

Silica deposition occurs most rapidly at the surface of the model where the highest temperature gradients and mass flux rates are encountered. This results in the formation, and growth, of a circular, low permeability cap-region above the central upflow zone. The cap-zone deflects rising fluids laterally to the plume margin and insulates the reservoir beneath from the cool atmosphere. Over time the cap-region is cooled by the atmosphere, which, when combined with the deflection of upflow, masks the field to a degree. Furthermore, the rate of silica deposition in a crust

with heterogeneous permeability, rather than being correlated to regions of high permeability, is controlled by the angle between the temperature gradient and mass flux.

Work presented in this chapter is drawn from a paper submitted to Journal of Geophysical Research in February 2012 and published in May 2012 (Dempsey *et al.*, 2012e). Results and text included in this chapter are largely unchanged from the published version as permitted by the University of Auckland under the *2008 Statute and Guidelines for the Degree of Doctor of Philosophy (PhD)*. Co-authors of this work Dr Julie Rowland, Dr George Zyvoloski and Dr Rosalind Archer advised and commented on the manuscript, however the bulk of the research and preparation for publication was undertaken by the thesis author (see accompanying declaration).

7.1 Introduction

Precipitation of SiO_2 as quartz into fractures and open pore spaces plays an important role in the development of veining (e.g., Sharp, 1960; Fisher and Brantley, 1992; Bons, 2001), cementation (e.g., Robinson and Gluyas, 1992; Walderhaug, 1994) and epithermal mineralisation (White and Hedenquist, 1990; Simmons and Browne, 2000). It also reduces the intrinsic permeability of rock, retarding its ability to conduct fluid and thereby exercising a negative feedback on the precipitation rate (Andre and Rajaram, 2005). Such processes have previously been considered in numerical models for the evolution of limestone karst systems (e.g., Andre and Rajaram, 2005; Chaudhuri *et al.*, 2009), and fracture apertures and networks (e.g., Chaudhuri *et al.*, 2008). Chaudhuri *et al.* (2012) modelled silica deposition in a gradient reaction regime and demonstrated rapid decrease in the transmissivity of a fracture network as the mean fracture aperture is reduced toward a critical value.

Precipitation of silica within a fracture or pore space occurs when a reduction in fluid temperature causes silica solubility to drop below the local concentration of dissolved silica. The manner in which the precipitation or dissolution reactions

proceed depends on reaction rate and fluid velocity (Phillips, 1979). For slow reaction rates and high fluid velocities, disequilibrium of mineralising chemical species may be widespread, and the reaction regime is classified as kinetic. Any numerical modelling must account for chemical transport and the relevant reaction kinetics (e.g., O'Brien *et al.*, 2003; Szymczak and Ladd, 2004). Where disequilibrium is minimised, silica concentration can be assumed equal to the local solubility. This occurs at lower fluid velocities, where there is sufficient time for reactions to adjust mineral concentrations to their equilibrium values. Such conditions define a gradient reaction regime, in which the reaction rate is proportional to the gradient in mineral solubility, which in turn depends on some controlling parameter, e.g., temperature. Modelling the latter regime requires less computational resources (e.g., Chaudhuri *et al.*, 2008, 2012), although does not account for the effects of boiling in the near-surface (Cline *et al.*, 1992).

This chapter details a numerical model that considers the heat and mass transfer of a single geothermal field with dimensions and heat characteristics similar to those of the Taupo Volcanic Zone (TVZ), New Zealand. The TVZ is a productive volcanic arc that hosts convective upflow of high temperature fluids ($> 250°C$) at more than twenty distinct locations (Bibby *et al.*, 1995). Geothermal circulation is thought to be driven by extensive magmatic intrusion in the lower and mid-crust, which supplies heat to the upper-crust at a depth of 6-8 km (Bryan *et al.*, 1999). This depth is commonly interpreted as the brittle-ductile transition and delineates the lower limit of the convective system (Bibby *et al.*, 1995). Fluid circulation is assisted by an abundance of normal fault structures, accommodating 5-15 $\mathrm{mm\,yr^{-1}}$ of tectonic extension (Wallace *et al.*, 2004), and which are presumed (Grindley and Browne, 1976) to make a significant contribution to the fracture permeability of basement rocks. Permeable pathways in the near-surface ($<$2 km depth) are supplied by connected pore space within high porosity, Quaternary volcanic deposits, disrupted by faulting and fracturing (Sibson, 1996; Rowland and Sibson, 2004).

The abundance of quartz silicification reported within the TVZ (Simmons and

Browne, 2000; Wood *et al.*, 2001; Arehart *et al.*, 2002; Bignall *et al.*, 2004; Rowland and Sibson, 2004; Hocking *et al.*, 2010) attests to the importance of hydrothermal alteration in geothermal fields. Alteration can be broadly divided into two styles (Simmons and Browne, 2000): replacement, in which precursor solid rock is converted to the alteration mineral, and direct deposition of minerals into open pore spaces or veins. The latter process reduces permeability and retards fluid flow, but also imparts improved tensile strength to the mineral assemblage. Silicification therefore influences structural evolution in the near-surface of geothermal fields by encouraging fluid overpressuring, hydrofracturing and the reactivation of existing structures (Grindley and Browne, 1976; Henneberger and Browne, 1988; Sibson, 1990). Such petrophysical changes are evident at the extinct Ohakuri geothermal system, where discrete quartz veins intersect a wider region of adularia (Henneberger and Browne, 1988). This implies distributed flow through unaltered porous deposits progressing to intermittent fracturing, perhaps modulated by overpressurisation, and mineralisation.

The aim of the numerical models presented here is to investigate the feedback effects that silica deposition exercises on circulation and subsequent permeability modification. The formation of a low permeability cap-zone at the surface of a geothermal field and its implications for surficial expression and subsurface flow are detailed. Results are discussed in the context of the Ohakuri and Te Kopia geothermal fields of the TVZ, both of which exhibit variety in the intensity and spatial extent of hydrothermal alteration. Te Kopia geothermal field is situated near the southern termination of the Paeroa Fault, which bounds the eastern margin of the Taupo Fault Belt. Geothermal expression on the Paeroa Fault also presents at the Waikite hotsprings in the north and at Orakeikorako geothermal field where the fault splays at its southern termination. Geothermal activity correlates with surface or inferred basement faulting elsewhere in the TVZ (e.g., Wood, 1992; Wood *et al.*, 2001), presumably operating in regions of episodically renewed permeability (e.g., Rojstaczer *et al.*, 1995; Sibson, 1990; Micklethwaite and Cox, 2004). A fault-rupture

scenario involving perturbation of a well-developed, low porosity cap-zone is considered; subsequent permeability sealing at the enhanced mass flow rates accompanying the renewed permeability is investigated.

7.2 Numerical model

Numerical modelling of crustal-scale geothermal circulation is carried out using the Finite Element Heat and Mass transfer (FEHM) code (Zyvoloski, 2007). FEHM solves conservation of mass and energy equations for Darcy flow through a porous medium and has previously been used to model convection by Stauffer *et al.* (1997). A computational domain is selected that is $15 \times 15 \times 8$ km along the x, y and z directions, which is regarded as sufficient to capture the central geothermal upflow zone and surrounding regions of recharge. Four meshes are used to partition the computational domain for the various models: mesh 1, shown in Figure 7.1(a), is a uniformly spaced grid with a node spacing of 200 m in each direction; mesh 2, shown in Figure 7.1(b), is a structured grid with a higher density of nodes in the central upflow zone and near the surface; mesh 3, shown in Figure 7.1(c), is the same as mesh 2 but double the resolution, i.e., half the nodal spacing; and mesh 4, shown in Figure 7.1(d-f), is a structured grid with the highest resolution at the near-surface and within a central fault plane. Mesh 3 is used for the majority of simulations while meshes 1 and 2 are used to evaluate the extent to which mesh non-uniformity and coarseness affect model results. Mesh 4, which contains the high density of nodes along a central fault plane, is used for modelling fault rupture through an evolved impermeable cap-zone (see Section 7.5).

A Gaussian temperature distribution, with maximum value 340°C, is applied at the centre of the base of the model to ensure upflow localises in the centre of the domain (Figure 7.2(c)). The maximum temperature corresponds to the approximate brittle-ductile transition temperature for quartzofeldspathic rock and its depth is consistent with seismogenic depths of 6-8 km within the TVZ (Bryan *et al.*, 1999).

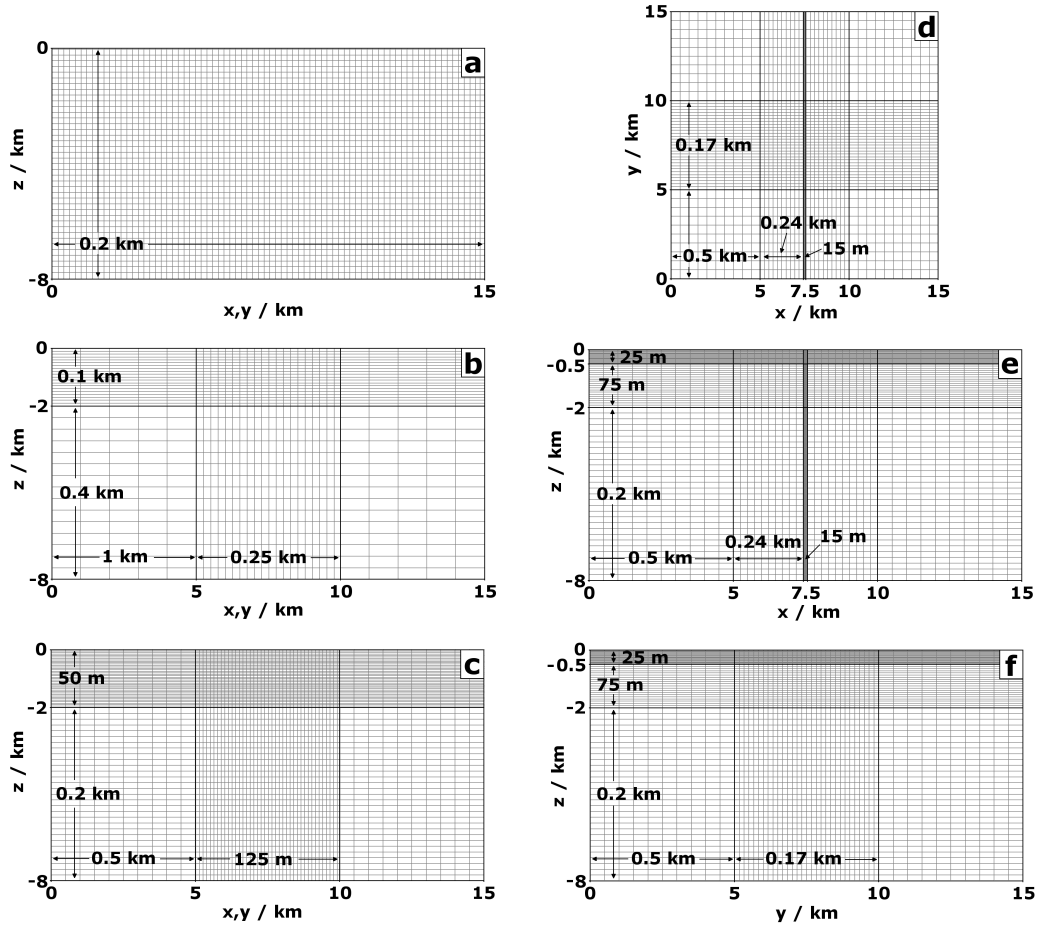

Figure 7.1: Model meshes used in simulations. (a) Mesh 1, uniform nodal spacing (200 m). (b) Mesh 2, coarse, higher resolution near the surface and centre of the domain. (c) Mesh 3, same as mesh 2 but half the nodal spacing. (d-f) Mesh 4, high resolution near-surface and centre of the domain. Highest resolution along a narrow fault plane centred at x=7.5 km. Arrows indicate extent over which each nodal spacing applies. Note that the unmarked fault width is 150 m and this has been partitioned into 10 slices.

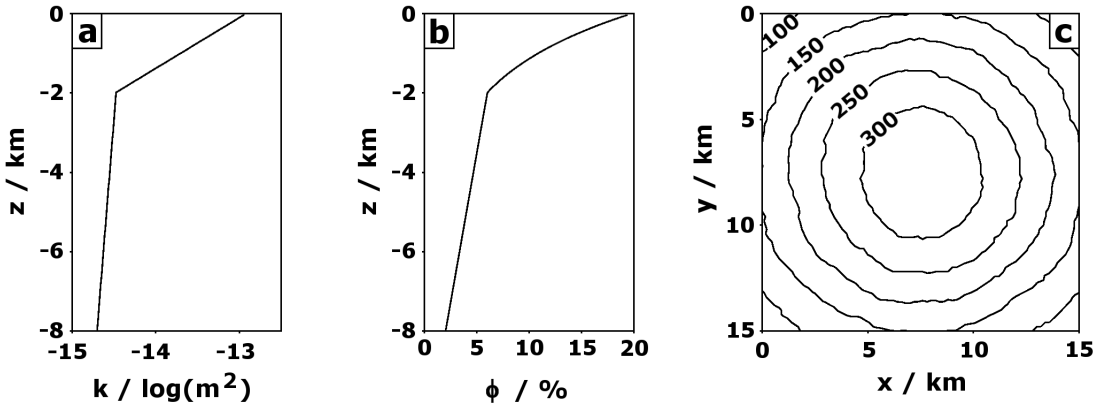

Figure 7.2: Imposed (a) permeability and (b) porosity properties with depth. (c) Temperature (°C) boundary condition imposed at the base of model.

No flow boundary conditions are maintained at the base and sides of the model and atmospheric temperature and pressure conditions are applied at the surface. Fixing temperature at the upper boundary precludes the formation of hot-springs, which are often modelled by setting the temperature gradient to zero (e.g., López and Smith, 1995; Zhang *et al.*, 2005). In these situations, the model over-estimates the temperature gradient and thus the rate of silica deposition.

Distributions of permeability and porosity exert an important control on the style and extent of silica deposition. Distributions modelled here are inferred from the geological structure of the TVZ, which is characterised by high porosity volcanic strata, overlying older, faulted meta-sedimentary greywacke. Frequent and voluminous volcanism within the TVZ (Wilson *et al.*, 1995) has evolved a 2 km thick layer of low density, moderately porous surficial strata. Horizontal fluid flow is assisted by a multitude of contacts between various deposits or rhyolitic intrusions. In contrast, vertical permeability is enhanced by extensive vertical and sub-vertical fracturing and faulting, which has evolved in response to high extensional strain rates (Wallace *et al.*, 2004). Deeper than 2 km, permeability of the largely homogeneous greywacke is probably controlled by fractures and faults, or possibly dike intrusion (Lewis, 1960;

Curewitz and Karson, 1998). Porosity at these depths is comparatively low and probably dependent upon fracture density. The effects of fracture closure and pore space compaction with increasing depth and confining pressure are approximated by an exponential reduction in permeability with depth (Saar and Manga, 2004). Bounding values for permeability and porosity used in the majority of simulations are shown in Figure 7.2(a-b).

The effects of spatial heterogeneity in the permeability and porosity distributions are investigated by overlaying a spatially correlated fluctuation field on these distributions. This perturbation to the homogeneous distribution approximates the effect of a random fracture distribution associated with a crust at criticality (Leary and Al-Kindy, 2002; Heffer, 2007).

Concentrations of dissolved ions, particularly salts that present in abundance, can affect the style and character of convection through modification of the fluid density. Denser fluids require a greater temperature perturbation to overcome ambient hydrostatic pressure conditions and initiate convective overturning. In mid-ocean ridge hydrothermal systems, this is an important consideration as parent fluids are oceanic in origin and approximately 3% salt by weight (e.g., Lewis and Lowell, 2009). For the TVZ systems considered here, chemical compositions vary widely (Giggenbach, 1995); however, maximum salt concentrations are on the order of 0.3% by weight, i.e., an order of magnitude less than sea water. Dissolved ion density effects are thus unlikely to represent a first order control on the systems under investigation and this effect is neglected.

7.2.1 Implementation of silica mineralisation

As a first approximation to the dynamics of silica deposition, it is assumed all fluids within the system are at their saturation point with respect to dissolved silica, i.e., the system can be described by a gradient reaction regime. In this regime, fluid transport is sufficiently slow that mineral concentrations are governed by temperature

dependent reactions. The equilibrium assumption will be disturbed in regions where rapid fluid flow is promoted, which may include high permeability conduits associated with fault rupture, or the drilling of geothermal production wells. Pressure drops associated with these high permeability conduits promote boiling and further silica deposition (Simmons and Browne, 2000). In regions where fluid transport outstrips the reaction rate, regions of fluid supersaturation will develop downstream. The silica deposition rate estimated under the gradient reaction assumption will then overestimate the true reaction rate.

The validity of the gradient reaction assumption can be assessed by consideration of silica-water reaction rates (Rimstidt and Barnes, 1980). Because silica concentration approaches equilibrium asymptotically, a useful parameter to consider is the time-constant, t_c. This parameterises how rapidly the system approaches equilibrium, with $5t_c$ corresponding to the time required to reach >99% of equilibrium concentration. The time constant varies with temperature and the available area for reactions to occur on. For a near-surface temperature of 150°C and representative interfacial areas of 1 to 100 (Rimstidt and Barnes, 1980), t_c is varies between one day and six months. For a maximum near-surface upflow velocity of $5 \times 10^{-7}\,\mathrm{m\,s^{-1}}$ (Figure 6.6), a range of disequilibrium distances of 0.02 to 8 m is calculated; this represents the distance the fluid has travelled during the equilibration time ($5t_c$). In general, this distance will be less than the model resolution, although at the very near-surface, as temperature drops and velocity increases, the modelled deposition rate may significantly over-estimate the true value.

The equilibrium assumption is further tested by plotting dissolved silica concentration versus temperature for TVZ geothermal reservoir fluids. These data do not include samples from surface geothermal features, e.g., hot-springs, where rapid cooling leads to silica super-saturation (i.e., the data plot to the left of the curves in Figure 7.3). It has previously been acknowledged that gradient reactions are unlikely to occur at the very near-surface.

The data in Figure 7.3 indicate that, in general, reservoir fluids are at, or near

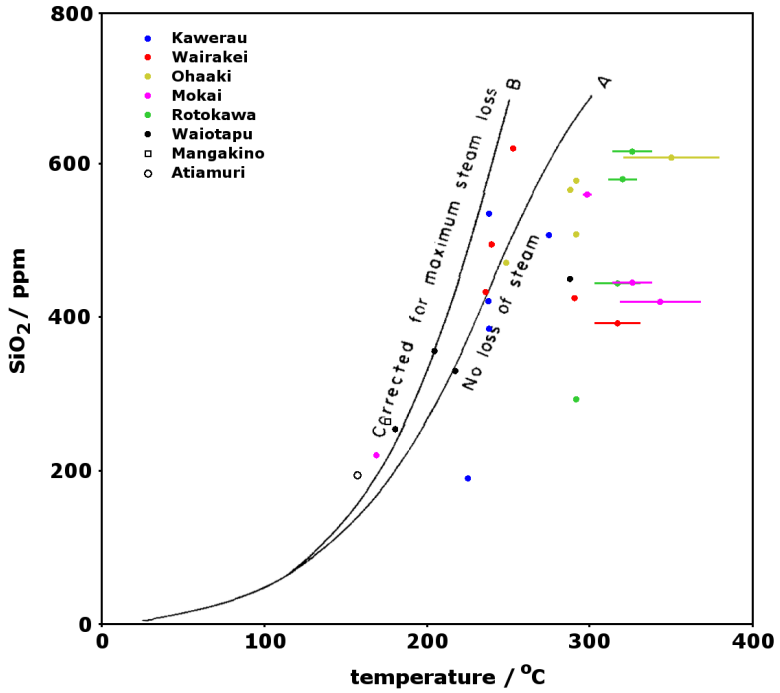

Figure 7.3: Dissolved silica concentration measured in wells for a selection of TVZ geothermal fields. Data are from Giggenbach *et al.* (1994) and Giggenbach (1995). Note: temperatures are calculated from enthalpy measurements with error bars reflecting uncertainty in sample depth. Saturation curves from Fournier (1977) are also shown.

---

to, the equilibrium silica concentration. Some fields tend to be under saturated, e.g., Rotokawa; for this system, it is unclear to what extent gradient reactions will occur. In contrast, geothermal waters at Kawerau, Wairakei and Waiotapu are relatively close to equilibrium (as are Atiamuri and Mangakino, although there is only one data point for each of these fields) and the gradient reaction assumption is likely to be more applicable for these systems.

Consistent with the gradient reaction assumption, a packet of fluid moving through a temperature gradient must either dissolve or precipitate silica to maintain an equilibrium concentration. The rate of deposition or dissolution at a particular location then depends principally on (i) the magnitude of the temperature gradient at that location, and (ii) the fluid throughput.

Consider a fluid flux, $\mathbf{M}$, through a volume element of dimensions, dx, dy and dz, porosity, ϕ, and temperature gradient, $\nabla T = dT/dz$. Fluids flowing perpendicular to the temperature gradient follow isotherms, and thus do not contribute to quartz dissolution or precipitation. Of interest is the amount of fluid flow parallel to the temperature gradient, i.e.,

$$\frac{1}{|\nabla T|}\mathbf{M} \cdot \nabla T. \tag{7.1}$$

Subsequent fluid references are to this component.

As fluid traverses the volume element, it changes temperature by some small increment, ΔT, and consequently, its silica solubility, m_q, changes by an amount

$$\Delta m_q = \frac{dm_q}{dT}\Delta T. \tag{7.2}$$

Silica solubility is defined as the maximum amount of dissolved silica, n_q, per mass of pure water and its functional dependence on temperature is described by Fournier and Potter (1982). For temperatures ranging from 25 and 900°C and specific volume, V, ranging from 1 to 10, silica solubility is given by

$$\log(m_q) = A + B\log(V) + C(\log(V))^2, \tag{7.3}$$

where the coefficients A, B and C are given in Table 7.1 as functions of temperature. The first derivative of silica solubility with respect to temperature is obtained from Equation (7.3).

As the volume element is oriented such that ∇T is directed along the z direction, the magnitude of the temperature change as the fluid traverses the cell is given by $|\nabla T|dz$. The mass of fluid transported (per unit time) is given by $\mathbf{M}\cdot\nabla T dxdy/|\nabla T|$, and thus an amount of silica is dissolved, or precipitated, at a rate given by

$$\dot{\Delta n_q} = \mathbf{M} \cdot \nabla T \frac{dm_q}{dT} dxdydz. \tag{7.4}$$

Table 7.1: Coefficients used in silica solubility Equation (7.3) as functions of temperature. From Fournier and Potter (1982)

Coefficient	Temperature dependence (K)
A	$-4.66206 + 0.0034063T + 2179.7T^{-1} - 1.1292 \times 10^{6}T^{-2} + 1.3543 \times 10^{8}T^{-3}$
B	$-0.0014180T - 806.97T^{-1}$
C	$3.9465 \times 10^{-4}T$

The volume of this precipitated or dissolved silica is used to calculate the change in porosity over some time period, τ, i.e.,

$$\Delta\phi = \int_{t_0}^{t_0+\tau} \mathbf{M}(t) \cdot \nabla T(t) \frac{dm_q}{dT} \frac{M_q^{mol}}{\rho_q} dt, \tag{7.5}$$

where M_q^{mol} is the molar mass and ρ_q is the density of quartz.

This formulation is implemented in FEHM through an iterative update of the porosity and permeability distributions. An initial simulation of 300 kyr of fluid circulation is performed to establish a benchmark circulation state. Geothermal circulation is then simulated for a nominal time period of 0.5-5 yr, within which temperature and mass flux distributions are output at ten evenly spaced time periods. For each time step, a porosity change, $d\phi_i$, is calculated using Equation (7.5), and porosity changes for the ten time steps summed to yield a total porosity change, $d\phi$, for the simulation.

A functional description of the relationship between k and ϕ is required to describe permeability evolution in response to silica deposition into open pore space. As discussed in Section 5.5.2, a cubic-law correlation between porosity and permeability is implemented for the upper 2 km, representing porous volcanic deposits; at depths greater than 2 km, i.e., the fractured greywacke basement, a log-law correlation is used. Equation (7.5) gives the change in porosity due to flow of silica saturated fluid through a volume element over a given time period. Equation (5.9) then relates the

change in porosity, $d\phi$, to a change in permeability, i.e.,

$$\begin{aligned} k &= A_1(\phi + d\phi)^3, \\ k &= 10^{(\phi + d\phi - B_2)/B_1}. \end{aligned} \tag{7.6}$$

In the upper layer of volcanics, a minimum achievable permeability of $10^{-16}\,\mathrm{m}^2$ ($0.1\,\mathrm{mD}$) is assigned, corresponding to a porosity of 2%. This is probably higher than the extensively silicified and sealed rock that would eventually be produced by a sufficient period of alteration. However, geothermal fields in the TVZ are juxtaposed on an extensional tectonic setting in which background fracturing and faulting enhance and maintain permeability. Furthermore, sealing of fluid pathways can lead to transient overpressures and subsequent hydraulic fracturing, which also places a lower limit on attainable permeability. This behaviour could be modelled in greater detail by the implementation of a coupled stress calculation that applied a permeability enhancement to regions where the pore-pressure increased above some failure criterion (e.g., Mohr-Coulomb yield). This has not been undertaken here.

At the conclusion of an FEHM simulation, an altered permeability distribution is calculated using Equations (7.5) and (7.6), and temperature and mass flux fields output during previous time steps. The following simulation uses the new permeability distribution and the final temperature and pressure values from the previous simulation. This iterative update scheme approximates the evolution of permeability, and thus geothermal flow, in response to simplified silica processes.

Under a gradient reaction regime, the extent of deposition or dissolution is critically dependent on the magnitude of the temperature gradient (see Equation (7.5)). Resolving these gradients on a discretised grid is therefore particularly important. First order differencing is used to approximate ∇T between adjacent nodes, e.g., $dT/dx \approx (T_{i+1} - T_i)/dx$. For coarse grid spacings, i.e., large dx, it is difficult to resolve very small and very large gradients. An improvement in accuracy is gained through the use of higher resolution grids in regions where large temperature gradi-

ents are expected.

Temperature profiles from drill holes at the Wairakei geothermal field, New Zealand, indicate that the largest vertical geothermal gradients (approximately 1-2 $\mathrm{K\,m^{-1}}$) are obtained within several hundred meters of the surface (O'Sullivan *et al.*, 2009). In this region, buoyant upflow, rising approximately adiabatically, come into contact with cooler meteoric waters, leading to the formation of a boundary layer. To capture thermal processes in this region, meshes with increased resolution (Figure 7.1) within 1-2 km of the surface are used. A similar boundary layer forms at the base of the crust where cold, recharging surface waters encounter the magmatic intrusions that supply the heat to drive geothermal convection. Mass flux in this boundary region is in the opposite direction to that at the top of the model and, consequently, quartz dissolution may play a significant role in permeability modification here. However, as the meshes used here are much coarser at the base of the model, this investigation is limited to near-surface processes.

7.3 Description of circulation

A single geothermal plume is evolved in the model domain by applying the basal temperature boundary condition for a period of 300 kyr (Figure 7.4). Initially, the model domain is a homogeneous 20°C and mass fluxes are everywhere zero. Fluids in the centre of the domain become buoyant and rise as they are heated. Convection occurs in systems where the Rayleigh number, Ra, exceeds a critical value ($\mathrm{Ra_{crit}} = 4\pi^2$). The Rayleigh number for a porous medium is given by Nield and Bejan (1998)

$$\mathrm{Ra} = \frac{\rho_f g \beta \Delta T L k}{\mu \alpha}, \tag{7.7}$$

where ρ_f is the density of the fluid, g is the acceleration due to gravity, β is the coefficient of thermal expansion of the fluid, ΔT is the temperature difference between the top and bottom of the system, L is the vertical dimension of the system,

k is permeability, μ is fluid viscosity and α is the coefficient of thermal diffusivity. For typical values of $\rho_f = 900\,\mathrm{kg\,m^{-3}}$, $g = 9.8\,\mathrm{m\,s^{-2}}$, $\beta = 10^{-3}\,\mathrm{K^{-1}}$, $\Delta T = 350°\mathrm{C}$, $L = 8\,\mathrm{km}$, $k = 10^{-14}\,\mathrm{m^2}$, $\mu = 3 \times 10^{-4}\mathrm{Pa\,s^{-1}}$ and $\alpha = 10^{-6}\,\mathrm{m^2\,s^{-1}}$, the Rayleigh number is ~ 800 and well-exceeds the threshold for free convection.

The upflow zone is situated at the centre of the model, i.e., $\{x, y\} = [7.5, 7.5]\,\mathrm{km}$, due to the Gaussian temperature boundary condition applied at the base of the model (Figure 7.2(c)). Constrained by the 200°C isotherm, the plume is approximately 5 km wide at the base and narrows as it approaches the surface, particularly within the high-porosity volcanic subdomain ($z > -2\,\mathrm{km}$). This is consistent with a decreasing permeability with depth, which requires a greater plume cross-section to host rising fluids (Bibby *et al.*, 1995). The maximum temperature at the surface of the model is approximately 200°C, which is somewhat cooler than fluids exiting from TVZ geothermal fields (≈250°C). Greater accuracy in modelling surface temperatures might be achieved through tighter controls on the permeability-depth relationship; however, for the deposition behaviour demonstrated here, these models serve as an acceptable approximation to reality.

Vectors of mass flux direction indicate mass recharge occurs at all depths along the plume. At significant distances from the upflow zone, cold down-welling fluids suppress the geothermal temperature gradient, such that temperatures as low as 100°C are encountered at depths of 6 km. This is consistent with the findings of Weir (2009) which also yielded cool temperatures for deep fluids. They show that the down-flow temperature profile depends on down-flow fluid velocity and thermal diffusivity. In these models, down-flow fluid velocities are consistent with rainfall recharge rates from the TVZ (Kissling, 2004).

The geothermal field boundary at the surface is constrained by a $1\,\mathrm{W\,m^{-2}}$ vertical heat flux contour. This value exceeds the average continental heat flux (0.05-$0.07\,\mathrm{W\,m^{-2}}$ from, e.g., Chapman, 1986) and the anomalously high heat flux of the TVZ (≈$0.8\,\mathrm{W\,m^{-2}}$ from Hochstein, 1995). Based on this demarcation, the geothermal field, prior to permeability modification, has a heat output of 120 MW and an

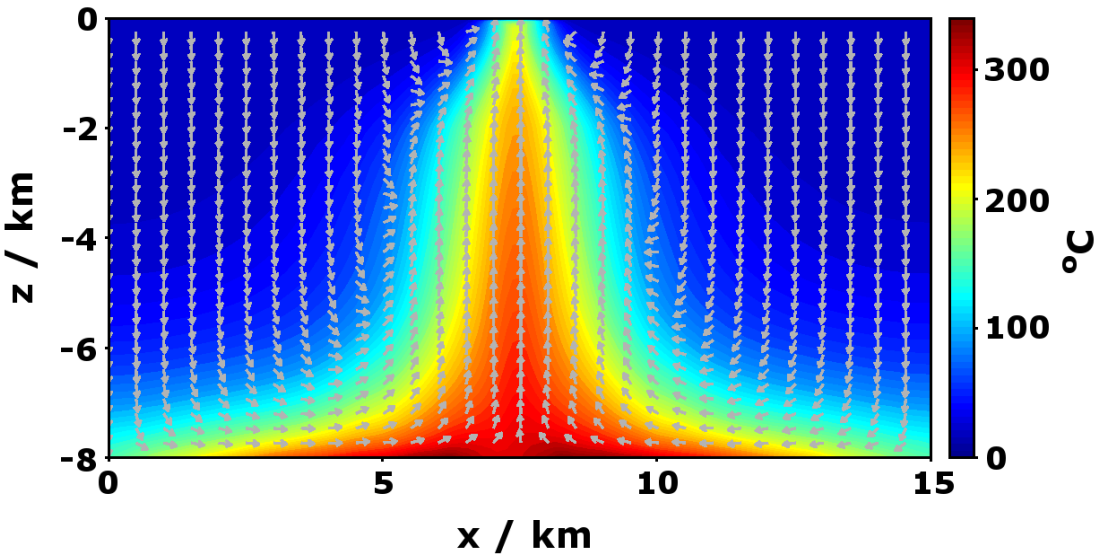

Figure 7.4: Temperature contours for a vertical slice through the centre of the upflow zone (y =7.5 km) after 300 kyr of simulation time (immediately prior to permeability modification). Vectors of mass flux direction have been superimposed. Note that mass flux magnitude is not represented by the arrow length.

area 1.4 km^2.

7.4 Model results

Both temperature gradients and mass flux attain their largest magnitude in the near-surface where contact with the atmosphere forms a thermal boundary layer and permeability is at its maximum value. Consequently, silica deposition and reduction of permeability proceeds most rapidly in the upper layers of the model. After 120 kyr of simulated alteration (t = 420 kyr) a region of low permeability has formed at the surface above the upflow zone (Figure 7.5). The geothermal field is demonstrating 'self-sealing' behaviour (e.g., Facca and Tonani, 1965; Dobson *et al.*, 2003), i.e., hydrothermal alteration of the surface strata has produced a low permeability cap-zone. Due to the symmetry of the model domain and permeability distribution, the cap-zone is circular with a diameter of 1-2 km. In profile, (Figure 7.5(a)) it increases

in thickness with proximity to the axis of upflow, attaining a maximum dimension of ∼200 m.

A smaller reduction in porosity and permeability occurs along the axis of upflow at depths of 200 to 500 m. Over this interval, temperature gradients and mass flux rates are considerably less than at the surface, and therefore alteration proceeds at a reduced rate. Nevertheless, porosity reductions of 2-5%, and consequent drops in permeability of up to half an order of magnitude, reduce the permeability-depth gradient in this region. The vertical temperature gradient decreases in response as less entrainment of cold recharge occurs, resulting in increased temperatures (more than 10°C at 500 m).

The formation of a near-surface, low permeability cap-zone is consistent with results of Martin and Lowell (2000) for transport and precipitation of silica in planar fractures under equilibrium conditions. Their analysis was also extended to address the effects of quartz precipitation controlled by first-order reaction kinetics. At higher mass flow rates, crack closure was slower than under equilibrium conditions as fluids are transported too rapidly for appreciable deposition on crack walls to occur. Furthermore, in addition to developing a near-surface low permeability region, a secondary low permeability zone is formed beneath as the flow is reduced and cooling pushes the maximum precipitation isotherm to greater depths.

The lowest rates of permeability reduction occur in the deep basement rock and are no more than a fraction of an order of magnitude. The slow alteration rate at these depths is due to: (i) the modest temperature gradient associated with the relatively low permeability-depth gradient; (ii) low mass flux rates associated with low permeability; and (iii) a tight permissible permeability range (see Table 5.1).

7.4.1 Redistribution of heat flow

Development of an impermeable cap-zone above hot fluids rising within the plume has a considerable effect on the heat flow characteristics of the geothermal field.

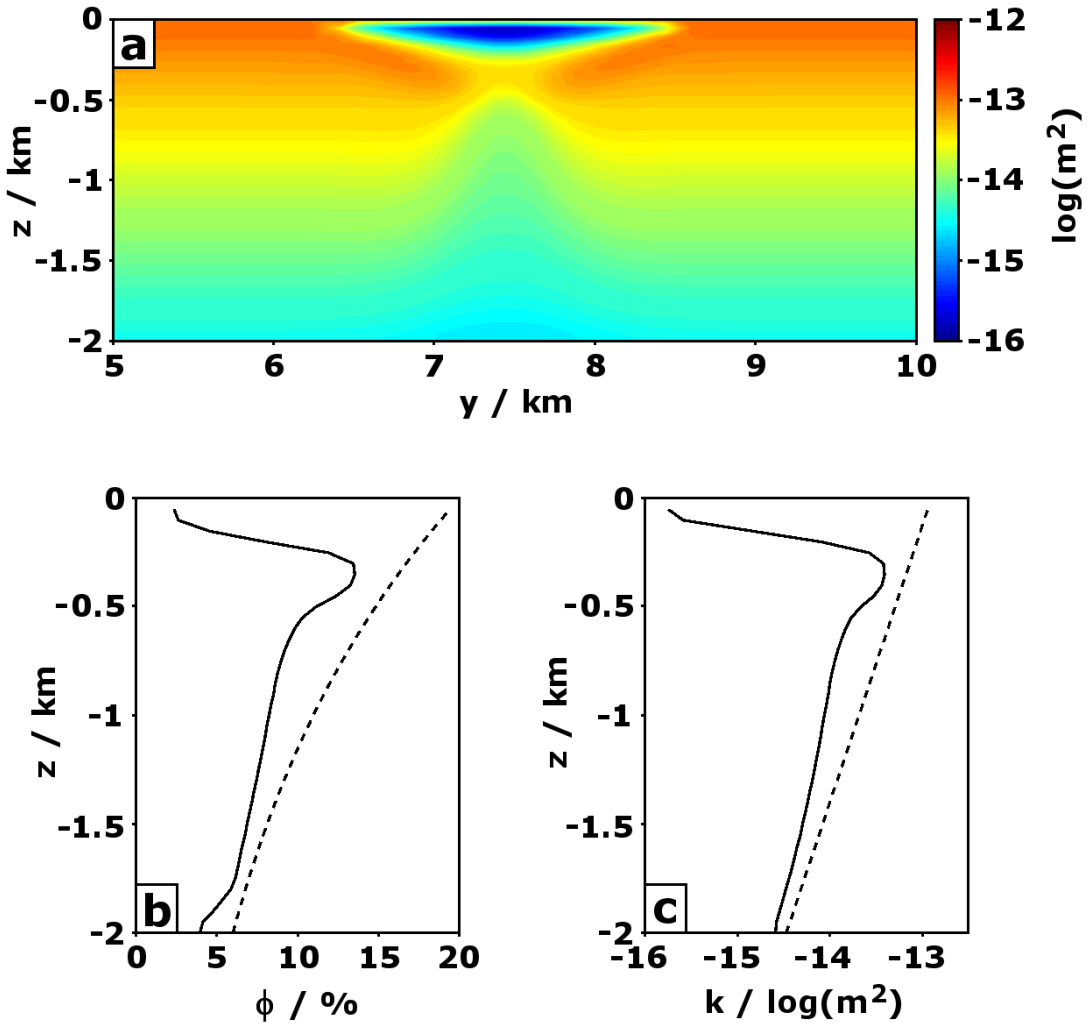

Figure 7.5: (a) Permeability distribution ($\log(m^2)$) after 120 kyr of silica deposition at the surface. Profiles of (b) porosity and (c) permeability with depth along the top 2 km of the plume axis at t =300 kyr (dashed: see Figure 7.2(a-b)) and 420 kyr (solid).

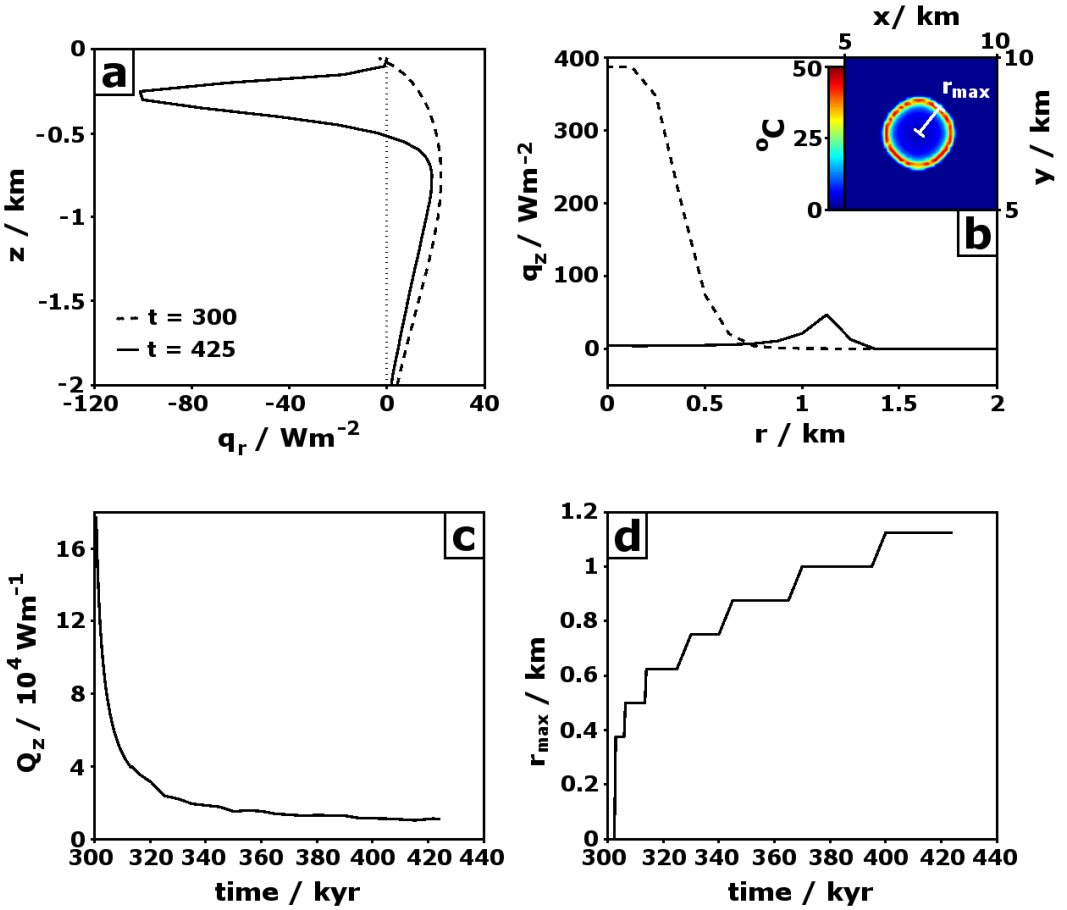

Figure 7.6: (a) Lateral heat flux with depth at a radial distance of 500 m from the plume axis at t =300 kyr (dashed) and 420 kyr (solid). Note that negative values represent heat transported away from the plume axis. (b) Vertical heat flux at the surface measured along a radial profile beginning at the centre of the plume (see inset). (c) Vertical heat output, Q_z, integrated along the radial profile in (b) over time. (d) Position of maximum vertical heat flux along the radial profile in (b), which is a proxy for field radius, r_{max}. The stepped profile is due to mesh discretisation.

The reduction in mass flux within the original field boundary causes an immediate reduction in heat output. However, the supply of buoyant fluids from depth is largely unchanged by self-sealing, which implies that ascending fluids, blocked from rising any further, must be deflected laterally. As heat transport is largely advective, this results in an increase in lateral heat flow beneath the cap-zone (Figure 7.6(a)).

Prior to the development of a cap-zone, lateral heat flow was small and typically

directed toward the upflow axis, representing entrainment of cold, but nevertheless heat bearing, recharge. However, by t =420 kyr heat and mass flow, deflected by the surface cap-zone, is directed away from the plume to a depth of 500 m. The largest lateral flows of $\sim 100\,\mathrm{W\,m^{-2}}$ occur at 300 m depth, although this varies with cap-zone thickness. In comparison, maximum surface heat fluxes of $400\,\mathrm{W\,m^{-2}}$, observed above the upflow zone prior to self-sealing, are reduced several orders of magnitude by the impermeable cap-rock (Figure 7.6(b)). Deflection of hot fluids to the edge of the cap-zone causes the vertical heat flux, and presumably surface thermal expression, to migrate radially away from the original plume centre. The intensity of the heat flux at the field boundary also decreases as a limited heat output is spread around an increasing larger field circumference (Figure 7.6(c)). Furthermore, the radial growth rate of the geothermal field, parameterised by its radius, r_{max}, decreases with time as increasingly larger volumes quartz must be deposited into the porous rock by a fixed source (silica saturated upflow).

Chaudhuri *et al.* (2012) found that silica precipitation in a fracture network led to the formation of elongated obstacles perpendicular to the mean flow direction. Growth occurs preferentially at the lateral edges of these objects due to the alignment of mass flux and temperature gradient streamlines. The formation of a low permeability cap-zone at the surface above the upflow zone is the macroscopic equivalent of this smaller scale phenomenon.

7.4.2 Evolution of field properties

Figure 7.7 tracks the evolution of several field properties as self-sealing proceeds over a 120 kyr period. Cap-zone formation has the immediate, short-term effect of reducing heat output of the field by insulating hot upflow from the atmosphere. Over a period of several thousand years, heat output drops rapidly from 120 to 80 MW and is sustained at this value for the duration of the simulation. However, heat flux through the original field boundary declines substantially as rising fluids are now

deflected to the (growing) field margin. Vertical heat flow below the cap exhibits an anomalous and sustained increase prior to a steady decline as silica deposition at depth thickens the cap-zone. This spike is caused by the reversal of lateral recharging inflows that had previously exerted a degree of quenching on hot upflow in the near-surface. Enhanced lateral outflow induced by the cap-zone negates the effects of these inflows, and the reduction in mixing permits more efficient operation of the plume at near-surface depths.

Geothermal field area, delineated here by the $1\,\mathrm{W\,m^{-2}}$ vertical heat flux contour but in practice by either resistivity contours or the extent of surface thermal manifestations, increases at a constant rate. Over a period of 120 kyr, field area increases by more than a factor of three, at a near-constant rate of $\approx 2.8\,\mathrm{km^2}$ per 100 kyr (Figure 7.7(b)). During the same period, total surface heat output is approximately constant; thus, the effect of the cap-zone is to spread a fixed heat output across a wider area (or more accurately, to distribute it to a longer field margin).

The negative feedback that silica deposition exerts on subsequent mass flow and further permeability reduction is evident in Figure 7.7(c). At 50 m depth permeability reduction is initially rapid but decreases with time as the low permeability region hosts a reduced mass flow rate. This feedback is also evident at 100 m depth, although is less conspicuous due to the overall lower rate of alteration.

The temporal behaviour of temperature at various depths (Figure 7.7(d)) within the plume reflects changes in the relative importance of advective heat transport versus conductive atmospheric cooling. Surface temperatures are initially set by the passage of heated fluids through open pore space as they rise to the surface. The immediate effect of the onset of self-sealing at the surface is an increase in temperature as lateral deflection shuts down the inflow of cool recharge. However, continued silica deposition reduces permeability to a point where hot upflow can no longer maintain high temperatures, and atmospheric cooling begins to prevail. Surface temperatures drop by up to 50°C, although deeper in the cap-zone temperature changes are smaller.

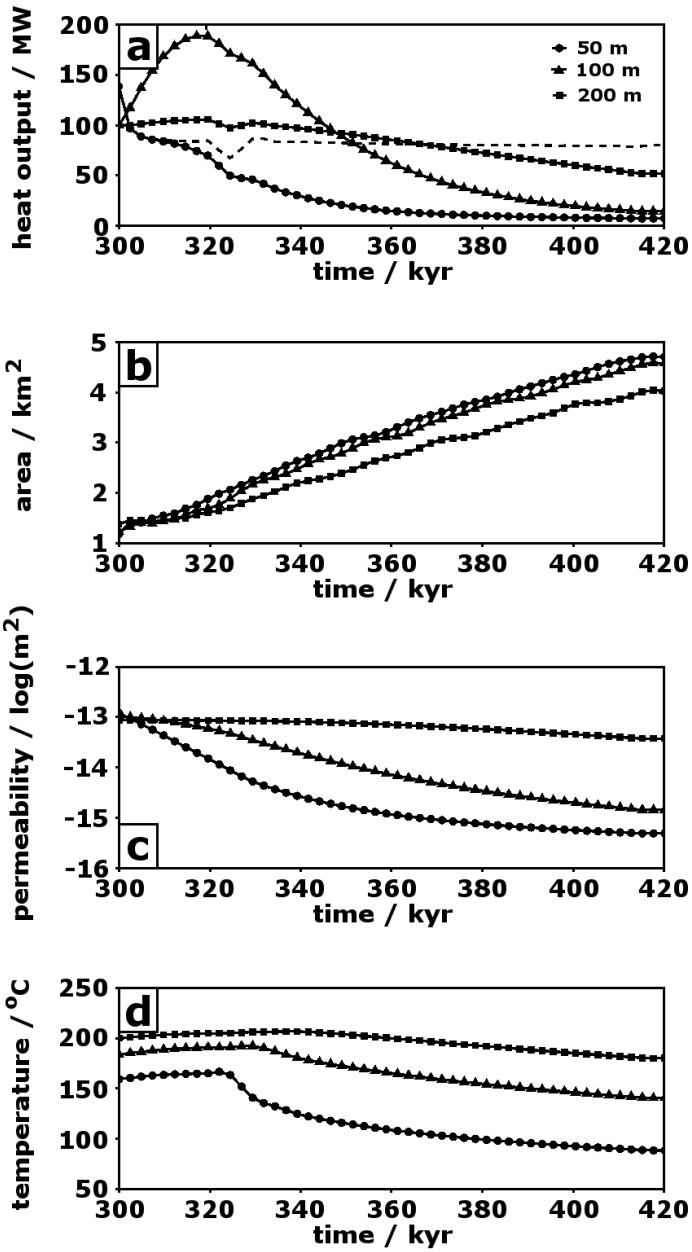

Figure 7.7: Evolution of geothermal field characteristics during 120 kyr of silica deposition. Profiles are given for three different depths: 50 (circles), 100 (triangles) and 200 m (squares). (a) Heat output through the original field boundary, as defined by the 1 W m^{-2} vertical heat flux contour at t =300 kyr. The black dashed line shows the total field output. (b) Geothermal field area delineated by the evolving 1 W m^{-2} vertical heat flux contour. (c) Arithmetic mean permeability within the original field boundary. (d) Temperature at the upflow axis, i.e., $x = y = 7.5$ km.

7.4.3 Spatial patterns of permeability change

In these models, processes of deposition or dissolution are dependent on the movement of silica saturated fluids through a temperature gradient. The local rate of change of porosity depends on the magnitude of both the mass flux vector, $\mathbf{M}$, and temperature gradient, ∇T, and is modulated by the value of the angle, θ, between the two. Where $\mathbf{M}$ and ∇T are close to orthogonal, fluid flux is approximately isothermal and minimal deposition or dissolution will occur. If $\mathbf{M}$ and ∇T are parallel but point in opposite directions, then fluid temperature is decreasing and precipitation will occur. Where $\mathbf{M}$ and ∇T are parallel and point in the same direction, fluid temperature is increasing and dissolution occurs.

Figure 7.8(a) plots contours of the angle between $\mathbf{M}$ and ∇T for a vertical slice through the centre of the plume at $t = 420\,\text{kyr}$. In the context of the plume structure, these contours delineate those regions in which precipitation, dissolution or no reaction is favoured. Along the axis of the upflow zone, both $\mathbf{M}$ and ∇T are near vertical, favouring precipitation within the centre of the plume (see Figure 7.5(a)). However, the porosity/permeability reduction rate here is modest due to the low temperature gradient relative to the surface. The largest gradients occur where hot upwelling fluids encounter the cold atmosphere in the upper layers of the model. At these depths, both $\mathbf{M}$ and ∇T are vertical, and, due to their large magnitudes, silica precipitation proceeds rapidly, resulting in the formation of a low permeability cap.

Moving horizontally from the plume axis, ∇T rapidly switches from vertical downward to horizontal (see Figure 7.8(b)), followed by a slow rotation to vertical upward. In this region, fluid temperatures decrease slowly from their maximum value at the centre of the plume, to their minimum value in the down-welling recharge zone. In contrast, mass flux responds much more rapidly, switching from vertically upward within the plume, to vertically downward outside the plume over a relatively short distance ($<1\,\text{km}$). This results in a $\approx 2\,\text{km}$ wide zone around the centre of the plume, in which $\mathbf{M}$ and ∇T are nearly orthogonal. Despite the appreciable tempera-

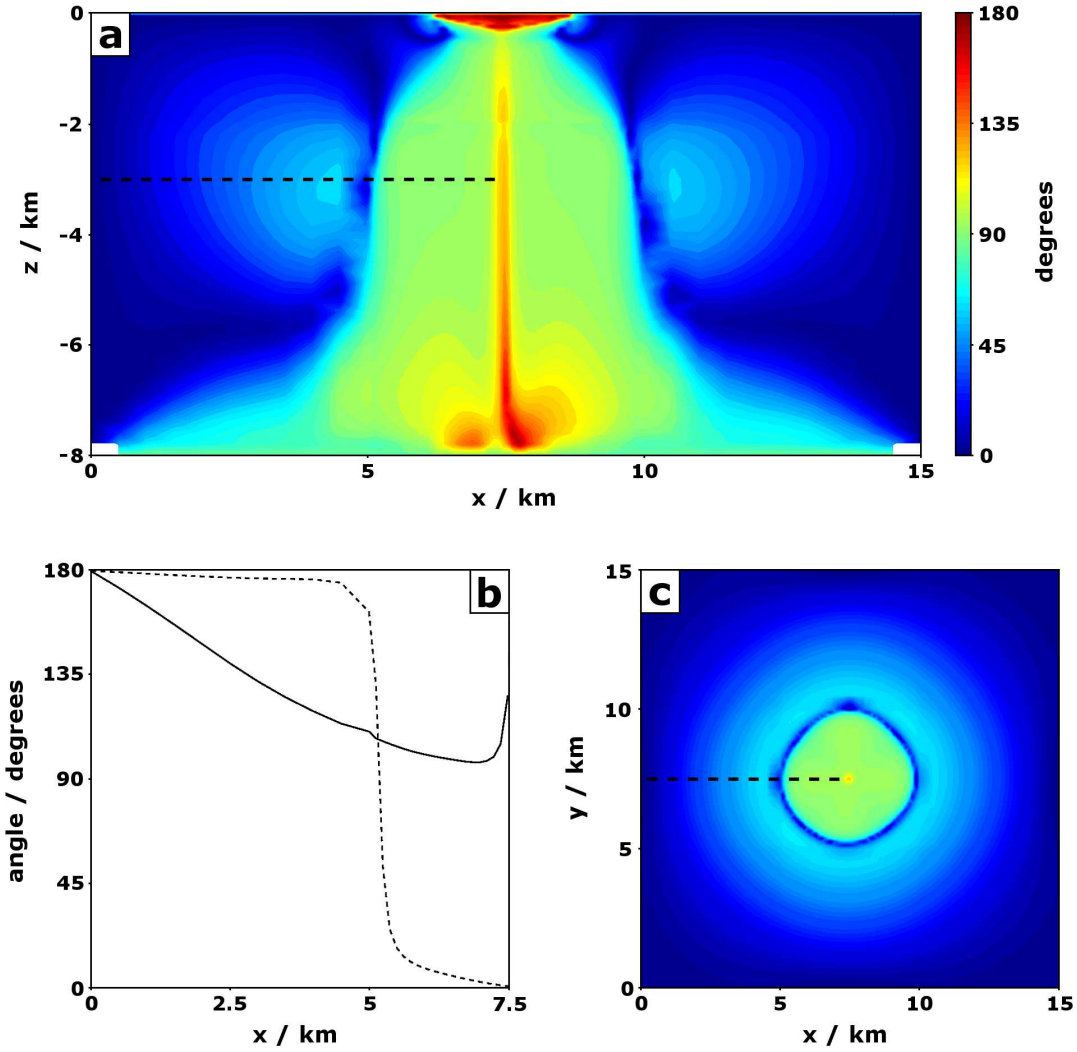

Figure 7.8: (a) Angle, θ, (in degrees) between temperature gradient and mass flux for a vertical slice through the centre of the plume (y =7.5 km)). (b) Profiles along dashed line in (a) showing the angle between temperature gradient (solid) and mass flux (dashed), and the vertical axis. (c) Angle between temperature gradient and mass flux for a horizontal slice at 3 km depth. Once again, the dashed line indicates the position of the profiles in (b).

ture gradients and mass flux that prevail in these regions, fluid flow is approximately isothermal and silica deposition is limited. These regions represent excellent conduits for the transport of minerals whose solubility characteristics depend strongly on temperature.

In the down-flow regions, i.e., $x < 5\,\text{km}$ and $x > 10\,\text{km}$, the angle between $\mathbf{M}$ and ∇T is small and dissolution is favoured. However, little increase in porosity or permeability occurs in these regions due to; (i) the low rate of mass flux compared to upwelling fluids, which are assisted by the buoyancy of low density fluid; and (ii) the comparatively low geothermal gradient, maintained by cold down-welling fluids that suppress the background, conductive temperature profile (Weir, 2009). In locations where down-welling fluids encounter the magmatic heat sources inferred to drive geothermal convection, a boundary layer with high temperature gradients would be expected to form. Under these conditions appreciable levels of silica dissolution at the base of the convective system would be expected. However, the model mesh used here is too coarse to resolve such gradients and this effect is thus not represented.

A toroidal region encircling the plume axis, in which $0 < \theta < 45°$, is observed (see Figure 7.8(a) and (c)) in the down-flow zone. This pattern arises due to the relatively slow rotation of ∇T with proximity to the plume axis (see Figure 7.8(b)) compared with $\mathbf{M}$, in the $x < 5\,\text{km}$ region. However, as both $\mathbf{M}$ and ∇T are small in the down-flow region, this effect is not printed on the larger pattern of permeability modification (Figure 7.5(a)).

7.4.4 Effect of a heterogeneous permeability field

In practice, constraints on mesh resolution and geophysical observation prevent the full heterogeneity of crustal porosity and permeability fields from being fully represented. However, its qualitative influence on the homogeneous solution (Figure 7.5) can be investigated by considering the effects of arbitrary heterogeneity in these distributions. Figure 7.9(a) shows a permeability distribution constructed by super-

imposing a Gaussian fluctuation field on the homogeneous distribution given in Figure 7.2(a). The heterogeneity is spatially correlated and follows a power-law scaling of spatial frequencies with a scaling exponent of 1.3. The fluctuations have a mean of zero and a standard deviation of 0.25 orders of magnitude and the corresponding heterogeneous porosity distribution is calculated from Equation (5.9).

Permeability changes generated after 120 kyr of silica deposition (Figure 7.9(b)) are qualitatively similar to those for the homogeneous permeability distribution (Figure 7.5(a)). A low permeability cap-zone is rapidly formed at the surface, and has similar lateral and vertical dimensions to the homogeneous simulation. Below the cap-zone, a lesser reduction in permeability is observed, again consistent in shape and dimension to the homogeneous model, and it is here that the effects of heterogeneity are apparent. The distribution of silica deposition is lumpy, and localises in specific regions while remaining conspicuously absent from others. Silica dissolution occurs in several localised regions within the upflow zone, but more commonly on its flanks and beneath the cap-zone. Regions of deposition and dissolution do not appear to correlate to fluctuations in the permeability field, which might be expected if mass flow were the controlling factor on the rate of permeability modification.

The presence of strong permeability contrasts distorts the flow field, and thus temperature distribution (Figure 7.9(c)), relative to the homogeneous model. Consequently, the angle between mass flux and temperature gradient, a key parameter modulating the intensity of silica deposition, can no longer be described in simple terms (Section 7.4.3 and Figure 7.8). Figure 7.9(d) shows that permeability distortion of the temperature and flow fields imparts a similar lumpiness to the $\mathbf{M} \cdot \nabla T$

Figure 7.9 *(following page)*: (a) Heterogeneous permeability ($\log(m^2)$) distribution prior to alteration. (b) Change in permeability, (c) temperature distribution, and (d) angle between mass flux and temperature gradient, i.e., $\theta = \cos^{-1}(\mathbf{M} \cdot \nabla T/(|\mathbf{M}||\nabla T|))$, after 120 kyr of silica deposition. Hatched region in (b) indicates regions of permeability increase, i.e., silica dissolution. Vertical heat flux at the surface at $t = 420$ kyr for (e) the heterogeneous, and (f) the homogeneous permeability distributions

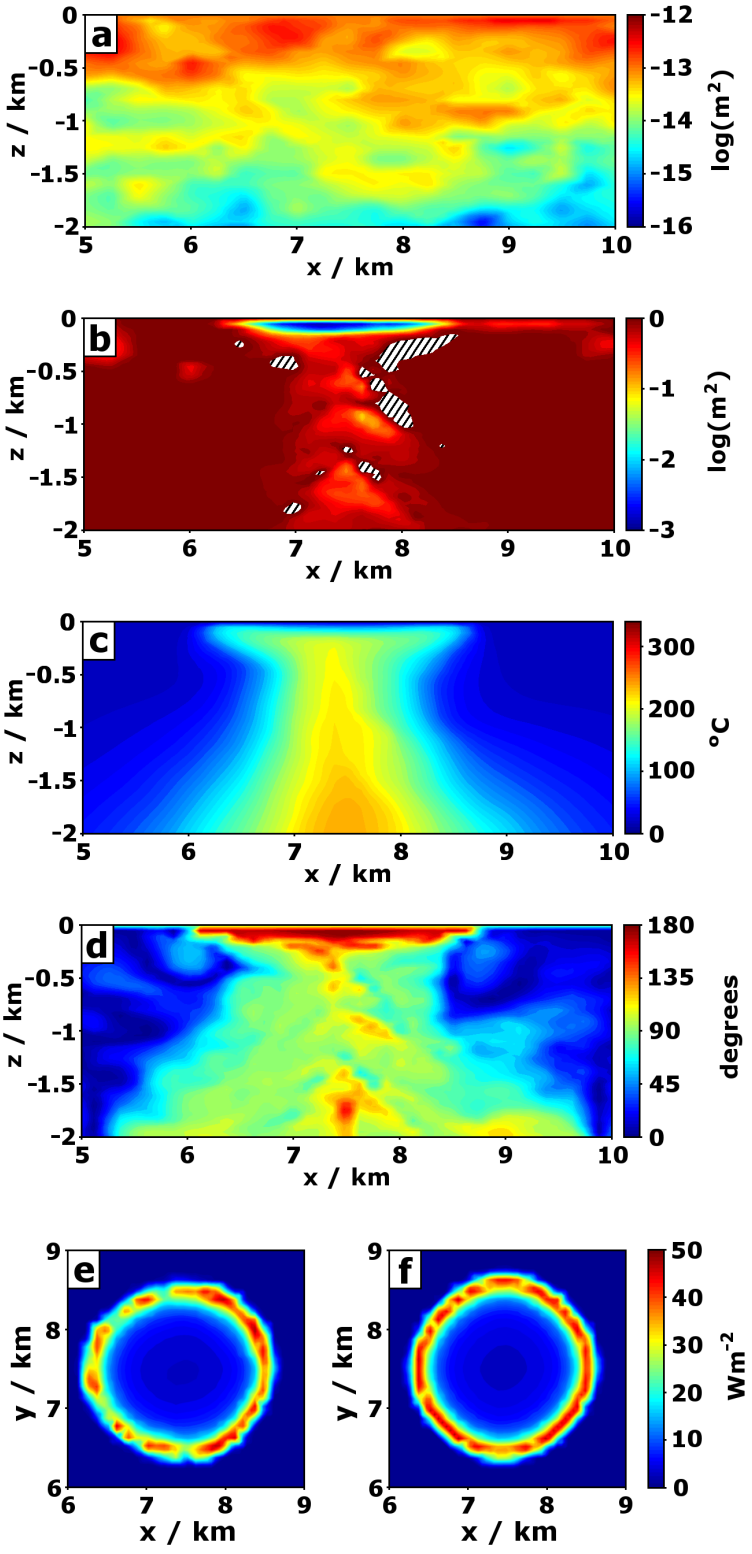

term in Equation (7.5). Local maxima in this distribution correspond to regions of enhanced deposition in Figure 7.9(b), attesting to the considerable influence this parameter exerts on field evolution. Furthermore, regions of quartz dissolution identified in Figure 7.9(b) correlate to regions of $\theta < 90°$.

The crustal heterogeneity described here imparts only a second order effect on surficial geothermal expression. Figure 7.9(e-f) shows that silica deposition and consequent lateral deflection of rising fluids forms a circular cap-zone of similar dimensions to the homogeneous solution, although upwelling of fluids around the cap is more sporadic in the heterogeneous simulation. Further control on surface expression would be expected for more distinctive permeability features, for example the large magnitudes and sharp contrasts associated with faults.

7.4.5 Mesh sensitivity

Node spacing, particularly in the surface boundary layer, is essential to the accurate resolution of temperature gradients. The effects of mesh uniformity and coarseness are investigated through the use of two alternative meshes: (i) a non-uniform mesh similar to that used in previous simulations but with nodal distances doubled (i.e., half the spatial resolution: see Figure 7.1(b)), and (ii) a uniform mesh in which the nodal spacing is 200 m in each direction. Thus, vertical resolution in the top 2 km for the original and two alternative meshes is 50, 100 and 200 m respectively. Maximum temperature gradients, encountered in the top surface layer, scale according to the node spacing and are for the three meshes, -1.70, -0.86 and -0.44 $\mathrm{K\,m^{-1}}$. The first two are consistent with maximum vertical gradients encountered in the near-surface of TVZ fields (e.g., Wairakei: 1-2 $\mathrm{K\,m^{-1}}$, O'Sullivan *et al.*, 2009; Ngatamariki: 0.9 $\mathrm{K\,m^{-1}}$, Burnell and Kissling, 2009).

Nodal spacing and the ability to resolve large temperature gradients in the near-surface influences the rate at which a cap-zone develops. This in turn effects field evolution to a depth of 1 km, due largely to the insulating effect of the cap. Figure 7.10

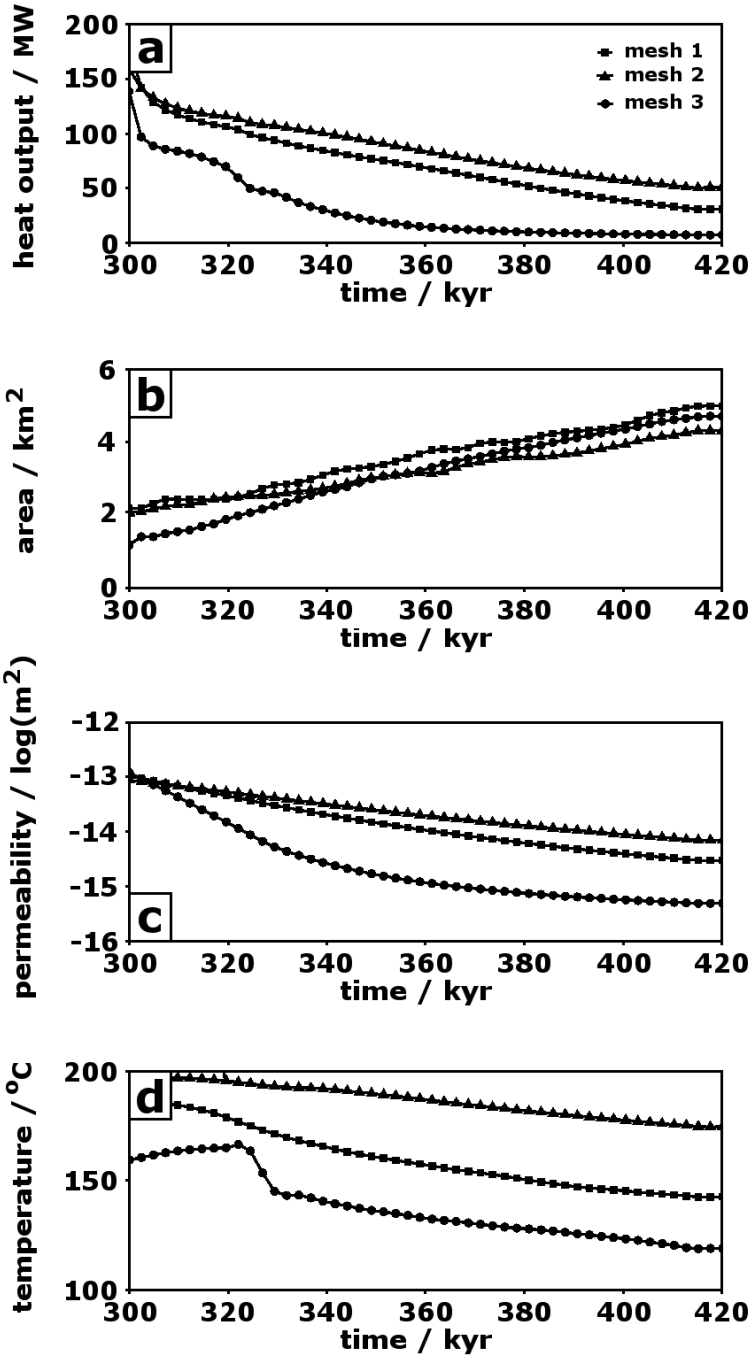

Figure 7.10: Evolution of geothermal field characteristics during 120 kyr of silica deposition for three different meshes: non-uniform, high resolution (circles: Figure 7.1(c)), non-uniform, low resolution (triangles: Figure 7.1(b)), and uniform (squares: Figure 7.1(a)). Quantities presented are for the uppermost crustal layer and are derived in the same manner as those in Figure 7.7(a-d).

plots the evolution of the upper layer of the model during 120 kyr of permeability modification for the three meshes. For finer resolution meshes, silica deposition and sealing of the geothermal system proceeds more rapidly, and ultimately results in lower permeability cap-zones. Consequently, heat output through the field is decreases for finer meshes, despite the development of similar sized fields.

7.5 Fault modulated silica sealing

Thus far, generic and largely artificial scenarios of geothermal circulation in a silica controlled permeability field have been considered. In practice, permeability in the Taupo Volcanic Zone evolves in response to a variety of forcings, including tectonic extension, hydraulic fracturing, and magmatic and volcanic processes. The effects of low level tectonic and hydraulic fracturing have been incorporated in an ad hoc way by imposing a lower limit on permeability for hydrothermally altered rock. This section extends the simulation to consider geothermal self-sealing behaviour perturbed by surface rupture of an active fault.

Episodic reactivation of fault structures modifies permeability by reshearing existing fractures or creating new ones, thereby supplying additional pathways for fluid transport. Furthermore, in the event that a mature, impermeable fault gouge has formed, fault rupture can provide temporary cross fault hydrological connections (see Chapter 8). Rupture of overpressured reservoirs at depth in the crust may also increase mass flow to the surface (Sibson, 1990). In the model presented here, rupture along a vertically oriented fault plane is considered, with the primary effect being the disturbance the impermeable cap-zone formed at the surface. While faults within the TVZ are typically inclined at angles of 50-70° (Beanland *et al.*, 1990; Villamor and Berryman, 2001), their dip steepens markedly at near-surface depths. Thus, description of vertical fault rupture through the near-surface cap-zone is an acceptable approximation. At depth, the discrepancy between the modelled vertical fault and a more realistic inclined fault is increased; however, as the greatest permeability

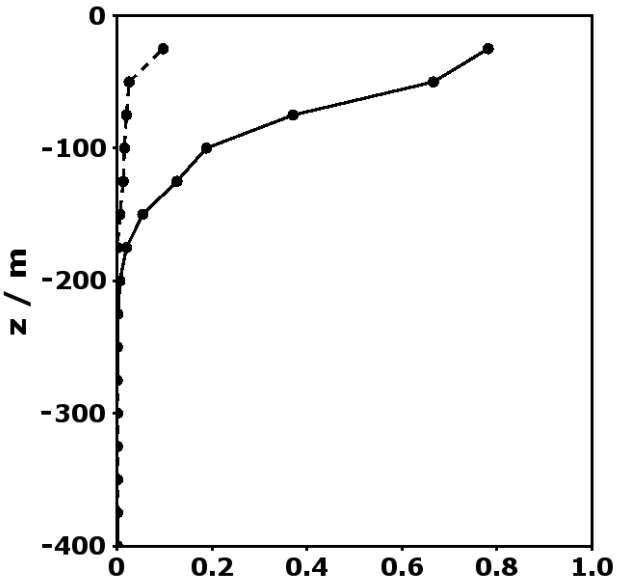

Figure 7.11: Proportion of vertical heat flux transmitted by conduction prior to ($t = 300$ kyr, dashed line) and following the formation of a cap-zone ($t = 420$ kyr, solid line). Profiles are taken at $x = y = 7.5$ km, i.e., vertical profiles through the centre of the model domain. Heat transfer is dominated by advection prior to the formation of the surface cap-zone and by conduction afterward.

changes are limited to shallow depths, the error introduced by this approximation should not greatly influence the results.

A geothermal plume is evolved for the mesh shown in Figure 7.1(d-f). This mesh permits very fine resolution of the near-surface region where silica sealing occurs, and along the fault plane where coseismic permeability modification is applied. At $t = 300$ kyr silica deposition begins throughout the model and after a period of 120 kyr an impermeable cap-zone is formed (see Section 7.4). The geothermal field attains a maximum area at the surface of 5.5 km^2 and the total field heat output is constant at 75 MW. At this time, heat flux through the cap-zone is primarily conductive, with advection of fluid through a sparse distribution of fractures accounting for only 20% of the total heat transfer (Figure 7.11). The ratio of conductive to advective heat flux is limited by the minimum obtainable permeability, which is set to 10^{-16} m^2. For increasing permeability beneath the cap, advection becomes the dominant heat

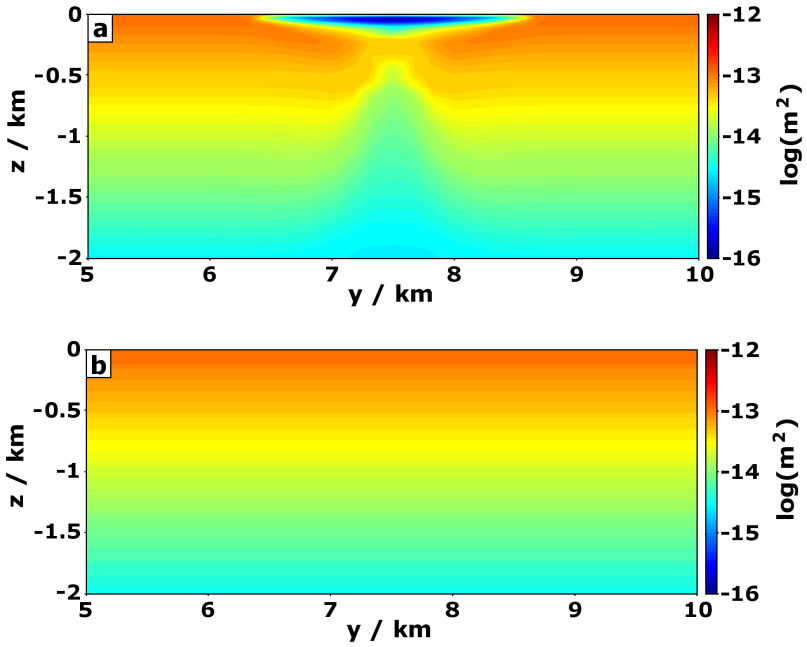

Figure 7.12: Permeability ($\log(m^2)$) along the fault plane (a) prior to, and (b) following fault rupture.

transfer component, and conduction is negligible at 200 m depth.

At $t = 420$ kyr, a step change in permeability along the fault plane is introduced representing rupture from depth to the surface. Permeability on the fault plane is reset to pre-alteration values (see Figure 7.12) while permeability outside the fault plane is unchanged. The permeability update period is reduced two orders of magnitude to 50 yr for twenty simulations. This allows resolution of both the high rate of silica deposition at the renewed mass flow rate and its short-term effect on permeability. The update period is then increased to 500 yr for another twenty simulations to observe medium-term effects.

7.5.1 Plume response to rupture

The opening of a fissure through the impermeable cap-zone has the immediate effect of increasing heat output through the central regions of the geothermal field (see

Figure 7.13). Prior to fault rupture, hot fluids beneath the cap had taken extended lateral routes to reach the surface, incurring substantial decreases in temperature. Following the earthquake, the same fluids rising along the axis of the plume have a direct conduit to the surface. The immediate thermal response of the system is an increase in output from 75 MW to 125 MW and an increase in maximum surface temperatures of 100°C to nearly 150°C.

The largest coseismic permeability changes occur at the surface where an increase of three orders of magnitude (10^{-16} to 10^{-13} m^2) permits a similar sized increase in the mass flow rate. Furthermore, the resumption of advection-dominated heat flux, over previously conduction-dominated, restores sharper temperature gradients and higher temperatures in the near-surface. Rapid silica deposition is favoured in the newly-created, high-permeability fissure opened through the centre of the geothermal field and, consequently, the greatest rates of reduction of porosity and permeability are encountered here. The localisation of silica deposition in a region of high permeability is consistent with findings of Martin and Lowell (2000), who showed that, under equilibrium conditions, the rate of precipitation was greater in regions of high permeability, providing the temperature gradient is not compromised by high flow rates. It is notable however, that this homogenising effect on permeability is not observed in simulations of a heterogeneous crust (Figure 7.9) where the variation in permeability is less. Under these circumstances, precipitation rate exhibited a stronger dependence on the temperature gradient and its alignment with mass flux.

Figure 7.13(c) shows that near-surface fluid pathways are steadily sealed over the following 10 kyr, while at depth the response is slower. The spike in field heat output is short lived, declining rapidly to its pre-rupture value after only 1-2 kyr. Resealing of the fault also restores the lateral heat and mass flows beneath the cap, diverting hydrothermal fluids to the field boundaries where further horizontal growth of the cap-zone resumes. The post-seismic sealing of the fault zone demonstrated here represents a minimum-time self-sealing response; Martin and Lowell (2000) showed that when reaction kinetics are accounted for, silica deposition occurs at a slower

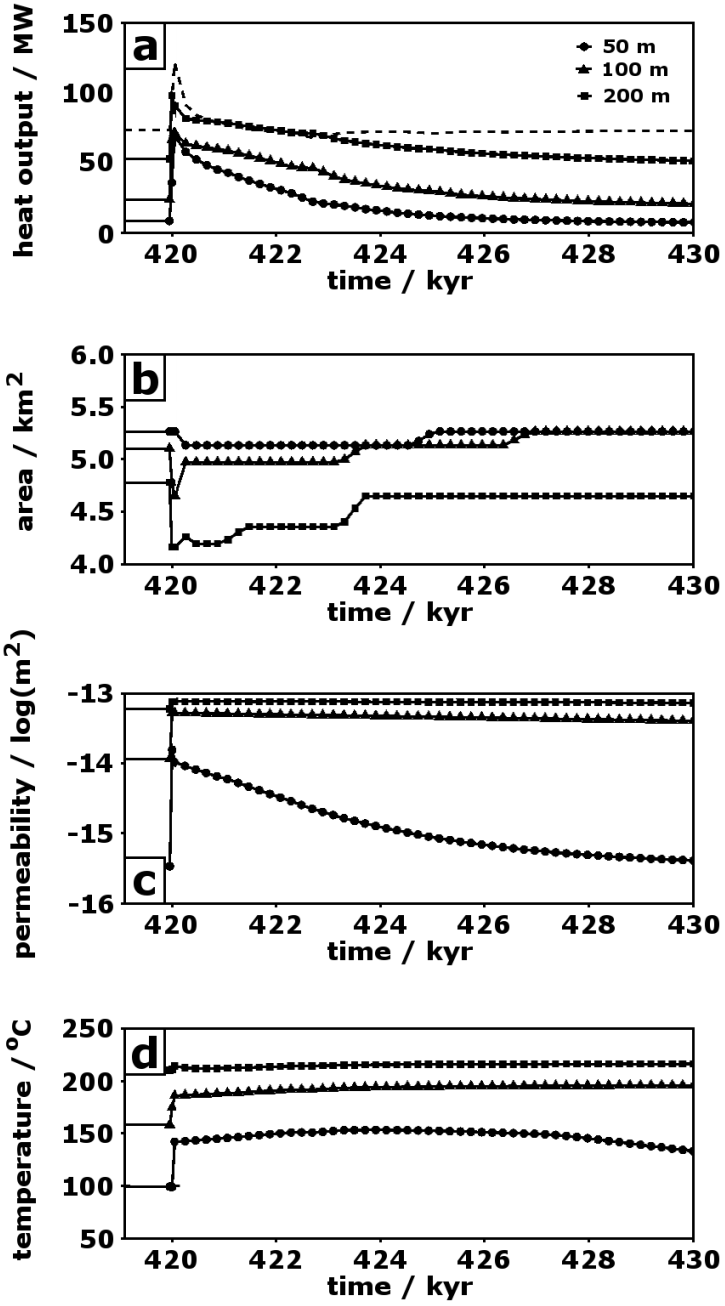

Figure 7.13: Change in four geothermal field parameters in response to, and following fault rupture. (a) Solid lines show heat output through the original field area at the surface (circles) and at 100 (triangles) and 200 m (squares) depth. The dashed line indicates the total heat output of the field, accounting for the evolving field area. (b) Field area, as constrained by the $1\,\mathrm{W\,m^{-2}}$ vertical heat flux contour, at the three depths. (c) Arithmetic mean permeability within the original field area for the three depths. (d) Temperature at the upflow axis, i.e., $x = y = 7.5\,\mathrm{km}$.

rate than that predicted by equilibrium considerations in high permeability regions, e.g., a recently opened fault.

7.5.2 Heat flow in the subsurface

Heat and mass flow evolve in the subsurface in response to the formation, growth and rupture of the impermeable cap-zone. Figure 7.14 illustrates the asymmetry introduced to these flows by permeability modification along a discrete plane. The time varying heat flux across four transects is considered: two are horizontal, oriented along and across the strike of the fault, intersect the centre of the plume and capture vertical heat flow at the surface; the other two are vertical, offset 500 m across and along strike from the plume centre, and capture lateral heat flows (directed away from the plume axis: Figure 7.14(a)).

For the first 120 kyr, heat flow evolves in response to self-sealing behaviour and a growing cap-zone. As described in Section 7.4, surface heat flux, which is initially maximum above the centre of the upflow zone, is steadily displaced to the lateral boundaries of the field by the growing lid. Intensity also decreases as a limited heat flux is spread along a longer circumference. Lateral heat flows in the subsurface develop and intensify after $\sim$ 20 kyr in response to cap-zone growth. Lateral flows are also steadily displaced to greater depths by thickening of the cap-zone. Due to mesh discretisation, along-strike heat flow is measured 60 m closer to the plume axis than its across-strike counterpart, which accounts for its slightly higher magnitude.

Asymmetry in the heat flow profiles is introduced by permeability enhancement along a preferred plane, i.e., coseismic fault permeability. At $t = 420$ kyr, considerable surface heat output is observed along strike of the fault plane as a permeable fissure is opened through the cap-zone. Vigorous heat flux occurs along a $\sim$ 1 km stretch of the fault, which is significantly wider than the same heat flux prior to cap-zone formation (Figure 7.14(b): $t = 300$ kyr). Two factors contribute to this effect: (i) channelling of a radially symmetric plume below the cap, through an elongated

fissure, and (ii) widening of the sub-cap-zone plume structure (see Figure 7.7(b)) by cap-zone insulation and the reversal of cold inflow in the near-surface. Across-strike heat flow (Figure 7.14(d)) is significant only at the fault trace and is otherwise suppressed by the developed cap-zone. Heat flux at the margins of the cap, which originates from the deflection of rising fluids, is also reduced as fault rupture provides a more direct pathway to the surface.

Figure 7.14(c,e) shows that lateral subsurface heat and mass flows are severely inhibited by fault rupture, but also that the redirection of fluids through the fault is relatively short lived. Silica deposition at the surface of the fault, where the largest temperature gradients and mass flux rates are encountered, ensures rapid resealing and return to the pre-rupture flow configuration. Permeability reduction occurs first in the centre of the cap-zone and grows outward along the fault trace, causing rapid displacement of outflow to the field boundaries. Silica deposition rates decrease with depth and thus, while the fault is sealed at the surface, significant along-strike lateral flows remain at shallow depths. Dimensionally, the cap-zone resembles a circular plug with a channel carved into its lower surface by fault rupture. For this reason, across-strike heat flow rapidly returns to its pre-rupture state as the across-strike permeability distribution is mostly unaffected by the earthquake. However, an along-strike low permeability channel immediately beneath the surface provides a favourable conduit for lateral fluid flow. Thus geothermal expression at the margins of the cap-zone is enhanced where it intersects the fault trace (Figure 7.15).

Figure 7.14 *(following page)*: Summary of evolving vertical and lateral heat flows during cap-zone formation and fault rupture. (a) Profile positions (solid) from which (b-e) are constructed, relative to the fault plane and plume axis (dashed). Arrows indicate positive heat flow direction. (b) Along-strike vertical heat flow ($x = 7.5\,\text{km}$, $z = 0$). (c) Along-strike lateral heat flow ($x = 7.5\,\text{km}$, $y = 7\,\text{km}$). (d) Across-strike vertical heat flow ($y = 7.5\,\text{km}$, $z = 0$). (e) Across-strike lateral heat flow ($x = 7\,\text{km}$, $y = 7.5\,\text{km}$). Note the discontinuities in (b-e) corresponding to fault rupture at $t = 420\,\text{kyr}$.

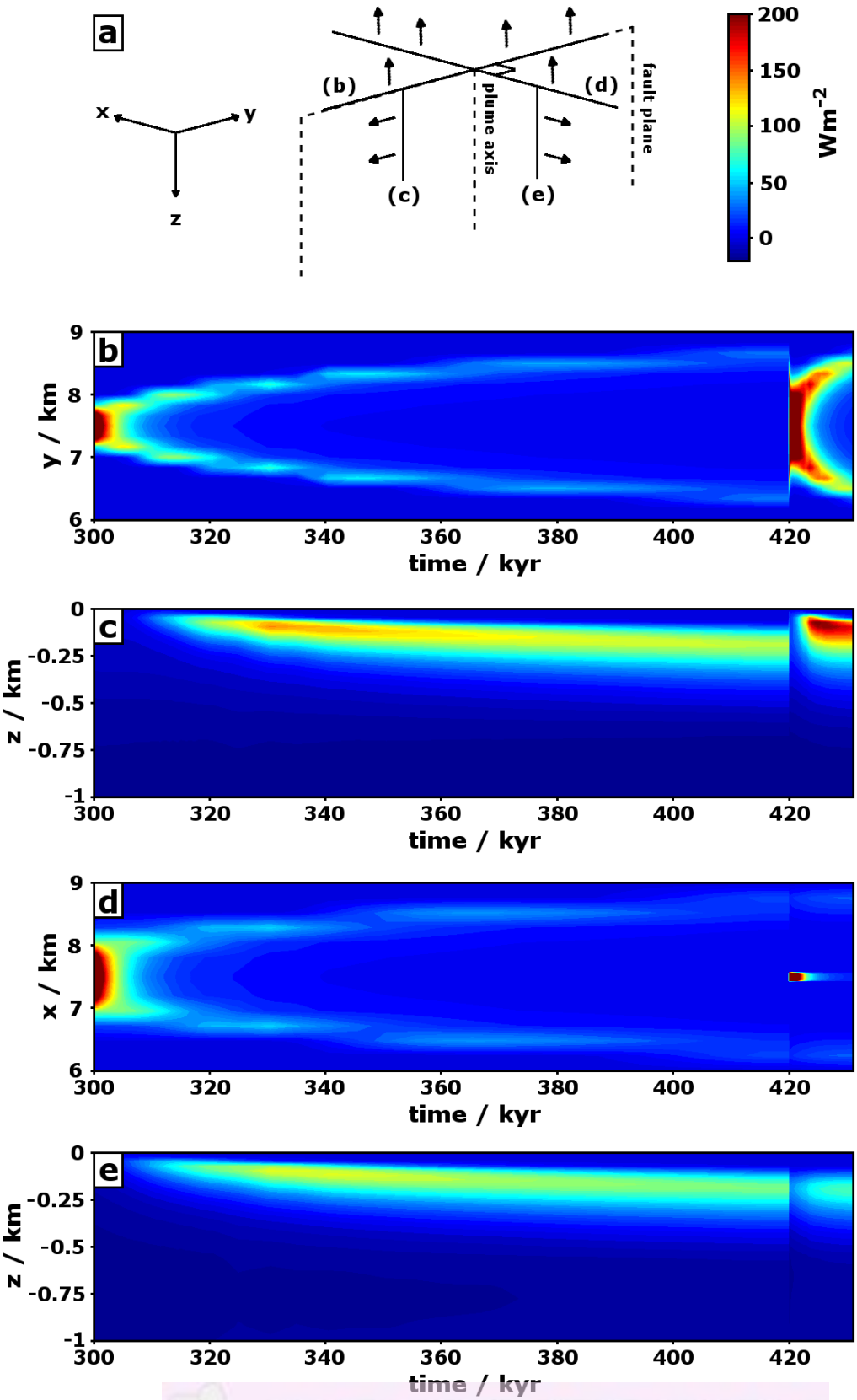

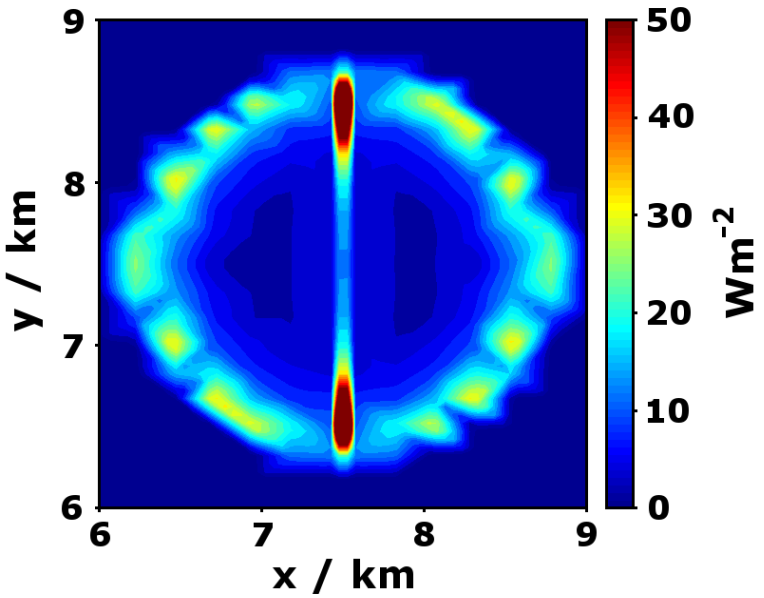

Figure 7.15: Surface heat flux at $t = 430\,\text{kyr}$, i.e., after resealing of the fault rupture.

7.5.3 Reservoir evolution

Cap-zone insulation and enhanced heat and mass flow along a recently rupture fault both play important roles in the development of the geothermal field as an energy bearing resource. The size of the geothermal reservoir is defined here using the stored heat method (Grant and Bixley, 2011), i.e.,

$$E = \int \rho C (T - T_0) dV, \tag{7.8}$$

where E is the energy of the reservoir, ρC is the specific heat of the wetted rock (taken as $2.5{\times}10^6\,\text{J}\,\text{m}^{-3}\text{K}^{-1}$), and T_0 is a reference temperature representing the end point of the thermodynamic cycle (taken as atmospheric 20°C). The integral in Equation (7.8) is performed over the top 2 km of the model domain, i.e., the porous surface volcanic layers. In the TVZ, production typically occurs in these geological units, rather than the low porosity and relatively less accessible basement (due to its depth). This calculation could be extended to greater depths; however, as the focus

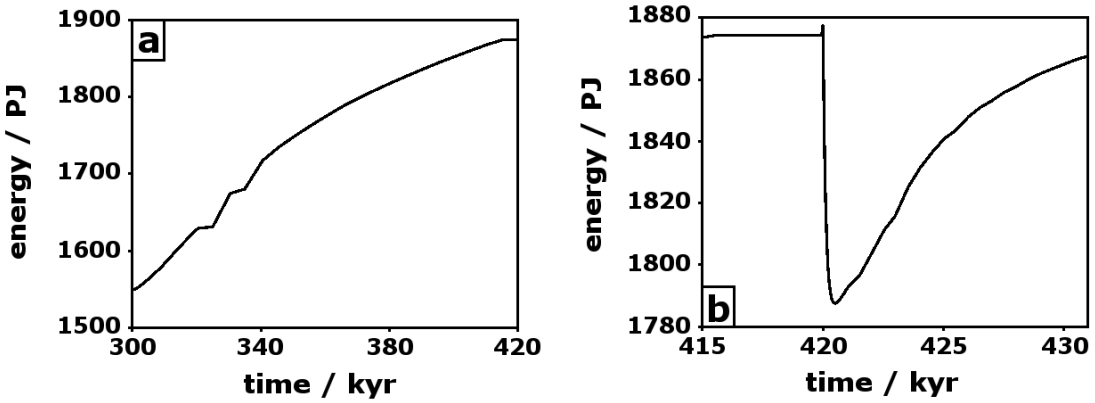

Figure 7.16: Stored reservoir energy (in petajoules) at depths less than 2 km. (a) Reservoir energy increases between 300 and 420 kyr in response to the formation of a low permeability cap-zone. (b) Reservoir energy begins to decrease from 420 kyr as the coseismic permeability reduction permits the escape of hot fluids.

here is on reservoir changes, this arbitrary demarcation is sufficient.

Figure 7.16 shows changes in the reservoir energy content during the 120 kyr of cap-zone formation, and the 10 kyr period following fault rupture. Formation and lateral extension of an impermeable cap-zone has an insulating effect on the plume below. Temperature increases during this period increase the heat content in the reservoir by approximately 20%, although the increase shows signs of slowing. Effectively, self-sealing of the geothermal system improves the energy potential of the resource. Disruption of the insulating cap-zone during fault rupture, and the vigorous heat and mass flows that follow, cause a small, but rapid, decline in reservoir heat content. After the loss of 100 PJ over a ∼500 yr period, the decline is arrested by silica deposition resealing the cap-zone at the surface. Steady recovery of the pre-rupture reservoir occurs over the following 10 kyr.

7.6 Discussion

Modification of the subsurface permeability structure by hydrothermal silica deposition is a common feature of many geothermal fields (e.g., Steiner, 1953; Henneberger

and Browne, 1988; Wood *et al.*, 2001; Bignall *et al.*, 2004; Stimac *et al.*, 2008). Within the TVZ, Henneberger and Browne (1988) report widespread alteration and silicification of the initially porous (>45%) Ohakuri ignimbrite at the extinct Ohakuri geothermal system. Quartz deposition occurs to depths of at least 150 m, which is consistent with the thickness of the low permeability cap-zone developed in numerical simulations. Evolution of the mechanical properties of the surface strata as a consequence of their reduced porosity and permeability is also observed. Punctuation of the altered rock by veining suggests a transition from diffuse flow through a permeable network, to episodic hydrofracturing of an impermeable, altered unit, followed by high mass flow rates and fracture sealing. Permeability modification by the latter process is not modelled here, although the imposition of a minimum obtainable cap-zone permeability is included as an approximation to the component of fracture permeability sustained by hydrofracturing.

At Ohaaki-Broadlands geothermal field, weak clay alteration occurs to depths of 700 m at the periphery of the field, and at shallow depths (< 200 m) above the upflow zone, with smectite grading to illite and then quartz with increasing temperature. Higher rank alteration products, e.g., K-feldspar and albite, are more abundant at depth than at the surface. Simmons and Browne (2000) propose this relationship can be used to delineate upflow zones based on thermal control of species synthesis, i.e., smectite occurring at < 150°, illite at > 200°C, providing other factors, such as overprinting, reaction time or mineral assemblage, can be controlled. At Ohakuri, high rank alteration products occur at the surface, with a quartz adularia mixture grading to mordenite and eventually weak clays at the periphery of the alteration zone. This may indicate a relationship between alteration rank and longevity, in which surface smectite or illite phases are steadily silicified to mordenite or adularia. Decreasing alteration rank toward the field periphery, in addition to correlating with lower alteration temperatures, is also consistent with an expanding field boundary. As the central region of silica deposition increases in dimension and impermeability, increased lateral flow of high temperature fluid would hasten the conversion of

smectite to illite and illite to higher rank products at the edge of the cap-zone. Alternatively, an abundance of high rank silicification at the surface of Ohakuri may be due to the erosion of low temperature, low rank surface clays following the cessation of geothermal activity.

Henneberger and Browne (1988) propose that geothermal activity at Ohakuri was not ended by self-sealing of pore space and fractures in the near-surface, but rather by changes in the deep plumbing or cooling of a heat source. This assertion is consistent with model results that suggest the development of a low permeability cap does not significantly reduce vertical heat flow, even in the absence of mechanisms that maintain or enhance permeability, e.g., fault reactivation, hydrofracturing. Rather, the cap-zone redirects a larger component of the rising fluids laterally, such that geothermal manifestations may be expected across a broader area. Evidence for the migration of activity at Ohakuri, first north and then east, is consistent with such an evolutionary scenario. The implication is that heat output through the surface is controlled by magmatic heat input processes at the base of the brittle crust. Providing fluids are being heated at depth, they will find some path to the surface.

The formation of thick, low porosity surface cap-zones has implications for exploration of blind geothermal systems. For example, Figure 7.9(e-f) shows that, in the absence of recent faulting, geothermal expression is diverted to the field margin where surface permeability remains. High levels of permeability heterogeneity are also likely to imprint on the heat flow, perhaps limiting these surface features to sporadic hotspring outflow at the margins, rather than a well-defined thermal rim. Sufficient cap-zone thickness and impermeability permits conductive atmospheric cooling (Figure 7.11) in the centre of the field, masking the high temperature resource beneath. Old sinters preserved at the surface may be worth targeting.

Te Kopia geothermal field, also within the TVZ, yields further insight into the nature of silicic alteration of permeability, in part due to its fortunate location on the active Paeroa Fault (Bignall and Browne, 1994; Bignall *et al.*, 2004). Geothermal

activity has occurred here for up to 120 kyr, which suggests that simulations presented here address the correct evolutionary time period. Changes in field activity are complicated by episodic normal rupture of the Paeroa Fault, and subsequent uplift and lowering of the water table in the footwall. Cessation of geothermal activity from parts of the footwall may then be due to both a reduction in permeability and the draining of fluids.

Fault slip and exposure of the fault scarp has the propitious consequence of exposing rocks altered at depth. A textural investigation of quartz crystals (Bignall *et al.*, 2004) indicates that in some locations deposition, followed by fracturing and partial dissolution, has occurred. In contrast to Ohakuri, quartz fracturing is attributed to rupture of the active Paeroa fault, although hydrofracturing due to fluid sealing may also contribute. Quartz crystals were grown at temperatures of approximately 215°C, which is consistent with temperatures of rising fluids in the modelled geothermal plume. The growth of these crystals at depths of at least 350 m, is deeper than the cap-zone formed in the model, but not beyond the zone of less intense precipitation that occurs in the high porosity strata below. Fracture and partial dissolution of quartz crystals implies evolution of the mass flow and permeability regimes. Figure 7.9(d) shows that heterogeneity in the permeability field, which is undoubtedly present in the faulted volcanic strata of the TVZ, can produce localised pockets in which fluid flows up a temperature gradient, favouring quartz dissolution (Figure 7.9(b)). Episodic reactivation of a pervasive fracture network by rupture of the Paeroa Fault would serve to maintain, enhance or reconfigure this heterogeneity, thereby modulating local deposition, fracturing and dissolution.

Geothermal expression at the margins of the Te Kopia field is correlated to the inferred position of the Paeroa Fault and associated smaller structures. Isolated regions of altered ground occur in the north and south of the field and are up to several hundred metres distant from the central region of alteration, hot spring activity and hydrothermal eruption cratering. Transport of fluids along the fault in the subsurface is likely to play an important role in the circulation and evolution of this

field. The most recent rupture on the northern sector of the Paeroa Fault occurred $\sim 400\,\mathrm{yr}$ ago (Berryman *et al.*, 2008), however it is not clear if the rupture travelled as far as Te Kopia. Villamor and Berryman (2001) use fault offset of the Paeroa ignimbrite to estimate a vertical slip rate near Te Kopia of $1.5\pm0.2\,\mathrm{mm\,yr^{-1}}$. For characteristic single event displacements of 2-3 m, this slip rate implies rupture recurrence on the order of 1-2 kyr, consistent with recurrence intervals of 1-10 kyr deduced for the northern Paeroa Fault (Berryman *et al.*, 2008). The current configuration of geothermal activity at Te Kopia has therefore evolved during multiple rupture events. Renewed flow along the strike of the fault may represent the norm, rather than a transient feature preceding reestablishment of a long-lived, flow-suppressing cap-zone. Simulations of cap-zone evolution in the presence of recurrent fault rupture and permeability heterogeneity may yield further insight into the geothermal circulation of the region.

7.7 Chapter summary

Alteration of the near-surface permeability structure by precipitation of silica into open pore spaces has an appreciable effect on the evolution of geothermal fields over geological timescales. A numerical model considering precipitation from a silica saturated fluid in a gradient reaction regime indicates the principle effect is the development of a low permeability cap-zone in the near-surface. This cap-zone forms directly above the upflow zone, where surface temperature gradients are greatest, and grows to a thickness of several hundred meters over a period of 120 kyr. The circular cap-zone also grows horizontally in response to increasing lateral flows as rising geothermal fluids are deflected by the cap. These flows imply a steady outward migration of geothermal activity but also thermal dilution when spread across a greater area. Development of a cap-zone has an insulating effect on the fluids below, causing increases in fluid temperature, enthalpy, and ultimately the potential of the geothermal reservoir.

The evolution of geothermal fields over geological timescales depends not only on hydrothermal alteration of the near-surface permeability structure, but also on changes to the deeper plumbing systems, an evolving chemical composition of fluids, changes to the deep heat sources, and mechanical alteration of permeability, e.g., hydrofracturing or fault reactivation. In addition, topographic pressure gradients and rainfall recharge may play important roles in establishing cold lateral surface flows, which promote mixing and further silica precipitation. As at least several of these factors are probably influencing the evolution of any given geothermal field, the consideration of a single factor in isolation begs a cautious interpretation. For instance, at Ohakuri there is evidence for silica deposition promoting fluid sealing and consequent hydrofracturing. In contrast, fault reactivation at Te Kopia has led to local adjustments of the water table, which has consequences for the extent of geothermal activity. Fault rupture also introduces transient changes to the lateral and vertical flow regimes, and favours along-strike migration of geothermal expression. Hydrothermal mineralisation may play a role in driving fault rupture, by sealing sections of the relatively weak fault plane, leading to transient fluid overpressures that lower the normal stress and promote reactivation. Coseismic permeability increases associated with fault reactivation promote high mass flow rates, an increased rate of mineral precipitation, particularly at the surface, leading to further hydrofracturing.

The force of the water crushes and splits the brittle rocks; and when they are broke and split, it forces its way through them and passes on...

- Georgius Agricola (1494-1555)

8 Seismic perturbation of geothermal systems

Hydrological effects associated with earthquakes have been noted for more than two thousand years and include changes in streamflow, well levels, geyser periodicity and hot spring temperature, or liquefaction. These effects are derived from either a change in pore-fluid pressure linked to changes in rock stress, or changes in permeability through seismic damage of the crust or fracture closure. In the TVZ, the active seismicity modelled in Chapters 2-4 is juxtaposed on a unique hydrological setting: a large-scale geothermal convection system. The models presented in this chapter consider three effects exerted by active dip-slip faults on geothermal circulation: (i) upflow that develops over long timescales in the presence of a low permeability, inclined fault; (ii) short-term effects on circulation caused by a diffusing, coseismic pore-pressure anomaly, obtained from rock stress changes modelled in Chapter 2; and (iii) coseismic increase in fault-plane permeability.

Geothermal upflow localises along the fault plane in both fault blocks but the greater heat output occurs in the footwall block. Here, rising fluids are physically deflected by the low permeability fault resulting in a high surface heat output in the footwall scarp; this is similar to surface expression at Te Kopia geothermal field, situated on the Paeroa Fault (see Figure 1.3). Of the two earthquake effects modelled

here, the near-surface pore-pressure disturbance has the greatest immediate effect on circulation, increasing heat and mass flow at the surface of the field for a period of several weeks. However, over longer time-periods, coseismic damage to fault permeability, and a consequent reduction in its efficacy as a fluid-flow baffle, results in a migration of geothermal expression into the hanging wall from its original locus on the footwall scarp.

Work presented in this chapter is drawn from a paper submitted to the Journal of Geophysical Research in April 2012 (Dempsey *et al.*, 2012a). Results and text included in this chapter are largely unchanged from the submitted version as permitted by the University of Auckland under the *2008 Statute and Guidelines for the Degree of Doctor of Philosophy (PhD)*. Co-authors of this work Dr Rosalind Archer, Dr Susan Ellis, and Dr Julie Rowland advised and commented on the manuscript, however the bulk of the research and preparation for publication was undertaken by the thesis author (see accompanying declaration).

8.1 Introduction

In addition to ground shaking and accumulated, permanent deformation, earthquakes are responsible for a host of hydrological changes in the subsurface. These include changes in ground-water levels (Quilty and Roeloffs, 1997; Grecksch *et al.*, 1999), spring outflow (Muir-Wood and King, 1993; Rojstaczer *et al.*, 1995), and hot-spring temperature (Mogi *et al.*, 1989), as well as liquefaction arising from undrained consolidation (e.g., Poulos *et al.*, 1985) or the passage of seismic waves (Wang and Manga, 2010). These effects are broadly divided into several categories (Montgomery and Manga, 2003): near-, intermediate- and far-field (Wang and Chia, 2008; Wang and Manga, 2010) with respect to the fault rupture; permanent versus transient; and immediate versus delayed response.

Static stress changes associated with coseismic compression and expansion of the crust have been proposed to explain changes in ground-water levels observed in wells. The theory underpinning this concept asserts that compression of the crust reduces

pore volume and increases the local pore-pressure, thereby raising groundwater levels in nearby wells. The idea has received some support from correlations of locations and magnitudes of coseismic well-level changes with changes in the coseismic stress field generated from elastic dislocation models (Okada, 1992) of the fault rupture. For instance, Quilty and Roeloffs (1997) applied the approach to the 1994, $M = 4.7$ Parkfield earthquake, California, and found quantitative agreement between strain changes and well-level changes at four locations, although disagreement at three others. Grecksch *et al.* (1999), in applying this technique to the 1992, $M = 5.4$ Roermond earthquake, Germany, recorded reasonable agreement between the sign of well-level and volume strain changes, although the amplitude of predicted well-level steps were less than those observed. Zhang and Huang (2011), in analysing the $M = 8.0$ Wenchuan earthquake, China, found a correlation between well-level response and the Skempton parameter, B, which couples coseismic rock stress and pore-pressure changes; they concluded that poroelastic effects on well-level are restricted to an epicentral distance 1.5 times the length of the fault. In terms of the aforementioned categorisation then, the poroelastic effect is typically near-field, transient, and exhibits an immediate response.

Sustained changes to well levels and streamflow are thought to represent permanent changes in the subsurface permeability from which those fluids are derived (Rojstaczer and Wolf, 1992). For instance, a reduction in surface permeability and subsequent expulsion of fluids through liquefaction and aquifer consolidation (Manga *et al.*, 2003; Montgomery *et al.*, 2003), has been proposed as the cause of increased post-seismic streamflow. Others (Briggs, 1999; Rojstaczer and Wolf, 1992) interpret an immediate, coseismic increase in streamflow followed by a gradual exponential decay, to represent an increase in subsurface permeability that facilitates the release of water from aquifers. As evidence, Briggs (1999) cites exponential decay from a post-seismic streamflow high, which is conceptually consistent with simple models of finite reservoir discharge through a restricted aperture. In comparison to poroelastic effects, these hydrological responses occur over a variety of epicentral distances, and may exhibit a delayed or building flow-rate (Rojstaczer and Wolf, 1992; Manga

et al., 2003) that persists over a range of time-frames (Briggs, 1999; Montgomery *et al.*, 2003).

Further evidence for far-field coseismic changes in permeability is derived from a study of geyser periodicity in response to earthquakes. Ingebritsen and Rojstaczer (1996), using numerical simulations and representing a geyser as a permeable conduit embedded in a less permeable rock matrix, showed that eruption frequency is highly sensitive to conduit permeability. Small increases in permeability associated with static or, more-likely in the far-field, dynamic strain changes can increase eruption frequency. Thus, a temporary decrease in eruption frequency at "Old Faithful" geyser in Calistoga, California following the Oroville and Loma Prieta earthquakes (Ingebritsen and Rojstaczer, 1996), both of which were centred more than 130 km from the geyser, suggests a transient drop in conduit permeability. Alternatively, geyser frequencies increased at Yellowstone following the Hegben Lake (Montana, $M = 7.3$, distance ∼50 km), Borah Peak (Idaho, $M = 7.0$, distance ∼230 km) (Ingebritsen and Rojstaczer, 1996) and Denali fault (Alaska, $M = 7.9$, distance ∼3100 km) earthquakes (Husen *et al.*, 2004). Similarly, an increase in the lake-level cycling-frequency at Inferno Crater Lake, Waimangu geothermal field, New Zealand, was observed in the period following Edgecumbe earthquake (New Zealand, $M = 6.3$, distance ∼50 km) (Vandemeulebrouck *et al.*, 2008). These changes suggest increases in conduit permeability associated with either static coseismic strain changes, or, in the case of the Denali fault earthquake, the passage of seismic waves.

Others have suggested that anomalous fluid expulsion from fault zones following major earthquakes may be caused by the rupture of deep, over-pressured reservoirs (Sibson, 1985; Byerlee, 1993). In these scenarios, the fluids themselves play a critical role in fault rupture by reducing the normal stress on the fault and increasing its likelihood of failure. Indeed, the migration of fluids in the post-seismic period has been linked with distributions of aftershocks (Miller *et al.*, 2004; Lindman *et al.*, 2010) through their interaction with the rock stress state.

This chapter presents results from a computational model that considers the effects on geothermal circulation of relatively rapid pore-pressure and permeability

changes associated with a normal fault earthquake. The principal objective of the study is to investigate and quantify the influence of dip-slip faults on geothermal upflow. The model is specific to earthquake rupture and natural geothermal circulation occurring within the Taupo Volcanic Zone (TVZ), New Zealand. The TVZ is a productive volcanic arc, which hosts convective upflow of high temperature fluids ($> 250°C$) at more than 20 distinct locations (Bibby *et al.*, 1995). Geothermal circulation is driven by extensive magmatic intrusion in the lower and mid-crust, which supplies heat to the upper-crust at a depth of 6-8 km (Bryan *et al.*, 1999). Fluid circulation is assisted by an abundance of normal fault structures, which accommodate 5-15 $\mathrm{mm\,yr^{-1}}$ of tectonic extension (Wallace *et al.*, 2004), and are presumed to make a significant contribution to the fracture permeability of basement rocks (Grindley and Browne, 1976; Wood *et al.*, 2001).

The model presented here specifically considers both the long-term influence of structural permeability associated with a mature normal fault on geothermal circulation, as well as the immediate hydrological effects of fault rupture. A distorted, structured mesh is used to describe flow and specify permeability properties along an inclined plane, representing the fault. Steady-state geothermal convection is simulated and the evolved circulation reflects the structural permeability of the fault. Coseismic changes in pore-pressure are imported from a separate mechanical model for fault rupture (Dempsey *et al.*, 2012b,c), which captures pressure changes in the near-surface and at seismogenic depths. A concurrent, coseismic increase in fault permeability that permanently reduces the effectiveness of the fault as a fluid-flow barrier is also considered.

8.2 Numerical methods

In this study, three effects of dip-slip faults on fluid flow are considered: a long-term, static perturbation of natural-state convection caused by an impermeable fault-core (Grindley and Browne, 1976; Caine *et al.*, 1996); a short-term disturbance of the pore fluid pressure; and a concurrent increase in fault-core permeability. The first effect

is distinct from the other two in the sense that the circulation state is permitted to evolve over long time-periods in the presence of the perturbation. In contrast, coseismic changes in pore-fluid pressure or fault permeability rapidly perturb steady-state circulation. The post-seismic period is characterised by diffusion of the fluid pressure disturbance, and a transition to a different steady-state under the new permeability distribution.

From a numerical perspective, short- and long-term effects of structural permeability on fluid flow are relatively straightforward to test. One requires a computational model for heat and mass transfer (Salve and Oldenburg, 2001; McLellan *et al.*, 2010), a mesh that honours the fault geometry (McLellan *et al.*, 2010), and a permeability distribution that accounts for structural permeability associated with the fault (López and Smith, 1996; McLellan *et al.*, 2010). In contrast, investigating the effects of pore-pressure disruption requires an additional source of information: a 3-D distribution of coseismic stress changes. In previous investigations, a 3-D elastic displacement model was obtained from an inversion of coseismic surface displacement associated with the specific earthquake (Okada, 1992; Quilty and Roeloffs, 1997; Grecksch *et al.*, 1999). In contrast, in this investigation a precursor model is used, which describes static stress changes associated with rupture of dip-slip faults. These stress changes are converted to a pore-pressure perturbation, which then modifies the pressure distribution of the natural-state circulation model. In low temperature settings, fluids can be approximated as isodense and isoviscous, and the diffusion of a pressure disturbance, ΔP, through a homogeneous permeability medium is governed by

$$\frac{d}{dt}\Delta P = D\nabla^2(\Delta P), \tag{8.1}$$

where D is hydraulic diffusivity (Neuzil, 2003; Lindman *et al.*, 2010). This approach, coupled to a Mohr-Coulomb failure criterion, has been used to model aftershock sequences in response to diffusing pore-pressure disturbance created by the main shock (Lindman *et al.*, 2010).

In geothermal settings, the isothermal assumption is not valid; viscosity and

permeability vary by several orders of magnitude depending on temperature and depth, and the density of hot upflow is up to 25% lower than cooler, meteoric waters. Under these conditions, a description of coupled heat and mass transfer is required to adequately model diffusion of a pore-pressure disturbance.

8.2.1 Mechanical fault model

Coseismic stress changes are modelled by considering displacement of an inclined, frictional contact surface embedded in a 2-D, plane-strain, elastic-viscous-plastic crust. This model has previously been used to investigate post-seismic surface deformation in compressional environments (Ellis *et al.*, 2006), and stress rotation, post-seismic recovery (Nüchter and Ellis, 2010), energy flow (Dempsey *et al.*, 2012b) and fault zone evolution (Dempsey *et al.*, 2012c) in extensional environments. Model methods are described briefly here, and the reader is directed to the aforementioned references for further detail.

The evolution of stress, strain and displacement in the vicinity of a normal fault over multiple seismic cycles is modelled using the finite element software package Abaqus/Standard (Dassaut Systèmes Simulia Corp., 2008). A single fault, approximated as a planar frictional contact surface, is hosted within a 60×25 km crust, which is loaded by extensional velocity boundary conditions of $12\,\mathrm{mm\,yr^{-1}}$ (Figure 8.1(a)). Deformation of the crust is linear elastic while the stress state is below yield, and limited by Mohr-Coulomb failure in the upper-crust transitioning to viscous creep in the lower-crust at a depth of 6-8 km (Dempsey *et al.*, 2012c). The depth to the brittle-ductile transition is determined by material parameters, the temperature gradient ($35^{\circ}\mathrm{C\,km^{-1}}$) and the bulk strain rate ($6 \times 10^{-15}\,\mathrm{s^{-1}}$).

An initial stress state (Figure 8.1(b)) for the model is "spun-up" (Hetland and Hager, 2006; Ellis *et al.*, 2006) by applying the extensional boundary conditions over a long time period (90 kyr). The seismic cycle is approximated by two steps: a 220 yr loading period in which relative displacement of the contact surfaces is prevented by an infinite friction coefficient; this is followed by a 60 s seismic period where fault slip at a weakened friction coefficient of 0.2 (e.g., Scholz and Engelder,

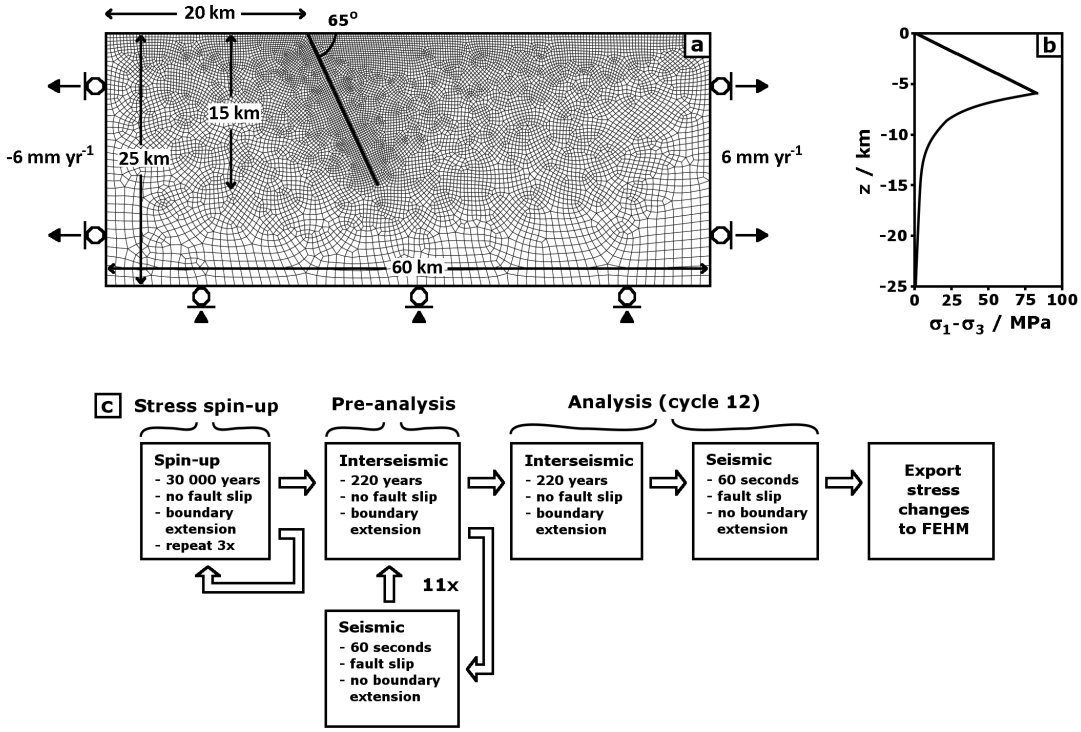

Figure 8.1: Set-up of the mechanical model. (a) Geometry and boundary conditions for the planar fault simulation superimposed on the model mesh. (b) Initial differential stress profile developed after the stress "spin-up" phase. (c) Flow diagram showing boundary conditions, fault properties and timescales associated with the mechanical model. This figure has been adapted from Dempsey *et al.* (2012c).

1976) is permitted. This approach ignores dynamic effects such as wave propagation and rate-state friction. Dynamic equilibrium, characterised by self-similar patterns of stress and elastic deformation, is observed after ten seismic cycles, and results exported to the circulation model are derived from the twelfth cycle (Figure 8.1(c)).

Stress changes associated with a planar fault geometry (Figure 8.1(a)) are considered; the fault dips at 65° and intersects the crust to a depth of 15 km. The chosen fault dip is consistent with the average dip of faults in the TVZ (Villamor and Berryman, 2001), although there is evidence for coseismic slip on fault planes as shallow as 45° (Anderson *et al.*, 1990). The model domain is meshed using approximately 10 000 elements.

8.2.2 Coseismic stress changes

Following Rice and Cleary (1976) and Lindman *et al.* (2010), a relation between changes in pore-pressure and rock stress is derived from

$$m - m_0 = \frac{3\rho_0(\nu_u - \nu)}{2GB(1+\nu)(1+\nu_u)}\left[-\sigma_{kk} - \frac{3}{B}p_f\right], \tag{8.2}$$

where $m - m_0$ is the change in fluid per unit volume, ρ_0 is fluid density, ν_u and ν are the undrained and drained Poisson ratios, G is shear modulus, B is Skempton's coefficient, σ_{ij} is the stress tensor (negative in compression), and p_f is pore fluid pressure. It is assumed that coseismic stress changes are sufficiently rapid that induced fluid transport is negligible during the seismic period. Then $m - m_0 = 0$ and Equation (8.2) reduces to a version of Skempton's (1954) original empirical equation

$$\Delta p_f = -\frac{B}{3}\Delta\sigma_{kk}. \tag{8.3}$$

Equation (8.3) allows the import of stress changes, $\Delta\sigma_{ij}$, derived from the mechanical model into the circulation model. In these simulations, B is set to 0.7 following Talwani *et al.* (1999) and Deng *et al.* (2010).

Figure 8.2(b) shows changes in mean rock stress, $\Delta(-\sigma_{kk}/3)$, associated with the modelled fault rupture. The distribution illustrates three significant stress changes associated with a normal fault earthquake. First, a widespread mean stress increase is observed in the hanging wall at the base of the fault; this is caused by subsidence of the upper-crust and a gradient in fault slip at mid-crustal depths (6-9 km). The greatest mean stress increase, $\sim$ 1 MPa, occurs on the fault plane at a depth of 7.5 km. Second, on the other side of the fault plane, in the footwall block, a large mean stress drop is observed. Expansion of the rock associated with this mean stress drop contributes to uplift of the footwall at the surface (Dempsey *et al.*, 2012b). Finally, at the surface of the footwall, as well as part of the hanging wall, a widespread increase in mean stress occurs. This is caused by horizontal recoil of the two fault blocks away from one another, and an associated horizontal compression of the crust.

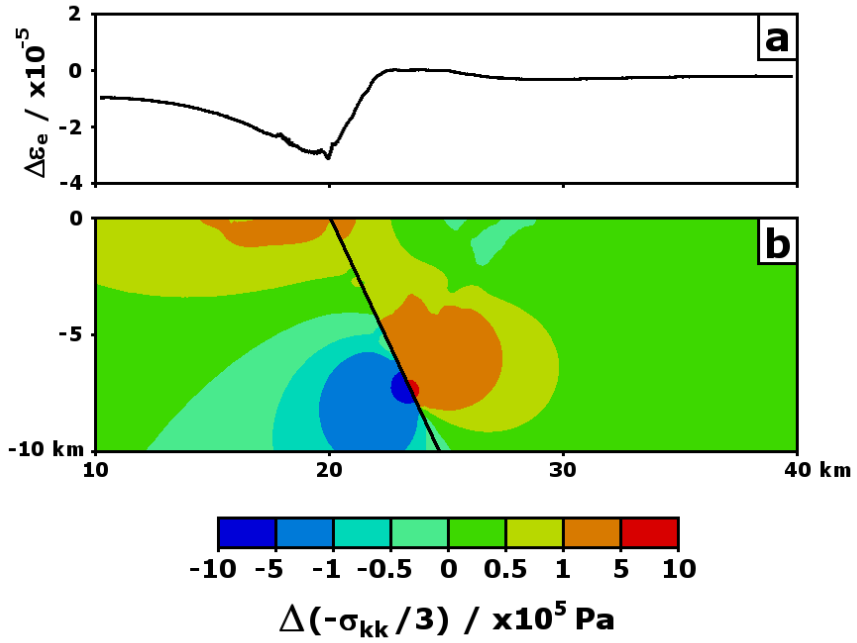

Figure 8.2: (a) Coseismic change in horizontal elastic strain, $\Delta\epsilon_e$, averaged over the top 500 m of the model for the planar fault geometry. A negative change in elastic strain indicates compression. (b) Coseismic change in mean rock stress ($\Delta(-\sigma_{kk}/3)$) for the twelfth seismic cycle. Note that contour intervals are not evenly spaced.

Figure 8.2 also indicates a small mean stress drop in the near-surface of the hanging wall at a distance of ∼5 km from the fault. This feature is associated with flexure of the hanging wall (e.g., Kusznir *et al.*, 1991) and brittle failure in the near-surface. While pore-pressure changes in this region are minor in comparison to others, permanent strain caused by reactivation or extension of existing fractures is relevant to the long-term evolution of the fault system (Dempsey *et al.*, 2012c). The development of structural permeability associated with this strain might also effect the long-term stability of fluid flow in the region, although this scenario has not be modelled here.

Single-event dip-slip displacement of the fault surface of 0.83 m can be used to derive an estimate for the magnitude of the modelled earthquake (Hanks and Kanamori, 1979). For a shear modulus of 4 GPa, and a 25-km-long surface rupture, the modelled

earthquake has an approximate magnitude, M, of 5.7.

8.2.3 Circulation model

Fluid flow models are constructed using the Finite Element Heat and Mass (FEHM) transfer code (Zyvoloski, 2007), which is capable of modelling multi-phase, multi-component Darcy flow through permeable media. This code has previously been used to model convection in air (Stauffer *et al.*, 1997), and groundwater convection modified by dynamic permeability in heated (Dempsey *et al.*, 2012e) and cool environments (Chaudhuri *et al.*, 2009). This chapter is concerned with perturbations to a single convective plume, and therefore the computational domain must be large enough to encompass both a central upflow region and downward recharge on the plume flanks. Figure 8.3(a) shows the grid used to model the fault geometry, assuming no change in the along-strike direction (y). This assumption is reasonable for faults that are considerably longer than the diameter of the geothermal plume (e.g., the 30 km long Paeroa Fault of the TVZ). The model domain is 15×15 km in plan view, which is large enough to encompass downward recharge for a single plume. The model extends to a depth of 8 km, which is presumed to correlate with the approximate depth of the brittle-ductile transition in the TVZ (Bryan *et al.*, 1999), the limit of fracture permeability, and thus the base of the convective system (Bibby *et al.*, 1995). This also corresponds to the transition between brittle and ductile deformation in the mechanical model, which occurs across a depth interval of 6-9 km (see Section 3.3).

A convection cell is produced in the centre of the computational domain by applying a spherical Gaussian temperature boundary condition at the base of the model. Temperatures range from 150°C on the edge of the domain to 340°C in the centre, the latter being consistent with brittle-ductile transition temperatures of 300-350°C for quartzofeldspathic rock. This is higher than the 280°C at 8 km depth in the mechanical model; however, temperatures at the base of the circulation model represent those conceivably perturbed by a magmatic intrusion upon which hydrothermal circulation is localised. In contrast, temperatures at 8 km depth in the

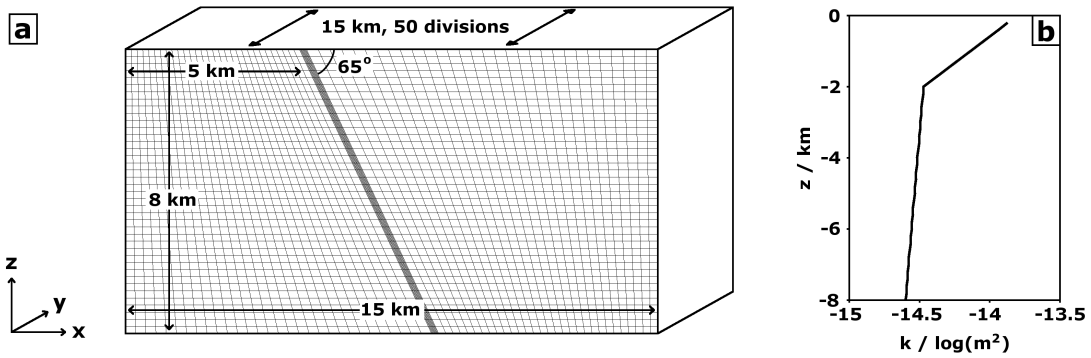

Figure 8.3: Set-up for the circulation model. (a) Model mesh and dimensions used to describe planar fault geometry. The mesh is discretised into 50 evenly spaced slices in the y-direction (not shown). The fault plane is comprised of ten layers, spaced 1 m apart in the x direction. (b) Background permeability distribution (i.e., not accounting for fault permeability) with depth.

mechanical model represent along-strike average rift properties.

Two zones of differing permeability properties are used in these models. The upper two kilometres of the TVZ is characterised by a variety of low density, Quaternary volcanic strata, laid down by frequent volcanic eruptions over the previous 2 Myr (Wilson *et al.*, 1995). Permeability is supplied by horizontal contacts between distinct geological units, as well as extensive faulting and fracturing maintained by the high horizontal extension rate (Wallace *et al.*, 2004). Below the surficial deposits, fluid flow is hosted within fractured, greywacke basement rock. The effects of pore compaction in the upper zone, and fracture closure in the lower zone, are approximated by an exponentially decreasing permeability profile with depth (Saar and Manga, 2004). Figure 8.3(b) shows model permeability with depth away from the fault zone.

Mesh design and fault permeability

The mesh used in the circulation model is specifically constructed to implement a description of cross-fault permeability. Faults exhibiting a mature core of clay or other gouge material, surrounded by extensive regions of fracturing (the damage

zone; e.g., Caine *et al.*, 1996), can operate as either fluid conduits or baffles (Caine *et al.*, 1996; Rowland and Sibson, 2004) depending on the direction of fluid flow. Cross-fault permeability is typically lower than that parallel to the fault plane, and several methods exist to implement these properties numerically. A non-diagonal permeability tensor provides the most direct method of distinguishing across and along fault permeability; however, this capability is not available in FEHM. Alternatively, for regular, structured grids, one can superimpose the geometry of the fault core on the mesh, and then reduce the permeability of nodes contained within. For dip-slip fault geometries, this produces a stepped mesh and, to prevent fluid communication, the fault core must be several elements wide. A refinement of the second method, implemented here, involves a steady distortion of the structured mesh so that it honours the geometry of the fault in the centre of the domain (McLellan *et al.*, 2010). For a planar fault (Figure 8.3(a)), this involves an incremental increase in the tilt of each successive vertical y-z nodal plane, and a complementary decrease on the opposite side of the fault. It is noted that this mesh does not account for the topographical offset between two fault blocks that naturally evolves after many seismic cycles. The mesh distortion creates relatively large aspect ratios for some elements; however, it is shown in Section 8.3 that the effect on the model results is minor.

The meshed fault zone is comprised of eleven, evenly spaced nodal planes. The fluid baffling effect of the fault is approximated by a permeability contrast between the fault core and the surrounding, undamaged country rock. In the model, two of the central nodal planes represent fault core and are assigned a permeability decrease of some specified order of magnitude. Thus, fault core is not characterised by some constant permeability value, but rather by some offset of the depth-dependent permeability distribution shown in Figure 8.3(b). This approach could be modified to consider enhanced fluid flow through a permeable fault damage zone. However, modelling the permeability increase in this region would require a description of the along-strike fault-tip geometry in three-dimensions, which has not been undertaken here.

The thickness of the fault core depends on the spacing between the fault-zone nodal planes assigned core permeability. These models use a nodal plane spacing of 1 m and a fault core permeability contrast of -4 orders of magnitude. Observations of well-developed, impermeable fault gouges indicate these are typically no thicker than 10 m (Caine *et al.*, 1996) and the modelled thickness is therefore reasonable. Fault core permeability varies with fault displacement, degree of thermal or chemical alteration (Olsen *et al.*, 1998), and the presence or absence of clay minerals (Morrow *et al.*, 1984). Assigning a constant permeability reduction to the modelled fault core therefore represents a significant, but necessary, simplification of its true distribution and variability in both time and space. Nevertheless, the chosen reduction of four orders of magnitude results in core permeabilities between $1.3 \times 10^{-18}\,\mathrm{m}^2$ and $2.5 \times 10^{-19}\,\mathrm{m}^2$, which is consistent with laboratory studies of simulated fault gouge (Morrow *et al.*, 1984; Ikari *et al.*, 2009).

Import of pore-pressure changes into circulation model

Coseismic pore-pressure disruption is modelled by exporting stress changes from the mechanical model as pore-pressure changes to the circulation model. As the mechanical model is two-dimensional, extrapolation of the stress changes in Figure 8.2(b) to three dimensions is required. There are several procedures for doing this, all of which are approximations of the true three-dimensional coseismic stress perturbation. The plane-strain model of fault mechanics describes the middle section of a fault and implicitly assumes that stress changes are constant for an infinite distance along-strike. In reality, this assumption is only accurate over a limited distance, which itself is a function of the length of the fault. In the construction of the computational mesh, and in applying fault core permeability, it is assumed that the dimension of the fault is large compared to the diameter of the geothermal plume. Consistent with this assumption, the stress changes in Figure 8.2(b) are extrapolated in the along-strike (y) dimension of the model without alteration; this 3-D distribution is used as the basis for pore-pressure perturbation in the circulation model.

This method might be extended to consider a reduction in the size of the stress

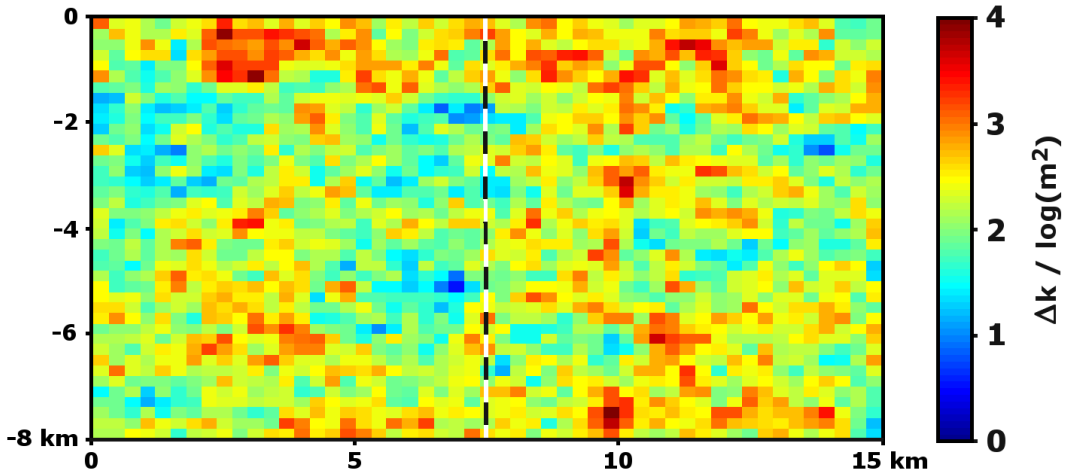

Figure 8.4: Example fluctuation field applied to the fault-plane permeability distribution to simulate the effects of fault rupture. The mean and standard deviation for the change in permeability (Δk) are 2.3 and 0.5 orders of magnitude, respectively. Maximum and minimum permeability increases are 3.9 and 0.5 orders of magnitude, respectively. The black and white dashed line at $y = 7.5\,\text{km}$ indicates the position of the observation plane in Figure 8.11

perturbation with increasing proximity to the along-strike fault tips. Both long-term displacement rates and single-event displacements on large normal faults indicate that dip-slip decreases towards ends of the fault trace (e.g., Scholz, 1990; Walsh *et al.*, 2002). This might reasonably be expected to manifest as a similar decrease in the magnitude of the coseismic stress change in an along-strike direction, and could be represented numerically using a displacement-length scaling relationships (Dawers *et al.*, 1993; Schlische *et al.*, 1996) that imposes a non-linear decrease in the pore-pressure perturbation with increasing along-strike distance from the centre of the computational domain. This approach does not account for along-strike changes in shape or position of the contours in Figure 8.2 associated with a shallowing tip line (e.g., Crider and Pollard, 1998) or decreased slip. The stress perturbation would be better resolved by a 3-D model of fault rupture; however, constraints on computational resources have thus far prevented description of a 3-D fault surface at the necessary resolution.

The coseismic pore-pressure perturbation, derived from changes in mean stress (Figure 8.2) and Equation 8.3, is introduced to the circulation model by modification of the fluid pressure distribution. A hydrothermal convection cell is established by applying the temperature boundary condition to the base of the model domain for a nominal time period (300 kyr). The steady-state flow-field that develops depends on the distribution of permeability modified by the presence of the fault. Temperatures and pressures at steady-state serve as initial conditions for the next simulation, with the initial pressure distribution modified to include the coseismic effect. Circulation is modelled for a period of ten years following the earthquake to investigate the temporal response of the system to seismic perturbation. Linear interpolation is used to export stress changes from the unstructured grid of the mechanical model (Figure 8.1(a)) to the structured grid of the circulation model (Figure 8.3(a)).

Several studies of hydrological changes following major earthquakes suggest long-lived or permanent changes in permeability may be responsible for increased stream-flow or well levels (e.g., Rojstaczer and Wolf, 1992; Montgomery *et al.*, 2003; Manga *et al.*, 2003). These explanations invoke either aquifer consolidation or changes in the distribution and conductivity of fracture networks. In addition to pore-pressure perturbations, the effect on circulation of permanent changes in fault-gouge permeability is considered; physically, this represents damage of the fault gouge and disruption of its role as a fluid baffle (Sibson, 1994). Seismic cycling of fault core permeability and subsequent mass flows associated with decompression boiling can lead to rapid silica precipitation and permeability sealing (e.g., Caine *et al.*, 2010); this second-order response of fault permeability is not considered here. To approximate the effects of a randomly disrupted fault gouge, a stochastic, spatially correlated fluctuation field (Figure 8.4) is superimposed upon the low permeability fault plane. This is an approximation to the inherent spatial heterogeneity associated with the material strength of the fault core and fracture networks. Based on observations of well-core from fractured oil reservoirs (Leary and Al-Kindy, 2002), a power-law with an exponent of -1.3 is used to describe the spatially correlated fluctuation; however, the method is not restricted to this specific choice and alternative distributions are easily

implemented. The permeability fluctuation imposes a mean increase of 2.3 orders of magnitude and is limited to a maximum increase of 4 orders of magnitude.

As with the pore-pressure model, ten years of circulation is modelled under the new permeability distribution using steady-state circulation as an initial condition. As post-seismic fault-plane permeability in any given simulation is arbitrary, a set of 100 simulations is performed to study the mean effects on circulation of cross-fault permeability disruption, as well as to provide some constraint on the variability that might be observed. It is noted that this approach does not consider the effects of mechanical or chemical sealing of the fault gouge in the modelled post-seismic period (Olsen *et al.*, 1998).

8.3 Plume development around an impermeable fault

The shape and structure of a geothermal plume is often constrained by considering the distribution of temperature contours (e.g., Kissling and Weir, 2005; Coumou *et al.*, 2008) or some proxy for temperature, e.g., hydrothermal alteration (Simmons and Browne, 2000) or resistivity (e.g, Heise *et al.*, 2008). Alternatively, if the principal interest in the convective cell is restricted to its ability to transport heat to the surface from depth, then contours of heat flux are also useful in demarcating plume structure. Figure 8.5 shows temperature and heat flux contours for a vertical slice through the centre of the modelled convection cell. As a point of comparison, and to illustrate that the influence of the distorted mesh (Figure 8.3(a)) on the modelled circulation is minor, a convective plume evolved in the absence of an impermeable fault is also shown (Figure 8.5(a,c)).

In the footwall block, fluids heated at the base of the model rise buoyantly until they encounter the impermeable fault core. Here they are deflected and guided along the underside of the fault to the surface; a process that drags the unperturbed temperature contours (Figure 8.5(a)) in the negative x direction. Heat transfer through the upper 4 km of the footwall is nearly adiabatic and averages 110-120 MW, with the greatest outflow of hot fluids occurring immediately adjacent to the fault

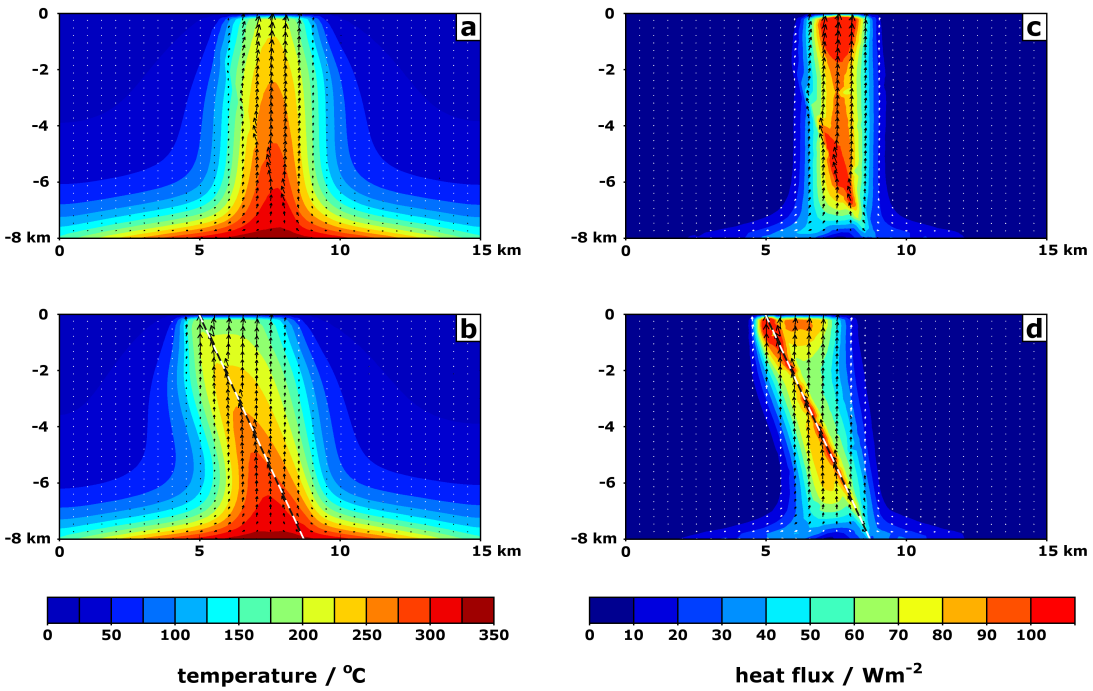

Figure 8.5: Thermal characteristics of a vertical slice through the centre of the modelled convective plumes. Temperature contours are shown for (a) an unperturbed plume (no fault permeability), and (b) a plume deflected by low fault core permeability. Vectors superimposed on (a-b) indicate the direction and relative magnitude of mass flux. Contours of heat flux magnitude are shown in (c-d) and correspond to the models in (a-b). Vectors superimposed on (c-d) indicate heat flux direction. The position of the fault in (b) and (d) is indicated by a black and white dashed line.

scarp. In comparison, heat transfer in the hanging wall is somewhat less than the adjacent footwall, averaging 90-110 MW.

Heat and mass flux in the hanging wall (Figure 8.5(d)) exhibit a tendency to adhere to the fault plane, although not to the extent of the footwall, where flow is physically restricted by a permeability barrier. Nevertheless, hanging wall upflow is directed up-dip in the near-fault region and the greatest heat fluxes occur immediately adjacent to the fault plane. As the temperature of the fault core is close to that of the high-temperature upflow in the footwall, the efficiency of vertical heat transfer in the hanging wall is maximised by positioning the high-temperature upflow zone alongside the high-temperature fault. Furthermore, mass recharge for the hanging

wall circulation cell occurs by down-welling of cold, denser fluids in the rest of the fault block. For a given depth, hydrostatic pressure is greater in the down-flow region than the upflow zone, and a horizontal force supplied by the down-flow region upon the upflow zone assists in pinning it to the fault plane.

This mode of circulation shares similarities with analytical and numerical solutions to conjugate conduction-natural-convection problems in vertically partitioned (e.g., Sakakibar *et al.*, 1992; Kahveci, 2007) and inclined (Varol *et al.*, 2010) domains. These studies solve for heat transfer by distinct convecting fluid cells coupled together by conductive heat transfer across a solid partition; however, they typically consider laterally heated domains relevant to the engineering of double-paned windows, fire spreading and nuclear reactors. In contrast, the models presented here consider non-equal basal heating of a domain containing an inclined vertical partition. Convection cells are generated in each fault block, although the degree of coupling across the fault plane distinguishes this problem from the aforementioned analytical and numerical treatments. Total conductive heat transfer across the fault plane totals $\approx$10 MW, which is small in comparison to vertical heat transfer of $\approx$ 200 MW.

Fluids rising along the fault in the hanging wall are slightly cooler than fluids at the same depth in the footwall, resulting in low-level conductive heat transfer between the two fault blocks. This operation is similar to that of a heat exchanger, albeit a very poor one, the efficiency of which depends on the temperature difference across, and the thickness of, the fault core. At 2 m, the thickness of the modelled fault core falls well within the range of field observations (e.g., Caine *et al.*, 1996), although both narrower and wider zones might be expected. In general, cross-fault coupling of the flow regimes would be expected to increase for narrower fault cores with diminished insulation properties. The issue of cross-fault circulation coupling is revisited in Section 8.5 when considering an increase in cross-fault permeability associated with fault rupture.

Heat flux widens perceptibly in the near-surface of the hanging wall as increased fluid velocities in the high permeability layer permit increased heat transfer. The same effect is observed in the footwall, although here flow is restricted to a narrower

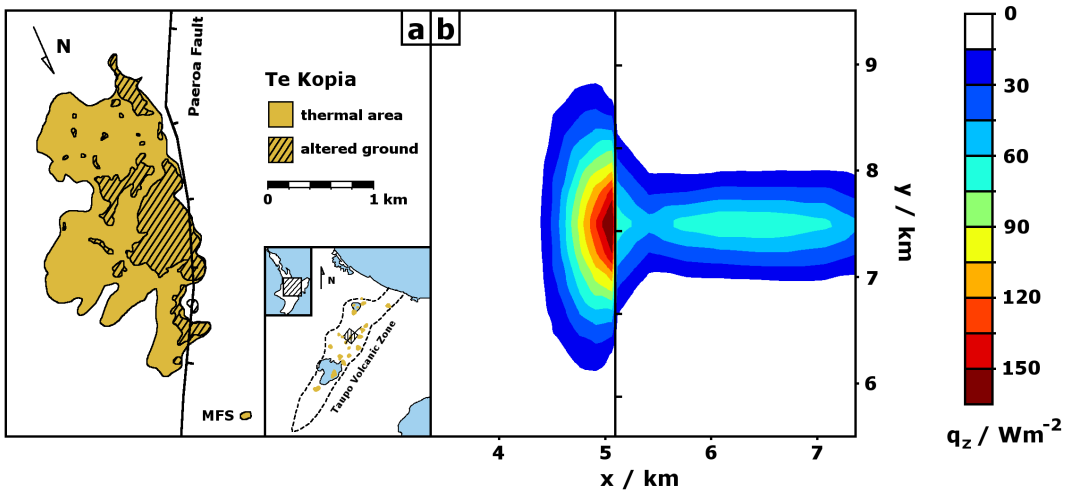

Figure 8.6: (a) Distribution of thermal areas and altered ground at Te Kopia geothermal field (after Bignall and Browne, 1994) on the Paeroa Fault. The location of Murphy's Farm thermal spring (MFS) is shown. Inset shows the regional context of Te Kopia and the Taupo Volcanic Zone. Note that north has been rotated with respect to the inset. (b) Vertical heat flux, q_z, of the model at a depth of 200 m. This plot has been framed so that spatial dimensions and the position of the fault are approximately equal to (a).

region by fault core permeability. Another interesting feature of Figure 8.5(d) is a region of lowered heat transfer at the base of the convective cell in the footwall block. Fluids in this area, while at high temperatures (Figure 8.5(b)), are trapped in a stagnant region in a corner of the model where the fault intersects the BDT.

Figure 8.6 compares the distribution of thermal activity at Te Kopia geothermal field with vertical heat flux at the surface of the model. Thermal manifestations at Te Kopia occur primarily in the footwall block and scarp of the Paeroa Fault, a 30 km long, active, normal fault within the TVZ (Berryman *et al.*, 2008). The fault scarp has been uplifted to a height of ∼220 m at Te Kopia, and geothermal expression in the back-tilted block has probably evolved in response to a gradual lowering of the water table (Bignall and Browne, 1994). The field has an estimated heat output of 125-250 MW (Bibby *et al.*, 1995), which is consistent with the heat output of the modelled plume.

As the models presented here do not account for local topography, permeability

heterogeneity, or a complex fault geometry, comparisons between the model and reality must necessarily discuss broad trends. Spatially, the thermal area and, in particular, regions of altered ground at Te Kopia demonstrate elongation along the strike of the fault. This is consistent with modelled heat flux in the surface of the footwall (Figure 8.6(b)), which demonstrates a similar along-strike trend. The thermal area at Te Kopia extends a greater distance into the footwall block than the modelled field, although this may be due to topographic flows in the back-tilted block that are not accounted for in the model. The modelled plume also demonstrates an elongated, low-level heat flux anomaly in the hanging wall that is apparently absent at Te Kopia. This suggests that the heat source for convection at Te Kopia does not extend into the hanging wall to the same extent that it does in the model.

8.4 Pore-pressure disturbances

As discussed in Section 8.2.2, there are several distinct features of the coseismic stress change that may affect flow at the surface. In summary, these are: an increase in pressure in the hanging wall at a depth of 6-8 km; a decrease in pressure in the footwall at similar depths; and an increase in pressure at the surface, in both fault blocks (see Figure 8.2). The first two effects are associated with slip arrest at the lower tip of the fault, while the latter is caused by horizontal recoil of the fault blocks. This section considers hydrological changes in response to the sum of these stress effects, as well as the contribution of each. Stress effects are denoted by their cause, recoil and slip-arrest, and are broadly differentiated as occurring above and below a depth of 3.5 km, respectively.

Figure 8.7 shows the effects of a diffusing pore-pressure anomaly on heat transport within the geothermal system, for three different times following the modelled earthquake (one day, sixty-two days, and three years). The heat flux anomaly, defined here as the difference between the seismically perturbed and steady-state heat flux distributions, is approximately an order of magnitude less in each successive plot. This simulation considers the total pore-pressure anomaly, i.e., both surface

recoil and the deeper slip-arrest components.

In response to the recoil component of the earthquake, vertical heat flux is increased through a 3 km wide region at the surface of the model. A maximum increase of $>20\,\mathrm{W\,m^{-2}}$ is observed at the footwall scarp, where the maximum steady-state outflow also occurs (see Figure 8.5 and 8.6). The heat flux anomaly is solely comprised of an increased mass flux; the contribution of increased fluid enthalpy is negligible. A corresponding increase in mass flux in the adjacent hanging wall has a lesser effect on geothermal heat output due to relatively low pre-seismic transfer in this fault block.

Pressure anomalies induced by slip-arrest at the base of the fault have contrasting effects on heat transfer in the different fault blocks. In the footwall, an abrupt decrease in pressure creates a tendency for fluids to be drawn towards the centre of the pressure drop. This results in a decrease in vertical velocity above the pressure drop, which, when superimposed on a broad trend of vertical heat flux, produces a negative heat flux anomaly. Effectively, hot, buoyant upflow that is guided along the underside of the fault plane is restrained by a suction created by rock expansion near the fault-tip. The opposite effect is observed in the hanging wall, where an increase in pressure causes expulsion of fluids in a radial direction from the centre of the pressure increase. However, as natural-state heat flux in this region is relatively low (Figure 8.5(d)), the associated heat-flux anomaly is small.

Fluid pressure disturbances caused by the modelled earthquake are naturally redistributed by mass transfer towards pressure lows and away from pressure highs. These flows, which are resisted by fluid viscosity and crustal permeability, occur slowly over periods of months to years. Furthermore, the pressure disturbance decays in magnitude as it propagates away from the source and is diffused within a larger

Figure 8.7 *(following page)*: Anomalous heat flux induced by coseismic perturbation of the pore-pressure at three different times after the earthquake: (a) one day, (b) sixty-two days, and (c) three years. Contours show the change in heat flux, Δq_T, and vectors indicate direction. Both contour intervals and vector dimensions are reduced an order of magnitude from (a) to (b), and from (b) to (c). The position of the fault is indicated by a black and white dashed line.

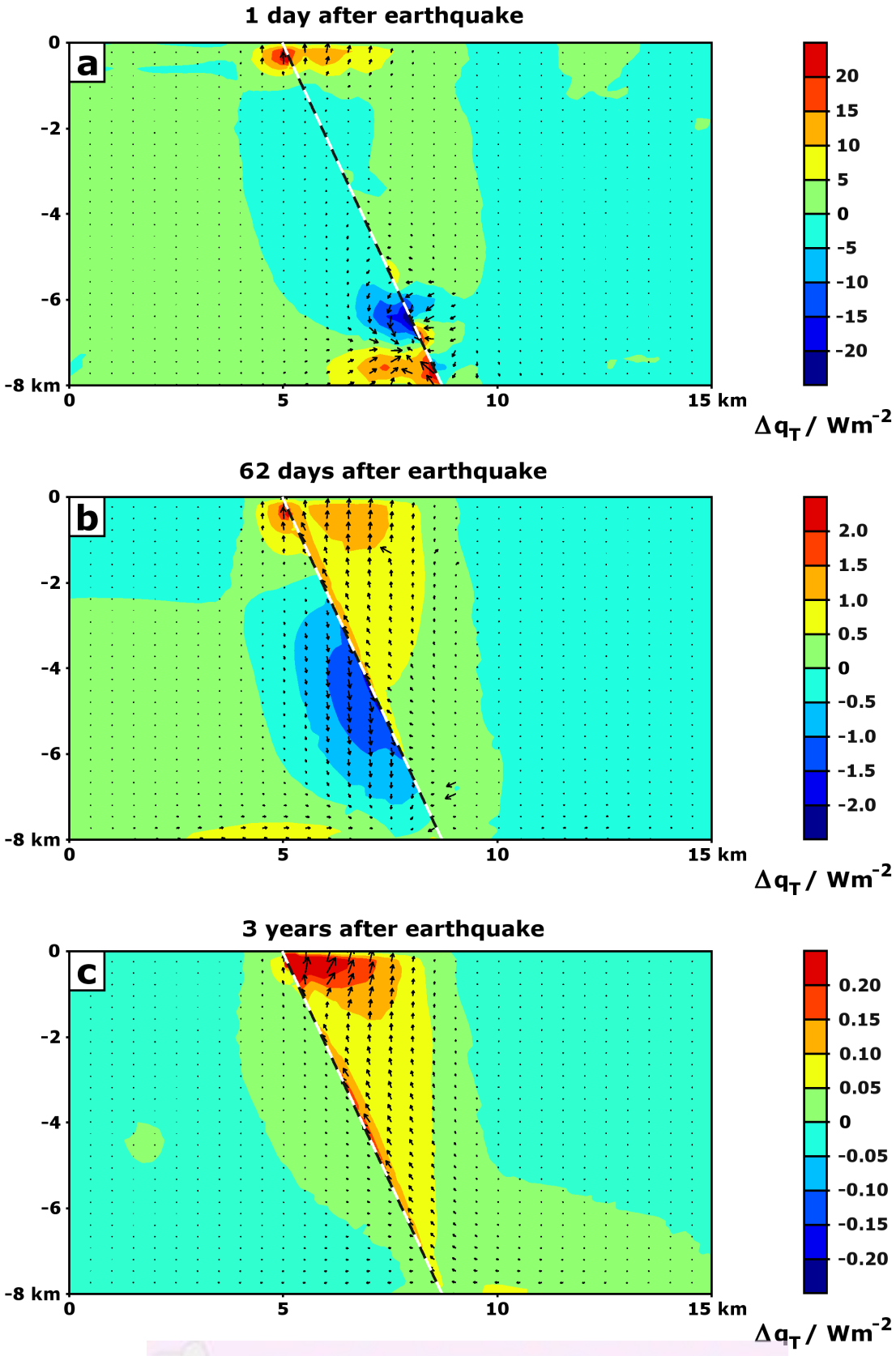

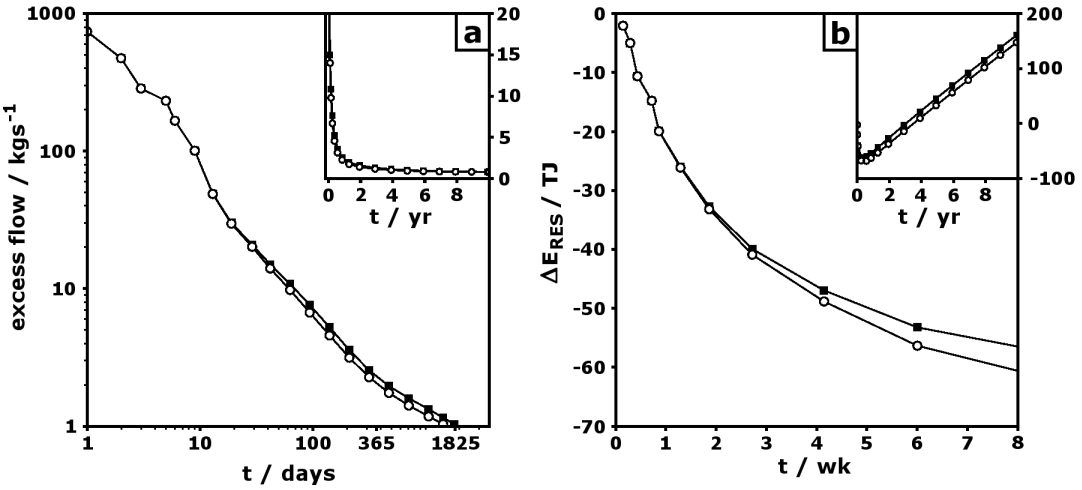

Figure 8.8: (a) Excess total mass flow at the surface in the period following a simulated coseismic pore-pressure perturbation. Post-seismic decay of mass flow is shown on both a log-log and linear (inset) axes. Open circles are for a simulation incorporating only pressure changes at depths shallower than 3.5 km. (b) Change in reservoir heat content (see Equation 8.4) over a period of eight weeks and ten years (inset) following the modelled earthquake.

volume of rock. Two months after the modelled earthquake, heat flux anomalies are approximately one order of magnitude less (Figure 8.7(b)) than their immediate post-seismic values, although surface heat flux still exceeds natural state conditions. Slip-arrest pressure anomalies, which are larger in magnitude than the surface recoil anomaly (Figure 8.2), have migrated upward from mid-crustal depths (6-8 km) and are beginning to exert an influence on surface flow. The initially local negative heat flux anomaly developed at the bottom of the footwall has migrated to a depth of 5 km and is now much broader. This feature continues to migrate upward, nullifying the positive heat flux anomaly produced by surface recoil after a period of 200 days.

In contrast, the positive heat flux anomaly at the base of the hanging wall produced by coseismic compression of the mid-crust, propagates upward and reinforces the positive recoil anomaly at the surface. The additive nature of these pressure disturbances contributes to a positive heat flux anomaly throughout the hanging wall that exceeds the corresponding negative anomaly in the footwall. Furthermore, the

low permeability fault core operates as an effective barrier between the adjacent high and low pressure disturbances, which are permitted to propagate outward into their respective fault blocks, but do not interfere with one another.

8.4.1 Mass discharge

Measurements of excess streamflow following earthquakes capture the anomalous vertical mass flux rate integrated over the area of the stream catchment. An analogous measure is obtained from the model by integrating anomalous mass flux rates at the surface of the model for the period following an earthquake (Figure 8.8(a)). At natural-state, mass is ejected at a rate of $360\,\mathrm{kg\,s^{-1}}$. The immediate effect of the modelled earthquake is to increase mass flux by $740\,\mathrm{kg\,s^{-1}}$, an increase of 206%. In comparison, Muir-Wood and King (1993) noted increases in river flow of 40% following the M 7.3, 1959 Hegben Lake earthquake, Montana, and the M 6.9, 1980 Irpinia earthquake, southern Italy, and an increase of 200% following the M 7.0, 1983 Borah Peak earthquake, Idaho. For these earthquakes, excess mass flow is interpreted in the context of natural, pre-seismic flow rates, which for Idaho were comparatively lower than Montana and Italy. Expulsion of fluids therefore had a larger proportional effect for Idaho. In these examples, both natural state and anomalous flow rates are 1-2 orders of magnitude larger than those modelled here. In terms of a natural state flow-rate, this reflects the discrepancy between the proportion of meteoric rainwater that infiltrates and is circulated through the crust ($\sim$2% for the TVZ; Weir, 2009) versus the larger proportion that ends up as runoff in streams and rivers. In the case of order-of-magnitude greater coseismic fluid expulsion, this is probably due to a comparatively larger magnitude pore-pressure disturbance associated with large magnitude earthquakes (M = 6.9, 7.0, and 7.3, c.f., modelled M = 5.7).

Excess streamflow recedes from its immediate post-seismic maximum, with half-, quarter- and one-eighth-maximum flows recorded 2.6, 5.8, and 9 days after the earthquake. Excess mass flow continues to decay over the following 10 years and the signal to noise ratio rapidly decreases. The likelihood of detecting a post-seismic flow signature is probably low after the first three weeks, as excess flow has receded to less than

10% above natural state. This is in contrast to examples presented in Muir-Wood and King (1993) where excess mass flow is recorded for 6-8 months following the earthquake. These long-lived changes may represent more permanent perturbation to the subsurface permeability structure.

Despite indications of the raw data (Figure 8.8(a) inset), excess flow from the geothermal field does not exhibit (under log transformation) the exponential decay demonstrated by Briggs (1999) for excess streamflow following the 1989, M 7.1 Loma Prieta earthquake, California. Nor does it exhibit a linear decrease proposed by Muir-Wood and King (1993) for increased streamflow following three major normal fault earthquakes in Montana, Idaho or southern Italy.

Excess mass flow profiles for the full pore-pressure disturbance (Figure 8.8, black squares) and for a simulation containing only the surface recoil component (open circles), indicate that changes to surface outflow are, in general, well described by surface processes alone. Profiles are indistinguishable for the first month, after which time migration of the deeper slip-arrest anomaly begins to exert an effect at the surface. An initial, small increase in mass flow is associated with the surface arrival of the hanging wall high-pressure anomaly (see Figure 8.7(b)), and this is followed by a decrease in flow accompanying the later arrival of the footwall low-pressure anomaly (see Figure 8.7(c)). Interestingly, the difference between the full-disturbance and recoil-only profiles corresponds nearly exactly (within an error of $<0.1\%$) to excess flow produced by the slip-arrest-only simulation. This suggests that the diffusive processes modelled here are additive, i.e., that the full phenomenon can be modelled as a superposition of its constituents.

8.4.2 Reservoir effects

Heat stored in the geothermal reservoir can be exploited for electricity generation through the extraction of geothermal fluids. The size of the geothermal reservoir is quantified in terms of stored heat (Grant and Bixley, 2011), calculated as

$$E_{RES} = \int \rho C(T - T_0) dV, \tag{8.4}$$

where E_{RES} is heat energy in the reservoir, ρC is the specific heat of wetted rock (taken as $2.5{\times}10^6\,\mathrm{J\,m^{-3}K^{-1}}$), and T_0 is a reference temperature representing the end point of the thermodynamic cycle (taken as atmospheric 20°C). Stored heat is calculated for the upper 2 km of the model domain, which corresponds to the porous Quaternary volcanic deposits that are typically targeted for production in the TVZ. As waste-water is generally reinjected at temperatures greater than 20°C, this method overestimates reservoir heat content; however, as the objective is to describe reservoir response to an earthquake, i.e., changes relative to some steady-state value, the approximation is sufficient.

Figure 8.8(b) shows changes in reservoir heat content relative to a pre-seismic value of $\sim$ 9 000 PJ. Deviation from the natural state is caused by increased heat fluxes across the boundaries delineating the reservoir, i.e., a horizontal plane at the surface, and a second at a depth of 2 km. Reservoir heat content initially declines in response to the earthquake, largely due to recoil-induced fluid expulsion at the surface. The decline is arrested after of a period of 4-5 months, and is eventually recovered by the background rate of reservoir heating that characterises the quasi-steady state of the system. The maximum reduction in E_{RES} is $\sim$60-80 TJ and the perturbation is therefore minor in comparison to the absolute size of the reservoir.

More significant changes in reservoir heat content require heat flux perturbations that operate on longer timescales. For example, self-sealing geothermal reservoirs that develop low permeability, insulating cap regions above the upflow zone show increases in heat content of $\sim$ 300 PJ over a period of 100 kyr (Dempsey *et al.*, 2012e). Similarly, fault rupture through the cap-zone, which permits enhanced mass flow at the surface for a period of several thousand years, is accompanied by a drop in heat content of $\sim$80 PJ. In contrast, the reservoir perturbations considered here, including pressure and permeability disruptions, suggest that significant changes in the natural state of the reservoir occur over long time periods.

8.5 Disruption of fault gouge

The immediate effect of fault gouge rupture is an increase in advective heat transfer across a fault plane that was previously restricted to conduction. Buoyant upflow, previously deflected along the underside of the fault and largely confined to the footwall block, now rises directly across the fault into the slightly cooler hanging wall. Cross-fault heat flux, which averaged 10 MW in the pre-seismic period, is increased to 215 MW. Depending on the timescales associated with healing and sealing processes (e.g., hydrothermal precipitation; Grindley and Browne (1976); Olsen *et al.* (1998); Dempsey *et al.* (2012e)), the increased heat transfer will have important implications for the post-seismic configuration of geothermal circulation. If self-sealing of the fault gouge is rapid, then an associated rapid-return to pre-seismic fluid flow should be expected, i.e., low-level coupling between footwall and hanging wall circulation.

Figure 8.9(a) shows the mean excess-mass-flow profile, along with two standard deviation limits (grey shading), for 100 simulations of a disrupted fault gouge (e.g., Figure 8.4). Fault rupture is accompanied by an immediate increase in mass flow of $17\,\mathrm{kg\,s^{-1}}$, which builds to a post-seismic maximum of $20\,\mathrm{kg\,s^{-1}}$ occurring 1-3 weeks after the earthquake. Mass flow then recedes to a new steady-state that is 14-$15\,\mathrm{kg\,s^{-1}}$ higher than pre-seismic levels. The initial response, in which mass flow builds, is similar to that recorded following the M 7.1, 1989 Loma Prieta earthquake, California, which also demonstrated increasing flow rates for a period of several days after the earthquake. In this instance, the post-seismic hydrologic response was attributed to an increase in aquifer permeability permitting increased groundwater flow (Rojstaczer and Wolf, 1992) followed by a slow decay in streamflow as the level of the water table dropped and the associated hydraulic gradient lowered. In this simulation, decay in mass flow from its post-seismic high is evident (Figure 8.9(a), inset), although less pronounced.

Changes in heat content of the geothermal reservoir in response to an increase in cross-fault permeability are relatively easier to conceptualise than surface mass flow. Except at very short timescales, an approximately linear increase in heat content

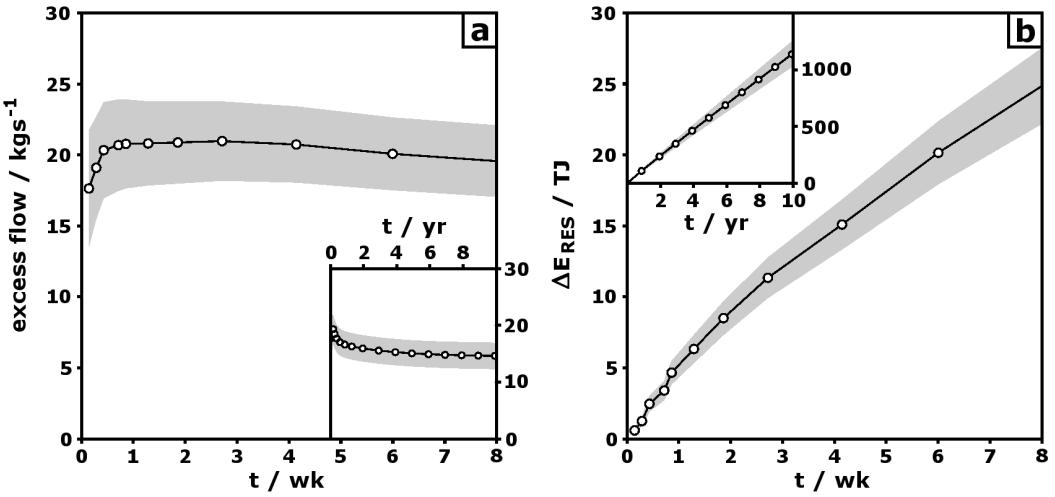

Figure 8.9: Circulation response to a change in fault plane permeability. (a) Excess mass flow averaged over 100 different simulated fault plane ruptures for a period of eight weeks and ten years (inset). The marked line shows the average excess flow, while the grey region demarcates two standard deviations from the mean profile. (b) Change in reservoir heat content (see Equation 8.4) following changes in fault plane permeability.

is observed for the ten years following fault rupture (Figure 8.9(b), inset). As the reservoir considered here is theoretically constrained by horizontal surfaces at $z = 0$ and -2 km, the linear trend in Figure 8.9(b) indicates that (i) basal heat flux into the reservoir exceeds surface heat flux out of the reservoir, and (ii) the total heat flux imbalance in the reservoir is constant over the ten year post-seismic period (such that integration in time produces a linear trend). Variability in the heat flux profiles also reflects the time integration, with an increasing spread with time. This feature is derived from the relatively constant spread recorded in the excess mass flow profiles (Figure 8.9(a)), and the accumulating effect of the excess fluid throughput on the heating of the reservoir.

Over a period of ten years the total perturbation to reservoir heat content is orders-of-magnitude larger than that associated with coseismic pore-pressure disturbances (Figure 8.8(b)). This is a consequence of the permanent, long-lived changes to circulation associated with fault permeability disruption, as opposed to the tem-

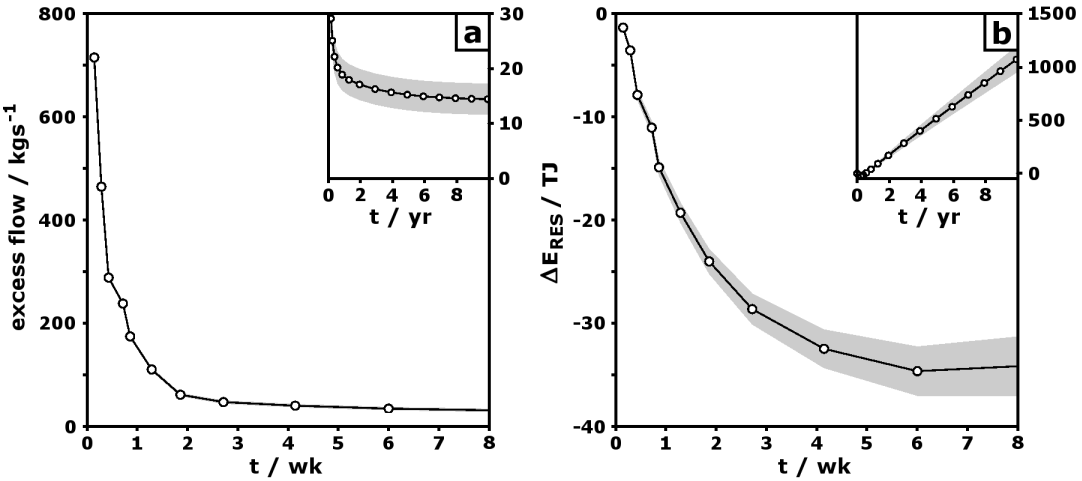

Figure 8.10: Circulation response to both the pore-pressure perturbation and a change in fault plane permeability. (a) Excess mass flow averaged over 100 different simulated fault plane ruptures for a period of eight weeks and ten years (inset). The marked line shows the average excess flow, while the grey region demarcates two standard deviations from the mean profile. (b) Change in reservoir heat content (see Equation 8.4) following changes in fault plane permeability.

porary influence of a pore-pressure perturbation.

8.5.1 Combined simulation

The combined effects of a diffusing pore-pressure disturbance and a fault-core permeability disruption are considered in Figures 8.10 and 8.11. Once more, a set of 100 different fault plane ruptures (Figure 8.4) was generated and ten years of flow simulated with the full-crust pore-pressure disturbance from Section 8.4 superimposed. Heat flux anomalies associated with one of these simulations (corresponding

Figure 8.11 *(following page)*: Anomalous heat flux induced by pore-pressure and fault permeability perturbations at three different times after the earthquake: (a) one day, (b) five days, and (c) sixty-two days. Contours show the change in heat flux, Δq_T, and vectors indicate direction. Note that, in contrast to Figure 8.7, contour intervals and vector magnitudes in (a)-(c) are identical. The position of the fault is indicated by a black and white dashed line. The specific change to fault core permeability applied in this simulation is shown in Figure 8.4.

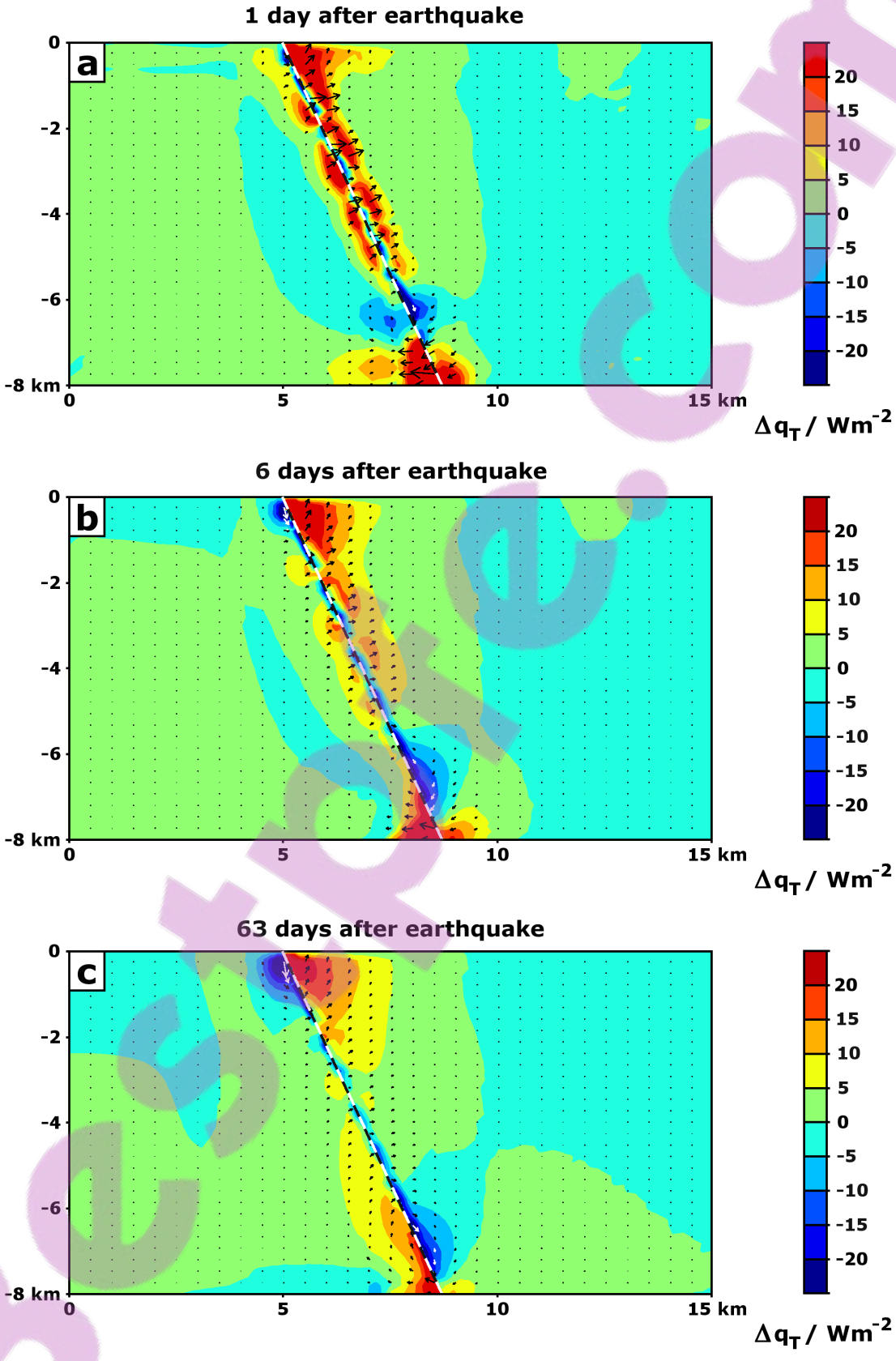
1 day after earthquake
a
0
-2
-4
-6
-8 km
0
5
10
15 km
20
15
10
5
0
-5
-10
-15
-20
Δq_T / Wm^{-2}
6 days after earthquake
b
63 days after earthquake
c

to the permeability disruption shown in Figure 8.4) is shown for three different times following the modelled earthquake (Figure 8.11).

Excess mass flow of the combined pore-pressure/permeability disruption simulations demonstrates characteristics identified in simulations of each of the constituent perturbations (Figures 8.8-8.9). For example, the short-term response is dominated by a large increase in mass flow associated with the near-surface pore-pressure anomaly. Recession of the initial flow-rate over the first two weeks is rapid, and similar to that shown in Figure 8.8(a). However, at longer timescales the permeability effect dominates by imposing, and sustaining, a higher natural-state flow-rate.

This superposition of behaviours is also evident in the reservoir response to the modelled earthquake. On short timescales, i.e., <100 days, the pore-pressure effect dominates (Figures 8.8(b)) and an initial drop in heat content, followed by a slow recovery, is recorded. Over longer time-periods, permanent changes to fault-plane permeability favour a steady heat flux into the reservoir, such that heat content increases at a constant rate over the next ten years (Figure 8.9(b)).

A break-down in the fluid baffling properties of the fault core results in an immediate increase in the cross-fault coupling between circulation in the adjacent fault blocks. Figure 8.11 shows that, in many locations, a reasonably large ($>20\,\mathrm{W\,m^{-2}}$) fault-normal heat-flow anomaly is generated. In the pre-seismic period, cross-fault heat flux was dominantly conductive (>90%) and totalled $\sim$10 MW; immediately following the earthquake this is increased to $\sim$215 MW of heat transfer from the footwall to the hanging wall for depths shallower than 6 km. The effects on heat flux of the near-surface recoil-induced pore-pressure anomaly, and the mid-crustal slip-arrest anomaly in the footwall, detailed in Section 8.4, are also evident at this early stage.

Cross-fault fluid transfer recedes from its initial maximum in the days following the earthquake, and the near-fault heat-flow anomaly widens as the effects of fluid diffusion penetrate further into the fault blocks. Heat flux across the fault plane is reduced to 80 MW after one week, and to 50 MW after two months. The diminished role of the fault as a vertical flow-partition also has an effect on the circulation

mode. Whereas before the low permeability fault core encouraged flow in both fault blocks to localise in an up-dip direction, its reduced effectiveness as a physical flow barrier now permits vertical upflow of footwall fluids into the hanging wall. As a consequence, geothermal upflow migrates from the footwall scarp into the hanging wall and away from the fault. Although not modelled here, permeability sealing of the fault gouge in the post-seismic period as a result of hydrothermal mineralisation would be expected to halt and reverse this migration.

8.6 Chapter summary

Structural permeability has long been considered a key factor in localising and shaping geothermal upflow in the Taupo Volcanic Zone (e.g., Grindley and Browne, 1976; Wood *et al.*, 2001). In this chapter models have been presented for geothermal circulation evolved in the presence of dip-slip faults that operate as fluid baffles. An impermeable fault severely impairs coupling between circulation in the footwall and hanging wall blocks, except via conductive heat transfer across the fault. In the simulations presented here, a 115 MW footwall circulation cell is coupled to a 100 MW hanging wall circulation cell via a 10 MW cross-fault conductive link. Stated differently, when a perfectly insulating fault is modelled, 125 and 90 MW cells are developed in the footwall and hanging wall, respectively.

The fault, operating in a similar manner to the partition in conjugate coupled-convection problems, also serves to localise upflow into its near vicinity. In the footwall, such flow is intuitive, as rising fluids are physically blocked by the fault core and deflected up-dip. In the hanging wall, instead of rising vertically, upflow is also localised along the fault plane; this is probably due to the thermodynamic stability of upflow along a heated partition, and the horizontal hydrostatic pressure of down-flow that occurs elsewhere in the fault block.

In addition to long-term influences on circulation, the model addresses two features of fault rupture that introduce an immediate perturbation to steady-state flow: coseismic changes in pore-pressure and permeability. The pore-pressure perturbation

is derived from a separate, mechanical model for fault rupture on a dip-slip normal fault, and is comprised of a near-surface increase in pressure, and antisymmetric pressure-change lobes at mid-crustal depths. It is shown that deep pressure changes have a negligible effect on surface geothermal expression; in comparison, coseismic recoil of the fault blocks results in a large increase in surface heat and mass flow. However, anomalous flow rates rapidly decline over a period of several weeks as the pore-pressure disturbance is diffused.

In contrast to the pore-pressure perturbation, changes in fault permeability produce a smaller short-term effect on surface expression but play an important role in the longer-term configuration of geothermal circulation. Following an increase in cross-fault permeability, which approximates the damaging effect of fault rupture on impermeable fault gouge, mass flow builds to a new steady-state that is approximately 5% higher than pre-seismic flow rates. This figure is sensitive to the degree of fault damage, e.g., a greater increase in permeability permits a greater increase in mass flow, but, more importantly, results in migration of the locus of geothermal expression. Upflow, which had previously localised in the footwall scarp, now begins to migrate into the hanging wall and away from the fault.

The numerical methods presented here consider one-way coupling between the mechanical and circulation systems, i.e., the earthquake, and its effects, perturb natural-state fluid-flow. In practice, coupling in both the pre- and post-seismic phases is likely two-way to some degree; indeed, diffusion of pore fluids at depth during the post-seismic period can exert control on the subsequent distribution of aftershocks (Miller *et al.*, 2004; Lindman *et al.*, 2010). While the approach employed here accounts for diffusion of pore-fluids at depth, no attempt has been made to represent the reverse coupling. Implementation of this interaction would produce an intriguing feedback loop, in which fault failure induces a fluid flow anomaly, which may induce subsequent failure on other fault planes and further fluid flow anomalies.

Vast, however, as these effects appear, they are in reality insignificant, mere scratches in the paint of the earth in whose history they will leave no permanent record.

- Richard D. Oldham (1858-1936)

9

Summary and conclusions

The first section of this thesis involves the development of a mechanical model of normal dip-slip faulting and details its use as a tool for investigating fault zones over multiple seismic cycles. A description of brittle failure in the upper-crust and ductile flow in the lower-crust is incorporated, enabling the model to capture several fault processes not accounted for by simpler elastic, elastic-plastic, or visco-elastic models. For instance, the depth to which coseismic fault slip penetrates the brittle and semi-brittle crust is not limited by the fault geometry (a modelling artefact), but rather by stress conditions maintained across the brittle-ductile transition. This stress state is obtained during a precursor "spin-up" period, during which extension boundary conditions are applied over long time-periods; as a consequence, a quasi-steady stress state is generated that reflects a realistic crustal rheology, i.e., one limited by brittle failure in the upper-crust, and by ductile flow in the lower.

Chapter 2 discusses self-similar cycles of stress and elastic deformation exhibited by the model over multiple seismic cycles, i.e., the state of dynamic-equilibrium. During an earthquake, the fault blocks displace relative to one another, with a constant dip-slip profile in the upper-crust ($< 6\,\mathrm{km}$) being reduced to zero over an interval of several kilometres in the mid-crust. Associated with the gradients in slip that occur at the fault tip are the largest changes in stress and elastic strain. In the hanging wall, at mid-crustal depths (6-8 km), compression of the rock is observed, while in the

adjacent footwall there is a corresponding expansion. These rock stress changes are incorporated in circulation models in Chapter 8 to quantify the hydrological effects of normal fault earthquakes on TVZ geothermal systems.

Chapter 3 details the use of the mechanical fault model as a tool to explore the evolution of fault zones in rifted settings. Central to this discussion is the concept of an extension budget for the region, i.e., the geodetic opening rate of the rift, applied in the model as a velocity boundary condition, must be accommodated within the rift by some combination of the available deformation mechanisms. In the upper-crust, the available mechanisms are fault slip and the accumulation of frictional plastic strain; elastic strain accumulated during the interseismic period is exchanged for fault slip during the seismic period, and is therefore a transient feature of the extension budget. Components of the extension budget can be inferred for more complex, natural systems. For example, a geodetic extension rate of the centre of the TVZ was obtained from campaign GPS data (Wallace *et al.*, 2004) and indicated opening rates of 10-12 $\mathrm{mm\,yr^{-1}}$. An estimate of the fault-slip component of the extension budget was obtained by Villamor and Berryman (2001) who undertook a fault trenching study across several normal faults in the same region. Their data indicated opening rates of 6.4 $\mathrm{mm\,yr^{-1}}$ at seismogenic depths over the previous 64 kyr, or 50-60% of the total extension rate. Several scenarios account for the shortfall, for example: (i) an underestimated fault-slip component where faults obscured by recent volcanic deposits are not accounted for; (ii) a discrepancy between the geodetic opening rate, representing the present extension rate, and fault slip rates averaged over the previous 64 kyr; or (iii) an unaccounted-for frictional-plastic component, representing displacements on fractures or other failure-planes, possibly localising in the adjacent Taupo-Reporoa Basin (Rowland *et al.*, 2010).

In situations where the geodetic extension rate is not sufficiently accommodated by existing faults, it is of interest to know where the shortfall, accommodated by the accumulation of frictional plastic strain, is occurring. In the model, conjugate frictional plastic shear-bands form in the hanging wall and dip at an angle of 45°. The apparent exclusivity of frictional failure to the hanging wall is explained in terms

of a stress-failure shadow representing the proximity to Mohr-Coulomb failure; this failure shadow flanks the fault and extends disproportionally into the footwall at the surface. In the near fault region, the failure shadow is derived from reduced shear stresses that are periodically lowered by the modelled earthquakes. In the near-surface of the footwall, shear stresses are lowered by horizontal compression associated with coseismic recoil of the fault blocks.

Shallowing of fault dip by rotation of the fault plane during both the seismic and interseismic periods is also observed. During the interseismic period, this deformation is similar to bookshelf or domino rotation (e.g., Wernicke and Burchfiel, 1982), although no fault-parallel displacement occurs. Rather, the rotation is due to an elastic vertical contraction caused by horizontal extension. During the seismic period, a similar sized rotation occurs; however, in the absence of boundary extension, an alternative mechanism must be advanced. It is proposed that coseismic rotation is caused by large changes in rock stress associated with slip-gradients at the fault tip at mid-crustal depths. An expansion in the footwall, and corresponding contraction in the hanging wall, exert a torque on the fault plane about a pivot at a depth of 4.7 km. In response to these two effects, a fault plane rotation rate of 23.5° per million years is calculated, although it is noted that this represents the instantaneous rotation rate. The actual rotation rate should be expected to decrease as the fault shallows towards an angle that is unfavourable for reactivation.

The concepts of an extension budget, stress-failure shadow and fault rotation are drawn together to propose a model for structural evolution in the vicinity of existing normal faults. For a given rift setting, some part of the total extension rate is accommodated by earthquakes on existing faults. The remainder is accommodated as small-scale frictional failure occurring outside the stress-failure shadows of those faults, localising in shear bands that eventually coalesce into new faults. Furthermore, these form preferentially within the hanging wall due to the diminished influence of the stress-failure shadow in this fault block; this is consistent with asymmetric fault migration in the basinward direction, which is observed in the Gulf of Corinth, Greece (Goldsworthy and Jackson, 2001), and other rifts around the world.

At the same time, existing faults rotate backward and eventually become inactive. The continuous operation of fault genesis and death ensure that the extension budget for the rift is never static in composition, but rather components wax and wane in response to the number of active faults in the rift.

In Chapter 4, conservation of energy is invoked and the concept of budgeting is once more applied to describe the seismic cycle in terms of energy flow and work. Earthquakes in compressional and strike-slip regimes are often conceptualised in terms of an interseismic period during which tectonic forces elastically load the crust, followed by a short seismic period during which this energy is released, i.e., an elastic rebound (Reid, 1911). Energy flow, as well as cause and effect, are relatively straightforward to assign in this model. However, for normal earthquakes in extensional settings, several lines of evidence are presented suggesting "tectonic-loading" to be a misnomer. Conceptually, extension applied to an overburdened crust is similar to unloading of a compressed spring. This concept is formalised to consider stress, strain and strain energy changes associated with extension of an arbitrary, unfaulted crustal volume under realistic stress conditions. The derived equations indicate that extension, rather than increasing strain energy, effects a net reduction; however, the principal negative change in volumetric strain energy, ΔEE_{VOL}, masks a smaller positive change in distortional strain energy, ΔEE_{DIS}. Furthermore, ΔEE remains negative with continued extension and increasing differential stress until an inflection point is encountered at $\sigma_{xx} = \frac{1}{3}\sigma_{zz}$. Further extension beyond this point leads to an increase in strain energy, although the stress state at the inflection points is generally not exceeded, as it also corresponds to the brittle failure limit of crustal rocks of typical frictional properties ($\mu = 0.6$).

Construction of an energy/work budget for the mechanical fault model reinforces these conceptual and analytical arguments. During the interseismic period, elastic strain energy trends downward, being dissipated as heat by viscous strain in the lower-crust, frictional-plastic strain in the upper-crust, and a remaining component of external work. This component represents work done *by* the crust in displacing its lateral boundaries, i.e., causing extension. In contrast, during the seismic period

a small increase in elastic strain energy is observed, accompanied by frictional heat generation on the fault. As boundary displacement is negligible during this period, the energy must be derived from work done by the gravitational body force, i.e., by changes in gravitational potential energy (GPE). These energy changes are resolved in space to distinguish contrasting styles of coseismic deformation in the adjacent fault blocks. Surface uplift of the footwall evidences a local increase in GPE, which is derived from a loss of strain energy and expansion at the base of the fault. In the hanging wall, a much larger decrease in GPE, associated with subsidence of the fault block, is responsible for compressing the crust at the base of the fault and increasing strain energy. A component of energy transfer from the footwall to the hanging wall is observed; this is associated with mid-crustal volume changes and the fault plane rotation discussed in Chapter 3. Energy flow in the hanging wall is shown to be inconsistent with an elastic-rebound model; the GPE that drives deformation is pre-existing and is not accumulated during the interseismic period. Instead, during the interseismic period, the balance of forces on the fault plane is altered to promote failure, eventually initiating an earthquake that restores force balance.

The second part of this thesis is concerned with the development of a set of circulation models that investigate several long-term, evolutionary features of TVZ geothermal systems. Heat and mass transport is modelled through a permeable crust for periods of several hundred thousand years using the code FEHM. Circulation is modelled to a depth of 8 km, corresponding to the base of the brittle crust and the convective system, i.e., a mass conserving model. Convection is driven by temperature boundary conditions applied at the base of the model and the circulation state evolves in a crust that is prescribed an exponential permeability-depth relationship. Differing porosity and permeability properties are prescribed to two sub-domains representing different geological components: (i) 2 km of highly porous, Quaternary volcanic deposits, underlain by (ii) fractured, low porosity, greywacke basement rock.

Issues of mass recharge and field stability in large-scale convective systems such as the TVZ are considered in Chapter 6. A model is constructed that approximates circulation in a 50×80 km central section of the TVZ. By applying a two-temperature

hotplate at the base of the model the across-strike heat distribution is calibrated to reproduce the bimodality of the TVZ. Bulk permeability properties and basal temperatures are calibrated against individual field properties of their TVZ counterparts, e.g., area and heat output. The large-scale convective system that is developed is not a representation of the TVZ per se; rather, it is a feasible realisation of a family of convective systems of which the TVZ is also a member. This permits a statistical investigation of the system's properties without needing to assign considerable computational resources to precisely replicate the distribution of TVZ circulation; a task undertaken earlier by Kissling (2004) and Kissling and Weir (2005).

Mass recharge of the geothermal fields in the modelled rift is investigated using a particle back-tracking technique coupled to a random walk that models the effects of dispersion and diffusion. Ensembles of several 10's of thousands of flow-paths, constructed for each of the ten modelled geothermal fields, indicate fluids exiting the crust are between 5 and 50 kyr old, with mean ages of ∼20 kyr. While this is higher than the 12 kyr upper limit based on isotopic analysis of fluids at Wairakei (Stewart, 1978), it is consistent with age estimates of 2 to 38 kyr at Waiotapu (Giggenbach *et al.*, 1994). Further improvements might be obtained through a parametric study of porosity and permeability properties in the greywacke subdomain in which fluids spend approximately 80% of the total transit time. The age of geothermal fluids is also observed to vary with position within the field and may be associated with similar intra-field variety in geochemical composition.

Mass recharge is drawn from minimally overlapping catchment zones adjacent to the boundary of the particular field. These catchment zones range in size from 70 to 500 km^2 with fluids travelling up to 10 km underground before exiting through the field. Rather than being evenly distributed around a field, catchments are asymmetric and not necessarily continuous. Their positions reflect proximity to nearby fields and suggest that determination of catchment zones in single convection cell models may neglect significant effects caused by interactions between fields. Catchment size is linearly related to both field area and output; coefficients of proportionality are order-of-magnitude consistent with 1-D arguments of geothermal circulation

proposed by Weir (2009).

An alternative method for generating geothermal field catchments is outlined and compared against the flow-path method. Voronoi catchments are constructed by the crystal growth method, in which catchment growth rate and area is proportional to the field output. The catchments produced are an acceptable first-order approximation to the flow-path catchments, reproducing the dominance of large fields over smaller ones, as well as the asymmetry in catchment distribution around a field. As knowledge of the subsurface flow field is not required to construct Voronoi catchments, the technique can be applied to the TVZ to generate a set of first-order recharge zones. The distribution of catchments indicates asymmetric recharge for some fields, e.g., southern recharge of Rotokawa and Tauhara, and western recharge of Orakeikorako, and symmetric recharge for others, e.g., Rotorua, Mokai and Ohaaki. Furthermore, a conspicuous gap in the recharge distribution suggests either underestimation of the potential geothermal resource at Horohoro, or crustal properties not typical of the TVZ. Catchments have also been constructed for high-temperature geothermal systems in Iceland; catchments are mostly isolated, except on the Reykjanes Peninsula where fields are spaced closer together and catchments extend into the ocean.

The large-scale model also permits an investigation of field and system stability over a period of 300 kyr, which is on the order of known ages of TVZ geothermal systems. During this time, several fields migrate in position by up to 5 km with instances of two fields merging into a new, larger field observed; in contrast, other fields are stable in position over long time periods. The instability inherent in large-scale TVZ-like convective systems has been documented previously by McLellan *et al.* (2010) and represents a minimum level of volatility that exists in the absence of time-varying magmatic processes at the brittle-ductile transition, or tectonic processes that control structural permeability in the brittle crust. This result has implications for patterns of relic hydrothermal alteration imprinted on the crust within several hundred metres of the surface.

In Chapter 7, the long-term effects of silica transport and deposition on patterns

of geothermal flow is investigated. Assuming an equilibrium gradient reaction regime, the change in porosity due to deposition or dissolution of silica can be related to the mass flux rate and temperature gradient. Coupled porosity and permeability distributions allow the implementation of an iterative update scheme to describe their time evolution with updates occurring every 500-5000 yr.

Silica deposition proceeds at the greatest rate in the near-surface due to the high temperature gradients encountered in the boundary layer, and the high mass fluxes associated with near-surface permeability. A low-permeability cap-zone rapidly forms above the main upflow zone resulting in the lateral deflection of rising fluids and significant lateral heat flows in the reservoir. The migration of surface geothermal expression to the margins of the cap-zone is accompanied by a corresponding migration in the locus of silica deposition; the cap-zone widens in time, spreading a fixed heat output across a wider area. The cap-zone also grows downward, thickening to several hundred metres over a period of 100 kyr; this is consistent with silicification at depths of up to 150 m at the extinct Ohakuri geothermal field (Henneberger and Browne, 1988). In reducing surface heat fluxes, the cap-zone has the dual effect of insulating the geothermal reservoir beneath, increasing temperatures, enthalpies and its potential as an energy bearing resource, and also masking the presence of the resource at the surface. This occurs in two ways; first, by spreading geothermal expression across a wider area such that heat flow anomalies are less distinct; and second, conductive cooling of the cap-zone by the atmosphere lowers the anomalous, near-surface temperature gradient.

Under a gradient reaction regime, the rate of silica deposition depends on the size of the mass flux and temperature gradient; this would intuitively suggest that in a heterogeneous crust the greatest deposition rates should correspond to regions of high permeability. However, the analysis presented here indicates this is only true to a limited extent; the greatest deposition rates occurred in regions where temperature gradient and mass flux are aligned. Indeed, a study of the angle between these two controlling parameters indicates large regions of the upflow zone where mass flux and temperature gradient are perpendicular; these regions could serve as excellent

conduits for mineral transport to the surface, where reorientation of the temperature gradient would result in high rates of deposition.

The self-sealing properties of these geothermal systems in the period following an earthquake has also been investigated. A hypothetical scenario is presented in which a fault rupture renews permeability along a fault plane through the centre of the cap-zone. Heated fluids that had originally taken deflected paths to the surface at the margins of the field, now rise directly through a fissure in the centre. The surface heat output of the field increases by 67% and is accompanied by disruption of the reservoir beneath. However, associated with the increased mass flux along the fault trace is an increased rate of silica deposition, which begins to rapidly seal permeability. In this region, high rates of silica deposition correspond with high permeability. Recovery of pre-earthquake heat flow is achieved by self-sealing 1-5 kyr after the fault rupture.

Finally, in Chapter 8, simulations are presented that investigate the hydrological effects of normal dip-slip earthquakes and their bearing on natural state geothermal systems. A computational domain is meshed using a curvilinear grid, which allows assignment of low permeability values to a narrow (2 m) plane inclined at 65° to the horizontal; this structure represents a mature fault operating as a fluid baffle. A geothermal upflow zone is evolved in the centre of the model domain, along the fault, over a period of 300 kyr; mass recharge occurs on the flanks of the plume. In the footwall, the highest heat and mass transfers occur along the fault plane, where rising fluids are deflected laterally by the physical fluid barrier presented by the fault. At the surface, the greatest geothermal heat output is spread along-strike in the fault scarp; this distribution is similar in size and shape to geothermal expression at Te Kopia geothermal field, located on the Paeroa Fault. In the hanging wall, upflow also localises along the fault plane, although in this case the flow configuration is probably due to a combination of the thermodynamic stability of an upward-directed wall-flow along the fault and the horizontal hydrostatic force of downward recharge occurring in the rest of the fault block.

Following the establishment of natural state circulation, short-term perturbation by two seismic effects is modelled: disturbance of the pore-fluid pressure, and a co-

seismic increase in fault plane permeability. Coseismic changes in pore-fluid pressure are caused by corresponding changes in mean crustal stress; these are obtained from the mechanical fault model and investigations of dip-slip fault rupture detailed in Chapters 2-4. Mean stress, and thus pore-pressure, changes exhibit three main features: (i) a near-surface pressure increase associated with recoil of the fault blocks; (ii) a pressure increase in the hanging wall at mid-crustal depths associated with collapse of the fault block above; and (iii) a corresponding pressure decrease at the same depth in the footwall. These pressure changes are introduced into the natural state model and the hydrological response modelled for a period of ten years. The results indicate that coseismic pore-pressure changes result in large increases in heat and mass transfer for a period of several weeks, but rapidly decay with diffusion of the initial, localised anomaly. Furthermore, only near-surface pressure changes associated with recoil of the fault blocks have an appreciable influence on surface hydrology; the mid-crustal pressure changes are deep enough that their effect is negligible by the time they have diffused to the surface, which occurs several months after the original earthquake.

During fault rupture, the impermeable fault core is damaged and, as a consequence, cross-fault hydrological communication is improved; in the model this is approximated by a step-increase in permeability on the fault plane. Cross-fault coupling between the two flow regimes is increased in the post-seismic period; cross-fault heat transfer increases from a predominantly conductive, pre-seismic value of 10 MW, to a predominantly advective, post-seismic value of 215 MW. The enhanced heat transfer is indicative of a shift in the flow configuration, from one in which the upflow zones of two convection cells are localised along a shared, inclined partition, to one in which a single upflow flow zone intersects both fault blocks in the centre of a non-partitioned domain. In terms of surface geothermal expression, this results in a steady migration of the locus of activity from its original location on the footwall scarp, into the hanging wall and away from the fault. The model also indicates that permeability changes, being, in general, longer-lived than pore-pressure disturbances, have the more significant long-term effect on the geothermal reservoir.

Bibliography

Acocella, V., Korme, T., and Salvini, F. (2003). Formation of normal faults along the axial zone of the Ethiopian Rift. *Journal of Structural Geology*, **25**, 503–513.

Aki, K. (1972). Earthquake mechanism. *Tectonophysics*, **13**, 423–446.

Allis, R. G. (1987). Geophysical and geochemical investigations of the Horohoro geothermal prospect. Technical Report 213, Department of Scientific and Industrial Research.

Anderson, E. M. (1951). *The Dynamics of Faulting*. Edinburgh: Oliver & Boyd.

Anderson, H., Smith, E., and Robinson, R. (1990). Normal faulting in a back arc basin: Seismological characteristics of the March 2, 1987, Edgecumbe, New Zealand, earthquake. *Journal of Geophysical Research*, **95**, 4709–4723.

Andre, B. J. and Rajaram, H. (2005). Dissolution of limestone fractures by cooling waters: Early development of hypogene karst systems. *Water Resources Research*, **41**.

Arehart, G. B., Christenson, B. W., Wood, C. P., Foland, K. A., and Browne, P. R. L. (2002). Timing of volcanic, plutonic and geothermal activity at Ngatamariki, New Zealand. *Journal of Volcanology and Geothermal Research*, **116**, 201–214.

Arehart, G. B., Wood, C. P., Christenson, B. W., Browne, P. R. L., and Foland, K. A. (1997). Timing of volcanism and geothermal activity at Ngatamariki and Rotokawa, New Zealand. In *Proceedings of the 19th NZ Geothermal Workshop*, 117–122.

Arnórsson, S. (1995). Geothermal systems in Iceland: structure and conceptual models - I. High-temperature areas. *Geothermics*, **24**, 561–602.

Arnórsson, S. and Gunnlaugsson, E. (1985). New gas geothermometers for geothermal exploration - Calibration and application. *Geochimica et Cosmochimica Acta*, **49**, 1307–1325.

Aurenhammer, F. (1991). Voronoi Diagrams - A Survey of a Fundamental Geometric Data Structure. *ACM Computing Surveys*, **23**, 345–405.

Barr, D. (1987). Lithospheric stretching, detached normal faulting and footwall uplift. *Geological Society of London Special Publications*, **28**, 75–94.

Barrientos, S. E., Stein, R. S., and Ward, S. N. (1987). Comparison of the 1959 Hebgen Lake, Montana and the 1983 Borah Peak, Idaho, earthquakes from geodetic observations. *Bulletin of the Seismological Society of America*, **77**, 784–808.

Bean, C. J. (1996). On the cause of 1/f-power spectral scaling in borehole sonic logs. *Geophysical Research Letters*, **23**, 3119–3122.

Beanland, S., Blick, G. H., and Darby, D. J. (1990). Normal faulting in a back arc basin: geological and geodetic characteristics of the 1987 Edgecumbe earthquake, New Zealand. *Journal of Geophysical Research*, **95**, 4693–4707.

Bell, R. E., McNeill, L. C., Bull, J. M., Henstock, T. J., Collier, R. E. L., and Leeder, M. R. (2009). Fault architecture, basin structure and evolution of the Gulf of Corinth Rift, central Greece. *Basin Research*, **21**, 824–855.

Berryman, K. R., Villamor, P., Nairn, I., Dissen, R. V., Begg, J., and Lee, J. (2008). Late Pleistocene surface rupture history of the Paeroa Fault, Taupo Rift, New Zealand. *New Zealand Journal of Geology and Geophysics*, **51**, 135–158.

Bertrand, E. A., Caldwell, T. G., Hill, G. J., Wallin, E. L., Bennie, S. L., Cozens, N., Onacha, S. A., Ryan, G. A., Walter, C., Zaino, A., and Wameyo, P. (2012). Magnetotelluric imaging of upper-crustal convection plumes beneath the Taupo Volcanic Zone, New Zealand. *Geophysical Research Letters*, **39**.

Bibby, H. M., Bennie, S. L., Stagpoole, V. M., and Caldwell, T. G. (1994). Resistivity structure of the Waimangu, Waiotapu, Waikite and Reporoa geothermal areas, New Zealand. *Geothermics*, **23**, 445–471.

Bibby, H. M., Caldwell, T. G., Davey, F. J., and Webb, T. H. (1995). Geophysical evidence on the structure of the Taupo Volcanic Zone and its hydrothermal circulation. *Journal of Volcanology and Geothermal Research*, **68**, 29–58.

Bibby, H. M., Risk, G. F., and Caldwell, T. G. (2002). Long offset tensor apparent resistivity surveys of the Taupo Volcanic Zone, New Zealand. *Journal of Applied Geophysics*, **49**, 17–32.

Bibby, H. M., Risk, G. F., Caldwell, T. G., and Bennie, S. L. (2005). Misinterpretation of Electrical Resistivity Data in Geothermal Prospecting: a Case Study from the Taupo Volcanic Zone. *Proceedings of the World Geothermal Congress*, **4**.

Bignall, G. (1994). *Thermal evolution and fluid-rock interactions in the Orakeikorako and Te Kopia geothermal systems*. Ph. D. thesis, University of Auckland.

Bignall, G. (2009). Ngatamariki Geothermal Field Geoscience Overview. Technical report, Institute of Geological & Nuclear Sciences Limited.

Bignall, G. and Browne, P. R. L. (1994). Surface hydrothermal alteration and evolution of the Te Kopia Thermal Area, New Zealand. *Geothermics*, **23**, 645–658.

Bignall, G. and Harvey, C. C. (2005). Geoscientific review of the Kawerau geothermal field. Technical report, Institute of Geological & Nuclear Sciences Limited.

Bignall, G., Sekine, K., and Tsuchiya, N. (2004). Fluid-rock interaction processes in the Te Kopia geothermal field (New Zealand) revealed by SEM-CL imaging. *Geothermics*, **33**, 615–635.

Bons, P. D. (2001). The formation of large quartz veins by rapid ascent of fluids in mobile hydrofractures. *Tectonophysics*, **336**, 1–17.

Bott, M. H. P. (1997). Modeling the formation of a half graben using realistic upper crustal rheology. *Journal of Geophysical Research*, **102**, 24,605–24,617.

Brace, W. F. (1980). Permeability of Crystalline and Argillaceous Rocks. *International Journal of Rock Mechanics, Mining Science & Geomechanics Abstracts*, **17**, 241–251.

Bradshaw, G. A. and Zoback, M. D. (1988). Listric normal faulting, stress refraction, and the state of stress in the Gulf Coast basin. *Geology*, **16**, 271–274.

Braun, J., Thieulot, C., Fullsack, P., DeKool, M., Beaumont, C., and Huismans, R. (2008). DOUAR: A new three-dimensional creeping flow numerical model for the solution of geological problems. *Physics of the Earth and Planetary Interiors*, **171**, 76–91.

Bredehoeft, J. D. and Papadopulos, I. S. (1965). Rates of Vertical Groundwater Movement Estimated from the Earth's Thermal Profile. *Water Resources Research*, **1**, 325–328.

Briggs, R. O. (1999). Effects of Loma Prieta earthquake on surface waters in Waddell Valley. *Water Resources Bulletin*, **27**, 991–999.

Briole, P., Rigo, A., Lyon-Caen, H., Ruegg, J. C., Papazissi, K., Mitsakaki, C., Balodimou, A., Veis, G., Hatzfeld, D., and Deschamps, A. (2000). Active deformation of the Corinth rift, Greece: Results from repeated Global Positioning System surveys between 1990 and 1995. *Journal of Geophysical Research*, **105**, 25,605–25,625.

Browne, P. R. L. (1978). Hydrothermal alteration in active geothermal fields. *Annual Review of Earth and Planetary Sciences*, **6**, 229–250.

Browne, P. R. L. (1979). Minimum age of the Kawerau geothermal field, North Island, New Zealand. *Journal of Volcanology and Geothermal Research*, **6**, 213–215.

Browne, P. R. L., Graham, I. J., Parker, R. J., and Wood, C. P. (1992). Subsurface andesite lavas and plutonic rocks in the Rotokawa and Ngatamariki geothermal systems, Taupo Volcanic Zone, New Zealand. *Journal of Volcanology and Geothermal Research*, **51**, 199–215.

Bruce, C. H. (1984). Smectite dehydration: Its relation to structural development and hydrocarbon accumulation in northern Gulf of Mexico basin. *American Association of Petroleum Geologists Bulletin*, **68**, 673–683.

Brun, J. P., Sokoutis, D., and Driessche, J. V. D. (1994). Analogue modeling of detachment fault systems and core complexes. *Geology*, **22**, 319–322.

Bryan, C. J., Sherburn, S., Bibby, H. M., Bannister, S. C., and Hurst, A. W. (1999). Shallow seismicity of the central Taupo Volcanic Zone, New Zealand: its distribution and nature. *New Zealand Journal of Geology and Geophysics*, **42**, 533–542.

Buck, W. R. (1988). Flexural rotation of normal faults. *Tectonics*, **7**, 959–973.

Buiter, S. J. H. (2012). A review of brittle compressional wedge models. *Tectonophysics*, **530-531**.

Buiter, S. J. H., Babeyko, A. Y., Ellis, S., Gerya, T. V., Kaus, B. J. P., Kellner, A., Schreurs, G., and Yamada, Y. (2006). The numerical sandbox: comparison of model results for a shortening and an extension experiment. In S. J. H. Buiter and G. Schreurs (Eds.), *Analogue and Numerical Modelling of Crustal-Scale Processes*, Volume 253, 29–64. Geological Society of London Special Publication.

Burnell, J. and Kissling, W. (2009). Ngatamariki reservoir model. Technical Report 2355, Industrial Research Limited.

Byerlee, J. (1993). Model for episodic flow of high-pressure water in fault zones before earthquakes. *Geology*, **21**, 303–306.

Byerlee, J. D. (1978). Friction of rocks. *Pure and Applied Geophysics*, **116**, 393–402.

Caine, J. S., Bruhn, R. L., and Forster, C. B. (2010). Internal structure, fault rocks, and inferences regarding deformation, fluid flow, and mineralization in the seismogenic Stillwater normal fault, Dixie Valley, Nevada. *Journal of Structural Geology*, **32**, 1576–1589.

Caine, J. S., Evans, J. P., and Forster, C. B. (1996). Fault zone architecture and permeability structure. *Geology*, **24**, 1025–1028.

Canora-Catalan, C., Villamor, P., Berryman, K. R., Martinez-Diaz, J. J., and Raen, T. (2008). Rupture history of the Whirinaki Fault, an active normal fault in the Taupo Rift, New Zealand. *New Zealand Journal of Geology and Geophysics*, **51**, 277–293.

Cathles, L. M., Erendi, A. H. J., and Barrie, T. (1997). How Long Can a Hydrothermal System Be Sustained by a Single Intrusive Event. *Economic Geology*, **92**, 766–771.

Chandrasekhar, S. (1961). *Hydrodynamic and Hydromagnetic Stability.* New York, NY: Dover Publications.

Chapman, D. S. (1986). Thermal gradients in the continental crust. *Geological Society of London Special Publications*, **24**, 63–70.

Charlier, B. L. A., Wilson, C. J. N., Lowenstern, J. B., Blake, S., Calsteren, P. W. V., and Davidson, J. P. (2005). Magma generation at a large, hyperactive silicic volcano (Taupo, New Zealand) revealed by U-Th and U-Pb systematics in zircons. *Journal of Petrology*, **46**, 3–32.

Chaudhuri, A., Rajaram, H., and Viswanathan, H. (2008). Alteration of fractures by precipitation and dissolution in gradient reaction environments: Computational results and stochastic analysis. *Water Resources Research*, **44**.

Chaudhuri, A., Rajaram, H., and Viswanathan, H. (2012). Fracture alteration by precipitation resulting from thermal gradients: Upscaled mean aperture-effective transmissivity relationship. *Water Resources Research*, **48**.

Chaudhuri, A., Rajaram, H., Viswanathan, H., Zyvoloski, G., and Stauffer, P. (2009). Buoyant convection resulting from dissolution and permeability growth in vertical limestone fractures. *Geophysical Research Letters*, **36**.

Chinnery, M. A. (1961). The deformation of the ground around surface faults. *Bulletin of the Seismological Society of America*, **50**, 355–372.

Christenson, B. W., Mroczek, E. K., Kennedy, B. M., van Soest, M. C., Stewart, M. K., and Lyon, G. (2002). Ohaaki reservoir chemistry: characteristics of an arc-type hydrothermal system in the Taupo Volcanic Zone, New Zealand. *Journal of Volcanology and Geothermal Research*, **115**, 53–82.

Clarke, P. J., Davies, R. R., England, P. C., Parsons, B. E., Billiris, H., Paradissis, D., Veis, G., Denys, P. H., Cross, P. A., Ashkenazi, V., and Bingley, R. (1997). Geodetic estimate of seismic hazard in the Gulf of Korinthos. *Geophysical Research Letters*, **24**, 1303–1306.

Clearwater, E. K., O'Sullivan, M. J., Brockbank, K., and Mannington, W. I. (2012). Modeling the Ohaaki geothermal system. In *Proceedings, TOUGH Symposium.*

Cline, J. S., Bodnar, R. J., and Rimstidt, J. D. (1992). Numerical simulation of fluid flow and silica transport and deposition in boiling hydrothermal solutions: application to epithermal gold deposits. *Journal of Geophysical Research*, **97**, 9085–9103.

Cook, N. G. W., Hoek, E., Pretorius, J. P. G., Ortlepp, W. D., and Salamon, M. D. G. (1966). Rock mechanics applied to the study of rockbursts. *Journal of the South African Institute of Mining and Metallurgy*, **66**, 435–528.

Cooke, M. L. and Murphy, S. (2004). Assessing the work budget and efficiency of fault systems using mechanical models. *Journal of Geophysical Research*, **109**.

Coumou, D., Driesner, T., and Heinrich, C. A. (2008). The Structure and Dynamics of Mid-Ocean Ridge Hydrothermal Systems. *Science*, **321**, 1825–1828.

Cowie, P. A. (1998). A healing-reloading feedback control on the growth rate of seismogenic faults. *Journal of Structural Geology*, **20**, 1075–1087.

Cowie, P. A. and Roberts, G. P. (2001). Constraining slip rates and spacings for active normal faults. *Journal of Structural Geology*, **23**, 1901–1915.

Cowie, P. A., Underhill, J. R., Behn, M. D., Lin, J., and Gill, C. E. (2005). Spatio-temporal evolution of strain accumulation derived from multi-scale observations of Late Jurassic rifting in the northern North Sea: A critical test of models for lithospheric extension. *Earth and Planetary Science Letters*, **234**, 401–419.

Craig, H. (1963). The isotopic geochemistry of water and carbon in geothermal areas. In E. Tongiorgi (Ed.), *Nuclear Geology of Geothermal Areas*, 17–53.

Crampin, S. (1994). The fracture criticality of crustal rocks. *Geophysical Journal International*, **118**, 428–438.

Crider, J. G. and Pollard, D. D. (1998). Fault linkage: Three-dimensional mechanical interaction between echelon normal faults. *Journal of Geophysical Research*, **103**, 24,373–24,391.

Croucher, A. E. and O'Sullivan, M. J. (2008). Application of the computer code TOUGH2 to the simulation of supercritical conditions in geothermal systems. *Geothermics*, **37**, 622–634.

Cruz, L., Malinski, J., Wilson, A., Take, W. A., and Hilley, G. (2010). Erosional control of the kinematics and geometry of fold-and-thrust belts imaged in physical and numerical sandbox. *Journal of Geophysical Research*, **115**.

Curewitz, D. and Karson, A. J. (1998). Geological consequences of dike intrusion at mid-ocean ridge spreading centers. In W. R. Buck, P. T. Delaney, J. A. Karson, and Y. Lgabrielle (Eds.), *Faulting and Magmatism at Mid-Ocean Ridges*, Volume 106, 117–136.

Darby, D. J., Hodgkinson, K. M., and Blick, G. H. (2000). Geodetic measurement of deformation in the Taupo Volcanic Zone, New Zealand: the north Taupo network revisited. *New Zealand Journal of Geology and Geophysics*, **43**, 157–170.

Darcy, H. (1856). Les Fontaines Publiques de la Ville de Dijon. Technical report, French Imperial Corps of Bridges, Highways, and Mines.

Dart, C., Cohen, H. A., Akyüz, H. S., and Barka, A. (1995). Basinward migration of rift-border faults: Implications for facies distributions and preservation potential. *Geology*, **23**, 69–72.

Dassaut Systèmes Simulia Corp. (2008). Abaqus/standard. v6.8, Providence, RI.

Dawers, N. H., Anders, M. H., and Scholz, C. H. (1993). Growth of normal faults: Displacement-length scaling. *Geology*, **21**, 1107–1110.

Del Castello, M. and Cooke, M. L. (2007). Underthrusting-accretion cycle: Work budget as revealed by the boundary element method. *Journal of Geophysical Research*, **112**.

Dempsey, D. E., Archer, R. A., Ellis, S. M., and Rowland, J. V. (2012a). Hydrological effects of dip-slip fault rupture on natural geothermal circulation. *Journal of Geophysical Research*, **In review**.

Dempsey, D. E., Ellis, S. M., Archer, R. A., and Rowland, J. V. (2012b). Energetics of normal earthquakes on dip-slip faults. *Geology*, **40**, 279–282.

Dempsey, D. E., Ellis, S. M., Rowland, J. V., and Archer, R. A. (2012c). The role of frictional plasticity in the evolution of normal fault systems. *Journal of Structural Geology*, **39**.

Dempsey, D. E., Langhorne, P. J., Robinson, N. J., Williams, M. J. M., Haskell, T. G., and Frew, R. D. (2010). Observation and modeling of platelet ice fabric in McMurdo Sound, Antarctica. *Journal of Geophysical Research*, **115**.

Dempsey, D. E., Rowland, J. V., Archer, R. A., and Ellis, S. M. (2011). Modelling geothermal circulation in a "TVZ-like" setting. In *Proceedings of the 32nd New Zealand Geothermal Workshop*.

Dempsey, D. E., Rowland, J. V., Zyvoloski, G. A., and Archer, R. A. (2012e). Modeling the effects of silica deposition and fault rupture on natural geothermal systems. *Journal of Geophysical Research*, **117**.

Dempsey, D. E., Simmons, S., Archer, R. A., and Rowland, J. V. (2012d). Delineation of catchment zones of geothermal systems in large-scale rift systems. *Journal of Geophysical Research*, **117**.

Deng, K., Zhou, S., Wang, R., Robinson, R., Zhao, C., and Cheng, W. (2010). Evidence that the 2008 M_W 7.9 Wenchuan Earthquake Could Not Have Been Induced by the Zipingpu Reservoir. *Bulletin of the Seismological Society of America*, **100**, 2805–2814.

Dieterich, J. H. (1979). Modeling of Rock Friction 1. Experimental Results and Constitutive Equations. *Journal of Geophysical Research*, **84**, 2161–2168.

Dobson, P. F., Kneafsey, T. J., Hulen, J., and Simmons, A. (2003). Porosity, permeability, and fluid flow in the Yellowstone geothermal system, Wyoming. *Journal of Volcanology and Geothermal Research*, **123**, 313–324.

Dolan, S. S., Bean, C. J., and Riollet, B. (1998). The broad-band fractal nature of heterogeneity in the upper crust from petrophysical logs. *Geophysical Journal International*, **132**, 489–507.

Drake, B., Campbell, K., Rowland, J., Guido, D., and Rae, A. (2012). Mangatete: evolution of a paleo-hydrothermal system, Taupo Volcanic Zone (TVZ). In *Proceedings of the 33nd New Zealand Geothermal Workshop*.

Ebinger, C. J. (1989). Tectonic development of the western branch of the East African rift system. *Geological Society of America Bulletin*, **101**, 885–903.

Ellis, A. J. and Wilson, S. H. (1955). The heat from the Wairakei-Taupo thermal region calculated from the chloride output. *New Zealand Journal of Science and Technology*, **36**, 622–631.

Ellis, S. M., Beavan, J., Eberhart-Phillips, D., and Stöckhert, B. (2006). Simplified models of the Alpine Fault seismic cycle: stress transfer in the mid-crust. *Geophysical Journal International*, **166**, 386–402.

Facca, G. and Tonani, F. (1965). The self-sealing geothermal field. In *Proceedings IAV International Symposium on Volcanology (New Zealand)*, 271–273.

Ferguson, G. and Grasby, S. E. (2011). Thermal springs and heat flow in North America. *Geofluids*, **11**, 294–301.

Ferrill, D. A. and Morris, A. P. (2001). Displacement gradient and deformation in normal fault systems. *Journal of Structural Geology*, **23**, 619–638.

Feyen, L., Dessalegn, A. M., Smedt, F. D., Gebremeskel, S., and Batelaan, O. (2004). Application of a Bayesian Approach to Stochastic Delineation of Capture Zones. *Ground Water*, **42**, 542–551.

Fisher, D. M. and Brantley, S. L. (1992). Models of quartz overgrowth and vein formation: deformation and episodic fluid flow in an ancient subduction zone. *Journal of Geophysical Research*, **97**, 20,043–20,061.

Flotté, N., Sorel, D., Müller, C., and Tensi, J. (2005). Along strike changes in the structural evolution over a brittle detachment fault: Example of the Pleistocene Corinth-Patras rift (Greece). *Tectonophysics*, **403**, 77–94.

Flóvenz, O. G. and Sæmundsson, K. (1993). Heat flow and geothermal processes in Iceland. *Tectonophysics*, **225**, 123–138.

Floyd, M. A., Billiris, H., Paradissis, D., Veis, G., Avallone, A., Briole, P., McClusky, S., Nocquet, J. M., Palamartchouk, K., Parsons, B., and England, P. C. (2010). A new velocity field for Greece: Implications for the kinematics and dynamics of the Aegean. *Journal of Geophysical Research*, **115**.

Forster, C. and Smith, L. (1989). The Influence of Groundwater Flow on Thermal Regimes in Mountainous Terrain: A Model Study. *Journal of Geophysical Research*, **94**, 9439–9451.

Fournier, R. O. (1977). Chemical geothermometers and mixing models for geothermal systems. *Geothermics*, **5**, 41–50.

Fournier, R. O. and Potter, R. W. (1982). An equation correlating the solubility of quartz in water from 25 °C to 900 °C at pressures up to 10,000 bars. *Geochimica et Cosmochimica Acta*, **46**, 1969–1973.

Freeze, R. A. (1994). Henry Darcy and the Fountains of Dijon. *Ground Water*, **32**, 23–30.

Freund, L. B. and Barnett, D. M. (1976). A two-dimensional analysis of surface deformation due to dip-slip faulting. *Bulletin of the Seismological Society of America*, **66**, 667–675.

Fridleifsson, G. O. and Elders, W. A. (2005). The Iceland Deep Drilling Project: a search for deep unconventional geothermal resources. *Geothermics*, **34**, 269–285.

Frind, E. O., Molson, J. W., and Rudolph, D. L. (2006). Well Vulnerability: A Quantitative Approach for Source Water Protection. *Ground Water*, **44**, 732–742.

Frind, E. O., Muhammad, D. S., and Molson, J. W. (2002). Delineation of Three-Dimensional Well Capture Zones for Complex Multi-Aquifer Systems. *Ground Water*, **40**, 586–598.

Gelhar, L. W., Welty, C., and Rehfeldt, K. R. (1992). A Critical Review of Data on Field-Scale Dispersion in Aquifers. *Water Resources Research*, **28**, 1955–1974.

Gerdes, M. L., Baumgartner, L. P., and Person, M. (1998). Convective fluid flow through heterogeneous country rocks during contact metamorphism. *Journal of Geophysical Research*, **103**, 23,983–24,003.

Giggenbach, W. F. (1982). Carbon-13 exchange between CO_2 and CH_4 under geothermal conditions. *Geochimica et Cosmochimica Acta*, **46**, 159–165.

Giggenbach, W. F. (1995). Variations in the chemical and isotopic composition of fluids discharged from the Taupo Volcanic Zone, New Zealand. *Journal of Volcanology and Geothermal Research*, **68**, 89–116.

Giggenbach, W. F., Sheppard, D. S., Robinson, B. W., Stewart, M. K., and Lyon, G. L. (1994). Geochemical structure and position of the Waiotapu geothermal field, New Zealand. *Geothermics*, **23**, 599–644.

Glover, R. B. and Mroczek, E. K. (2009). Chemical changes in natural features and well discharges in response to production at Wairakei, New Zealand. *Geothermics*, **38**, 117–133.

Glynn-Morris, T., King, T., and Winmill, R. (2009). Drilling history and evolution at Wairakei. *Geothermics*, **38**, 30–39.

Goldsworthy, M. and Jackson, J. (2001). Migration of activity within normal fault systems: examples from the Quaternary of mainland Greece. *Journal of Structural Geology*, **23**, 489–506.

Goode, D. J. (1996). Direct simulation of groundwater age. *Water Resources Research*, **32**, 289–296.

Grant, M. A. and Bixley, P. F. (2011). *Geothermal Reservoir Engineering (Second Edition)*. Burlington, MA: Academic Press.

Gravely, D. M., Wilson, C. J. N., Leonard, G. S., and Cole, J. W. (2007). Double trouble: Paired ignimbrite eruptions and collateral subsidence in the Taupo Volcanic Zone, New Zealand. *Geological Society of America Bulletin*, **119**, 18–30.

Grecksch, G., Roth, F., and Kümpel, H. J. (1999). Coseismic well-level changes due to the 1992 Roermond earthquake compared to static deformation of half-space solutions. *Geophysical Journal International*, **138**, 470–478.

Grindley, G. W. (1960). *Sheet 8 Taupo, Geological map of New Zealand 1:250 000*. Wellington, New Zealand: DSIR.

Grindley, G. W. (1965). The Geology, Structure and Exploitation of the Wairakei Geothermal Field, Taupo, New Zealand. *Department of Scientific and Industrial Research Bulletin*, **75**.

Grindley, G. W. (1982). The deeper structure of the Wairakei geothermal field. In *Proceedings of the Pacific Geothermal Conference*, 69–74.

Grindley, G. W. and Browne, P. R. L. (1976). Structural and hydrological factors controlling the permeabilities of some hot-water geothermal fields. In *Proceedings of the 2nd United Nations Symposium on the Development and Use of Geothermal Resources*, 377–386.

Grindley, G. W., Mumme, T. C., and Kohn, B. P. (1994). Stratigraphy, paleomagnetism, geochronology and structure of silicic volcanic rocks, Waiotapu/Paeroa range area, New Zealand. *Geothermics*, **23**, 473–499.

Gudmusson, A. (2004). Effects of Young's modulus on fault displacement. *Comptes Rendus Geosciences*, **336**, 85–92.

Gupta, A. and Scholz, C. H. (1998). Utility of elastic models in predicting fault displacement fields. *Journal of Geophysical Research*, **103**, 823–834.

Gupta, S., Cowie, P. A., Dawers, N. H., and Underhill, J. R. (1998). A mechanism to explain rift-basin subsidence and stratigraphic patterns through fault-array evolution. *Geology*, **26**, 595–598.

Haar, L., Gallagher, J. S., and Kell, G. S. (1984). *NBS/NRC Steam Tables*. New York: Hemisphere.

Hanks, T. C. and Kanamori, H. (1979). A Moment Magnitude Scale. *Journal of Geophysical Research*, **84**, 2348–2350.

Hassanzadeh, H., Pooladi-Darvish, M., and Keith, D. W. (2009). The Effect of Natural Flow of Aquifers and Associated Dispersion on the Onset of Buoyancy-Driven Convection in a Saturated Porous Medium. *American Institute of Chemical Engineers Journal*, **55**, 475–485.

Hedenquist, J. W. (1990). The thermal and geochemical structure of the Broadlands-Ohaaki geothermal system, New Zealand. *Geothermics*, **19**, 151–185.

Heffer, K. J. (2007). Proximity to a critical point: evidence from, and implications for, hydrocarbon reservoirs. *Geological Society of London Special Publications*, **289**, 227–239.

Heffer, K. J. and Bevan, T. G. (1990). Scaling Relationships in Natural Fractures: Data, Theory, and Application. *Society of Petroleum Engineers Paper*, **20981**.

Heise, W., Bibby, H. M., Caldwell, T. G., Bannister, S. C., Ogawa, Y., Takakura, S., and Uchida, T. (2007). Melt distribution beneath a young continental rift: The Taupo Volcanic Zone. *Geophysical Research Letters*, **34**.

Heise, W., Caldwell, T. G., Bibby, H. M., and Bannister, S. C. (2008). Three-dimensional modelling of magnetotelluric data from the Rotokawa geothermal field, Taupo Volcanic Zone, New Zealand. *Geophysical Journal International*, **173**, 740–750.

Henk, A. (2006). Stress and strain during fault-controlled lithospheric extension - insights from numerical experiments. *Tectonophysics*, **415**, 39–55.

Henneberger, R. C. and Browne, P. R. L. (1988). Hydrothermal alteration and evolution of the Ohakuri hydrothermal system, Taupo Volcanic Zone, New Zealand. *Journal of Volcanology and Geothermal Research*, **34**, 211–231.

Hetland, E. A. and Hager, B. H. (2006). The effects of rheological layering on post-seismic deformation. *Geophysical Journal International*, **166**, 277–292.

Hochstein, M. P. (1995). Crustal heat transfer in the Taupo Volcanic Zone (New Zealand): comparison with other volcanic arcs and explanatory heat source models. *Journal of Volcanology and Geothermal Research*, **68**, 117–151.

Hocking, M. W. A., Hannington, M. D., Percival, J. B., Stoffers, P., Schwarz-Schampera, U., and de Ronde, C. E. J. (2010). Clay alteration of volcaniclastic material in a submarine geothermal system, Bay of Plenty, New Zealand. *Journal of Volcanology and Geothermal Research*, **191**, 180–192.

Horton, B. K. and Schmitt, J. G. (1998). Development and exhumation of a Neogene sedimentary basin during extension, east-central Nevada. *Geological Society of America Bulletin*, **110**, 163–172.

Horton, C. W. and Rogers, F. T. (1945). Convection currents in a porous medium. *Journal of Applied Physics*, **16**, 367–370.

Houghton, B. F., Wilson, C. J. N., McWilliams, M. O., Lanphere, M. A., Weaver, S. D., Briggs, R. M., and Pringle, M. S. (1995). Chronology and dynamics of a large silicic magmatic system: Central Taupo Volcanic Zone, New Zealand. *Geology*, **23**, 13–16.

Huismans, R. S., Buiter, S. J. H., and Beaumont, C. (2005). Effect of plastic-viscous layering and strain softening on mode selection during lithospheric extension. *Journal of Geophysical Research*, **110**.

Hulston, J. R. and Lupton, J. E. (1996). Helium isotope studies of geothermal fields in the Taupo Volcanic Zone, New Zealand. *Journal of Volcanology and Geothermal Research*, **74**.

Hunt, T. M., Glover, R. B., and Wood, C. P. (1994). Waimangu, Waiotapu, and Waikite geothermal systems, New Zealand: background and history. *Geothermics*, **23**, 379–400.

Hurst, A. W., Bibby, H. M., and Robinson, R. R. (2002). Earthquake focal mechanisms in the central Taupo Volcanic Zone and their relation to faulting and deformation. *New Zealand Journal of Geology and Geophysics*, **45**, 527–536.

Husen, S., Taylor, R., Smith, R. B., and Healser, H. (2004). Changes in geyser eruption behavior and remotely triggered seismicity in Yellowstone National Park produced by the 2002 M 7.9 Denali fault earthquake, Alaska. *Geology*, **32**, 537–540.

Ikari, M. J., Saffer, D. M., and Marone, C. (2009). Frictional and hydrologic properties of clay-rich fault gouge. *Journal of Geophysical Research*, **114**.

Illies, J. H. (1972). he Rhine Graben rift system - plate tectonics and transform faulting. *Geophysical Surveys*, **1**, 27–60.

Ingebritsen, S. E., Geiger, S., Hurwitz, S., and Driesner, T. (2010). Numerical simulation of magmatic hydrothermal systems. *Reviews of Geophysics*, **48**.

Ingebritsen, S. E. and Rojstaczer, S. A. (1996). Geyser periodicity and the response of geysers to deformation. *Journal of Geophysical Research*, **101**, 21,891–21,905.

Isacks, B., Oliver, J., and Sykes, L. R. (1968). Seismology and the new global tectonics. *Journal of Geophysical Research*, **73**, 5855–5899.

Jackson, J. (1999). Fault death: a perspective from actively deforming regions. *Journal of Structural Geology*, **21**, 1003–1010.

Jackson, J. and McKenzie, D. (1983). The geometrical evolution of normal fault systems. *Journal of Structural Geology*, **5**, 471–482.

Janecke, S. U., Vandenburg, C. J., and Blankenau, J. J. (1998). Geometry, mechanisms and significance of extensional folds from examples in the Rocky Mountain Basin and Range province, U.S.A. *Journal of Structural Geology*, **20**, 841–856.

Jupp, T. and Schultz, A. (2000). A thermodynamic explanation for black smoker temperatures. *Letters to Nature*, **403**, 880–882.

Kahveci, K. (2007). Natural Convection in a Partitioned Vertical Enclosure Heated With a Uniform Heat Flux. *Journal of Heat Transfer*, **129**, 717–726.

Kanamori, H. (2001). Energy budget of earthquakes and seismic efficiency. *International Geophysics*, **76**, 293–305.

Kaus, B. J. P. (2010). Factors that control the angle of shear bands in geodynamic numerical models of brittle deformation. *Tectonophysics*, **484**, 36–47.

Kawano, Y. and Ohashi, T. (2006). Numerical simulation of development of sea ice microstructure under temperature gradient. In *Proceedings of the 18th IAHR International Symposium on Ice*, 97–103.

Kennedy, B. M. and van Soest, M. C. (2007). Flow of Mantle Fluids Through the Ductile Lower Crust: Helium Isotope Trends. *Science*, **318**, 1433–1436.

Ketilsson, J., Björnsson, H., Halldórsdóttir, S., and Axelsson, G. (2009). Production Capacity of High Temperature Geothermal Systems in Iceland. Technical Report OS-2009/09, Orkustofnun.

Kim, Y.-S., Peacock, D. C. P., and Sanderson, D. J. (2004). Fault damage zones. *Journal of Structural Geology*, **26**, 503–517.

King, G. C. P., Stein, R. S., and Rundle, J. B. (1988). The Growth of Geological Structures by Repeated Earthquakes. *Journal of Geophysical Research*, **93**, 13,307–13,318.

Kiryukhin, A. V. (1996). Modeling studies: the Dachny geothermal reservoir, Kamchatka, Russia. *Geothermics*, **25**, 63–90.

Kissling, W. M. (1998). Source models for the TVZ geothermal fields. In *Proceedings 20th New Zealand Geothermal Workshop*, 147–152.

Kissling, W. M. (1999). Modeling of cooling plutons in the Taupo Volcanic Zone, New Zealand. In *Proceedings 24th Workshop on Geothermal Reservoir Engineering*, 1–7.

Kissling, W. M. (2004). *Large-scale hydrology of the Taupo Volcanic Zone, New Zealand*. Ph. D. thesis, University of Auckland.

Kissling, W. M. and Ellis, S. M. (2011). Modelling the flow of hydrothermal fluids above an evolving continental rift. In *Proceedings of the 32nd New Zealand Geothermal Workshop*.

Kissling, W. M. and Weir, G. J. (2005). The spatial distribution of the geothermal fields in the Taupo Volcanic Zone, New Zealand. *Journal of Volcanology and Geothermal Research*, **145**, 136–150.

Kitanidis, P. K. (1994). Particle-tracking equations for the solution of the advection-dispersion equation with variable coefficients. *Water Resources Research*, **30**, 3225–3227.

Kobayashi, K. and Sugihara, K. (2002). Crystal Voronoi diagram and its applications. *Future Generation Computer Systems*, **18**, 681–692.

Koseluk, R. A. and Bischke, R. E. (1981). An elastic rebound model for normal fault earthquakes. *Journal of Geophysical Research*, **86**, 1081–1090.

Koukouvelas, I. K. and Doutsos, T. T. (1996). Implications of structural segmentation during earthquakes: the 1995 Egion earthquake, Gulf of Corinth, Greece. *Journal of Structural Geology*, **18**, 1381–1388.

Kunstmann, H. and Kinzelbach, W. (2000). Computation of stochastic wellhead protection zones by combining first-order second-moment method and Kolmogorov backward equation analysis. *Journal of Hydrology*, **237**, 127–146.

Kusznir, N. J., Marsden, G., and Egan, S. S. (1991). A flexural-cantilever simple-shear/pure-shear model of continental lithosphere extension: applications to the Jeanne d'Arc Basin, Grand Banks and Viking Graben, North Sea. *Geological Society of London Special Publications*, **56**, 41–60.

Lamarche, G., Barnes, P. M., and Bull, J. M. (2006). Faulting and extension rate over the last 20,000 years in the offshore Whakatane Graben, New Zealand continental shelf. *Tectonics*, **25**.

Lapwood, E. R. (1948). Convection of a fluid in a porous medium. *Proceedings Cambridge Philosophical Society*, **44**, 508–521.

Leary, P. (1991). Deep borehole log evidence for fractal distribution of fractures in crystalline rock. *Geophysical Journal International*, **107**, 615–627.

Leary, P. C. (2002). Fractures and physical heterogeneity in crustal rock. In J. A. Goff and K. Hollinger (Eds.), *Heterogeneity in the crust and upper mantle: Nature, scaling and seismic properties*, 155–186. Kluwer Academic.

Leary, P. C. and Al-Kindy, F. (2002). Power-law scaling of spatially correlated porosity and log(permeability) sequences from north-central North Sea Brae oilfield well core. *Geophysical Journal International*, **148**, 426–442.

Lewis, D. V. (1960). Relationships of ore bodies to dikes and sills. *Economic Geology*, **50**, 495–516.

Lewis, K. C. and Lowell, R. P. (2009). Numerical modeling of two-phase flow in the NaCl-H_2O system: Introduction of a numerical method and benchmarking. *Journal of Geophysical Research*, **114**.

Li, Y.-G., Vidale, J. E., Day, S. M., Oglesby, D. D., , and Cochran, E. (2003). Postseismic fault healing on the rupture zone of the 1999 M 7.1 Hector Mine, California, Earthquake. *Bulletin of the Seismological Society of America*, **93**, 854–869.

Lindman, M., Lund, B., and Roberts, R. (2010). Spatiotemporal characteristics of aftershock sequences in the South Iceland Seismic Zone: interpretation in terms of pore pressure diffusion and poroelasticity. *Geophysical Journal of Research*, **183**, 1104–1118.

López, D. L. and Smith, L. (1995). Fluid flow in fault zones: Analysis of the interplay of convective circulation and topographically driven groundwater flow. *Water Resources Research*, **31**, 1489–1503.

López, D. L. and Smith, L. (1996). Fluid flow in fault zones: Influence of hydraulic anisotropy and heterogeneity on the fluid flow and heat transfer regime. *Water Resources Research*, **32**, 3227–3235.

Lowell, R. P. and Burnell, D. K. (1991). Mathematical modeling of conductive heat transfer from a freezing, convecting magma chamber to a single-pass hydrothermal system: implications for seafloor black smokers. *Earth and Planetary Science Letters*, **104**, 59–69.

Manga, M., Brodsky, E. E., and Boone, M. (2003). Response of streamflow to multiple earthquakes. *Geophysical Research Letters*, **30**.

Manning, C. E. and Ingebritsen, S. E. (1999). Permeability of the continental crust: implications of geothermal data and metamorphic systems. *Reviews of Geophysics*, **37**, 127–150.

Mannington, W., O'Sullivan, M., and Bullivant, D. (2004). Computer modelling of the Wairakei-Tauhara geothermal system, New Zealand. *Geothermics*, **33**, 401–419.

Mansinha, L. and Smylie, D. E. (1971). The displacement field of inclined faults. *Bulletin of the Seismological Society of America*, **61**, 1433–1449.

Marcelpoil, R. and Usson, Y. (1992). Methods for the Study of Cellular Sociology: Voronoi Diagrams and Parameterization of the Spatial Relationships. *Journal of Theoretical Biology*, **154**, 359–369.

Martin, J. T. and Lowell, R. P. (2000). Precipitation of quartz during high-temperature, fracture-controlled hydrothermal upflow at ocean ridges: Equilibrium versus linear kinetics. *Journal of Geophysical Research*, **105**, 869–882.

Matthäi, S. K., Heinrich, C. A., and Driesner, T. (2004). Is the Mount Isa copper deposit the product of forced brine convection in the footwall of a major reverse fault. *Geology*, **32**, 357–360.

McClay, K. R. and Ellis, P. G. (1987). Geometries of extensional fault systems developed in model experiments. *Geology*, **15**, 341–344.

McGarr, A. (1994). Some comparisons between mining-induced and laboratory earthquakes. *Pure and Applied Geophysics*, **142**, 467–489.

McKenzie, D. (1978). Active tectonics of the Alpine-Himalayan belt: the Aegean Sea and surrounding regions. *Geophysical Journal of the Royal Astronomical Society*, **55**, 217–254.

McKenzie, D., Nimmo, F., Jackson, J. A., Gans, P. B., and Miller, E. L. (2000). Characteristics and consequences of flow in the lower crust. *Journal of Geophysical Research*, **105**, 11,029–11,046.

McLellan, J. G., Oliver, N. H. S., Hobbs, B. E., and Rowland, J. V. (2010). Modelling fluid convection stability in continental faulted rifts with applications to the Taupo Volcanic Zone, New Zealand. *Journal of Volcanology and Geothermal Research*, **190**, 109–122.

McNabb, A. (1975). Geothermal physics. Applied Mathematics Technical Report 32, Department of Scientific and Industrial Research.

McNabb, A. (1992). The Taupo-Rotorua hot-plate. In *Proceedings 14th New Zealand Geothermal Workshop*, 111–114.

McNeill, L. C., Cotterill, C. J., Henstock, T. J., Bull, J. M., Stefatos, A., Collier, R. E. L., Paptheoderou, G., Ferentinos, G., and Hicks, S. E. (2005). Active faulting within the offshore western Gulf of Corinth, Greece: Implications for models of continental rift deformation. *Geology*, **33**, 241–244.

Melosh, H. J. and Williams Jr., C. A. (1989). Mechanics of Graben Formation in Crustal Rocks: A Finite Element Analysis. *Journal of Geophysical Research*, **94**, 13,921–13,973.

Micklethwaite, S. and Cox, S. F. (2004). Fault-segment rupture, aftershock-zone fluid flow, and mineralization. *Geology*, **32**, 813–816.

Miller, S. A., Collettini, C., Chiaraluce, L., Cocco, M., Barchi, M., and Kaus, B. J. P. (2004). Aftershocks driven by a high-pressure CO_2 source at depth. *Letters to Nature*, **427**, 724–727.

Mogi, K., Mochizuki, H., and Kurokawa, Y. (1989). Temperature changes in an artesian spring at Usami in the Izu Peninsula (Japan) and their relation to earthquakes. *Tectonophysics*, **159**, 95–108.

Montgomery, D. R., Greenberg, H. M., and Smith, D. T. (2003). Streamflow response to the Nisqually earthquake. *Earth and Planetary Science Letters*, **209**, 19–28.

Montgomery, D. R. and Manga, M. (2003). Streamflow and Water Well Responses to Earthquakes. *Science*, **300**, 2047–2049.

Moore, J. C. and Vrolijk, P. (1992). Fluids in accretionary prisms. *Reviews of Geophysics*, **30**, 113–135.

Moreno, L., Tsang, Y. W., Tsang, C. F., Hale, F. V., and Neretnieks, I. (1988). Flow and Tracer Transport in a Single Fracture: A Stochastic Model and Its Relation to Some Field Observations. *Journal of Geophysical Research*, **24**, 2033–2048.

Morrow, C. A., Shi, L. Q., and Byerlee, J. D. (1984). Permeability of Fault Gouge Under Confining Pressure and Shear Stress. *Journal of Geophysical Research*, **89**, 3193–3200.

Mortimer, N. (1994). Origin of the Torlesse terrane and coeval rocks, North Island, New Zeland. *International Geology Review*, **36**, 891–9101.

Mouslopoulou, V., Nicol, A., Little, T. A., and Walsh, J. J. (2007). Displacement transfer between intersecting regional strike-slip and extensional fault systems. *Journal of Structural Geology*, **29**, 100–116.

Muhuri, S. K., Dewers, T. A., Jr., T. E. S., and Reches, Z. (2003). Interseismic fault strengthening and earthquake-slip instability: Friction or cohesion? *Geology*, **31**, 881–884.

Muir-Wood, R. (1994). Earthquakes, strain-cycling and the mobilization of fluids. In J. Parnell (Ed.), *Geofluids: Origin, Migration and Evolution of Fluids in Sedimentary Basins*, 85–98. Geological Society Special Publication.

Muir-Wood, R. and King, G. C. P. (1993). Hydrological Signatures of Earthquake Strain. *Journal of Geophysical Research*, **98**, 22,035–22,068.

Nairn, I., Wood, C. P., and Bailey, R. A. (1994). The Reporoa Caldera, Taupo Volcanic Zone: source of the Kaingaroa Ignimbrites. *Bulletin of Volcanology*, **56**, 529–537.

Nairn, I. A. and Cole, J. W. (1981). Basalt dikes in the 1886 Tarawera Rift. *New Zealand Journal of Geology and Geophysics*, **24**, 585–592.

Nairn, I. A., Hedenquist, J. W., Villamor, P., Berryman, K. R., and Shane, P. A. (2005). The ∼AD1315 Tarawera and Waiotapu eruptions, New Zealand: contemporaneous rhyolite and hydrothermal eruptions driven by an arrested basalt dike system. *Bulletin of Volcanology*, **67**, 186–193.

Needleman, A. (1988). Material rate dependence and mesh sensitivity in localization problems. *Computer Methods in Applied Mechanics and Engineering*, **67**, 69–85.

Neupauer, R. M. and Wilson, J. L. (2003a). Backward location and travel time probabilities for a decaying contaminant in an aquifer. *Journal of Contaminant Hydrology*, **66**, 39–58.

Neupauer, R. M. and Wilson, J. L. (2003b). Numerical Implementation of a Backward Probabilistic Model of Ground Water Contamination. *Ground Water*, **42**, 175–189.

Neuzil, C. E. (2003). Hydromechanical coupling in geologic processes. *Hydrogeology Journal*, **11**, 41–83.

Nicol, A., Mazengarb, C., Chanier, F., Rait, G., Uruski, C., and Wallace, L. (2007). Tectonic evolution of the active Hikurangi subduction margin, New Zealand, since the Oligocene. *Tectonics*, **26**.

Nicol, A. and Wallace, L. M. (2007). Temporal stability of deformation rates: Comparison of geological and geodetic observations, Hikurangi subduction margin, New Zealand. *Earth and Planetary Science Letters*, **258**, 397–413.

Nicol, A., Walsh, J., Berryman, K., and Villamor, P. (2006). Interdependence of fault displacement rates and paleoearthquakes in an active rift. *Geology*, **34**, 865–868.

Nield, D. A. and Bejan, A. (1998). *Convection in Porous Media (Second Edition)*. New York: Springer.

Nüchter, J.-A. and Ellis, S. M. (2010). Complex states of stress during the normal faulting seismic cycle: Role of midcrustal postseismic creep. *Journal of Geophysical Research*, **115**.

Nur, A., Ron, H., and Scotti, O. (1986). Fault mechanics and the kinematics of block rotations. *Geology*, **14**.

O'Brien, G. S., Bean, C. J., and McDermott, F. (2003). Numerical investigations of passive and reactive flow through generic single fractures with heterogeneous permeability. *Earth and Planetary Science Letteres*, **213**, 271–284.

Oglesby, D. D., Archuleta, R. J., and Nielsen, S. B. (1998). Earthquakes on dipping faults: the effects of broken symmetry. *Science*, **280**, 1055–1059.

Oglesby, D. D., Archuleta, R. J., and Nielsen, S. B. (2000). The three-dimensional dynamics of dipping faults. *Bulletin of the Seismological Society of America*, **90**, 616–628.

Okada, Y. (1985). Surface deformation due to shear and tensile faults in a half-space. *Bulletin of the Seismological Society of America*, **75**, 1135–1154.

Okada, Y. (1992). Internal deformation due to shear and tensile faults in a half-space. *Bulletin of the Seismological Society of America*, **82**, 1018–1040.

Olsen, M. P., Scholz, C. H., and Léger, A. (1998). Healing and sealing of a simulated fault gouge under hydrothermal conditions: Implications for fault healing. *Journal of Geophysical Research*, **103**, 7421–7430.

O'Sullivan, M. J., Yeh, A., and Mannington, W. I. (2009). A history of numerical modelling of the Wairakei geothermal field. *Geothermics*, **38**, 155–168.

Paterson, M. S. and Luan, F. S. (1990). Quartzite rheology under geological conditions, in: *Deformation Mechanisms, Rheology and Tectonics. Geological Society of London Special Publication*, **54**, 299–307.

Phillips, O. M. (1979). *Flow and Reactions in Permeable Rocks.* U. K.: Cambridge University Press.

Pollard, D. D. and Fletcher, R. C. (2005). *Fundamentals of Structural Geology.* Cambridge, U. K.: Cambridge University Press.

Popov, A. A. and Sobolev, S. V. (2008). SLIM3D: A tool for three-dimensional thermomechanical modeling of lithospheric deformation with elasto-visco-plastic rheology. *Physics of the Earth and Planetary Interiors*, **171**, 55–75.

Poulos, S. J., Castro, G., and France, J. W. (1985). Liquefaction Evaluation Procedure. *Journal of Geotechnical Engineering ASCE*, **111**, 772–792.

Price, R. C., Gamble, J. A., Smith, I. E. M., Smith, R. B., Eggins, S., and Wright, I. C. (2005). An integrated model for the temporal evolution of andesites and rhyolites and crustal development in New Zealand's North Island. *Journal of Volcanology and Geothermal Research*, **140**, 1–24.

Profett, J. M. J. (1977). Cenozoic geology of the Yerington district, Nevada, and implications for the nature and origin of Basin and Range faulting. *Geological Society of America Bulletin*, **88**, 247–266.

Puskas, C. M., Smith, R. B., Meertens, C. M., and Chang, W. L. (2007). Crustal deformation of the Yellowstone-Snake River Plain volcano-tectonic system: Campaign and continuous GPS observations, 1987-2004. *Journal of Geophysical Research*, **112**.

Quilty, E. G. and Roeloffs, E. A. (1997). Water-Level Changes in Response to the 20 December 1994 Earthquake near Parkfield, California. *Bulletin of the Seismological Society of America*, **87**, 310–3174.

Rabinowicz, M., Broulégue, J., and Genthon, P. (1998). Two- and three-dimensional modeling of hydrothermal convection in the sedimented Middle Valley segment, Juan de Fuca Ridge. *Journal of Geophysical Research*, **103**, 24,045–24,065.

Ranalli, G. and Murphy, D. C. (1987). Rheological stratification of the lithosphere. *Tectonophysics*, **132**, 281–295.

Rayleigh, L. (1916). On convection currents in a horizontal layer of fluid where the higher temperature is on the under side. *Philosophical Magazine*, **32**, 529–546.

Regenauer-Lieb, K. and Yuen, D. A. (1998). Rapid conversion of elastic energy into plastic shear heating during incipient necking of the lithosphere. *Geophysical Research Letters*, **25**, 2737–2740.

Reid, H. F. (1911). The elastic-rebound theory of earthquakes. *Bulletin of the Department of Geology, University of California*, **6**, 413–444.

Rice, J. R. and Cleary, M. P. (1976). Some Basic Stress Diffusion Solutions for Fluid-Saturated Elastic Porous Media With Compressible Constituents. *Reviews of Geophysics and Space Physics*, **14**, 227–241.

Rimstidt, J. D. and Barnes, H. L. (1980). The kinetics of silica-water reactions. *Geochimica et Cosmochimica Acta*, **44**, 1683–1699.

Risk, G. F., Caldwell, T. G., and Bibby, H. M. (1994). Deep resistivity surveys in the Waiotapu-Waikite-Reporoa region, New Zealand. *Geothermics*, **23**, 423–443.

Robinson, A. and Gluyas, J. (1992). Model calculations of loss of porosity in sandstones as a result of compaction and quartz cementation. *Marine and Petroleum Geology*, **9**, 319–323.

Rock., G. and Kupfersberger, H. (2002). Numerical delineation of transient capture zones. *Journal of Hydrology*, **269**, 134–149.

Rogan, M. (1982). A geophysical study of the Taupo Volcanic Zone, New Zealand. *Journal of Geophysical Research*, **87**, 4073–4088.

Rohais, S., Eschard, R., Ford, M., Guillocheau, F., and Moretti, I. (2007). Stratigraphic architecture of the Plio-Pleistocene infill of the Corinth Rift: Implications for its structural evolution. *Tectonophysics*, **440**, 5–28.

Rojstaczer, S. and Wolf, S. (1992). Permeability changes associated with large earthquakes: An example from Loma Prieta, California. *Geology*, **20**, 211–214.

Rojstaczer, S., Wolf, S., and Michel, R. (1995). Permeability enhancement in the shallow crust as a cause of earthquake-induced hydrological changes. *Letters to Nature*, **373**, 237–239.

Rosenberg, M. D., Bignall, G., and Rae, A. J. (2009). The geological framework of the Wairakei-Tauhara Geothermal System, New Zealand. *Geothermics*, **38**, 72–84.

Rowan, C. J. and Roberts, A. P. (2008). Widespread remagnetizations and a new view of the Neogene tectonic rotations within the Australia-Pacific plate boundary zone, New Zealand. *Journal of Geophysical Research*, **113**.

Rowland, J. V., Baker, E., Ebinger, C. J., Keir, D., Kidane, T., Biggs, J., Hayward, N., and Wright, T. J. (2007). Fault growth at a nascent slow-spreading ridge: 2005 Dabbahu rifting episode, Afar. *Geophysical Journal International*, **171**, 1226–1246.

Rowland, J. V. and Sibson, R. H. (2001). Extensional fault kinematics within the Taupo Volcanic Zone, New Zealand: soft-linked segmentation of a continental rift system. *New Zealand Journal of Geology and Geophysics*, **44**, 271–283.

Rowland, J. V. and Sibson, R. H. (2004). Structural controls on hydrothermal flow in a segmented rift system, Taupo Volcanic Zone, New Zealand. *Geofluids*, **4**, 259–283.

Rowland, J. V. and Simmons, S. F. (2012). Hydrologic, Magmatic, and Tectonic Controls on Hydrothermal Flow, Taupo Volcanic, Zone, New Zealand: Implications for the Formation of Epithermal Vein Deposits. *Economic Geology*, **107**, 427–457.

Rowland, J. V., Wilson, C. J. N., and Gravley, D. M. (2010). Spatial and temporal variations in magma-assisted rifting, Taupo Volcanic Zone, New Zealand. *Journal of Volcanology and Geothermal Research*, **190**, 89–108.

Rubin, A. M. and Pollard, D. D. (1982). Dike-induced faulting in rift zones of Iceland and Afar. *Geology*, **16**, 413–417.

Rudnick, R. L. and Fountain, D. M. (1995). Nature and composition of the continental crust: a lower crustal perspective. *Reviews of Geophysics*, **33**, 267–309.

Rudnicki, J. W. and Rice, J. R. (1975). Conditions for the localization of deformation in pressure-sensitive dilatant materials. *Journal of the Mechanics and Physics of Solids*, **23**, 371–394.

Ruina, A. (1983). Slip Instability and State Variable Friction Laws. *Journal of Geophysical Research*, **88**, 10,359–10,370.

Rundle, J. B. (1980). Static Elastic-Gravitational Deformation of a Layered Half Space by Point Couple Sources. *Journal of Geophysical Research*, **85**.

Saar, M. O. and Manga, M. (2004). Depth dependence of permeability in the Oregon Cascades inferred from hydrogeologic, thermal, seismic, and magmatic modeling constraints. *Journal of Geophysical Research*, **109**.

Sakakibar, M., Amaya, H., Mori, S., and Tanimoto, A. (1992). Conjugate heat transfer between two natural convections separated by a vertical plate. *International Journal of Heat and Mass Transfer*, **35**, 2289–2297.

Salve, R. and Oldenburg, C. M. (2001). Water flow within a fault in altered nonwelded tuff. *Water Resources Research*, **37**, 3043–3056.

Sanchez, V. I., Murphy, M. A., Dupre, W. R., Ding, L., and Zhang, R. (2010). Structural evolution of the Neogene Gar Basin, western Tibet: Implications for releasing bend development and drainage patterns. *Geological Society of America Bulletin*, **122**, 926–945.

Schellert, W. P. (2007). North-eastward subduction followed by slab detachment to explain ophiolite obduction and Early Miocene volcanism in Northland, New Zealand. *Terra Nova*, **19**, 211–218.

Schlische, R. W., Young, S. S., Ackermann, R. V., and Gupta, A. (1996). Geometry and scaling relations of a population of very small rift-related normal faults. *Geology*, **24**, 683–686.

Scholz, C. H. (1988). The brittle-plastic transition and the depth of seismic faulting. *Geologische Rundschau*, **77**, 319–328.

Scholz, C. H. (1990). *The Mechanics of Earthquakes and Faulting*. New York, NY: Cambridge University Press.

Scholz, C. H. (1998). Earthquakes and friction laws. *Nature*, **391**, 37–42.

Scholz, C. H. (2002). *The Mechanics of Earthquakes and Faulting*. Cambridge University Press, New York.

Scholz, C. H. and Engelder, J. T. (1976). The role of asperity indentation and ploughing in rock friction: I. Asperity creep and stick slip. *International Journal of Rock Mechanics and Mining Science*, **13**, 149–154.

Schueller, S., Gueydan, F., and Davy, P. (2010). Mechanics of the transition from localized to distributed fracturing in layered brittle-ductile systems. *Tectonophysics*, **484**, 48–59.

Schulze-Makuch, D. (2005). Longitudinal Dispersivity Data and Implications for Scaling Behavior. *Ground Water*, **43**, 443–456.

Scott, B. J. and Cody, A. D. (2000). Response of the Rotorua geothermal system to exploitation and varying management regimes. *Geothermics*, **29**, 573–592.

Seebeck, H. and Nicol, A. (2009). Dike intrusion and displacement accumulation at the intersection of the Okataina Volcanic Centre and Paeroa Fault zone, Taupo Rift, New Zealand. *Tectonophysics*, **475**, 575–585.

Segall, P. (2010). *Earthquake and Volcano Deformation*. Princeton University Press, Princeton, New Jersey.

Sharp, W. E. (1960). The deposition of hydrothermal quartz and calcite. *Economic Geology*, **60**, 1635–1644.

Sherburn, S., Bannister, S., and Bibby, H. (2003). Seismic velocity structure of the central Taupo Volcanic Zone, New Zealand, from local earthquake tomography. *Journal of Volcanology and Geothermal Research*, **122**, 69–88.

Sibson, R. H. (1974). Frictional constraints on thrust, wrench and normal faults. *Nature*, **249**, 542–544.

Sibson, R. H. (1977). Fault rocks and fault mechanisms. *Journal of the Geological Society of London*, **133**, 191–213.

Sibson, R. H. (1985). A note on fault reactivation. *Journal of Structural Geology*, **7**, 751–754.

Sibson, R. H. (1990). Conditions for fault-valve behaviour. *Geological Society of London Special Publications*, **54**, 15–28.

Sibson, R. H. (1994). Crustal stress, faulting and fluid flow. In J. Parnell (Ed.), *Geofluids: Origin, Migration and Evolution of Fluids in Sedimentary Basins*, Volume 78, 69–84. Geological Society.

Sibson, R. H. (1996). Structural permeability of fluid-driven fault-fracture meshes. *Journal of Structural Geology*, **18**, 1031–1042.

Sibson, R. H. (2000). Fluid involvement in normal faulting. *Journal of Geodynamics*, **29**, 469–499.

Simmons, S. F. and Browne, P. R. L. (2000). Hydrothermal minerals and precious metals in the Broadlands-Ohaaki geothermal system: implications for understanding low-sulfidation epithermal environments. *Economic Geology*, **95**, 971–999.

Simmons, S. F., Keywood, M., Scott, B. J., and Keam, R. F. (1993). Irreversible change of the Rotomahana-Waimangu hydrothermal system (New Zealand) as a consequence of a volcanic eruption. *Geology*, **21**, 643–646.

Simmons, S. F., Stewart, M. K., Robinson, B. W., and Glover, R. B. (1994). The chemical and isotopic composition of thermal waters at Waimangu, New Zealand. *Geothermics*, **23**, 539–553.

Skempton, A. W. (1954). The pore-pressure coefficients *A* and *B*. *Geotechnique*, **4**, 143–147.

Smith, L. and Chapman, D. S. (1983). On the Thermal Effects of Groundwater Flow 1. Regional Scale Systems. *Journal of Geophysical Research*, **88**, 593–608.

Smith, R. B. and Bruhn, R. L. (1984). Intraplate extensional tectonics of the Eastern Basin-Range: inferences on structural style from seismic reflection data, regional tectonics, and thermal-mechanical models of brittle-ductile deformation. *Journal of Geophysical Research*, **89**, 5733–5762.

Soengkono, S. (1999). Te Kopia geothermal system (New Zealand) - the relationship between its structure and extent. *Geothermics*, **28**, 767–784.

Stauffer, P. H., Auer, L. H., and Rosenberg, N. D. (1997). Compressible gas in porous media: a finite amplitude analysis of natural convection. *International Journal of Heat and Mass Transfer*, **40**, 1585–1589.

Stein, R. S., King, G. C. P., and Rundle, J. B. (1988). The Growth of Geological Structures by Repeated Earthquakes 2. Field Examples of Continental Dip-Slip Faults. *Journal of Geophysical Research*, **93**, 13,319–13,331.

Steiner, A. (1953). Hydrothermal rock alteration at Wairakei, New Zealand. *Economic Geology*, **48**, 1–13.

Stern, T. A. (1987). Asymmetric back-arc spreading, heat flux and structure associated with the Central Volcanic Region of New Zealand. *Earth and Planetary Science Letters*, **85**, 265–276.

Stern, T. A., Stratford, W. R., and Salmon, M. L. (2006). Subduction evolution and mantle dynamics at a continental margin: Central North Island, New Zealand. *Reviews of Geophysics*, **44**, Paper 2005RG000171.

Stewart, J. H. (1980). Regional tilt patterns of late Cenozoic basin-range fault blocks, western United States. *Geological Society of America Bulletin*, **91**, 460–464.

Stewart, M. (1978). Stable isotopes in waters from the Wairakei geothermal area, New Zealand. *DSIR Bulletin*, **220**, 113–119.

Stimac, J., Nordquist, G., Suminar, A., and Sirad-Azwar, L. (2008). An overview of the Awibengkok geothermal system, Indonesia. *Geothermics*, **37**, 300–331.

Stow, D. A. V., Bishop, C. D., and Mills, S. J. (1982). Sedimentology of the Brae oilfield, North Sea: fan models and controls. *Journal of Petroleum Geology*, **5**, 129–148.

Stratford, W. R. and Stern, T. A. (2006). Crust and upper mantle structure of a continental backarc: central North Island, New Zealand. *Geophysical Journal International*, **166**, 469–484.

Strauss, J. M. and Schubert, G. (1977). Thermal convection of water in a porous medium: effects of temperature and pressure dependent thermodynamic and transport properties. *Journal of Geophysical Research*, **82**, 325–333.

Szymczak, P. and Ladd, A. J. C. (2004). Microscopic simulations of fracture dissolution. *Geophysical Research Letters*, **31**.

Talwani, P. and Acree, S. (1985). Pore Pressure Diffusion and the Mechanism of Reservoir-Induced Seismicity. *Pure and Applied Geophysics*, **122**, 947–965.

Talwani, P., Cobb, J. S., and Schaeffer, M. F. (1999). In situ measurements of hydraulic properties of a shear zone in northwestern South Carolina. *Journal of Geophysical Research*, **104**, 14,993–15,003.

Tarantola, A., Ruegg, J. C., and Lepine, J. C. (1979). Geodetic evidence for rifting in Afar: A brittle-elastic model of the behaviour of the lithosphere. *Earth and Planetary Science Letters*, **45**, 435–444.

Taymaz, T., Jackson, J., and McKensie, D. (1991). Active tectonics of the north and central Aegean Sea. *Geophysical Journal International*, **106**, 433–490.

Thatcher, W. and Rundle, J. B. (1984). A viscoelastic coupling model for cyclic deformation due to periodically repeated earthquakes at subduction zones. *Journal of Geophysical Research*, **89**, 7631–7640.

Thompson, G. E. K. (1980). Temperature gradients within and adjacent to the Taupo Volcanic Zone. *New Zealand Journal of Geology and Geophysics*, **23**, 407–412.

Townend, J. and Zoback, M. D. (2000). How faulting keeps the crust strong. *Geology*, **28**, 399–402.

Tsang, C. F. and Neretnieks, I. (1998). Flow channeling in heterogeneous fractured rocks. *Reviews of Geophysics*, **36**, 275–298.

Tyvand, P. A. (1977). Heat dispersion effect on thermal conductivity in anisotropic porous media. *Journal of Hydrology*, **34**, 335–342.

Uffink, G. (1989). Application of Kolmogrov's backward equation in random walk simulations of groundwater contaminant transport. In D. Kobus and W. Kinzelbach (Eds.), *Contaminant Transport in Groundwater*, 283–289. Brookfield.

Van Dissen, R. J., Berryman, K., Webb, T., Stirling, M., Villamor, P., Wood, P. R., Nathan, S., Nicol, A., Begg, J., Barrel, D., McVerry, G., Langridge, R., Litchfield, N., and Pace, B. (2003). An interim classification of New Zealand's active faults for the mitigation of surface rupture hazard. In *Proceedings of the 2003 Pacific Conference on Earthquake Engineering*, Number Paper Number 155, 1–8.

Vandemeulebrouck, J., Hurst, A. W., and Scott, B. J. (2008). The effects of hydrothermal eruptions and a tectonic earthquake on a cycling crater lake (Inferno Crater Lake, Waimangu, New Zealand). *Journal of Volcanology and Geothermal Research*, **178**, 271–275.

Varol, Y., Oztop, H. F., and Koca, A. (2010). Effects of inclination angle on conduction-natural convection in divided enclosures filled with different fluids. *International Communications in Heat and Mass Transfer*, **37**, 182–191.

Vassolo, S., Kinzelbach, W., and Schäfer, W. (1998). Determination of well head protection zone by stochastic inverse modeling. *Journal of Hydrology*, **206**, 268–280.

Villamor, P. and Berryman, K. R. (2001). A late Quaternary extension rate in the Taupo Volcanic Zone, New Zealand, derived from fault slip data. *New Zealand Journal of Geology and Geophysics*, **44**, 243–269.

Villamor, P. and Berryman, K. R. (2006). Evolution of the southern termination of the Taupo Rift, New Zealand. *New Zealand Journal of Geology and Geophysics*, **49**, 23–37.

Walderhaug, O. (1994). Precipitation rates for quartz cement in sandstones determined by fluid-inclusion microthermometry and temperature history modeling. *Journal of Sedimentary Research*, **A64**, 324–333.

Wallace, L., Beavan, J., McCaffrey, R., and Darby, D. J. (2004). Subduction zone coupling and tectonic block rotations in the North Island, New Zealand. *Journal of Geophysical Research*, **109**.

Walsh, J. J., Nicol, A., and Childs, C. (2002). An alternative model for the growth of faults. *Journal of Structural Geology*, **24**, 1669–1675.

Wang, C. Y. and Chia, Y. (2008). Mechanism of water level changes during earthquakes: Near field versus intermediate field. *Geophysical Research Letters*, **35**.

Wang, C. Y. and Manga, M. (2010). Hydrologic responses to earthquakes and a general metric. *Geofluids*, **10**, 206–216.

Weir, G. J. (2009). A mathematical model of rainfall-controlled geothermal fields. *Transport in Porous Media*, **77**, 323–334.

Weissel, J. K. and Karner, G. D. (1989). Flexural uplift of rift flanks due to mechanical unloading of the lithosphere. *Journal of Geophysical Research*, **94**, 13,919–13,950.

Wells, D. L. and Coopersmith, K. J. (1994). New empirical relationships among magnitude, rupture length, rupture width, rupture area, and surface displacement. *Bulletin of the Seismological Society of America*, **84**, 974–1002.

Wernicke, B. (1995). Low-angle normal faults and seismicity: A review. *Journal of Geophysical Research*, **100**, 20,159–20,174.

Wernicke, B. and Burchfiel, B. C. (1982). Modes of extensional tectonics. *Journal of Structural Geology*, **4**, 105–115.

Westaway, R. (1992). Analysis of tilting near normal faults using calculus of variations: implications for upper crustal stress and rheology. *Journal of Structural Geology*, **14**, 857–971.

Westaway, R. (1999). The mechanical feasibility of low-angle normal faulting. *Tectonophysics*, **308**, 407–443.

White, N. C. and Hedenquist, J. W. (1990). Epithermal environments and styles of mineralization: variations and their causes, and guidelines for exploration. *Journal of Geochemical Exploration*, **36**, 445–474.

Williams, R. E. (1968). Space-Filling Polyhedron: Its Relation to Aggregates of Soap Bubbles, Plant Cells, and Metal Crystallites. *Science*, **161**, 276–277.

Wilson, C. J. N. (1993). Stratigraphy, chronology, styles and dynamics of late Quaternary eruptions from Taupo volcano, New Zealand. *Philosophical Transactions of the Royal Society of London*, **A343**, 205–306.

Wilson, C. J. N., Charlier, B. L. A., Rowland, J. V., and Browne, P. R. L. (2010). U-Pb dating of zircon in subsurface, hydrothermally altered pyroclastic deposits and implications for subsidence in a magmatically active rift: Taupo Volcanic Zone, New Zealand. *Journal of Volcanology and Geothermal Research*, **191**, 69–78.

Wilson, C. J. N., Gravley, D. M., Leonard, G. S., and Rowland, J. V. (2009). Volcanism in the central Taupo Volcanic Zone, New Zealand: tempo, styles and controls. In T. Thordarson, S. Self, G. Larsen, S. K. Rowland, and A. Hoskuldsson (Eds.), *Studies in Volcanology: The Legacy of George Walker*, Volume 2, 225–247. Geological Society.

Wilson, C. J. N., Houghton, B. F., and Lloyd, E. F. (1986). Volcanic history and evolution of the Maroa-Taupo area, central North Island. *Royal Society of New Zealand Bulletin*, **23**, 194–223.

Wilson, C. J. N., Houghton, B. F., McWilliams, M. O., Lanphere, M. A., Weaver, S. D., and Briggs, R. M. (1995). Volcanic and structural evolution of Taupo Volcanic Zone, New Zealand: a review. *Journal of Volcanology and Geothermal Research*, **68**, 1–28.

Wilson, C. J. N., Rogan, A. M., Smith, I. E. M., Northey, D. J., Nairn, I. A., and Houghton, B. F. (1984). Caldera volcanoes of the Taupo Volcanic Zone, New Zealand. *Journal of Geophysical Research*, **89**, 8463–8484.

Wood, B. D., Cherblanc, F., Quintard, M., and Whitaker, S. (2003). Volume averaging for determining the effective dispersion tensor: Closure using periodic unit cells and comparison with ensemble averaging. *Water Resources Research*, **39**.

Wood, C. P. (1992). Geology of the Rotorua geothermal system. *Geothermics*, **21**, 25–41.

Wood, C. P. (1994a). Aspects of the geology of Waimangu, Waiotapu, Waikite and Reporoa geothermal systems, Taupo Volcanic Zone, New Zealand. *Geothermics*, **23**, 401–421.

Wood, C. P. (1994b). The Waiora formation geothermal aquifer, Taupo Volcanic Zone, New Zealand. In *Proceedings 16th NZ Geothermal Workshop*, 121–126.

Wood, C. P. (1996). Basement geology and structure of TVZ geothermal fields, New Zealand. In *Proceedings 18th NZ Geothermal Workshop*, 157–162.

Wood, C. P., Brathwaite, R. L., and Rosenberg, M. D. (2001). Basement structure, lithology and permeability at Kawerau and Ohaaki geothermal fields, New Zealand. *Geothermics*, **30**, 461–481.

Wooding, R. A. (1978). Large-scale geothermal field parameters and convection theory. *New Zealand Journal of Science*, **21**, 219–228.

Zhang, S., Paterson, M. S., and Cox, S. F. (1994). Porosity and permeability evolution during hot isostatic pressing of calcite aggregates. *Journal of Geophysical Research*, **99**, 15,741–15,760.

Zhang, Y. and Huang, F. (2011). Mechanism of Different Coseismic Water-Level Changes in Wells with Similar Epicentral Distances of Intermediate Field. *Bulletin of the Seismological Society of America*, **101**, 1531–1541.

Zhang, Y., Person, M., Merino, E., and Szpakiewcz, M. (2005). Evaluation of soluble benzene migration in the Uinta Basin. *Geofluids*, **5**, 106–123.

Zoback, M. D., Daniel, M., Mastin, L., and Anderson, R. N. (1985). Well bore breakouts and in situ stress. *Journal of Geophysical Research*, **90**, 5523–5530.

Zyvoloski, G. (1983). Finite element methods for geothermal reservoir simulation. *International Journal for Numerical and Analytical Methods in Geomechanics*, **7**, 75–86.

Zyvoloski, G. (2007). FEHM: A control volume finite element code for simulating subsurface multi-phase multi-fluid heat and mass transfer. *Los Alamos National Laboratory Document LAUR-07-3359*.